Efficient computation techniques for Galerkin MoM antenna design

Efficient computation techniques

for Galerkin MoM antenna design

Efficient computation techniques

for Galerkin MoM antenna design

Cecilia Marasini

geboren te Lucca, Italië

Dit proefschrift is goedgekeurd door de promotoren:

prof.dr. A.G. Tijhuis
en
prof.dr.ir. A.P.M. Zwamborn

Copromotor:
dr.ir. E.S.A.M. Lepelaars

'Begin at the beginning,' the King said, very gravely,
'and go on till you come to the end: then stop.'
Lewis Carrol $(1832 - 1898)$

To mum and dad
To Luca

Abbreviations

CG	Conjugate Gradient
EFIE	Electric Field Integral Equation
GA	Genetic Algorithm
GTD	Geometric Theory of Diffraction
MFIE	Magnetic Field Integral Equation
MoM	Method of Moments
GEKMoM	Galerkin Exact Kernel Method of Moments
GEKMoM+	Galerkin Exact Kernel Method of Moments Plus
GMoMOS	Galerkin Method of Moments Open Surface
PEC	Perfectly Electrically Conducting
PSO	Particle Swarm Optimization
RMS	Root Mean Square
RWG	Rao Wilton Glisson
SEM	Singularity Expansion Method
SVD	Singular Value Decomposition
UHF	Ultra High Frequencies
VHF	Very High Frequencies
VSWR	Voltage Standing Wave Ratio

Contents

Chapter 1

Introduction

1.1 Background

In 2002 and 2003 TNO carried out a study for the Royal Netherlands Navy concerning the HF antenna suite on board of ships [1]. Three antenna systems were planned to cover the entire HF band: low-, mid- and high-band range. The objective was to determine whether or not it would be possible to leave out the mid-band system and to extend the ranges for low-band and high-band so that they would overlap. To answer this question typically two paths could be followed. One is to build a scale model of the ship and its relevant antennas and to carry out measurements. The other one is to build a computer model and to calculate the electromagnetic field distribution. The latter was chosen since TNO had the availability of the Numerical Electromagnetics Code (NEC), developed by Lawrence Livermore National Laboratory in Livermore, California [2,3]. This code is internationally known and used by many research groups for similar calculations. During the project it became clear that among the smart ideas behind the NEC code there were also quite some drawbacks. These resulted in problematic and unreliable calculations of the electric current distribution and electromagnetic field around the ship. In 2004 and 2005 TNO investigated the possibilities to build its own code from scratch for this purpose. The idea was to combine the good parts of NEC with state of the art scientific knowledge of scattering problems available at TNO and at the Electromagnetic Section of the Faculty of Electrical Engineering of the Eindhoven University of Technology (TU/e).

From the above, it is recognized that there is a strong need for efficient, accurate and reliable EM design tools. This work describes the mathematical formulation and the numerical implementation of some key elements (i.e., loaded wires, open surfaces, wire-surface connections) to be integrated in an appropriate design tool.

1.2   The goal of the research project

The key objective of this research work is to study the development of an electromagnetic design tool with focus to obtain an integrated approach for the development of wire antennas. As suggested by the title of this thesis: "**Efficient computation** techniques for **Galerkin MoM** antenna **design**", the key words in bold correspond to fundamental topics of the research described.

As a first motivation of this work we have considered a **design** problem where the engineer has to dimension antenna parameters to cope with given technical performance specifications. Figure 1.1 shows a typical design scheme.
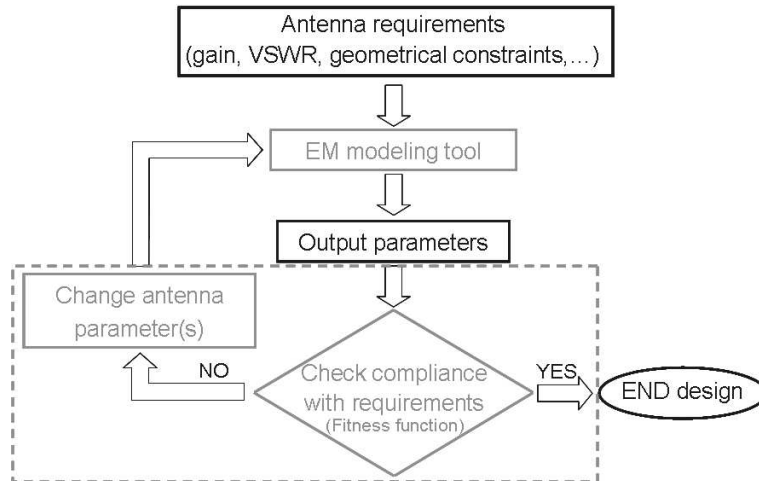
Figure 1.1: *Typical design scheme.*

Generally, an accurate EM modeling tool is used to analyze the problem and to assess antenna performance, which are then compared with requirements. Usually, some antenna parameters need to be changed and optimized to fully satisfy the design specifications. This tedious process can be performed manually or preferably automatically by optimization algorithms with properly defined "objective" functions. The choice of the so called "objective" or "fitness" function requires a major effort from the designer. In this perspective, it is of paramount importance for an EM modeling tool to be efficient in terms of CPU time to allow the design loop to end within a reasonable amount of time. In this thesis, the main effort is devoted to the formulation and numerical implementation of an accurate and efficient EM modeling tool able to analyze unloaded and loaded wire

antennas installed on open Perfectly Electrically Conducting (PEC) surfaces. In many cases, due to the large number of optimization parameters and problem unknowns, a full optimization loop may become very time consuming. Therefore, in the first iterations of the optimization, we can consider to reduce accuracy of the EM modeling tool in favor of computation time reduction. During the fine tuning of the design, the accuracy then has to be increased to arrive at correct predictions. As an alternative, CPU time reduction can also be achieved by applying analytical models to describe parameters' changes (in the antenna configuration) in closed form.

As addressed above, to perform EM calculations of wire antennas, a suitable and accurate EM modeling tool is required. A wire antenna structure is modeled by means of basic key elements, for instance: unloaded and loaded wires, open surfaces and connections between a wire and a surface. Basically, we consider an external source present in the environment which induces a current distribution along the antenna (i.e., wires, open surfaces, etc.). In turn this current radiates a scattered field. For each of the basic elements this scattering problem is formulated in terms of a relevant Electric Field Integral Equation (EFIE). The scattered field is subsequently calculated as a function of the computed current distribution. The choice of using the EFIE is supported by the fact that this integral equation remains valid also when open surfaces are analyzed while the Magnetic Field Integral Equation (MFIE) breaks down [4]. Subsequently, this EFIE is discretized by applying the **Galerkin Method of Moments (MoM)** [5], [6, pp. 206–259]. Thus, first, the unknown current distribution is approximated by means of "basis" functions (defined on "source" elements). Second, a set of linearly independent "testing" functions (defined on "observation" elements) is used to approximate the electric field quantities and a suitable inner product is applied on both sides of the integral equation. The MoM procedure leads to a system of linear equations (i.e., a matrix equation) which has to be solved numerically. Generally speaking, MoM matrix elements express the interaction of a current along a "source" element with an "observation" element. In particular, the matrix elements that describe the interaction between source and observation points on the same geometrical support are referred to as self terms and are found on the diagonal of the system matrix. When the testing and basis functions are chosen to be equal, the method is referred to as the Galerkin Method of Moments. In this case the numerical solution found can converge to the physical solution when the source/observation element dimensions reduce [7], [8, pp. 212]. Moreover, the symmetry property is preserved in the system matrix. Typically, when the Galerkin MoM is applied, the evaluation of matrix elements requires four-dimensional integrations since surface current distributions are considered. The com-

putation time is consequently negatively affected. Nevertheless, in this work we will show possible techniques to efficiently deal with the above mentioned computational burden without loss of accuracy. Besides, for coincident source and observation points or source points approaching the observation points, the integrand exhibits a singular or a nearly singular behavior. In this case, special care has to be taken to accurately compute the integrals.

As the method stands now, it appears evident that calculating the matrix elements is one of the most time consuming tasks of the numerical method proposed. Our aim is to increase the **efficiency** of our EM modeling tool by reducing the computation time without downgrading the accuracy of the calculated results. To this end, throughout this thesis several techniques are described:

- By exploiting the symmetry property of the MoM matrix, we can restrict the computation to half of its elements. In particular, for a single straight wire the linear system associated to the MoM procedure is characterized by a Toeplitz symmetric matrix. Thanks to this property a reduction of a factor N in the CPU time is achieved (where N is the dimension of the matrix).

- In general, the evaluation of off-diagonal matrix elements involves integrals that are never singular and are numerically calculated by a quadrature rule. When the distance between the observation and the source patch becomes large (with respect to the wavelength), a quadrature rule can be reduced to a midpoint integration rule which guarantees the desired accuracy in favor of a CPU time reduction. The evaluation of diagonal matrix elements requires special attention due to the presence of a singularity in the integrand function. Thus, a different approach is pursued. A singular term is extracted that can be integrated analytically, while the remaining regular function is integrated numerically. This technique is applied in the analysis of a single wire and of an open surface.

- If we consider the interaction between two wires, matrix elements representing their coupling need to be calculated. In this case, we will show that the most efficient evaluation is obtained by computing the field radiated by a current on the axis of a "source" wire in a point on the surface of an "observation" wire. This leads to a one-dimensional integral for the transmitting wire, and a two-dimensional integral for the receiving wire. To estimate the error due to considering the current on the axis of the source wire instead of on its mantle, an error analysis is performed. The same

approximation (current on source-wire axis) is used when studying the interaction between a wire and a surface.

- For the case of a current flowing along the mantle of a source wire, computation time reduction can be achieved thanks to an interpolation algorithm. In fact, since the field radiated by a wire segment is rotationally symmetric, it can be completely determined by the field values in a half plane. In this plane, a grid of points is defined where the field is evaluated. Subsequently, the electric field in intermediate points can be approximated by means of interpolation. Following this procedure we obtain a CPU time reduction of a factor 6 in the calculation of coupling matrices requiring the calculation of the radiated field only in a limited number of points (i.e., grid).

Returning to the original aim of the antenna design, in this thesis, a practical design problem will be studied. In particular, the previously described numerical code is included in a stochastic optimization algorithm, to design a broadband loaded monopole of fixed length for naval application. Design goals are maximizing the antenna gain and minimizing the VSWR, while positions and values (R,L,C) of loadings are the optimization parameters considered. Since the antenna size is fixed and only loading parameters are changing in the optimization, additional efficiency of the EM modeling tool can be gained by solving the problem of the unloaded wire only during the first iteration of the optimizer. The effect of the loadings is separately calculated along the optimization procedure at each iteration. This tailored scheme allows us to reduce the CPU time for a single iteration up to a factor of twenty.

After investigating candidate optimization algorithms, we have selected a Particle Swarm Optimization (PSO) scheme. Thanks to an improved procedure for the velocity update of the swarm's particles in the PSO algorithm we achieved a convergence improvement combined without stagnation in local minima.

1.3 Historical context

This section provides a historical overview of main research developments of scattering by wire antenna structures yielding an insight of the state of the art in this topical research.

Thin-wire modeling has been studied for quite a long time. About a century ago Pockling-ton [9] first and then Hallén [10] presented their well-known integral equations. Since then, the formulation and the solution of the wire equation have been a subject of continuous investigations by many scientists. Most authors use one of the two possible formulations

of Pocklington's equation, namely the so-called exact kernel or the reduced kernel. The simplicity and accuracy of these thin-wire integral equations are never surpassed by other approaches as, for instance, finite-difference and finite-element techniques [11, 12]. Typically, from the two-dimensional electric field integral equation written in terms of surface current distribution, a simpler one-dimensional form is derived by assuming that the wire radius is small compared to the length of the wire and the wavelength [13, 14]. In this case the fundamental unknown of the problem turns out to be the total current flowing along the wire. The main objective of our wire formulation is to show that the electromagnetic behavior of the wire (e.g., input impedance, radiated field) is governed by the total current. To this end, we use the well-posed thin-wire equation with exact kernel [7], implementing one of the most efficient techniques to numerically calculate the integration [15]. Despite the extra computational effort required by the exact kernel, numerical stability in the calculated current is shown in contrast with more conventional implementations of the reduced kernel which exhibits an oscillatory behavior in the delta-gap region and near the wire end faces [14].

Electromagnetic scattering by surfaces of arbitrary shape is extensively discussed by Rao, Wilton and Glisson in [16, 17]. The state of art in surface modeling is the starting point of our analysis of open surfaces. Following the formulation in [17] an electric field integral equation is discretized applying the Galerkin MoM by means of well-known Rao-Wilton-Glisson (RWG) functions defined on triangular domains. Then, in the calculation of matrix elements we pursue different approaches depending on the relative position between source triangle and observation triangle. Besides, we use modern techniques known from the literature [18, 19] to analytically calculate the extracted singular term.

Several authors have studied the modeling of a wire connection onto a surface. Among the various approaches the frequently used strategies are a full Method of Moments (MoM) analysis of the problem [20–22] and a hybrid MoM/GTD (Geometrical Theory of Diffraction) [23]. In particular, the latter requires the definition of a Green's function pertaining to the particular problem under consideration, while the first approach uses the free-space Green's function and requires only the definition of a proper basis function. Following the full-MoM scheme we introduce an attached-mode basis function derived from the one presented in [24] .

Nowadays it is more and more common to use methods of synthesis and optimization techniques to support electromagnetics and antenna design. Generally speaking, optimizers can

be subdivided into two big classes: deterministic (e.g., gradient optimization, least squares, etc.) [25, pp. 117–139] and evolutionary (or stochastic) algorithms (e.g., genetic algorithm, simulated annealing, etc.) [26]. The main drawback of the first class is that they may get caught in local minima, while stochastic techniques have a better chance to converge to a global minimum. On the other hand, stochastic techniques require many more field computations for candidate configurations. A tutorial on stochastic optimization techniques in electromagnetics is given by Rahmat-Samii in [26,27] where Genetic Algorithms (GA) and Particle Swarm Optimization (PSO) algorithms are presented. Because of the simplicity and robustness of PSO, along with a reduced tendency to converge to local minima, we implement a modified technique to increase efficiency in optimization convergence [28].

1.4 Outline of the thesis and notation conventions

The presentation of this thesis is organized as follows.

In *Chapter 2*, the problem of electromagnetic scattering by a perfectly electrically conducting (PEC) thin wire is analyzed. The Pocklington integro-differential equation in the frequency domain is introduced and both the reduced kernel and exact kernel formulations are derived and discussed.

Chapter 3 presents the solution of Pocklington's integral equation with exact kernel by applying the Galerkin Method of Moments. An efficient technique for the evaluation of matrix elements is described following the procedure proposed by Davies et al. [15].

In *Chapter 4*, the study is extended to wire antennas with distributed as well as concentrated RLC loadings.

In *Chapter 5*, an accurate numerical method to compute the natural frequencies of loaded thin wires is developed. Natural frequencies are calculated by applying the Singular Value Decomposition (SVD) to the system matrix together with a suitable search algorithm. By gradually increasing the impedance value, a marching-on-in-loading approach is used to increase efficiency. The numerical technique is described and validated by comparing our results with results from the literature.

In *Chapter 6*, the electromagnetic coupling between arbitrary oriented wires is analyzed. For the evaluation of coupling matrix elements, two approaches are described and compared in terms of accuracy and CPU time, namely: the thin-wire axis approximation where the current flows along the wire axis of the source wire, and the thin-wire mantle approximation which leaves the current flowing along the mantle of the source wire. For the case of the mantle approximation, a numerically efficient interpolation algorithm for the

evaluation of coupling terms is investigated and proposed.

In *Chapter 7*, the problem of electromagnetic scattering by a perfectly electrically conducting (PEC) surface with vanishing thickness is studied by means of the Galerkin MoM where RWG functions are introduced. Efficient evaluation of system matrix elements is pursued.

Chapter 8 analyzes the case of a PEC wire attached to a PEC surface. A special basis function (attachment mode) is developed to model the current distribution in the neighborhood of the junction. It is also described how the matrix elements related to the attachment can be computed numerically.

In *Chapter 9*, a practical design problem is studied. The developed MoM numerical code has been embedded in a stochastic optimization algorithm (Particle Swarm Optimization) to design and optimize loaded wire antennas. To enhance the computational efficiency, a tailored scheme is introduced for the computation of matrix elements together with a modified PSO algorithm.

In *Chapter 10*, a summary of the main results obtained during this research is given. Some general conclusions are drawn together with recommendations for future developments.

Throughout this dissertation, the following conventions are used. Bold capitals denote vector fields. Partial derivatives are written as subscripts, for example the partial derivative of $f(t)$ with respect to time t is written as $\partial_t f(t)$. Fourier transforms are written in capital Latin letters, i.e., the Fourier transform of $\mathcal{F}(t)$ is $F(\omega)$. Cartesian unit vectors are written as $\mathbf{i}_x$, $\mathbf{i}_y$, $\mathbf{i}_z$. Unit vectors of circularly-cylindrical coordinate system are written as $\mathbf{i}_r(\phi)$, $\mathbf{i}_\phi(\phi)$ and $\mathbf{i}_z$, with the dependence on ϕ-coordinate indicated explicitly.

Chapter 2

Thin-wire equations

Modeling the electromagnetic behavior of a single thin wire (probably the simplest antenna structure) has a long history and remains an important problem. Since Pocklington [9] and Hallén [10] first formulated their integral equations, many scientists have been discussing the various ways to analytically and/or numerically calculate the current induced along a thin wire by an incident field and/or by a delta-gap excitation [13, 29]. The mathematical formulation of this canonical problem leads to a one-dimensional integro-differential equation in which the induced current and the scattered field are interrelated by a so called "kernel". Choosing the observation point on the central axis of the wire results in the "reduced kernel" formulation, while choosing the observation point on the mantle surface results in the "exact kernel" formulation (see e.g., [13, 30]). Most authors use one of these two formulations (i.e., exact or reduced/approximated kernel) derived through the application of the electric field integral equation and by the assumption that the current flows along the wire surface. The full merit of the "reduced form" was not realized until it was shown in [13] that for a straight thin wire with circular cross section the wire equation with reduced kernel is exact, except for wire end effects.

In this chapter, the thin-wire integro-differential equation is formulated both with reduced and exact kernel for the total current along the wire.

2.1   Maxwell's equations

The behavior of the electromagnetic field in the presence of objects is governed by Maxwell's equations. When magnetic current sources are not present, the time-domain Maxwell

equations are given by

$$\nabla \times \boldsymbol{\mathcal{E}} + \partial_t \boldsymbol{\mathcal{B}} = \mathbf{0}, \tag{2.1}$$

$$\nabla \times \boldsymbol{\mathcal{H}} - \partial_t \boldsymbol{\mathcal{D}} = \boldsymbol{\mathcal{J}}. \tag{2.2}$$

Equation (2.1) is referred to as the Faraday-Henry law and expresses the relation between the electric-field intensity $\boldsymbol{\mathcal{E}}$ and the magnetic-flux density $\boldsymbol{\mathcal{B}}$. Equation (2.2) is referred to as the Ampère-Maxwell law and expresses the relation between the magnetic-field intensity $\boldsymbol{\mathcal{H}}$ and the density of the electric flux $\boldsymbol{\mathcal{D}}$ on one hand and the electric current density $\boldsymbol{\mathcal{J}}$ on the other hand. The equations (2.1) and (2.2) are called in short Maxwell's equations and are accompanied by the equation of continuity of electric current and charge (also referred to as conservation of charge)

$$\nabla \cdot \boldsymbol{\mathcal{J}} + \partial_t \rho = 0, \tag{2.3}$$

where ρ is the electric charge density. When we take the divergence of (2.1) and (2.2) and combine equations (2.2) and (2.3) we find that

$$\partial_t \left(\nabla \cdot \boldsymbol{\mathcal{B}} \right) = 0, \qquad \partial_t \left(\nabla \cdot \boldsymbol{\mathcal{D}} - \rho \right) = 0. \tag{2.4}$$

With the additional assumption that the fields $\nabla \cdot \boldsymbol{\mathcal{B}}$ and $\nabla \cdot \boldsymbol{\mathcal{D}} - \rho$ vanish at some initial instant $t = t_0$, it follows that these quantities must vanish for all instants, which yields the auxiliary equations

$$\nabla \cdot \boldsymbol{\mathcal{D}} = \rho, \tag{2.5}$$

$$\nabla \cdot \boldsymbol{\mathcal{B}} = 0. \tag{2.6}$$

In addition, constitutive relations are needed to describe the influence of the medium on the electromagnetic field and vice versa. Even though these relations may be more complicated, in this thesis we consider a homogeneous, time-invariant, isotropic media with permittivity ε and permeability μ. In this case, the electric-field intensity $\boldsymbol{\mathcal{E}}$ and the electric-flux density $\boldsymbol{\mathcal{D}}$, as well as the magnetic-field intensity $\boldsymbol{\mathcal{H}}$ and the magnetic-flux density $\boldsymbol{\mathcal{B}}$ are related as

$$\boldsymbol{\mathcal{D}} = \varepsilon_0 \int_{0^-}^{t} \left[\delta(\tau) + \kappa_e(\tau) \right] \boldsymbol{\mathcal{E}}(t - \tau) d\tau, \qquad \boldsymbol{\mathcal{B}} = \mu_0 \int_{0^-}^{t} \left[\delta(\tau) + \kappa_m(\tau) \right] \boldsymbol{\mathcal{H}}(t - \tau) d\tau, \tag{2.7}$$

where $\varepsilon_0 = 8.854 \times 10^{-12}$ F/m and $\mu_0 = 4\pi \times 10^{-7}$ H/m are the free-space permittivity and permeability, and κ_e and κ_m are the dielectric and magnetic relaxation scalar functions,

respectively. The lower integration limit in (2.7) can be chosen 0^-, i.e., δ in the limit for $\delta \uparrow 0$ according to the principle of causality, for which a reaction to a source cannot take place prior the instant of action. This lower limit is chosen with care, since we need to account for the case of an instantaneous reaction. Furthermore, we assume that no sources act before the instant $t = 0$. Then, the upper integration limit in (2.7) can be chosen equal to t. With the aid of a Fourier transformation, the electromagnetic quantities can be transformed from the space-time domain to the space-frequency domain. Let us introduce the Fourier transformation and its inverse as

$$F(\omega) = \int_{-\infty}^{\infty} \mathcal{F}(t) \exp(-j\omega t)\, dt, \quad \mathcal{F}(t) = \frac{1}{2\pi} \int_{-\infty}^{\infty} F(\omega) \exp(j\omega t)\, d\omega, \tag{2.8}$$

where ω is the angular frequency and j is the imaginary unit (i.e., $j^2 = -1$). It is noted that the frequency-domain quantities are complex-valued. For a real-valued, causal function, i.e., a function $\mathcal{F}(t)$ that is identical to zero for negative time values, the temporal Fourier transformation and its inverse can be written as

$$F(\omega) = \int_{0}^{\infty} \mathcal{F}(t) \exp(-j\omega t)\, dt, \quad \mathcal{F}(t) = \frac{1}{\pi} \mathrm{Re} \left\{ \int_{0}^{\infty} F(\omega) \exp(j\omega t)\, d\omega \right\}. \tag{2.9}$$

Hence, after applying the temporal Fourier transformation, Maxwell's equations (2.1), (2.2) become

$$\nabla \times \mathbf{E} + j\omega\mu\mathbf{H} = \mathbf{0}, \tag{2.10}$$

$$\nabla \times \mathbf{H} - j\omega\varepsilon\mathbf{E} = \mathbf{J}, \tag{2.11}$$

where we have used the Fourier transforms of the electric-flux and magnetic-flux density relations in (2.7)

$$\begin{aligned} \mathbf{D}(\omega) &= \varepsilon(\omega)\mathbf{E}(\omega), && \text{with } \varepsilon(\omega) = \varepsilon_0\varepsilon_r(\omega), \\ \mathbf{B}(\omega) &= \mu(\omega)\mathbf{H}(\omega), && \text{with } \mu(\omega) = \mu_0\mu_r(\omega). \end{aligned} \tag{2.12}$$

The functions $\varepsilon_r(\omega) = 1 + \chi_e(\omega)$ and $\mu_r(\omega) = 1 + \chi_m(\omega)$ are the relative permittivity and the relative permeability of the medium, respectively. Moreover, $\chi_e(\omega)$ and $\chi_m(\omega)$ are defined as the Fourier transforms of the relaxation functions $\kappa_e(t)$ and $\kappa_m(t)$ and are denoted as the electric and magnetic susceptibility, respectively.

Applying the temporal Fourier transformation to the auxiliary equations (2.5) and (2.6) for the flux densities leads to

$$\nabla \cdot \mathbf{B} = 0, \tag{2.13}$$

$$\nabla \cdot \mathbf{D} = \rho. \tag{2.14}$$

We supplement these relations with the law of current continuity (2.3) in the frequency domain

$$\nabla \cdot \mathbf{J} + j\omega\rho = 0. \tag{2.15}$$

2.2   Formulation of the problem

We model a straight thin wire of length h with a circular cross section of radius a as a perfectly electrically conducting cylinder embedded in a homogeneous, isotropic, dielectric with permittivity ε and permeability μ. Throughout this dissertation, we will consider the ω dependence of ε and μ as implicit. As shown in Fig. 2.1 the volume inside the wire is represented by D, the surface of the wire by ∂D, and the volume outside the wire by $\overline{D}$.
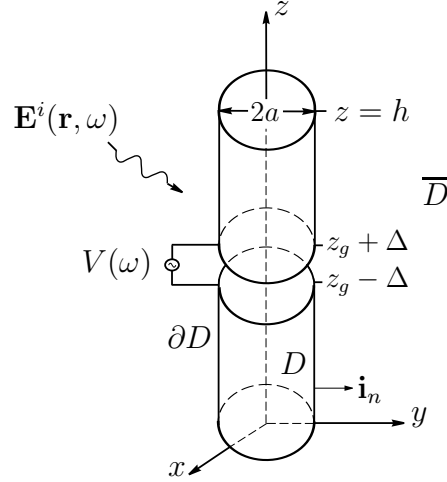
Figure 2.1: *Wire geometry.*

Next we introduce a cylindrical coordinate system (r, ϕ, z) such that the axis of the wire corresponds with $r = 0$ and $0 < z < h$ and we define a normal vector $\mathbf{i}_n(\mathbf{r})$ pointing into the region $\overline{D}$. We introduce vector $\mathbf{r} = r\mathbf{i}_r(\phi) + z\mathbf{i}_z$ and vector $\mathbf{r}' = r'\mathbf{i}_r(\phi') + z'\mathbf{i}_z$ as shown in Fig. 2.2. The unit vector $\mathbf{i}_r(\phi')$ can also be regarded as the normal on the surface of the wire, with the exception of the end faces.

The wire antenna can act as a transmitter or as a receiver, depending on the type of the external source present. The wire behaves as a receiver when an incident electromagnetic field $\left\{ \mathbf{E}^i(\mathbf{r}, \omega), \mathbf{H}^i(\mathbf{r}, \omega) \right\}$, which satisfies Maxwell's equations in absence of the wire, induces a current along the wire. The wire acts as a transmitter when the current along the

wire is driven by an impressed voltage $V(\omega)$ across a small gap $z_g - \Delta < z < z_g + \Delta$. More-over, the dimension of the wire satisfies the condition $\Delta \ll a \ll h$. The entire derivation is carried out in the frequency domain.
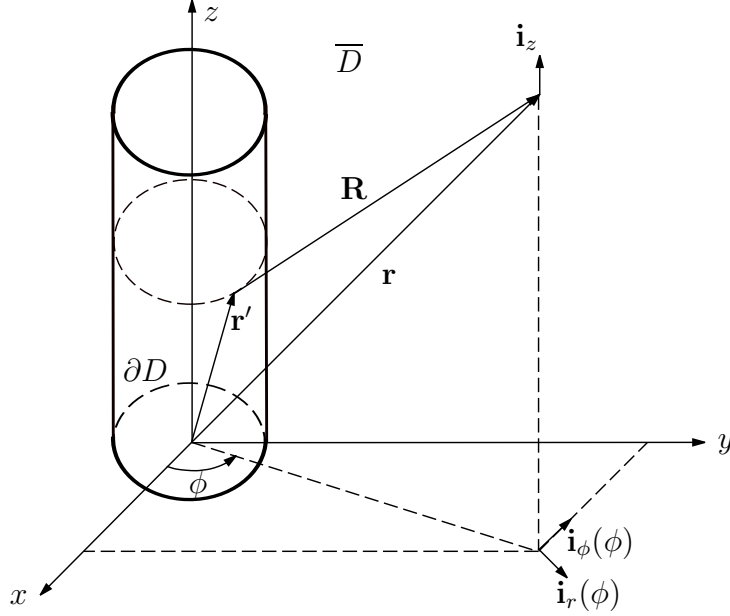
Figure 2.2: *Unit vectors $\mathbf{i}_r(\phi)$, $\mathbf{i}_\phi(\phi)$ and $\mathbf{i}_z$.*

The most suitable starting point is the integral relation for the electric field

$$-\nabla\Phi + k^2 \mathbf{A}(\mathbf{r}, \omega) = j\omega\varepsilon \left[S_{\overline{D}}(\mathbf{r})\mathbf{E}(\mathbf{r}, \omega) - \mathbf{E}^i(\mathbf{r}, \omega) \right], \tag{2.16}$$

where $k = \omega\sqrt{\varepsilon\mu}$ and $S_{\overline{D}}$ is the shape function [13,31]

$$S_{\overline{D}}(\mathbf{r}) = \begin{cases} 0, & \mathbf{r} \in D, \\ 1/2, & \mathbf{r} \in \partial D, \\ 1, & \mathbf{r} \in \overline{D}. \end{cases} \tag{2.17}$$

Since $\mathbf{r}'$ runs over ∂D, the current flows along the surface of the wire and the vector potential $\mathbf{A}$ and the scalar potential Φ are defined as

$$\mathbf{A}(\mathbf{r}, \omega) = \oiint_{\partial D} G(R, \omega)\, \mathbf{J}_S(\mathbf{r}', \omega) dS', \tag{2.18}$$

$$\Phi(\mathbf{r}, \omega) = -\oiint_{\partial D} G(R, \omega)\, \nabla_{S'} \cdot \mathbf{J}_S(\mathbf{r}', \omega) dS', \tag{2.19}$$

where $\nabla_{S'}$ indicates differentiation with respect to $\mathbf{r}'$ taking into account only components that lie on the surface ∂D. The distance R is $R = |\mathbf{r} - \mathbf{r}'|$, the source point $\mathbf{r}' \in \partial D$ and

the observation point $\mathbf{r} \in \overline{D}$, see Fig. 2.2. The surface current density $\mathbf{J}_S(\mathbf{r}', \omega)$ is expressed in A/m and

$$G(R, \omega) = \frac{\exp(-jkR)}{4\pi R}, \quad \text{or} \quad G(\mathbf{r} - \mathbf{r}', \omega) = \frac{\exp(-jk|\mathbf{r} - \mathbf{r}'|)}{4\pi |\mathbf{r} - \mathbf{r}'|}, \tag{2.20}$$

is the Green's function of the Helmholtz operator, chosen in accordance with the definition (2.9) of the temporal Fourier transform and the radiation condition. For details of deriving the integral relation (2.16), we refer to [31]. Substituting the expressions (2.18) and (2.19) in (2.16) yields

$$\nabla \oiint_{\partial D} G(R, \omega) \, \nabla_{S'} \cdot \mathbf{J}_S(\mathbf{r}', \omega) dS' + k^2 \oiint_{\partial D} G(R, \omega) \, \mathbf{J}_S(\mathbf{r}', \omega) dS'$$
$$= j\omega\varepsilon \left[S_{\overline{D}}(\mathbf{r})\mathbf{E}(\mathbf{r}, \omega) - \mathbf{E}^i(\mathbf{r}, \omega) \right], \tag{2.21}$$

where the right-hand side represents the scattered electric field.

2.2.1   Motivation for considering only the total current

In principle, the integro-differential equation (2.21) completes the formulation of the problem. However, the information that the radius a is small compared with the length of the wire can be used to arrive at a simpler formulation for the total current

$$I(z', \omega) = \int_{\phi=0}^{2\pi} \mathbf{J}_S(\mathbf{r}', \omega) \cdot \mathbf{i}_z a d\phi, \tag{2.22}$$

that flows along the wire. The motivation for considering only the total current is based on two observations. First the total current at the location of the voltage source is needed to determine the impedance of a wire antenna. Second, on the fact that the field radiated by the current induced on the wire can be determined up to $O(a^2)$, where a is the small radius of the wire.

The derivation of the latter result proceeds as follows. We write the longitudinal and the transverse components of the current density as

$$J_z(\mathbf{r}', \omega) = \widehat{J}_z(z', \omega) + \left(J_z(\mathbf{r}', \omega) - \widehat{J}_z(z', \omega) \right) = \widehat{J}_z(z', \omega) + \Delta J_z(\mathbf{r}', \omega), \tag{2.23}$$

$$J_\phi(\mathbf{r}', \omega) = \widehat{J}_\phi(z', \omega) + \left(J_\phi(\mathbf{r}', \omega) - \widehat{J}_\phi(z', \omega) \right) = \widehat{J}_\phi(z', \omega) + \Delta J_\phi(\mathbf{r}', \omega), \tag{2.24}$$

where $\mathbf{r}'$ is a point on the surface of the wire $\mathbf{r}' \in \partial D$, see Fig. 2.2. Moreover, $\widehat{J}_z(z', \omega)$ and $\widehat{J}_\phi(z', \omega)$ denote the values averaged over $\phi' \in [0, 2\pi)$. For $\widehat{J}_z(z', \omega)$, we have

$$\widehat{J}_z(z', \omega) = \frac{I(z', \omega)}{2\pi a}. \tag{2.25}$$

Further, with the aid of (2.23) and (2.24) we can write the surface current $\mathbf{J}_S$ as

$$
\begin{aligned}
\mathbf{J}_S(\mathbf{r}', \omega) &= J_z(\mathbf{r}', \omega)\mathbf{i}_z + J_\phi(\mathbf{r}', \omega)\mathbf{i}_\phi(\phi') & \text{(2.26)} \\
&= \left[\widehat{J}_z(z', \omega) + \Delta J_z(\mathbf{r}', \omega)\right]\mathbf{i}_z + \left[\widehat{J}_\phi(z', \omega) + \Delta J_\phi(\mathbf{r}', \omega)\right]\mathbf{i}_\phi(\phi'). & \text{(2.27)}
\end{aligned}
$$

From the closed-form separation-of-variables expression for the current density induced by an incident plane wave [32], [33, pp.481–483], [34], the following estimates are copied

$$
\widehat{J}_z(z', \omega) = O\left(\frac{1}{a \ln a}\right), \quad \Delta J_z(\mathbf{r}', \omega) = O(1), \tag{2.28}
$$

$$
\widehat{J}_\phi(z', \omega) = O(1), \quad \Delta J_\phi(\mathbf{r}', \omega) = O(a), \tag{2.29}
$$

as $a \downarrow 0$. At this point, we recall that the vector potential $\mathbf{A}$ (2.18) assumes the form

$$
\mathbf{A}(\mathbf{r}, \omega) = \int\limits_{z'=0}^{h} \int\limits_{\phi'=0}^{2\pi} \frac{\exp(-jk|\mathbf{r} - \mathbf{r}'|)}{4\pi|\mathbf{r} - \mathbf{r}'|}\mathbf{J}_S(\mathbf{r}', \omega)a\,d\phi'dz', \tag{2.30}
$$

with the observation point $\mathbf{r} \in \overline{D}$, see Fig. 2.2. Moreover, the vector potential (2.30) can be written as the sum of the longitudinal and transverse components

$$
\mathbf{A}(\mathbf{r}, \omega) = A_z(\mathbf{r}, \omega)\mathbf{i}_z + \mathbf{A}_T(\mathbf{r}, \omega). \tag{2.31}
$$

In a similar fashion as in (2.23) and (2.24) we can write the Green's function in (2.30) as

$$
\begin{aligned}
G(\mathbf{r} - \mathbf{r}', \omega) &= \widehat{G}(z - z', \omega) + \left(G(\mathbf{r} - \mathbf{r}', \omega) - \widehat{G}(z - z', \omega)\right) \\
&= \widehat{G}(z - z', \omega) + \Delta G(\mathbf{r} - \mathbf{r}', \omega), \tag{2.32}
\end{aligned}
$$

where $\widehat{G}(z - z', \omega)$ is the ϕ'-averaged Green's function

$$
\widehat{G}(z - z', \omega) = \frac{1}{2\pi} \int\limits_{\phi'=0}^{2\pi} G(\mathbf{r} - \mathbf{r}', \omega)d\phi'. \tag{2.33}
$$

We proceed now in the derivation of the vector potential (2.30), (2.31). First, we focus on the component A_z which, with the aid of (2.23) and (2.32) can be written as

$$
\begin{aligned}
A_z(\mathbf{r}, \omega) &= \int\limits_{z'=0}^{h} \int\limits_{\phi'=0}^{2\pi} J_z(\mathbf{r}', \omega)G(\mathbf{r} - \mathbf{r}', \omega)a\,d\phi'dz' \\
&= \int\limits_{z'=0}^{h} \int\limits_{\phi'=0}^{2\pi} \left[\widehat{J}_z(z', \omega) + \Delta J_z(\mathbf{r}', \omega)\right]\left[\widehat{G}(z - z', \omega) + \Delta G(\mathbf{r} - \mathbf{r}', \omega)\right]a\,d\phi'dz'. \tag{2.34}
\end{aligned}
$$

Now, substituting the explicit expression $\widehat{J}_z$ (2.25) in (2.34) yields

$$
\begin{aligned}
A_z(\mathbf{r}, \omega) &= \int\limits_{z'=0}^{h} \int\limits_{\phi'=0}^{2\pi} \left[\frac{I(z', \omega)}{2\pi a} + \Delta J_z(\mathbf{r}', \omega) \right] \left[\widehat{G}(z - z', \omega) + \Delta G(\mathbf{r} - \mathbf{r}', \omega) \right] a d\phi' dz' \\
&= \int\limits_{z'=0}^{h} \int\limits_{\phi'=0}^{2\pi} \left\{ \frac{I(z', \omega)}{2\pi a} \widehat{G}(z - z', \omega) + \Delta J_z(\mathbf{r}', \omega) \widehat{G}(z - z', \omega) \right. \\
&\quad + \left. \frac{I(z', \omega)}{2\pi a} \Delta G(\mathbf{r} - \mathbf{r}', \omega) + \Delta J_z(\mathbf{r}', \omega) \Delta G(\mathbf{r} - \mathbf{r}', \omega) \right\} a d\phi' dz',
\end{aligned} \tag{2.35}
$$

where the first term represents the leading contribution. Since $I(z', \omega)$ and $\widehat{G}(z - z', \omega)$ do not depend on ϕ' and the term $\Delta G(\mathbf{r} - \mathbf{r}', \omega)$ is of order $O(a)$, expression (2.35) becomes

$$
\begin{aligned}
A_z(\mathbf{r}, \omega) &= \int\limits_{z'=0}^{h} dz' a \left\{ \widehat{G}(z - z', \omega) \frac{I(z', \omega)}{a} \right. \\
&\quad + \left. \widehat{G}(z - z', \omega) \int\limits_{\phi'=0}^{2\pi} \Delta J_z(\mathbf{r}', \omega) d\phi' + \frac{I(z', \omega)}{2\pi a} \int\limits_{\phi'=0}^{2\pi} \Delta G(\mathbf{r} - \mathbf{r}', \omega) d\phi' + O(a) \right\}.
\end{aligned} \tag{2.36}
$$

Moreover the terms $a\Delta J_z(\mathbf{r}', \omega)$ and $\Delta G(\mathbf{r} - \mathbf{r}', \omega)$ are of order $O(a)$. However, in both cases they have been organized such that the integral over ϕ' reduces them to zero. Thus, (2.36) can be simplified as

$$
A_z(\mathbf{r}, \omega) = \int\limits_{z'=0}^{h} \widehat{G}(z - z', \omega) I(z', \omega) dz' + O(a^2). \tag{2.37}
$$

Second, the transverse component of the vector potential (2.31) is considered

$$
\mathbf{A}_T(\mathbf{r}, \omega) = \int\limits_{z'=0}^{h} \int\limits_{\phi'=0}^{2\pi} J_\phi(\mathbf{r}', \omega) G(\mathbf{r} - \mathbf{r}', \omega) \mathbf{i}_\phi(\phi') a d\phi' dz', \tag{2.38}
$$

and a similar derivation is performed. In this case, the assumptions $\widehat{J}_\phi = O(1)$ and $\Delta J_\phi = O(a)$ in (2.29) together with $\Delta G(\mathbf{r} - \mathbf{r}', \omega) = O(a)$ lead to the conclusion that

$$
\mathbf{A}_T = O(a^2). \tag{2.39}
$$

We give the detailed derivation of this result in the Appendix A. Finally, substituting (2.39) and (2.37) in (2.31) leads to

$$
\mathbf{A}(\mathbf{r}, \omega) = A_z(\mathbf{r}, \omega) \mathbf{i}_z + \mathbf{A}_T(\mathbf{r}, \omega) = \mathbf{i}_z \int\limits_{z'=0}^{h} \widehat{G}(z - z', \omega) I(z', \omega) dz' + O(a^2), \tag{2.40}
$$

which is the mathematical formulation of the conclusion that the vector potential and consequently the radiated field are determined up to $O(a^2)$ by replacing the current density $\mathbf{J}_S(\mathbf{r}')$ with the total current $I_z(z', \omega)\mathbf{i}_z$. This important observation represents the motivation for deriving in the upcoming sections the thin-wire equation only for the total current $I(z', \omega)$.

We derive now an expression for the vector potential (2.40) when the total current $I(z', \omega)$ is on the central axis showing that it is second-order accurate. To this end we proceed in two steps. First, we write (2.40) as

$$\mathbf{A}(\mathbf{r}, \omega) = \mathbf{i}_z \int\limits_{z'=0}^{h} \frac{I(z', \omega)}{2\pi} \int\limits_{\phi'=0}^{2\pi} \frac{\exp(-jk|\mathbf{r} - \mathbf{r}'|)}{4\pi|\mathbf{r} - \mathbf{r}'|} d\phi' dz' + O(a^2). \tag{2.41}$$

Second, the distance $R = |\mathbf{r} - \mathbf{r}'|$ is written as

$$R = |\mathbf{r} - \mathbf{r}'| = |\mathbf{r} - \mathbf{r}_a - \boldsymbol{\rho}'| = \sqrt{(\mathbf{r} - \mathbf{r}_a - \boldsymbol{\rho}') \cdot (\mathbf{r} - \mathbf{r}_a - \boldsymbol{\rho}')}, \tag{2.42}$$

where $\mathbf{r}_a = z'\mathbf{i}_z$ is a point along the wire axis, $\boldsymbol{\rho}' = a\mathbf{i}_r(\phi')$ and $\mathbf{r}' = \mathbf{r}_a + \boldsymbol{\rho}'$, see Fig. 2.3.
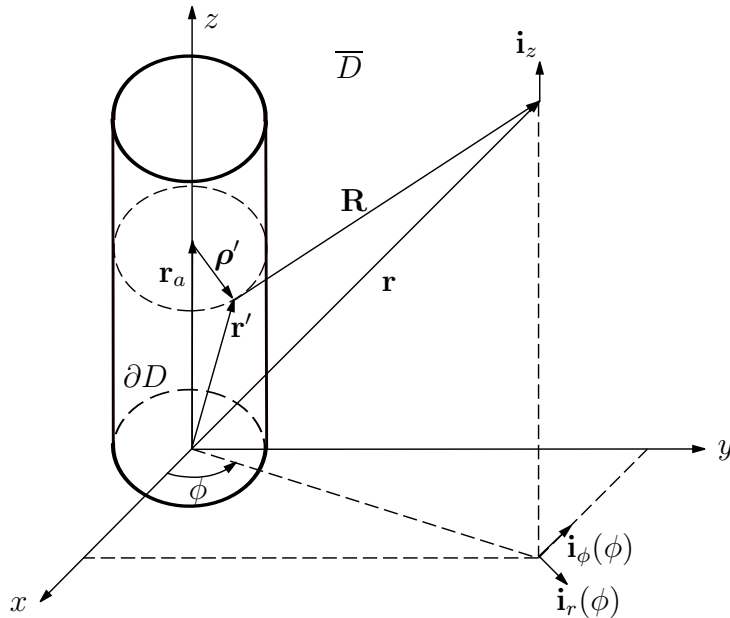
Figure 2.3: *Vectors* $\mathbf{r}_a = z'\mathbf{i}_z$ *and* $\boldsymbol{\rho}' = a\mathbf{i}_r(\phi')$.

Next, from (2.42) it follows

$$\begin{aligned} R &= \sqrt{|\mathbf{r} - \mathbf{r}_a|^2 - 2(\mathbf{r} - \mathbf{r}_a) \cdot \boldsymbol{\rho}' + |\boldsymbol{\rho}'|^2} = \sqrt{|\mathbf{r} - \mathbf{r}_a|^2 - 2(\mathbf{r} - \mathbf{r}_a) \cdot \boldsymbol{\rho}' + a^2} \\ &= |\mathbf{r} - \mathbf{r}_a|\sqrt{1 - \frac{2(\mathbf{r} - \mathbf{r}_a) \cdot \boldsymbol{\rho}'}{|\mathbf{r} - \mathbf{r}_a|^2} + \frac{a^2}{|\mathbf{r} - \mathbf{r}_a|^2}}, \end{aligned} \tag{2.43}$$

and, expanding the latter in Taylor's series yields

$$R = |\mathbf{r} - \mathbf{r}_a| \left(1 - \frac{(\mathbf{r} - \mathbf{r}_a) \cdot \boldsymbol{\rho}'}{|\mathbf{r} - \mathbf{r}_a|^2}\right) + O(a^2) = |\mathbf{r} - z'\mathbf{i}_z| \left(1 - a\frac{\mathbf{r} \cdot \mathbf{i}_r(\phi')}{|\mathbf{r} - z'\mathbf{i}_z|^2}\right) + O(a^2). \quad (2.44)$$

Subsequently, we substitute this result in (2.41). Carrying out a Taylor expansion for the exponential term, considering $|\mathbf{r} - \mathbf{r}'| \gg a$ and $ka \ll 1$, we then obtain a one-dimensional expression of the vector potential

$$\mathbf{A}(\mathbf{r}, \omega) = \mathbf{i}_z \int\limits_{z'=0}^{h} \frac{\exp(-jk|\mathbf{r} - z'\mathbf{i}_z|)}{4\pi|\mathbf{r} - z'\mathbf{i}_z|} I(z', \omega) dz' + O(a^2). \quad (2.45)$$

From (2.45), as described in Appendix B, we derive the following one-dimensional expression of the electric field

$$\begin{aligned} \mathbf{E}(\mathbf{r}) &= \frac{1}{j\omega\varepsilon}\frac{1}{4\pi} \int\limits_{z'=0}^{h} \frac{\exp(-jk|\mathbf{r} - z'\mathbf{i}_z|)}{|\mathbf{r} - z'\mathbf{i}_z|^3} \left\{ -\left[(jk|\mathbf{r} - z'\mathbf{i}_z|)^2 + jk|\mathbf{r} - z'\mathbf{i}_z| + 1\right] \mathbf{i}_z \right. \\ &+ \left. \left[3 + 3jk|\mathbf{r} - z'\mathbf{i}_z| + (jk|\mathbf{r} - z'\mathbf{i}_z|)^2\right] \frac{z - z'}{|\mathbf{r} - z'\mathbf{i}_z|^2} (\mathbf{r} - z'\mathbf{i}_z) \right\} I(z') dz', \quad (2.46) \end{aligned}$$

neglecting a second-order error (i.e., $O(a^2)$). We refer to (2.46) as the radiated field thin-wire axis approximation. In words, (2.45) and (2.46) states that the vector potential and the radiated field are determined up to $O(a^2)$ by replacing the current density $\mathbf{J}_S(\mathbf{r}', \omega)$ with the total current $I(z', \omega)$ on the wire axis.

2.2.2 Thin-wire equations

We proceed now with the derivation of thin-wire equations. From the integral relation (2.21), we derive the integro-differential equation for a perfectly electrically conducting (PEC) thin wire as in [14]. Since $\mathbf{r}'$ runs over ∂D, **the current flows along the surface of the wire**, which, apart from end faces, means that

$$\mathbf{J}_S(\mathbf{r}', \omega) = \mathbf{J}_S(r' = a, \phi', z', \omega). \quad (2.47)$$

Let us consider now the surface current density at the end faces. For a thin wire, the surface of the end faces $2\pi a^2$ is small compared to the surface of the rest of the wire $2\pi ah$ and $a \ll \lambda$ with $\lambda = 2\pi/(\omega\sqrt{\varepsilon\mu})$. Therefore we assume that **the current at the end faces can be neglected**. In general (for thicker wires) this approximation may not be correct, but, in the case that a contribution from the end faces will be taken into account, extra

terms have to be considered in the formulation. An argument in favor of this approximation also consistent with the other approximation made in deriving the scattered field can be found in [13]. In fact, analysis of the radial current done in [13] shows that the error made is negligible for sufficiently thin wires with respect to the wavelength.

From the integro-differential equation (2.21), we can write the z-component of the scattered field, due to the current density on the mantle, as

$$\partial_z \int_{z'=0}^{h} \int_{\phi'=0}^{2\pi} G(R,\omega) \nabla_{S'} \cdot \mathbf{J}_S(a,\phi',z',\omega) a d\phi' dz'$$

$$+k^2 \int_{z'=0}^{h} \int_{\phi'=0}^{2\pi} G(R,\omega) \mathbf{i}_z \cdot \mathbf{J}_S(a,\phi',z',\omega) a d\phi' dz' = j\omega\varepsilon \left[S_{\overline{D}} E_z(\mathbf{r},\omega) - E_z^i(\mathbf{r},\omega) \right], \qquad (2.48)$$

where

$$G(R,\omega) = \frac{\exp(-jk\sqrt{r^2 + a^2 - 2ra\cos(\phi - \phi') + (z - z')^2})}{4\pi\sqrt{r^2 + a^2 - 2ra\cos(\phi - \phi') + (z - z')^2}}, \qquad (2.49)$$

is the Green's function expressed in cylindrical coordinates. The surface divergence $\nabla_{S'} \cdot \mathbf{J}_S$ with respect to the primed coordinates can be explicitly written as

$$\nabla_{S'} \cdot \mathbf{J}_S(\phi',z',\omega) = \frac{1}{a}\partial_{\phi'} J_\phi(\phi',z',\omega) + \partial_{z'} J_z(\phi',z',\omega), \qquad (2.50)$$

where J_ϕ and J_z are the ϕ- and z-components of the surface current density $\mathbf{J}_S$. Since the surface current density is always located at $r' = a$, from now on we will write $\mathbf{J}_S(\phi',z',\omega)$ instead of $\mathbf{J}_S(a,\phi',z',\omega)$. Further, we recall that **the integral of the z-component of $\mathbf{J}_S$ gives rise to the total current in the z-direction**, i.e., the definition (2.22). As suggested in [14], a very elegant way to get rid of the J_ϕ component, is to average both sides of the integral equation (2.48) with respect to ϕ. The right-hand side is then written as

$$j\omega\varepsilon\frac{1}{2\pi} \int_{\phi=0}^{2\pi} \left[S_{\overline{D}} E_z(\mathbf{r},\omega) - E_z^i(\mathbf{r},\omega) \right] d\phi. \qquad (2.51)$$

The left-hand side is the sum of three contributions that will be considered separately

$$
\frac{1}{2\pi}\partial_z \int\limits_{\phi=0}^{2\pi} \int\limits_{z'=0}^{h} \int\limits_{\phi'=0}^{2\pi} G(R,\omega)\left(\partial_{\phi'}J_\phi(\phi',z',\omega)\right)d\phi'dz'd\phi
$$

$$
+\frac{1}{2\pi}\partial_z \int\limits_{\phi=0}^{2\pi} \int\limits_{z'=0}^{h} \int\limits_{\phi'=0}^{2\pi} G(R,\omega)\left(\partial_{z'}J_z(\phi',z',\omega)\right)ad\phi'dz'd\phi
$$

$$
+\frac{k^2}{2\pi} \int\limits_{\phi=0}^{2\pi} \int\limits_{z'=0}^{h} \int\limits_{\phi'=0}^{2\pi} G(R,\omega)J_z(a,\phi',z',\omega)ad\phi'dz'd\phi. \tag{2.52}
$$

Observing that the Green's function (2.49) depends on $\phi - \phi'$, we introduce the ϕ' independent function

$$
g(r,z-z',\omega) = \frac{1}{2\pi} \int\limits_{\phi=0}^{2\pi} G(R,\omega)d\phi, \qquad R = \sqrt{r^2 + a^2 - 2ra\cos\phi + (z-z')^2}. \tag{2.53}
$$

Therefore, the first term in (2.52) is evaluated as follows

$$
\frac{1}{2\pi}\partial_z \int\limits_{\phi=0}^{2\pi} \int\limits_{z'=0}^{h} \int\limits_{\phi'=0}^{2\pi} G(R,\omega)\left(\partial_{\phi'}J_\phi(\phi',z',\omega)\right)d\phi'dz'd\phi
$$

$$
= \partial_z \int\limits_{z'=0}^{h} \int\limits_{\phi'=0}^{2\pi} g(r,z-z',\omega)\left(\partial_{\phi'}J_\phi(\phi',z',\omega)\right)d\phi'dz'
$$

$$
= \partial_z \int\limits_{z'=0}^{h} g(r,z-z',\omega) \int\limits_{\phi'=0}^{2\pi} \partial_{\phi'}J_\phi(\phi',z',\omega)d\phi'dz' = 0. \tag{2.54}
$$

The second term can be written as

$$\frac{1}{2\pi}\partial_z \int\limits_{\phi=0}^{2\pi} \int\limits_{z'=0}^{h} \int\limits_{\phi'=0}^{2\pi} G(R,\omega)\left(\partial_{z'} J_z(\phi',z',\omega)\right) a d\phi' dz' d\phi$$

$$= \partial_z \int\limits_{z'=0}^{h} \int\limits_{\phi'=0}^{2\pi} g(r,z-z',\omega)\left(\partial_{z'} J_z(\phi',z',\omega)\right) a d\phi' dz'$$

$$= \partial_z \int\limits_{z'=0}^{h} g(r,z-z',\omega)\left(\partial_{z'} I(z',\omega)\right) dz' = -\partial_z \int\limits_{z'=0}^{h} \left(\partial_{z'} g(r,z-z',\omega)\right) I(z',\omega) dz'$$

$$= \partial_z^2 \int\limits_{z'=0}^{h} I(z',\omega) g(r,z-z',\omega) dz'. \tag{2.55}$$

For the third contribution we have

$$\frac{k^2}{2\pi} \int\limits_{\phi=0}^{2\pi} \int\limits_{z'=0}^{h} \int\limits_{\phi'=0}^{2\pi} G(R,\omega) J_z(a,\phi',z',\omega) a d\phi' dz' d\phi$$

$$= k^2 \int\limits_{z'=0}^{h} \int\limits_{\phi'=0}^{2\pi} g(r,z-z',\omega) J_z(a,\phi',z',\omega) a d\phi' dz'$$

$$= k^2 \int\limits_{z'=0}^{h} g(r,z-z',\omega) \int\limits_{\phi'=0}^{2\pi} J_z(a,\phi',z',\omega) a d\phi' dz' = k^2 \int\limits_{z'=0}^{h} g(r,z-z',\omega) I(z',\omega) dz'. \tag{2.56}$$

In conclusion, combining the results, we have obtained the following integro-differential equation for the total current flowing along the wire

$$\left(\partial_z^2 + k^2\right) \int\limits_{z'=0}^{h} g(r,z-z',\omega) I(z',\omega) dz' = \frac{1}{2\pi} \int\limits_{\phi=0}^{2\pi} j\omega\varepsilon \left[S_{\overline{D}} E_z(\mathbf{r},\omega) - E_z^i(\mathbf{r},\omega)\right] d\phi. \tag{2.57}$$

At this point, the two formulations of the thin-wire equation depart. By choosing the position of the observation point $\mathbf{r}$ on the central axis of the wire, we obtain a so-called "reduced kernel" formulation, while choosing the observation point on the mantle results in the "exact kernel" formulation. Both formulations are exact.

2.2.3   Reduced kernel formulation

First we consider the case of the observation point on the central axis of the wire, i.e., $\mathbf{r} = z\mathbf{i}_z$ with $0 < z < h$. For this choice, the distance between the source point and the

observation point is given by

$$R = |(z\mathbf{i}_z) - (z'\mathbf{i}_z + a\mathbf{i}_r)| = \sqrt{(z - z')^2 + a^2} \ . \tag{2.58}$$

As a consequence the Green's function G no longer depends on $\phi - \phi'$, and from the integro-differential equation (2.57), it follows that

$$\left(\partial_z^2 + k^2\right) \int\limits_{z'=0}^{h} K_R(z - z', \omega) I(z', \omega) dz' = j\omega\varepsilon \left[S_{\overline{D}} E_z(z\mathbf{i}_z, \omega) - E_z^i(z\mathbf{i}_z, \omega)\right], \tag{2.59}$$

where the "reduced kernel" is defined as

$$K_R(z - z', \omega) = \frac{\exp(-jk\sqrt{(z - z')^2 + a^2})}{4\pi\sqrt{(z - z')^2 + a^2}}. \tag{2.60}$$

Equation (2.59) is referred to as the "reduced form" of Pocklington's equation. Note that, apart from neglecting end effects, no approximations have been made to arrive at (2.59). Hence, this integro-differential equation is exact, see also [13].

2.2.4   Exact kernel formulation

As a second choice we consider the observation point on the surface of the wire. In this case the distance R is

$$
\begin{aligned}
R &= |(z\mathbf{i}_z + a\mathbf{i}_r(\phi)) - (z'\mathbf{i}_z + a\mathbf{i}_r(\phi'))| = \sqrt{2a^2(1 - \cos(\phi - \phi')) + (z - z')^2} \\
&= \sqrt{(z - z')^2 + 4a^2 \sin^2\left(\frac{\phi - \phi'}{2}\right)} = \sqrt{(z - z')^2 + 4a^2 \sin^2(\varphi)},
\end{aligned}
\tag{2.61}
$$

and the Green's function

$$G(R, \omega) = \frac{\exp(-jk\sqrt{(z - z')^2 + 4a^2 \sin^2(\varphi)})}{4\pi\sqrt{(z - z')^2 + 4a^2 \sin^2(\varphi)}} \ , \tag{2.62}$$

is periodic in $\varphi = \dfrac{\phi - \phi'}{2}$. The integro-differential equation (2.57) then can be written as

$$\left(\partial_z^2 + k^2\right) \int\limits_{z'=0}^{h} K_E(z - z', \omega) I(z', \omega) dz' = \frac{1}{2\pi} \int\limits_{\phi=0}^{2\pi} j\omega\varepsilon \left[S_{\overline{D}} E_z(\mathbf{r}, \omega) - E_z^i(\mathbf{r}, \omega)\right] d\phi, \tag{2.63}$$

where the "exact kernel" is defined as

$$K_E(z - z', \omega) = g(a, z - z', \omega) = \frac{1}{2\pi^2} \int\limits_{\varphi=0}^{\pi/2} \frac{\exp(-jk\sqrt{(z - z')^2 + 4a^2 \sin^2 \varphi})}{\sqrt{(z - z')^2 + 4a^2 \sin^2 \varphi}} d\varphi. \tag{2.64}$$

Equation (2.63) is known as "Pocklington's equation with exact kernel". In this case the integral in (2.64) contains a singularity when z approaches z' and extra numerical effort is required to evaluate the unknown current in (2.63) due to the presence of this singular behavior [15]. Moreover, the integro-differential equation (2.63) is well-posed [35–37] and its solution (i.e., the current distribution) is unique [38].

2.2.5   Delta-gap voltage excitation

In order to have a complete description, we may consider the current to be generated by a delta-gap voltage excitation, see Fig. 2.1 and [13]. The electric field in the gap region satisfies the relation

$$\int_{z_g-\Delta}^{z_g+\Delta} E_z(\mathbf{r},\omega)dz = -V(\omega) \ . \tag{2.65}$$

Even though the electric field may not be infinite in a region of infinitesimal width (i.e., $\Delta \downarrow 0$), a mathematical delta-gap model has been used. For the exact kernel formulation, the observation point $\mathbf{r} = z\mathbf{i}_z + a\mathbf{i}_r$, with $|z - z_g| < \Delta$, is on the extension of the wire surface, therefore from (2.65), taking the limit $\Delta \downarrow 0$, yields

$$E_z(z\mathbf{i}_z + a\mathbf{i}_r,\omega) = -V(\omega)\delta(z - z_g). \tag{2.66}$$

Inside the wire and outside the gap, the electric field vanishes. Consequently, we have

$$S_{\overline{D}}E_z(z\mathbf{i}_z + a\mathbf{i}_r\omega) = -V(\omega)\delta(z - z_g), \tag{2.67}$$

and therefore Pocklington's equation with exact kernel (2.63) becomes

$$\left(\partial_z^2 + k^2\right)\int_{z'=0}^{h} K_E(z - z',\omega)I(z',\omega)dz' = -j\omega\varepsilon\left[V(\omega)\delta(z - z_g) + \widehat{E}_z^i(\mathbf{r},\omega)\right], \tag{2.68}$$

where the averaged field $\widehat{E}_z^i$ is defined as

$$\widehat{E}_z^i(\mathbf{r},\omega) = \frac{1}{2\pi}\int_{\phi=0}^{2\pi} E_z^i(\mathbf{r},\omega)d\phi. \tag{2.69}$$

For the reduced kernel formulation, the delta-gap voltage excitation is

$$E_z(z\mathbf{i}_z,\omega) = -V(\omega)\delta(z - z_g), \tag{2.70}$$

where the observation point $\mathbf{r} = z\mathbf{i}_z$ is on the central axis of the wire. Therefore, equation (2.59) becomes

$$\left(\partial_z^2 + k^2\right) \int\limits_{z'=0}^{h} K_R(z - z', \omega) I(z', \omega) dz' = -j\omega\varepsilon \left[V(\omega)\delta(z - z_g) + E_z^i(\mathbf{r}, \omega)\right]. \qquad (2.71)$$

2.2.6   Incident Field

Let us consider Pocklington's equation with exact kernel (2.68). Even if the exact kernel formulation is adopted, we note that, in the literature, most authors evaluate the incident electric field on the axis of the wire rather than on the mantle. To illustrate the difference between these two choices of excitation functions, let us consider a plane wave incident on the wire from a direction defined by the unit vector $\mathbf{i}_k$ as in Fig. 2.4.
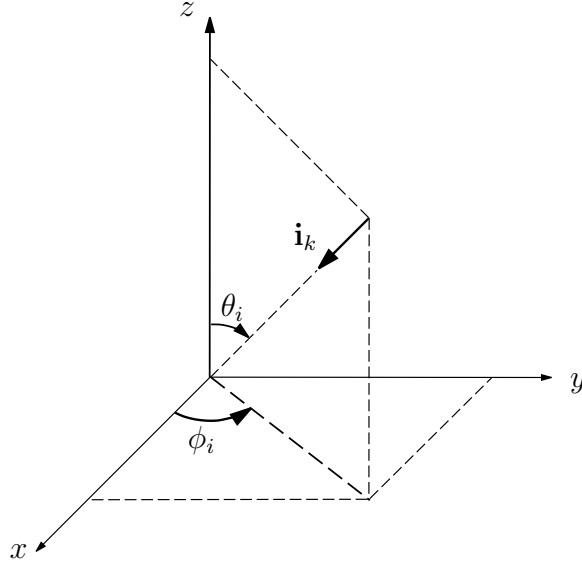
Figure 2.4: *Definition of the unit incident vector $\mathbf{i}_k$.*

The origin of the coordinate system is considered to be the phase reference point. Even though in the following other types of incident field are considered, we assume now that a plane wave is incident on the wire. The expression is then given by

$$\mathbf{E}^i(\mathbf{r}) = \mathbf{E}_0 \exp(-j\mathbf{k}^i \cdot \mathbf{r}), \qquad (2.72)$$

where $\mathbf{E}_0$ is the amplitude vector, $\mathbf{k}^i = k^i \mathbf{i}_k$ is the incident wave vector, $k^i = |\mathbf{k}^i| = \omega\sqrt{\varepsilon\mu}$ is the phase coefficient and $\mathbf{r} = x\mathbf{i}_x + y\mathbf{i}_y + z\mathbf{i}_z$ is the observation point expressed in Cartesian

coordinates. According to Fig. 2.4, the incident wave unit vector $\mathbf{i}_k$ can be decomposed into Cartesian unit vectors as follows

$$\mathbf{i}_k = -\sin\theta_i\cos\phi_i\mathbf{i}_x - \sin\theta_i\sin\phi_i\mathbf{i}_y - \cos\theta_i\mathbf{i}_z. \tag{2.73}$$

In general the wave is elliptically polarized. We confine ourselves to a linearly polarized wave $\mathbf{E}^i$ and since $\mathbf{E}_0 \cdot \mathbf{k}^i = 0$ we can write $\mathbf{E}_0$ in Cartesian coordinates as

$$\begin{aligned}\mathbf{E}_0 &= (E_{0\theta}\cos\theta_i\cos\phi_i - E_{0\phi}\sin\phi_i)\mathbf{i}_x + \\ &\quad (E_{0\theta}\cos\theta_i\sin\phi_i + E_{0\phi}\cos\phi_i)\mathbf{i}_y + (-E_{0\theta}\sin\theta_i)\mathbf{i}_z,\end{aligned} \tag{2.74}$$

where $E_{0\theta}$ and $E_{0\phi}$ are the θ and ϕ components of the field, respectively. In particular the z-component of the incident plane wave (2.72) is $E_{0z} = -E_{0\theta}\sin\theta_i$ and the scalar product $\mathbf{k}^i \cdot \mathbf{r}$ is

$$\mathbf{k}^i \cdot \mathbf{r} = (-k^i\sin\theta_i\cos\phi_i\mathbf{i}_x - k^i\sin\theta_i\sin\phi_i\mathbf{i}_y - k^i\cos\theta_i\mathbf{i}_z) \cdot (x\mathbf{i}_x + y\mathbf{i}_y + z\mathbf{i}_z). \tag{2.75}$$

As a **first choice**, placing **the observation point $\mathbf{r} = z\mathbf{i}_z$ on the central axis of the wire**, yields

$$\mathbf{k}^i \cdot \mathbf{r} = -k^i z\cos\theta_i. \tag{2.76}$$

In this case, with the aid of (2.74), the averaging over ϕ has no effect and we write

$$\widehat{E}_z^i(z\mathbf{i}_z, \omega) = E_z^i(z\mathbf{i}_z, \omega) = -E_{0\theta}\sin\theta_i\exp(jzk^i\cos\theta_i), \tag{2.77}$$

which does not depend on ϕ.

As a **second choice**, placing **the observation point on the wire surface** leads to

$$\mathbf{r} = a\cos\phi\mathbf{i}_x + a\sin\phi\mathbf{i}_y + z\mathbf{i}_z, \tag{2.78}$$

and, consequently, the scalar product $\mathbf{k}^i \cdot \mathbf{r}$ and the z-component of the incident field become $\mathbf{k}^i \cdot \mathbf{r} = -k^i a\sin\theta_i\cos(\phi_i - \phi) - k^i z\cos\theta_i$ and

$$E_z^i(\mathbf{r}, \omega) = -E_{0\theta}\sin\theta_i\exp(jzk^i\cos\theta_i)\exp(jak^i\sin\theta_i\cos(\phi_i - \phi)), \tag{2.79}$$

respectively. Thus in the exact kernel equation (2.63) and (2.68), the averaged field can be written as

$$\begin{aligned}\widehat{E}_z^i(\mathbf{r}, \omega) &= \frac{1}{2\pi}\int_{\phi=0}^{2\pi} E_z^i(\mathbf{r}, \omega)d\phi \\ &= -\frac{1}{2\pi}E_{0\theta}\sin\theta_i\exp(jzk^i\cos\theta_i)\int_{\phi=0}^{2\pi}\exp(jak^i\sin\theta_i\cos(\phi_i - \phi))d\phi.\end{aligned} \tag{2.80}$$

Let us **focus on the azimuthal, ϕ-dependent factor** in the previous expression. According to [39, eq. (9.1.21)],

$$\int\limits_{\phi=0}^{2\pi} \exp(jak^i \sin\theta_i \cos(\phi_i - \phi))d\phi = 2\pi J_0(ak^i \sin\theta_i), \qquad (2.81)$$

where J_0 is the Bessel function of the first kind and order zero. Substituting this result in (2.80) leads to

$$\begin{aligned} \widehat{E}_z^i(\mathbf{r}, \omega) = \frac{1}{2\pi}\int\limits_{\phi=0}^{2\pi} E_z^i(\mathbf{r}, \omega)d\phi &= -E_{0\theta} \sin\theta_i \exp(jzk^i \cos\theta_i) J_0(ak^i \sin\theta_i) \\ &= \widehat{E}_z^i(z\mathbf{i}_z, \omega) J_0(ak^i \sin\theta_i), \end{aligned} \qquad (2.82)$$

where $\widehat{E}_z^i(z\mathbf{i}_z, \omega)$ is the averaged field in (2.77) when the observation point is placed on the wire axis. We observe that the correction factor $J_0(ak^i \sin\theta_i)$ in the above equation depends on the angle of incidence θ_i and on the product ak^i.

2.2.7   Hallén's Equation

For the sake of completeness we write here Hallén's integral equation [10]. Irrespective of the choices of the observation point, Pocklington's integro-differential equation (2.57)

$$\left(\partial_z^2 + k^2\right) \int\limits_{z'=0}^{h} g(r, z - z', \omega)I(z', \omega)dz' = \frac{1}{2\pi}\int\limits_{\phi=0}^{2\pi} j\omega\varepsilon \left[S_{\overline{D}}E_z(\mathbf{r}, \omega) - E_z^i(\mathbf{r}, \omega)\right] d\phi, \quad (2.83)$$

can be written in short as

$$\left(\partial_z^2 + k^2\right) \Upsilon(z) = \Phi(z), \qquad (2.84)$$

where $\Upsilon(z)$ and $\Phi(z)$ are the unknown term and the source term, respectively. The general solution of this equation is given by

$$\Upsilon(z) = A \exp(-jkz) + B \exp(-jk(h - z)) + \frac{1}{2jk}\int\limits_{z'=0}^{z} \Phi(z') \exp(-jk|z - z'|)dz', \quad (2.85)$$

where A and B are arbitrary constants. This inversion of the one-dimensional wave equation may be used to transform Pocklington's equation. The result is

$$
\int\limits_{z'=0}^{h} g(z-z',\omega)I(z',\omega)dz' = A\exp(-jkz) + B\exp(-jk(h-z))
$$

$$
+\frac{Y}{2}\left[V(\omega)\exp\left(-jk|z-z_g|\right) + \int\limits_{z'=0}^{h} \widehat{E}_z^i(\mathbf{r},\omega)\exp(-jk|z-z'|)dz' \right], \tag{2.86}
$$

for $0 \leq z \leq h$ and where $Y = \sqrt{\varepsilon/\mu} = \omega\varepsilon/k$ is the wave admittance. The latter equation is known as Hallén's integral equation. The coefficients A and B must be determined such that the current vanishes at the end points of the wire.

2.3 Conclusions

In this chapter two thin-wire integral equations for the total current that flows along the wire have been introduced: "Pocklington's equation with reduced kernel" and "Pocklington's equation with exact kernel". We have described that the motivation for considering only the total wire current is that this quantity governs the behavior of the scattered field. Moreover, a one-dimensional integral representation of this field is derived: the radiated field is determined up to $O(a^2)$ by replacing the actual current density on the mantle with the total current on the wire axis.

The logical following step is the development of an accurate and efficient numerical method to solve them, calculating the unknown current distribution. As will be described in Chapter 3, the wire is subdivided into segments and the current is approximated by means of a linear combination of expansion functions defined on these subdomains. The question now is which Pocklington's equation is preferred between the one with exact and the one with reduced kernel. In the literature it is observed that, the integral equation with the reduced kernel is ill-posed (i.e., the linear operator has an unbounded inverse) because the solution I does not depend continuously on the source terms (the known right-hand side term) [35–37]. As a consequence, by refining the discretization it is not possible to improve the accuracy of the current approximation [14]. A good alternative is the integral equation with exact kernel which is well-posed [7].

In conclusion, despite the extra numerical effort in evaluating the current due to the singularity of the Green's function in the exact kernel formulation (2.64), we choose Pocklington's equation with exact kernel (2.63) as the starting point of our subsequent numerical analysis.

Chapter 3

The solution of the thin-wire equation

In this chapter Pocklington's equation with exact kernel is solved numerically by the Method of Moments (MoM) [5]. First, the unknown current distribution is expanded in a sequence of basis functions. Second, a set of linearly independent "weighting/testing" functions is defined and a suitable inner product is applied on both sides of the integral equation. This leads to a system of linear equations which has to be solved numerically. Even though direct methods (e.g., LU decomposition) are the most obvious way for solving the discretized equation for a single wire, we use an iterative technique as the Conjugate Gradient (CG) method [25, 40, 41]. Indeed, especially for large problems (e.g., structures comprising coupled wires, surfaces and wire-to-surface junctions) non-iterative methods require considerable computational time and storage capacity. In this case, iterative methods present an alternative [42]. An iterative method offers the possibility to terminate the procedure once the solution is approximated within a fixed tolerance. In practice, this can lead to a considerable reduction in computation time.

In Section 3.1 we introduce the Galerkin Method of Moments with our choice of expansion and testing functions. Then in Sections 3.2 and 3.3 we discuss how elements of the system matrix can be computed accurately and efficiently. Finally some results are shown in Sec. 3.4.

3.1   Numerical Formulation

Starting from Pocklington's equation with exact kernel (2.68)

$$\left(\partial_z^2 + k^2\right) \int\limits_{z'=0}^{h} K_E(z - z', \omega) I(z', \omega) dz' = -j\omega\varepsilon \left(V(\omega)\delta(z - z_g) + \widehat{E}_z^i(\mathbf{r}, \omega)\right), \qquad (3.1)$$

we implement an accurate numerical scheme able to find the solution (i.e., the unknown current) of this integro-differential problem. The previous form may be symbolically written as

$$\mathcal{L}\{I(z)\} = f(z), \qquad (3.2)$$

where $\mathcal{L}$ represents a linear operator acting on the current $I(z)$ and where $f(z)$ is the known excitation. Henceforth, the dependence on the frequency ω will no longer be indicated explicitly.

3.1.1   Method of Moments

Aiming at the evaluation of the current $I(z)$, we apply the Method of Moments (MoM) to find an approximate solution of the continuous integral equation. Let $I(z)$ be expanded as a series of linearly independent functions $\psi_1(z), \psi_2(z), \psi_3(z), \ldots$ which satisfy the problem's boundary conditions and are defined in the domain of the operator $\mathcal{L}$, as

$$I(z) = \sum_{n=1}^{\infty} I_n \psi_n(z). \qquad (3.3)$$

I_n are complex unknown coefficients and $\psi_n(z)$ are referred to as "expansion" or "basis" functions. For exact solutions, (3.3) is an infinite summation, while for approximate solution the current $I(z)$ is expanded by means of a finite number N of basis functions as

$$I(z) \approx \sum_{n=1}^{N} I_n \psi_n(z). \qquad (3.4)$$

In the literature, two classes of basis functions are described, namely "global" (i.e., defined over the entire wire domain $(0, h)$) and "local" (i.e., defined over a sub-domain of the total domain of interest) basis functions [5]. When local basis functions are used, each I_n of the expansion (3.4) affects the approximation of $I(z)$ only over a subsection of the region of interest. For ease of implementation, we have decided to use local basis functions. Our choice

is to define N triangular (also referred to as rooftop) basis functions $\psi_n(z) = \psi(z - n\Delta z)$ on a uniform mesh with mesh size Δz

$$\psi(z) = \begin{cases} 1 - \left|\dfrac{z}{\Delta z}\right|, & \text{if } |z| \leq \Delta z, \\ 0, & \text{otherwise.} \end{cases} \tag{3.5}$$

The linear combination (3.4) will then be a piecewise linear function with the observation that functions (3.5) do not properly represent the known square-root behavior of the current at the ends of the wire (i.e., $O(\sqrt{z(h-z)})$ for $z \approx 0, h$). Nevertheless, increasing the number of functions ψ_n used, improves the approximation (3.4) on the local sub-domains and, for $N \to \infty$, the local approximation converges to the exact solution [7]. As shown in Fig. 3.1, the wire is segmented in $N + 1$ intervals, each of length $\Delta z = h/(N+1)$ and each basis function ψ_n is defined over two adjoining segments.

The second step is to use the linearity of the operator $\mathcal{L}$. Thus, we can interchange the order of the summation and the operator $\mathcal{L}$ on the left-hand side of equation (3.2)

$$\mathcal{L}\left\{\sum_{n=1}^{N} I_n \psi_n(z)\right\} = \sum_{n=1}^{N} I_n \mathcal{L}\left\{\psi_n(z)\right\}. \tag{3.6}$$
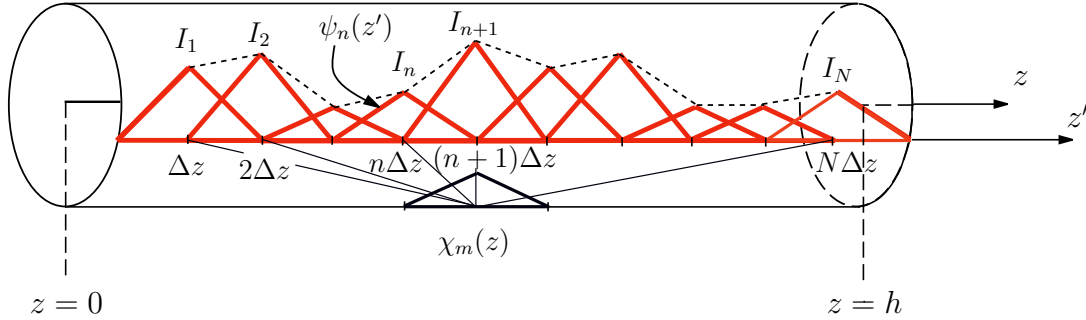
Figure 3.1: *Basis, testing functions and total current approximation.*

Next, we define a suitable inner product

$$< f(z), g(z) > = \int_{z=0}^{h} f^*(z)g(z)dz, \tag{3.7}$$

where f and g are two general complex functions defined in $0 \leq z \leq h$ and where the superscript $*$ indicates the complex conjugate. Now, we define a set of N linearly independent "weighting" or "testing" functions $\{\chi_m\}_{m=1}^{N}$ for the operator $\mathcal{L}$. Finally, taking the

inner product of equation (3.2) with a testing function χ_m and applying the property of linearity (3.6) in the left-hand side, yields a system of N equations in N unknowns which can be written in matrix form as

$$\underline{\underline{Z}}\,\mathbf{I} = \underline{\mathbf{F}}. \tag{3.8}$$

The $N \times N$ matrix

$$\underline{\underline{Z}} = \begin{bmatrix} \langle \chi_1, \mathcal{L}\{\psi_1\} \rangle & \langle \chi_1, \mathcal{L}\{\psi_2\} \rangle & \dots & \langle \chi_1, \mathcal{L}\{\psi_N\} \rangle \\ \langle \chi_2, \mathcal{L}\{\psi_1\} \rangle & \langle \chi_2, \mathcal{L}\{\psi_2\} \rangle & \dots & \langle \chi_2, \mathcal{L}\{\psi_N\} \rangle \\ \vdots & \vdots & \vdots & \vdots \\ \langle \chi_N, \mathcal{L}\{\psi_1\} \rangle & \langle \chi_N, \mathcal{L}\{\psi_2\} \rangle & \dots & \langle \chi_N, \mathcal{L}\{\psi_N\} \rangle \end{bmatrix}, \tag{3.9}$$

is referred to as the "system matrix" and the N-dimensional vectors

$$\underline{\mathbf{F}} = -j\omega\varepsilon \begin{bmatrix} \left\langle \chi_1, V(\omega)\delta(z - z_g) + \widehat{E}_z^i(\mathbf{r}, \omega) \right\rangle \\ \left\langle \chi_2, V(\omega)\delta(z - z_g) + \widehat{E}_z^i(\mathbf{r}, \omega) \right\rangle \\ \vdots \\ \left\langle \chi_N, V(\omega)\delta(z - z_g) + \widehat{E}_z^i(\mathbf{r}, \omega) \right\rangle \end{bmatrix}, \qquad \mathbf{I} = \begin{bmatrix} I_1 \\ I_2 \\ \vdots \\ I_N \end{bmatrix}, \tag{3.10}$$

represent the excitation (known vector) and the unknown current, respectively. We choose to have real-valued weighting functions identical to the basis functions, i.e., $\chi_m(z) = \psi_m(z)$, for $m = 1, \dots, N$. In this particular case the Method of Moments (MoM) is referred to as the Galerkin Method of Moments [5], (see Fig. 3.1) and, for a straight wire, this discretization process gives rise to a Toeplitz symmetric system matrix $\underline{\underline{Z}}$. Moreover, the latter formulation (3.8) converges to the correct solution for $\Delta z \to 0$ as shown in [7], [8, pp. 212]. It is worth noticing that the storage required for the system matrix $\underline{\underline{Z}}$ is reduced from $O(N^2)$ to $O(N)$, since $\underline{\underline{Z}}$ is a symmetric Toeplitz matrix. Thanks to this property we achieve a reduction of CPU time of a factor N in the computation of the matrix and the solution only requires $O(N^2)$ flops instead of $O(N^3)$ [43, Sec. 4.7]. From the exact kernel equation (3.1), applying the Galerkin MoM, we have

$$\sum_{n=1}^{N} I_n \int_{z=0}^{h} \psi_m(z) \left(\int_{z'=0}^{h} \left(\partial_z^2 + k^2 \right) K_E(z - z') \psi_n(z') dz' \right) dz$$

$$= -j\omega\varepsilon \int_{z=0}^{h} \psi_m(z) \left(V(\omega)\delta(z - z_g) + \widehat{E}_z^i(\mathbf{r}, \omega) \right) dz, \tag{3.11}$$

for $m = 1, \ldots, N$. Hence, the (m, n)-th element of the system matrix $\underline{\underline{Z}}$ in (3.8) is

$$
Z_{m,n} = \int\limits_{z=0}^{h} \psi_m(z) \left(\int\limits_{z'=0}^{h} \left(\partial_z^2 + k^2 \right) K_E(z - z') \psi_n(z') dz' \right) dz,
\tag{3.12}
$$

with ψ_m, ψ_n being the $m-$th testing and the $n-$th basis function, respectively. The obvious next step is to solve the linear system (3.8) of N equations in N unknowns. For a single wire the solution can be computed efficiently by using a CG-FFT scheme [25, Sec. 4.3] [41] where for a Toeplitz matrix the solution complexity goes from $O(N^2)$ flops for the entire computation to $O(N \ln N)$ per iteration step. Since we aim at the analysis of structures more complex than a single wire, we will employ the CG method only.

3.2 Evaluation of the known excitation

In this section we describe how to evaluate the generic m-th element of the known excitation vector $\underline{F}$ in (3.10)

$$
F_m = -j\omega\varepsilon \int\limits_{z=(m-1)\Delta z}^{(m+1)\Delta z} \psi_m(z) \left(V(\omega)\delta(z - z_g) + \widehat{E}_z^i(\mathbf{r}, \omega) \right) dz,
\tag{3.13}
$$

for the two types of excitation considered: the delta-gap voltage excitation and the incident plane wave.

3.2.1 Delta-gap voltage excitation

Focusing on the delta gap, we have

$$
F_m = -j\omega\varepsilon \int\limits_{z=(m-1)\Delta z}^{(m+1)\Delta z} \psi_m(z) V(\omega)\delta(z - z_g) dz = -j\omega\varepsilon V(\omega)\psi_m(z_g),
\tag{3.14}
$$

or more explicitly,

$$
F_m = \begin{cases} -j\omega\varepsilon V(\omega) \left(1 - \dfrac{|z_g - m\Delta z|}{\Delta z} \right), & |z_g - m\Delta z| \leq \Delta z, \\ 0, & \text{otherwise.} \end{cases}
\tag{3.15}
$$

With respect to discretization it is worth noticing that, if the delta gap is placed on a lattice point (i.e., $z_g = m\Delta z$), only a single testing function ψ_m contributes to the computation of

F_m. Thus, the previous expression is identically equal to the delta-gap voltage value $V(\omega)$ apart from a constant $-j\omega\varepsilon$:

$$F_m = \begin{cases} -j\omega\varepsilon V(\omega), & z_g = m\Delta z, \\ 0, & \text{otherwise.} \end{cases} \tag{3.16}$$

For positions $z_g \neq m\Delta z$ in between the lattice points, on the other hand, two testing functions are involved in the computation of F_m.

3.2.2   Incident field

From (3.10), for an incident field $\mathbf{E}^i(\mathbf{r}, \omega)$ we obtain

$$F_m = -j\omega\varepsilon < \psi_m, \widehat{E}_z^i(\mathbf{r}, \omega) >= -j\omega\varepsilon < \psi_m, \frac{1}{2\pi}\int\limits_{\phi=0}^{2\pi} E_z^i(\mathbf{r}, \omega)d\phi >, \tag{3.17}$$

where $E_z^i(\mathbf{r}, \omega)$ is the z-component of $\mathbf{E}^i$.
In particular, for an incident plane wave $\mathbf{E}^i = \mathbf{E}_0\exp(-j\mathbf{k}^i \cdot \mathbf{r})$, recalling the expression (2.82) in Sec. 2.2.6, we can write

$$\frac{1}{2\pi}\int\limits_{\phi=0}^{2\pi} E_z^i(\mathbf{r}, \omega)d\phi = -E_{0\theta}\sin\theta_i\exp(jzk^i\cos\theta_i)J_0(ak^i\sin\theta_i). \tag{3.18}$$

Substituting this result in (3.17) yields

$$F_m = j\omega\varepsilon E_{0\theta}\sin\theta_i J_0(ak^i\sin\theta_i)\int\limits_{z=(m-1)\Delta z}^{(m+1)\Delta z}\psi_m(z)\exp\left(jzk^i\cos\theta_i\right)dz. \tag{3.19}$$

The integral over z depends only on the exponent and on $\psi_m(z)$, and can be determined in a closed form (see Appendix C.1). Moreover, the first-kind Bessel function J_0 in (3.19) can be written by means of series expansion [39, eq. 9.1.10] and, for wires with $ak^i \ll 1$, we can approximate J_0 by

$$J_0(ak^i\sin\theta_i) = 1 + O\left((ak^i)^2\right). \tag{3.20}$$

3.3   Efficient evaluation of the system matrix elements

At this stage, our aim is to efficiently evaluate the expression (3.12) for each m, $n = 1, \ldots, N$ to fill the system matrix $\underline{\mathbf{Z}}$. First, we write (3.12) as the sum of two constituting elements

$$Z_{m,n} = Z_{m,n}^E + Z_{m,n}^M$$

$$Z_{m,n}^E = \int\limits_{z=0}^{h} \psi_m(z) \left(\partial_z^2 \int\limits_{z'=0}^{h} K_E(z - z') \, \psi_n(z')dz' \right) dz, \tag{3.21}$$

$$Z_{m,n}^M = k^2 \int\limits_{z=0}^{h} \int\limits_{z'=0}^{h} K_E(z - z')\psi_m(z)\psi_n(z')dz'dz. \tag{3.22}$$

The integrals given above cannot be determined analytically and they have to be approximated efficiently. Their evaluation involves a 3D integration: one in dz and one in dz' as can be observed in (3.21), (3.22), and a third integration in φ present in the exact kernel K_E (2.64). Special attention is needed when the argument of K_E approaches 0.

First, we focus on the element $Z_{m,n}^E$. Following the scheme proposed by Butler and Wilton [44] we re-write $Z_{m,n}^E$ in (3.21) as

$$Z_{m,n}^E = \int\limits_{z=0}^{h} \psi_m(z)\partial_z^2 u(z)dz, \tag{3.23}$$

where

$$u(z) = \int\limits_{z'=0}^{L} K_E(z - z') \, \psi_n(z')dz'. \tag{3.24}$$

Integrating (3.23) by parts twice yields

$$Z_{m,n}^E = \int\limits_{z=0}^{h} \left(\partial_z^2 \psi_m(z) \right) u(z)dz$$

$$= \frac{1}{\Delta z} \int\limits_{z=0}^{h} \left[\delta(z - (m-1)\Delta z) - 2\delta(z - m\Delta z) + \delta(z - (m+1)\Delta z) \right] u(z)dz. \tag{3.25}$$

The right-hand side of (3.25) can be written as a difference rule:

$$Z_{m,n}^E = u_{m-1,n} - 2u_{m,n} + u_{m+1,n}, \tag{3.26}$$

with

$$u_{m,n} = \frac{1}{\Delta z} \int\limits_{z'=(n-1)\Delta z}^{(n+1)\Delta z} \psi_n(z')K_E(m\Delta z - z')dz', \qquad m, n = 1, \ldots, N, \tag{3.27}$$

since the basis function $\psi_n(z')$ is identical to zero outside the interval $|z'/\Delta z - n| < 1$. Writing the explicit expression of ψ_n and applying the change of variable $s = -z'/\Delta z + n$ yields

$$
\begin{aligned}
u_{m,n} = u_{m-n} &= \int_{s=0}^{1} (1-s)K_E((s+m-n)\Delta z)ds + \int_{s=-1}^{0} (1+s)K_E((s+m-n)\Delta z)ds \\
&= \int_{s=0}^{1} (1-s)\left[K_E((s+m-n)\Delta z) + K_E((m-n-s)\Delta z)\right]ds. \quad (3.28)
\end{aligned}
$$

The same result is obtained following the scheme proposed by Davies et al. [15]. We proceed from (3.28) defining $\ell = m - n$, and therefore we write

$$
u_{m-n} = u_\ell = \int_{s=0}^{1} (1-s)\left[K_E((\ell+s)\Delta z) + K_E((\ell-s)\Delta z)\right]ds, \quad (3.29)
$$

where we have restricted the index ℓ to $\ell = 0, 1, ..., N - 1$ since $u_\ell = u_{-\ell}$. In conclusion, the constituting element in (3.26) becomes

$$
Z^E_{m,n} = Z^E_{m-n} = Z^E_\ell = (u_{\ell-1} - 2u_\ell + u_{\ell+1}). \quad (3.30)
$$

Second, we consider the element $Z^M_{m,n}$ in (3.22). Following the procedure described in [15], we have verified that by changing the variables z and z' as follows

$$
\begin{cases}
x = \dfrac{z}{\Delta z} - m, \\
x' = \dfrac{z'}{\Delta z} - n,
\end{cases}
\quad \text{and} \quad
\begin{cases}
s = x - x', \\
s' = x + x',
\end{cases}
\quad (3.31)
$$

leads to

$$
Z^M_\ell = k^2(\Delta z)^2 \int_{s=0}^{2} \gamma(s)\left[K_E((\ell+s)\Delta z) + K_E((\ell-s)\Delta z)\right]ds, \quad (3.32)
$$

where $\gamma(s)$ is a twice continuously differentiable function [15], (see Fig. 3.2):

$$
\gamma(s) = \begin{cases}
\left(\dfrac{s^3}{2} - s^2 + \dfrac{2}{3}\right), & 0 \le s \le 1, \\
\dfrac{(2-s)^3}{6}, & 1 < s \le 2.
\end{cases}
\quad (3.33)
$$
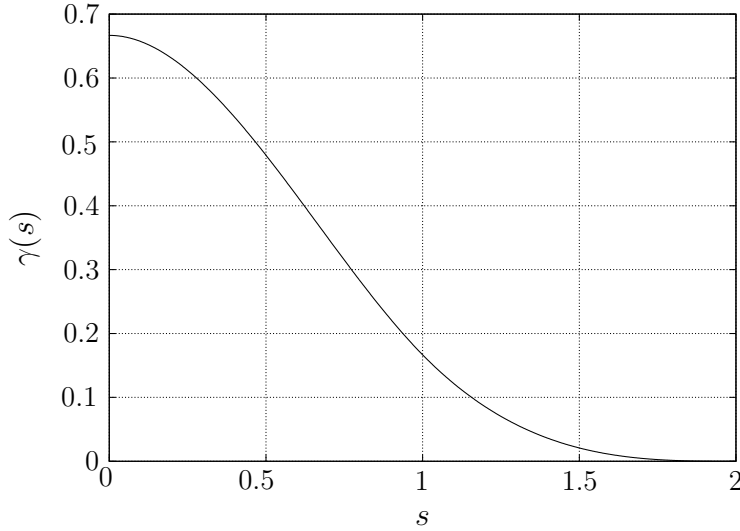
Figure 3.2: *Behavior of the function $\gamma(s)$, expression (3.33).*

In conclusion, the coefficients u_ℓ, $u_{\ell-1}$, $u_{\ell+1}$ in (3.29), (3.30) and the constituting element Z_ℓ^M in (3.32) require the evaluation of integrals of the form

$$I_\mathrm{g}(\overline{\theta}) = \int\limits_{s=s_1}^{s_2} P(s)K_E((s+\overline{\theta})\Delta z)ds, \tag{3.34}$$

with $P(s)$ a polynomial and $\overline{\theta} = \pm\ell$. It is noted that the 3D integrals in (3.21) and (3.22) have been simplified to 2D integrals of the given form (3.34) by a change of variables. When $(s+\overline{\theta})\Delta z$ vanishes, the integrand in (3.34) exhibits a logarithmic singularity as we will show in Secs. 3.3.1 and 3.3.2. In this case, special care has to be taken in computing the integral. We proceed as follows

$$I_\mathrm{g}(\overline{\theta}) = \underbrace{\int\limits_{s=s_1}^{s_2} P(s)\left[K_E((s+\overline{\theta})\Delta z) - K_\mathrm{sing}((s+\overline{\theta})\Delta z)\right]ds}_{=I_1} + \underbrace{\int\limits_{s=s_1}^{s_2} P(s)K_\mathrm{sing}((s+\overline{\theta})\Delta z)ds}_{=I_2},$$

$$\tag{3.35}$$

where K_sing is a properly chosen function that follows the asymptotic behavior of K_E when its argument approaches 0 and it is chosen such that the evaluation of I_2 can be carried out analytically. We give the detailed expression of function K_sing in Sec. 3.3.2. In this way the integrand of the first term I_1 is non-singular, continuously differentiable and its integral is finite. The function K_sing has a singular behavior, but its integral I_2 is known analytically.

3.3.1   Efficient evaluation of the exact kernel

We focus now on the evaluation of $K_E(z - z')$ as defined in (2.64). Basically we follow the elegant and reliable algorithm proposed by Davies et al. [15], implementing the algorithm into a numerical code in double precision. The introduction of $\rho = z - z'$ leads to

$$K_E(\rho) = \frac{1}{4\pi^2 a} \int\limits_{\varphi=0}^{\pi/2} \frac{\exp\left(-j2ak\sqrt{\left(\frac{\rho}{2a}\right)^2 + \sin^2\varphi}\right)}{\sqrt{\left(\frac{\rho}{2a}\right)^2 + \sin^2\varphi}} d\varphi. \tag{3.36}$$

Introducing the two "scaled" variables

$$\widetilde{\lambda} = \frac{|\rho|}{2a}, \qquad \widetilde{\nu} = 2ka, \tag{3.37}$$

we can write a "scaled" form of the exact kernel

$$K_E(\widetilde{\lambda}) = \frac{1}{4\pi^2 a} \int\limits_{\varphi=0}^{\pi/2} \frac{\exp\left(-j\widetilde{\nu}\sqrt{\widetilde{\lambda}^2 + \sin^2\varphi}\right)}{\sqrt{\widetilde{\lambda}^2 + \sin^2\varphi}} d\varphi = \frac{F(\widetilde{\lambda}, \widetilde{\nu})}{4\pi^2 a}, \tag{3.38}$$

with

$$F(\widetilde{\lambda}, \widetilde{\nu}) = \int\limits_{\varphi=0}^{\pi/2} \frac{\exp\left(-j\widetilde{\nu}\widetilde{R}\right)}{\widetilde{R}} d\varphi, \qquad \text{and } \widetilde{R} = \sqrt{\widetilde{\lambda}^2 + \sin^2\varphi}. \tag{3.39}$$

To show some properties of this scaled form F we decompose it into two parts

$$F(\widetilde{\lambda}, \widetilde{\nu}) = \int\limits_{\varphi=0}^{\pi/2} \frac{d\varphi}{\widetilde{R}} + \int\limits_{\varphi=0}^{\pi/2} \frac{\exp\left(-j\widetilde{\nu}\widetilde{R}\right) - 1}{\widetilde{R}} d\varphi. \tag{3.40}$$

We note that the second integrand is bounded (in fact we extract the singularity at $\widetilde{R} = 0$) while the first integral can be written as

$$\int\limits_{\varphi=0}^{\pi/2} \frac{d\varphi}{\widetilde{R}} = \int\limits_{\varphi=0}^{\pi/2} \frac{d\varphi}{\sqrt{\widetilde{\lambda}^2 + \sin^2\varphi}} = \int\limits_{\varphi=0}^{\pi/2} \frac{d\varphi}{\sqrt{\widetilde{\lambda}^2 + \cos^2\varphi}} = \frac{1}{\sqrt{\widetilde{\lambda}^2 + 1}} K^{\text{ell}}\left(\frac{1}{\sqrt{\widetilde{\lambda}^2 + 1}}\right), \quad \tag{3.41}$$

where

$$K^{\text{ell}}(q) = \int\limits_{\varphi=0}^{\pi/2} \frac{d\varphi}{\sqrt{1 - q^2 \sin^2\varphi}}, \qquad \text{with } 0 \le q < 1, \tag{3.42}$$

is the complete elliptic integral of the first kind [39, eq. 17.3.1]. Since K^{ell} has a logarithmic singularity as its argument approaches 1 [39], this means also that K_E in (3.38) has the property

$$K_E(\widetilde{\lambda}) = O(\ln|\widetilde{\lambda}|), \qquad \text{as } \widetilde{\lambda} \to 0. \tag{3.43}$$

To overcome the difficulties in evaluating $F(\widetilde{\lambda}, \widetilde{\nu})$ and consequently $K_E(\widetilde{\lambda})$ due to the presence of a singularity, we follow the procedure suggested in [15]. We distinguish between the cases where $\widetilde{\lambda}$ is large and $\widetilde{\lambda}$ is small. As a "rule of thumb" this transition is made at a switching value

$$\widetilde{\lambda}_{\text{switch}} = \frac{10}{10 + |\widetilde{\nu}|}. \tag{3.44}$$

In the case of large $\widetilde{\lambda}$, (i.e., $\widetilde{\lambda} \geq \widetilde{\lambda}_{\text{switch}}$), the integral (3.39) is computed by applying a composite trapezoidal rule. For small $\widetilde{\lambda}$ (i.e., $\widetilde{\lambda} < \widetilde{\lambda}_{\text{switch}}$) we treat the real and imaginary parts of (3.39) separately, thus

$$F(\widetilde{\lambda}, \widetilde{\nu}) = F_1(\widetilde{\lambda}) - jF_2(\widetilde{\lambda}, \widetilde{\nu}), \tag{3.45}$$

with

$$F_1(\widetilde{\lambda}) = \int\limits_{\varphi=0}^{\pi/2} \frac{\cos(\widetilde{\nu}\widetilde{R})}{\widetilde{R}} d\varphi, \qquad F_2(\widetilde{\lambda}, \widetilde{\nu}) = \int\limits_{\varphi=0}^{\pi/2} \frac{\sin(\widetilde{\nu}\widetilde{R})}{\widetilde{R}} d\varphi. \tag{3.46}$$

The integrand of the imaginary part F_2 is a smooth function and does not show a singular behavior. Hence, the evaluation of F_2 can be carried out numerically with a composite trapezoidal rule. It is worth noticing that when performing integration by use of a trapezoidal rule, a better approximation of the integral can be obtained with the Romberg rule [45] which is an extrapolated version of the trapezoidal rule estimating the error term without requiring any further function evaluations. Focusing on the real part F_1, we note that the integral is similar to the complete elliptic integral in (3.41) and (3.42)

$$F_1(\widetilde{\lambda}, \widetilde{\nu} = 0) = \int\limits_{\varphi=0}^{\pi/2} \frac{d\varphi}{\widetilde{R}} = \int\limits_{\varphi=0}^{\pi/2} \frac{d\varphi}{\sqrt{\widetilde{\lambda}^2 + \sin^2\varphi}} = \frac{1}{\sqrt{\widetilde{\lambda}^2 + 1}} K^{\text{ell}}\left(\frac{1}{\sqrt{\widetilde{\lambda}^2 + 1}}\right). \tag{3.47}$$

This similarity gave rise to the idea to apply a well-known method for the computation of elliptic integrals to evaluate F_1 (3.46). This method uses a Landen transform [15] and it is discussed in Appendix C.2.

3.3.2   Definition of function K_{sing}

Aiming at the evaluation of integrals I_1 and I_2 in (3.35), once the exact kernel K_E is computed, we still have to determine the singular function K_{sing}. We choose K_{sing} such that it follows the asymptotic behavior of K_E for small values of its argument. Starting from the expression (3.41) we know that the following asymptotic behavior of the complete elliptic integral of the first kind is valid

$$K^{\mathrm{ell}}\left(\frac{1}{\sqrt{\widetilde{\lambda}^2+1}}\right) \approx a_0 + \frac{1}{2}\ln\left(\frac{1+\widetilde{\lambda}^2}{\widetilde{\lambda}^2}\right) \approx -\ln\widetilde{\lambda}, \quad \text{for } \widetilde{\lambda} \to 0, \tag{3.48}$$

with $a_0 \approx 1.38629$ [39, eq. 17.3.33]. Consequently from (3.40) and (3.41) we obtain

$$F(\widetilde{\lambda},\widetilde{\nu}) \approx -\ln\widetilde{\lambda}, \qquad \widetilde{\lambda} \to 0, \tag{3.49}$$

and

$$K_E(\widetilde{\lambda}) \approx \frac{-1}{4\pi^2 a}\ln|\widetilde{\lambda}|, \qquad \widetilde{\lambda} \to 0. \tag{3.50}$$

In order to arrive at a continuously differentiable function K_{sing}, we finally write

$$K_{\mathrm{sing}}(\widetilde{\lambda}) = \begin{cases} \dfrac{1}{4\pi^2 a}\left[-\ln|\widetilde{\lambda}| + |\widetilde{\lambda}| - 1\right], & |\widetilde{\lambda}| < 1, \\ 0, & \text{otherwise.} \end{cases} \tag{3.51}$$

The behavior of the function K_{sing} is illustrated in Fig. 3.3.
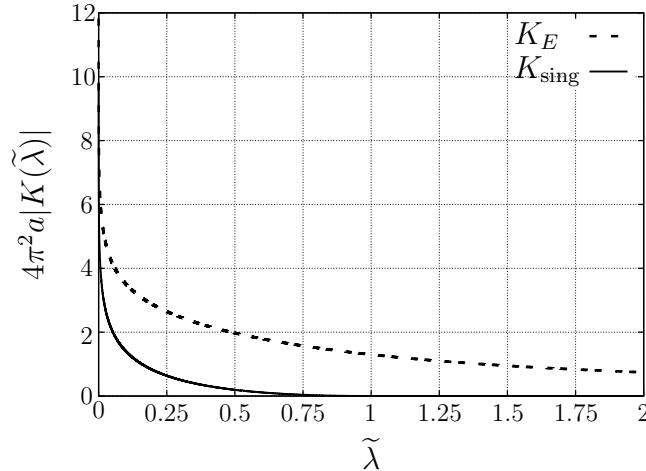
Figure 3.3: *Behavior of the absolute value of the exact kernel K_E (3.38) and of the singular function K_{sing} (3.51) normalized to* $\dfrac{1}{4\pi^2 a}$ *for $\widetilde{\nu} = 1$.*

Once the singular function K_{sing} is defined, we can determine the integral I_2 in (3.35) analytically. The explicit closed form of this integral is given in Appendix C.3.

3.4   Numerical results

Following the numerical method presented so far, we have implemented a FORTRAN program referred to as Galerkin Method of Moments with Exact Kernel (GEKMoM) to calculate the current distribution.

3.4.1   Total current of a thin wire

Representative results are shown for a perfectly electrically conducting (PEC) straight thin wire in free space. First, we compute the current distribution of a thin wire placed along the positive z-axis illuminated by a normally incident plane wave $|\mathbf{E}^i| = 1$ V/m, polarized in the z-direction. The wire has length $h = \lambda/2$ and radius $a = \lambda/200$ and its current is expanded by means of $N = 31$ basis functions (i.e., 32 segments). Figure 3.4-(a) shows good agreement between the current computed by using the described numerical scheme (namely "GEKMoM"), the commercial software NEC 4.1 [2] and results in the literature [25, Fig. 4.2] using a numerical implementation of the integral equation with reduced kernel. Further, the discretization is refined and 155 basis functions (i.e., 156 segments) are used to approximate the wire current. Results are shown in Fig. 3.4-(b).

Second, a different excitation function is considered. The wire is fed by a delta-gap voltage $V(\omega) = V_0 = 1$ V placed in its center. The physical dimensions of the wire are the same of the previous example. Results are given in Fig. 3.5-(a) for $N = 31$ and in Fig. 3.5-(b) for $N = 155$. The magnitudes of the current I computed by GEKMoM and NEC 4.1 are shown. In both examples (i.e., a plane wave and a delta-gap voltage) it is observed that, by refining the discretization, the solution to the equation with reduced kernel and the one computed by NEC 4.1 produce unstable and oscillatory results, which can easily be rejected from physical considerations. Nevertheless, it is known that in NEC 4.1 this kind of oscillatory behavior may occur for $\Delta z/a$ less than about 0.5, where Δz is the segment length [2]. We observe that for a delta-gap voltage source these oscillations occur in the center of the wire, while for a smooth incident field they start slightly near the end faces. The cause of these oscillations lies in the ill-posed nature of the integral equation with reduced kernel [14], [25, Secs. 3.3.3 and 4.4.1]. It is our conclusion that the erroneous behavior of results calculated by NEC 4.1 is most probably caused by the reduced kernel used in NEC 4.1 [3]. An effective regularization procedure to avoid these instabilities is proposed in [25, Sec. 3.3.4].

(a)

(b)
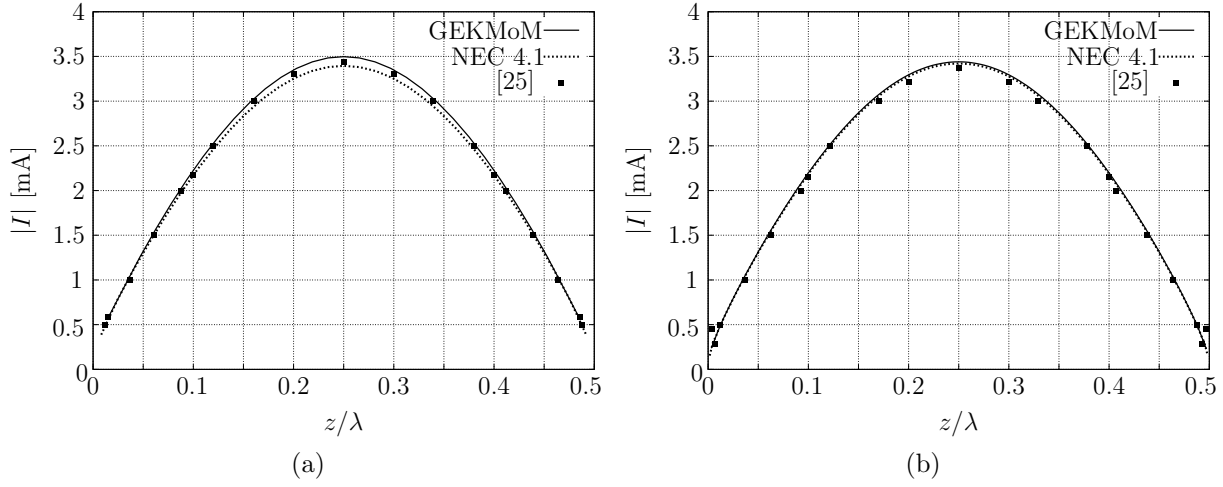
Figure 3.4: *Magnitude of the current distribution versus the position along a thin wire, $h = \lambda/2$ and $h/a = 100$, illuminated by a normally incident z-polarized plane wave. (a)- Using $N = 31$ basis functions; (b)- using $N = 155$ basis functions.*

(a)

(b)
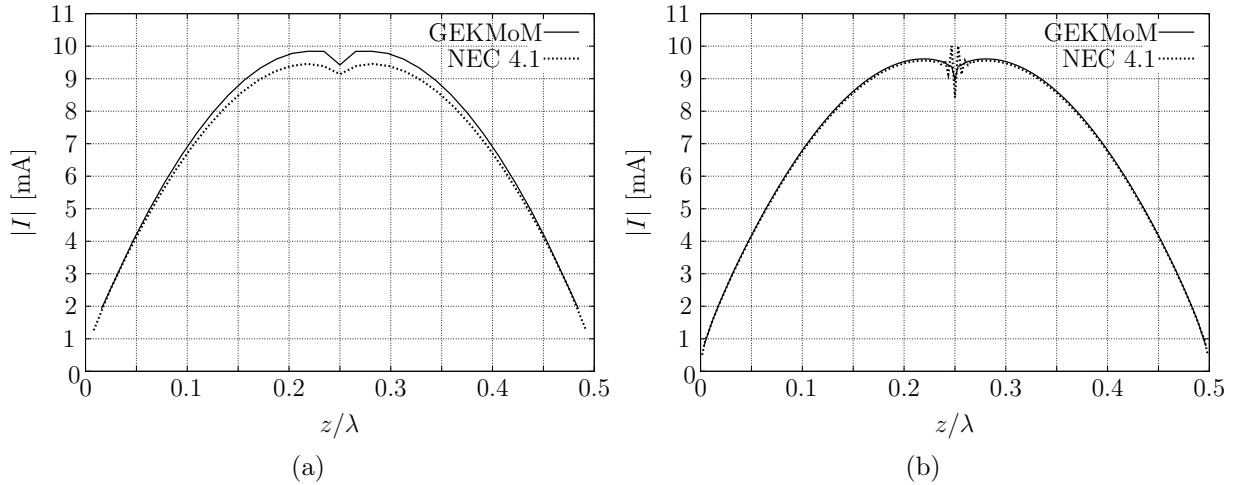
Figure 3.5: *Magnitude of the current distribution versus the position along a thin wire, $h = \lambda/2$ and $h/a = 100$, fed by a delta-gap voltage $V_0 = 1$ V in its center. (a)- Using $N = 31$ basis functions; (b)- using $N = 155$ basis functions.*

3.4.2   Total current of a thick wire

As further test, we consider the same $h = \lambda/2$ straight wire studied in the previous section with a different radius of $a = \lambda/60$. For this straight thick wire fed by a delta-gap source in its center, we have calculated the modulus of the current using 31 and 51 basis functions. In Fig. 3.6 the results are compared with those computed by NEC 4.1 [2]. The main discrepancies between the two models are observed near the delta-gap where an oscillatory behavior for the current calculated by NEC 4.1 is present. The exact kernel formulation gives stable results whereas approximations used in NEC 4.1 [3] do not.
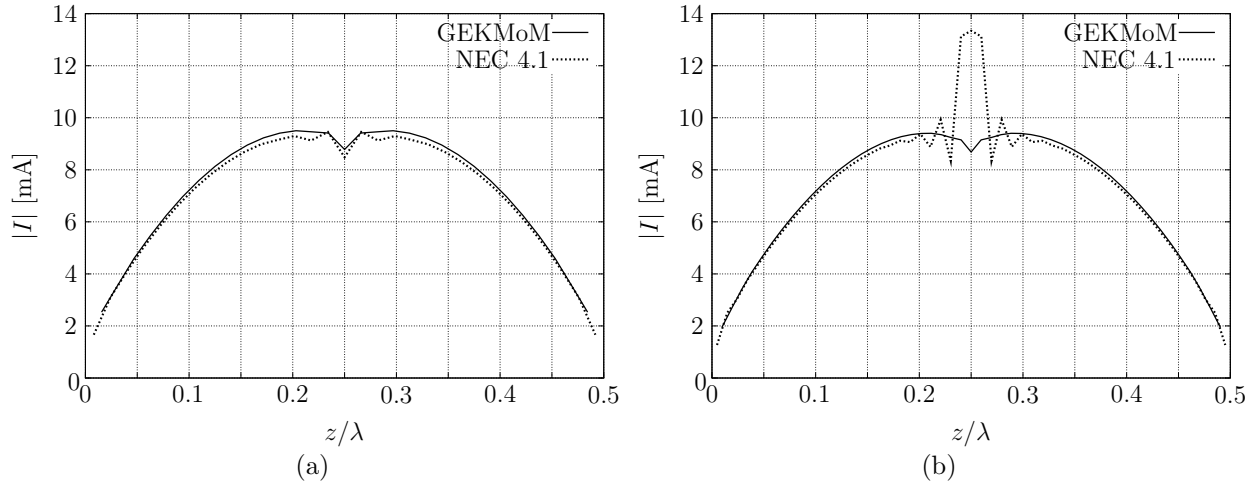
Figure 3.6: *Magnitude of the current distribution versus the position along a thick wire, $h = \lambda/2$ and $h/a = 30$, fed by a delta-gap voltage $V_0 = 1$ V in its center. (a)- Using $N = 31$ basis functions; (b)- using $N = 51$ basis functions.*

3.4.3   Convergence study

For a $\lambda/2$ thin wire of radius $a = \lambda/200$ illuminated by a normally incident z-polarized plane wave $|\mathbf{E}^i| = 1$ V/m, we have computed the current along the wire by varying the number N of basis functions used. Figures 3.7 and 3.8 show a converging behavior of the numerical method implemented, both for the real and the imaginary parts of the current distribution. The same analysis has been performed for a thick wire with $h = \lambda/2$ and radius $a = \lambda/40$. Also in this case, a good convergence is achieved, see Figs. 3.9 and 3.10.
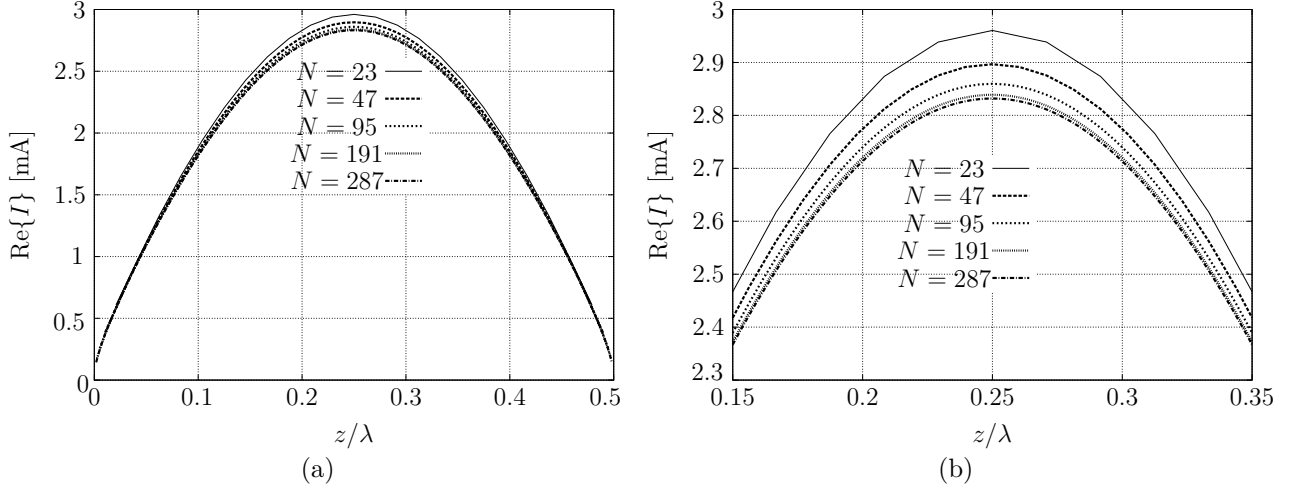
Figure 3.7: *Real part of the total current versus the normalized position z/λ for a $\lambda/2$ wire, with $h/a = 100$, illuminated by a normally incident z-polarized plane wave, varying the number N of basis functions used: (a)- current along the entire wire; (b)- current in the central region of the wire (zoom).*
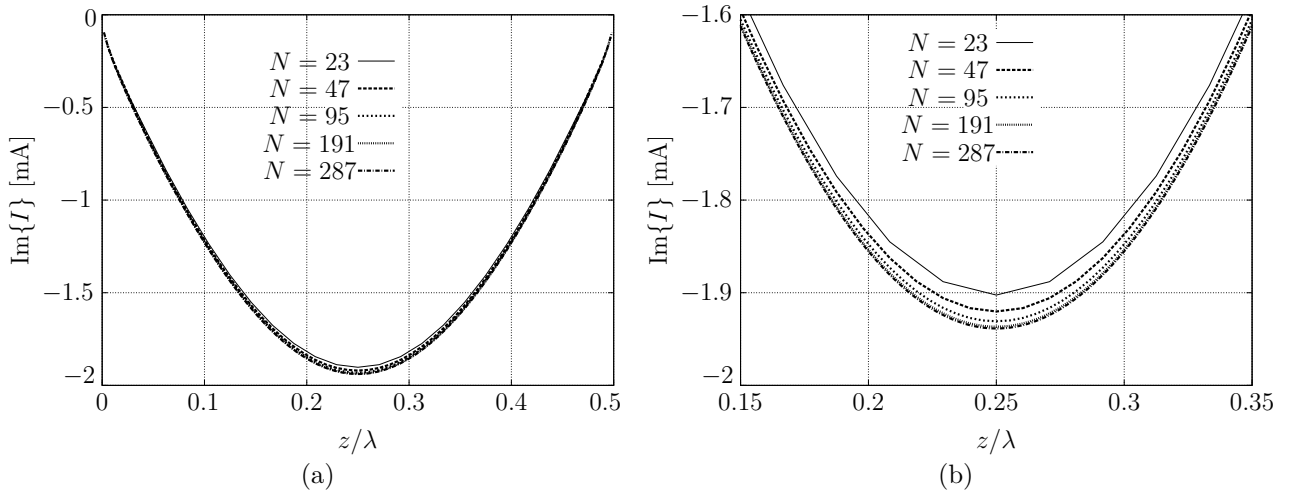
Figure 3.8: *Imaginary part of the total current versus the normalized position z/λ for a $\lambda/2$ wire, with $h/a = 100$, illuminated by a normally incident z-polarized plane wave, varying the number N of basis functions used: (a)- current along the entire wire; (b)- current in the central region of the wire (zoom).*
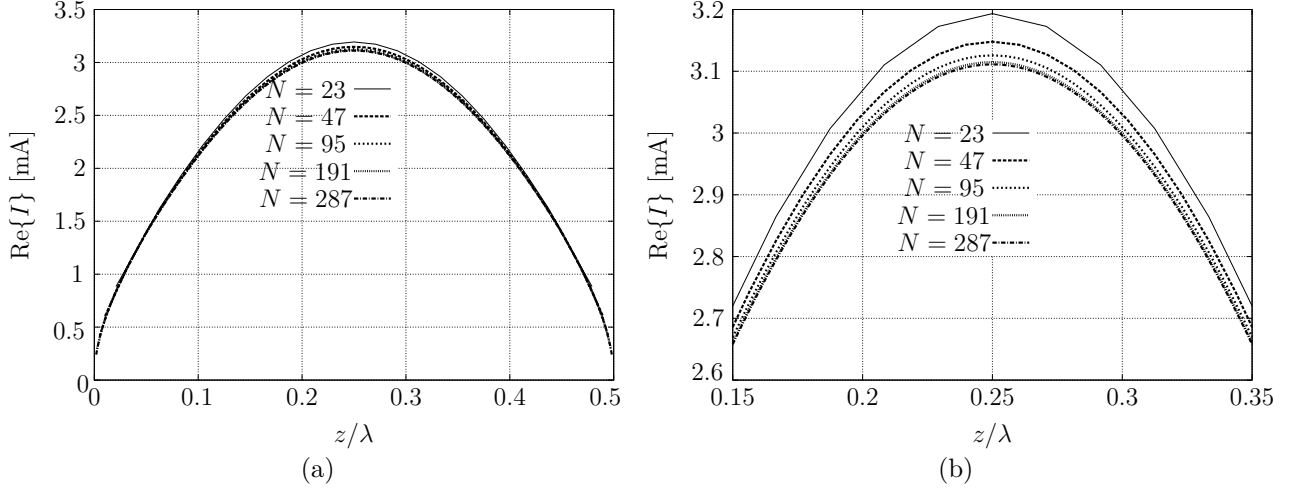
Figure 3.9: *Real part of the total current versus the normalized position z/λ for a $\lambda/2$ wire, with $h/a = 20$, illuminated by a normally incident z-polarized plane wave, varying the number N of basis functions used: (a)- current along the entire wire; (b)- current in the central region of the wire (zoom).*
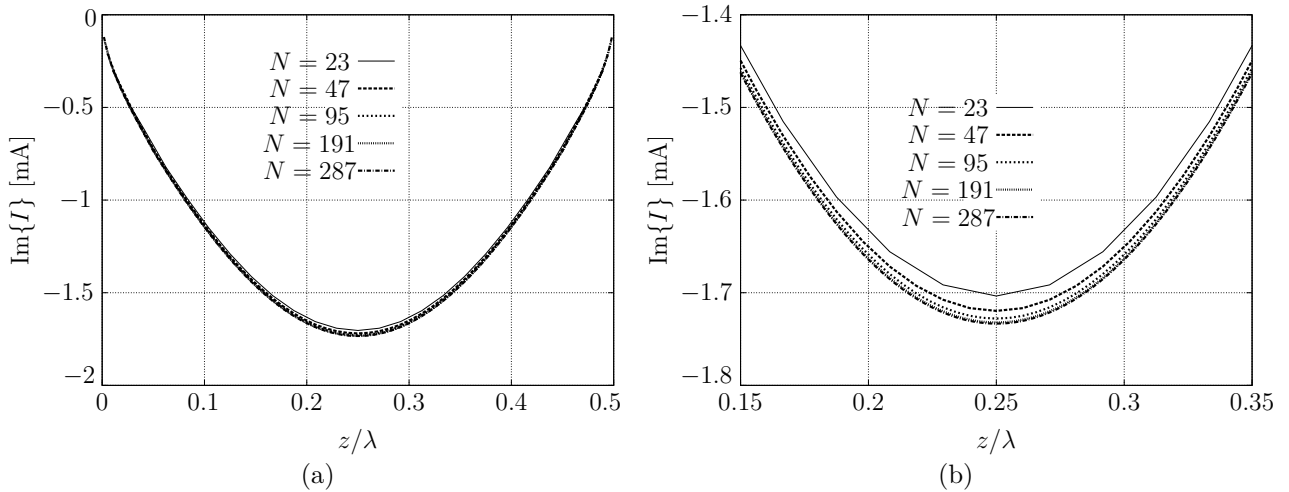
Figure 3.10: *Imaginary part of the total current versus the normalized position z/λ for a $\lambda/2$ wire, with $h/a = 20$, illuminated by a normally incident z-polarized plane wave, varying the number N of basis functions used: (a)- current along the entire wire; (b)- current in the central region of the wire (zoom).*

To study the accuracy of the evaluated current distribution more thoroughly, we have calculated the root-mean-square (RMS) error ζ_{cur} along the wire as

$$\zeta_{\mathrm{cur}} = \sqrt{\frac{\int\limits_{z=0}^{h} \left| I(z) - \widetilde{I}(z) \right|^2 dz}{\int\limits_{z=0}^{h} |I(z)|^2 dz}}. \tag{3.52}$$

As a reference $I(z)$, we have considered the value of the current when a high number of basis functions (e.g., $N = 575$) are used and the method is assumed to have converged. The approximated value $\widetilde{I}(z)$ represents the current along the wire when it is expanded by a number $N \leq 575$ of basis functions. Figures 3.11, 3.12 and 3.13 show the error ζ_{cur} associated with different numbers N of basis functions for a $\lambda/2$ wire with $h/a = 100$, $h/a = 30$ and $h/a = 20$, respectively. We have observed that in all these cases the root-mean-square (RMS) error is order $1/N$ as found in numerical results by Davies et al. [15] and predicted in [7, 36]. The deviation observed for increasing discretization number N comes from the residual error at $N = 575$.
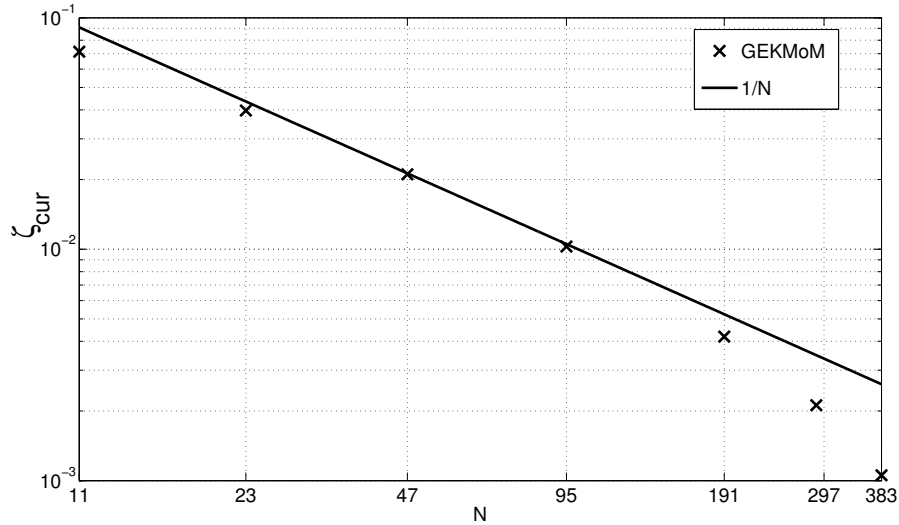
Figure 3.11: *RMS error ζ_{cur} as defined in (3.52) versus the number N of basis functions used. $\lambda/2$ wire with $h/a = 100$ illuminated by a normally incident z-polarized plane wave.*
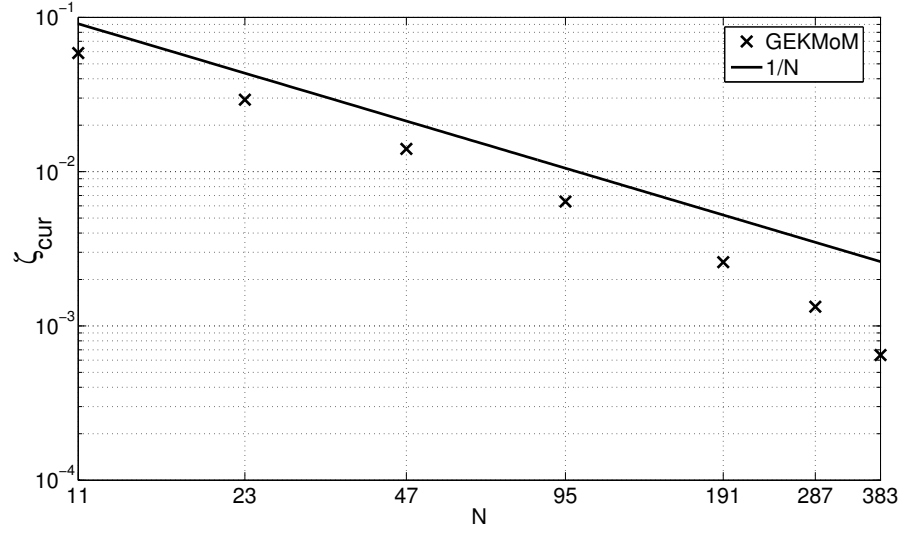
Figure 3.12: *RMS error ζ_{cur} as defined in (3.52) versus the number N of basis functions used. $\lambda/2$ wire with $h/a = 30$ illuminated by a normally incident z-polarized plane wave.*
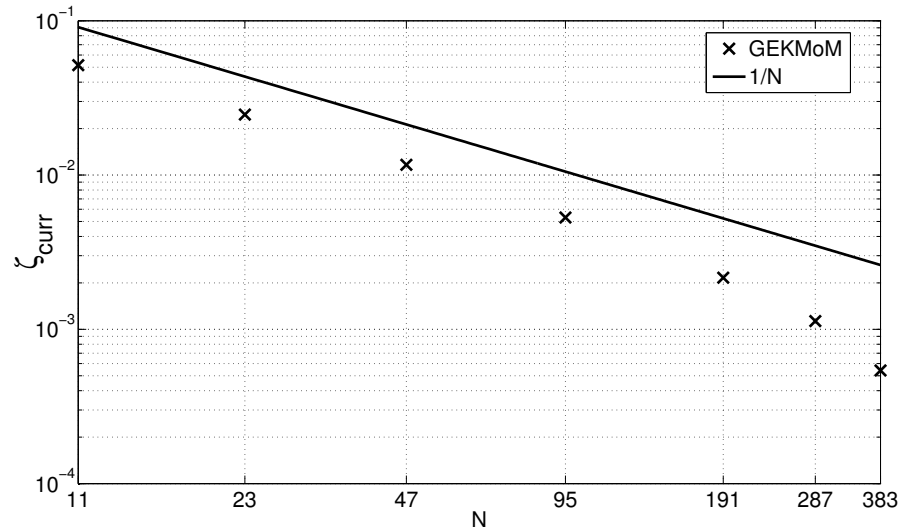
Figure 3.13: *RMS error ζ_{cur} as defined in (3.52) versus the number N of basis functions used. $\lambda/2$ wire with $h/a = 20$ illuminated by a normally incident z-polarized plane wave.*

3.4.4 Calculation of a realistic dipole input impedance

As additional validation, we are interested here in the value of input impedance Z_{in} and admittance Y_{in} of a dipole of radius $a = 0.7$ cm, length $h = 56$ cm in a frequency range $f \in [50, 700]$ MHz. The dipole consists of perfectly electrically conducting (PEC) material, fed by a voltage gap $V(\omega) = V_0 = 1$ V in its center ($z = z_g = h/2$). We compute Z_{in} and Y_{in} at $N_f = 120$ frequency steps.

From the numerical formulation developed so far, we define the antenna impedance and admittance as

$$Z_{\text{in}} = V_0/I(z_g = h/2), \qquad Y_{\text{in}} = I(z_g = h/2)/V_0, \tag{3.53}$$

where V_0 and $I(z_g = h/2)$ are the voltage and the current in the gap. The complex impedance and complex admittance are written in real and imaginary parts as

$$Z_{\text{in}} = R + jX, \qquad Y_{\text{in}} = G + jB, \tag{3.54}$$

where R is the resistance, X the reactance, G the conductance and B the susceptance. The results calculated with the Galerkin MoM with Exact Kernel (GEKMoM) are given in Figs. 3.14 and 3.15 for an even number of segments, and in Figs. 3.16 and 3.17 for an odd number of segments. The black boxes indicate measured values extracted from [46, Figs. 4.3 and 4.4]. From the measured values of R and X in [46] we calculate the conductance G and the susceptance B as

$$G = \frac{R}{R^2 + X^2}, \qquad B = \frac{-X}{R^2 + X^2}. \tag{3.55}$$

The way in which the delta-gap voltage source is modeled (see Sec. 3.2.1) implies that the source configuration changes as the number of segments changes. From the computed results we observe that the antenna impedance converges with an increasing number of segments. Moreover, by comparing results in Figs. 3.14 and 3.15 with those in Figs. 3.16 and 3.17, we conclude that the method has a better convergence if an even number of segments (i.e., an odd number N of expansion functions) is used, that means placing the delta-gap voltage exactly at lattice points. As already pointed out in Sec. 3.2.1, an even segmentation number corresponds to only one testing function ϕ_m (instead of two) being involved in the computation of the excitation term F_m in (3.15) and, consequently, also in the evaluation of current $I(h/2)$ in the gap and of input impedance Z_{in}. In this way the value F_m computed is identically equal to the delta-gap voltage $V(\omega) = V_0$.
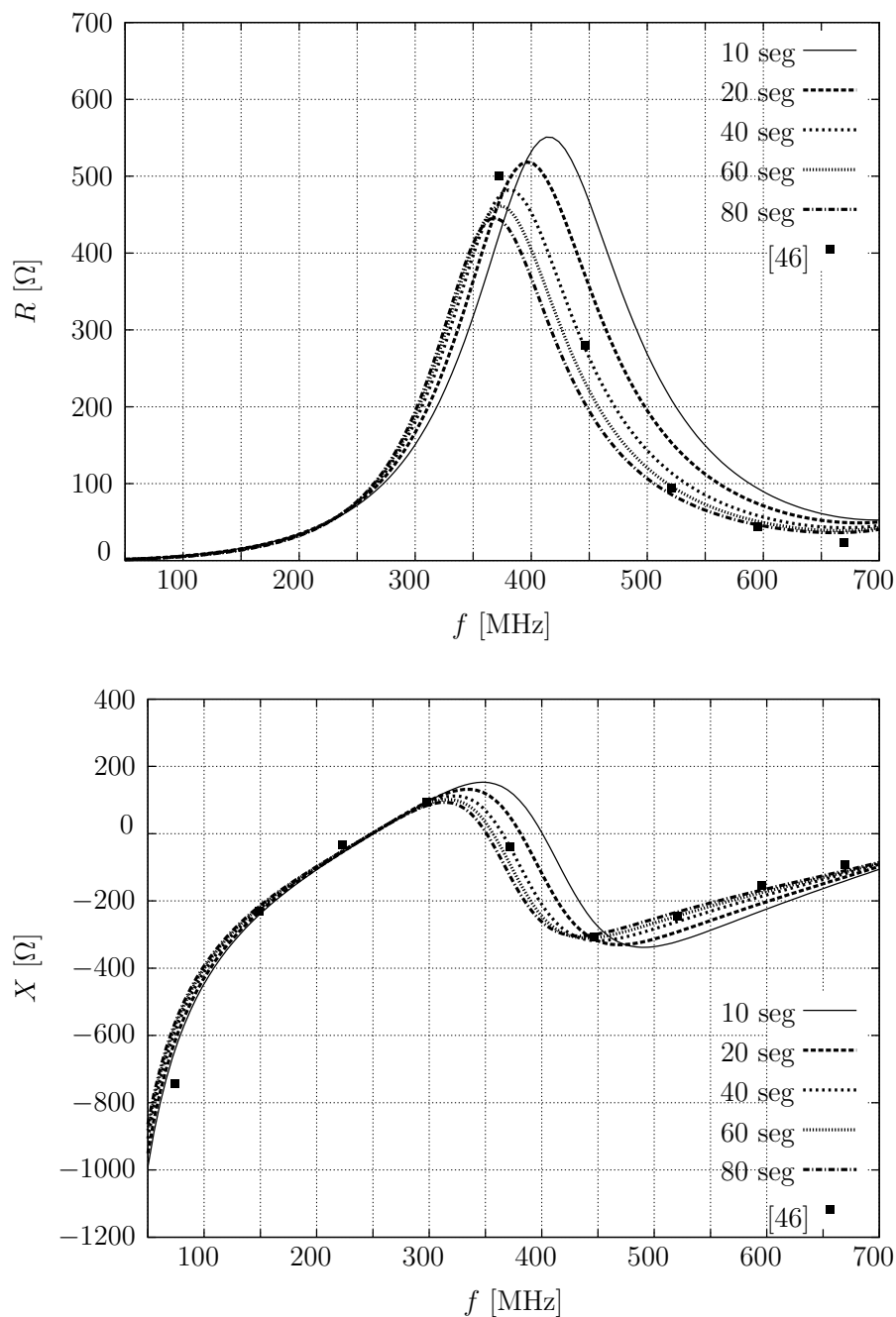
Figure 3.14: *Impedance for a dipole of radius a = 7* mm *and length h = 56* cm *as a function of frequency. Even number of segments.*
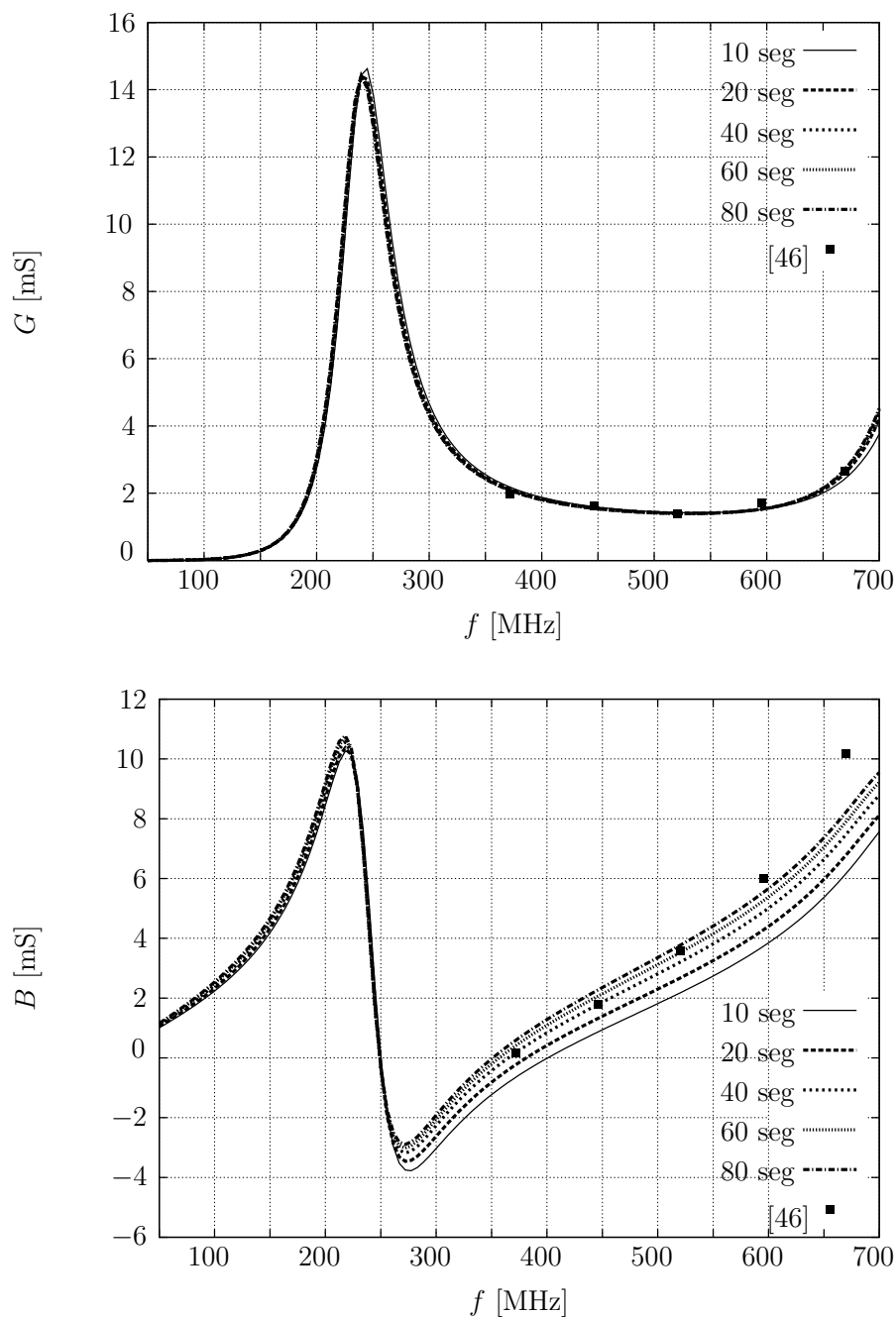
Figure 3.15: *Admittance for a dipole of radius* $a = 7$ mm *and length* $h = 56$ cm *as a function of frequency. Even number of segments.*
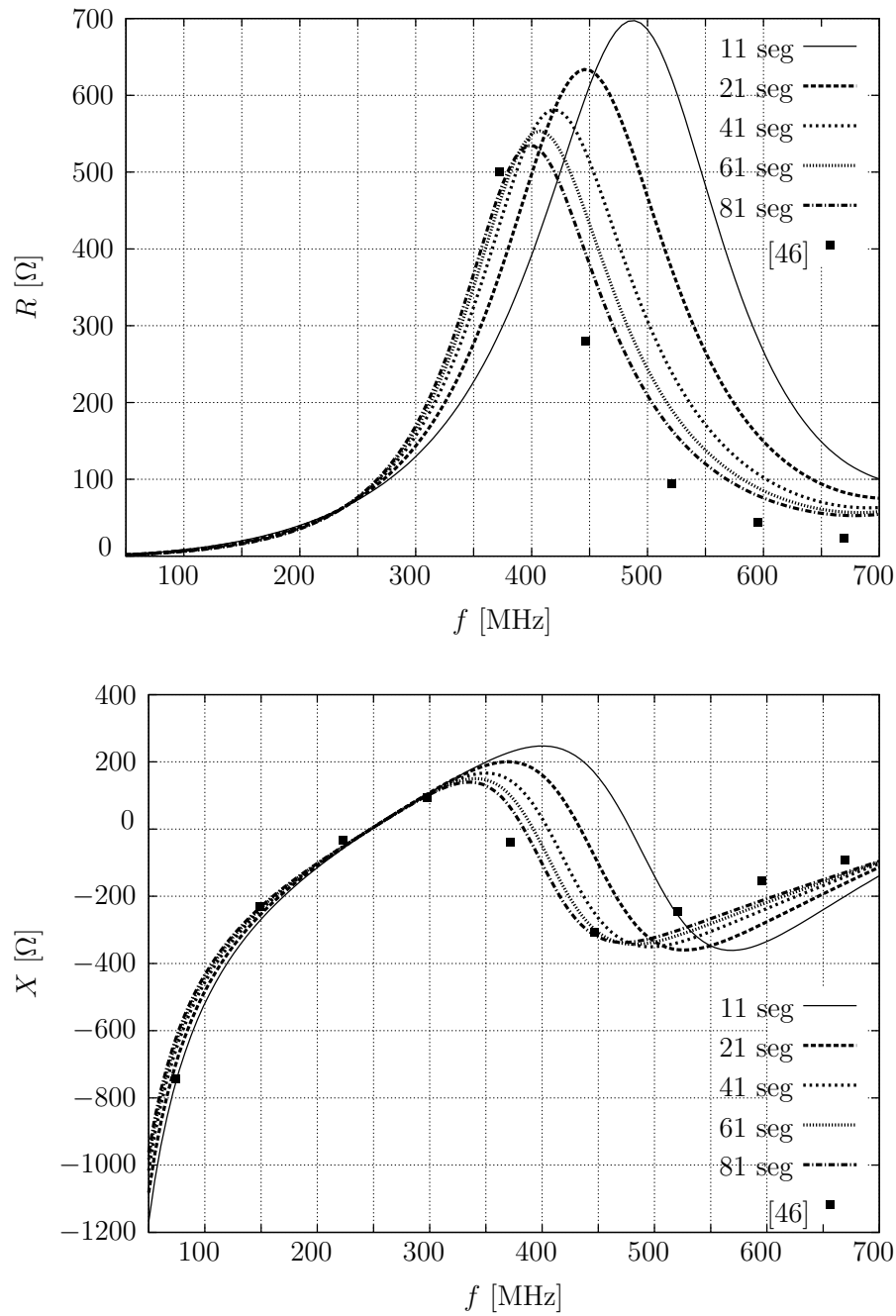
Figure 3.16: *Impedance for a dipole of radius* $a = 7$ mm *and length* $h = 56$ cm *as a function of frequency. Odd number of segments.*
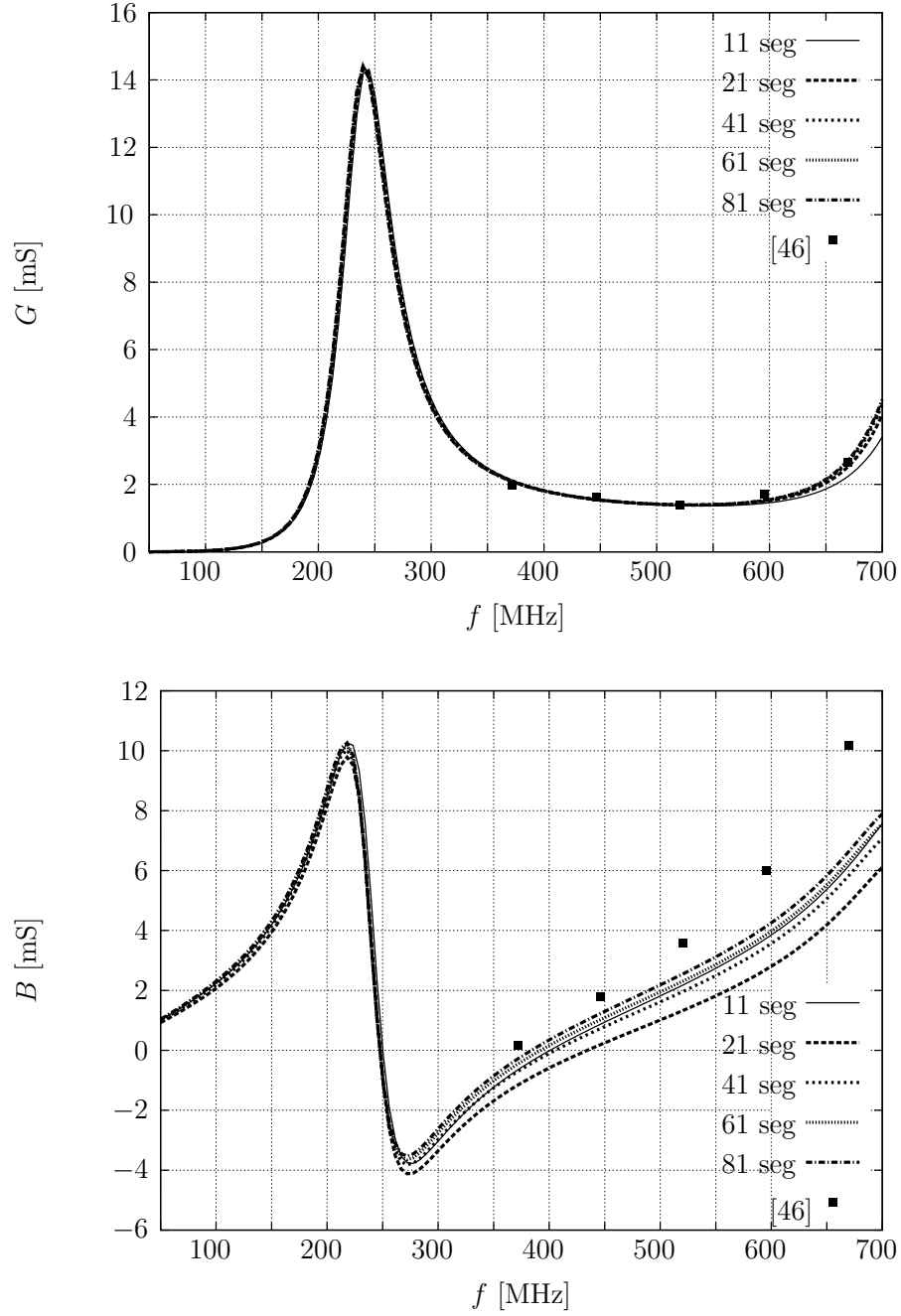
Figure 3.17: *Admittance for a dipole of radius* $a = 7$ mm *and length* $h = 56$ cm *as a function of frequency. Odd number of segments.*

3.5   Conclusions and discussion

In this chapter, we have described a numerical technique for solving Pocklington's equation with exact kernel. By means of the Galerkin Method of Moments the thin-wire integro-differential equation has been discretized and subsequently solved numerically. Special attention has been devoted to show how system matrix elements can be accurately calculated performing a singularity extraction and a Landen transform. The model of the delta-gap voltage source implemented so far implies that the source configuration changes as the number of segments changes.

Moreover, some of the results presented may be significant in the further development of this thesis and are here summarized:

- The exact kernel implementation does show a stable solution while the reduced kernel exhibits an oscillatory behavior in the delta-gap region and near the wire end faces. The numerical effort in handling the Green's function singularity present in the exact kernel formulation is therefore well rewarded. The improved stability may then allow to use the exact kernel formulation in the treatment of coupled wires.

- The current computed by the method developed shows a converging behavior when an incident plane wave is considered.

- The accuracy of the evaluated current distribution has been analyzed by a convergence study of the numerical method implemented. We can conclude that expanding the wire current with N basis functions leads to a root-mean-square error of order $1/N$ in the evaluation of the current.

- In the calculation of the wire impedance, the method shows a better convergence when an even number of segments is used.

Finally, in the further development of this thesis, the Galerkin Method of Moments proposed will be generalized to more complicate structures, such as loaded wires, coupled wires, a wire coupled with a surface and a wire connected to a surface.

Chapter 4

Loaded thin wires

In this chapter, the numerical method presented in Section 3.1 is extended to analyze wire antennas with distributed as well as concentrated (lumped) loadings. From a practical point of view, by introducing appropriate loadings along the wire, it is possible to obtain significant variations in the electrical properties of wire antennas (e. g., input impedance, radiation pattern, reflection coefficient, bandwidth).

In practical realizations, a resistive distributed loading is usually made by a resistive layer (spraying resistive paint) on a dielectric cylindrical rod [47]. Wire antennas with continuous capacitive loading are made in the form of a dielectric rod onto which very thin brass rings are arranged in a row [48]. Moreover, it is possible to realize inductive distributed loading by making the antenna in the form of a wire spiral with variable, slowly varying pitch. For what concerns the practical realization of concentrated loadings, as the frequency increases, a progressively increasing capacitive effect is present at the two faces of the wire where the loading is connected. Thus it is difficult to accurately realize desired loadings since this "parasitic" effect is not easily predictable. For a wire antenna loaded with a lumped element, this undesired impedance should be measured in the operating range of frequencies and taken into account as an additional impedance.

4.1   Formulation of the integral equation

The presence of a passive, distributed or lumped loading Z^{load} causes a field drop E^{load}

$$E^{\text{load}}(z, \omega) = -Z^{\text{load}}(z, \omega)I(z, \omega), \tag{4.1}$$

that reduces the exciting field. If the wire is loaded by an impedance profile $Z^{\text{load}}(z,\omega)$ expressed in Ohm per meter (Ω/m) the integro-differential equation (3.1) is modified as

$$\left(\partial_z^2 \; + \; k^2\right) \int\limits_{z'=0}^{h} K_E(z - z', \omega) I(z', \omega) dz' - j\omega\varepsilon Z^{\text{load}}(z, \omega) I(z, \omega) =$$

$$-j\omega\varepsilon \left(V(\omega)\delta(z - z_g) + \widehat{E}_z^i(z\mathbf{i}_z, \omega)\right). \tag{4.2}$$

Subsequently, considering the ω dependence implicitly, having expanded the current $I(z)$ in terms of basis functions, we modify expression (3.6) as

$$\sum_{n=1}^{N_z} I_n \left[\mathcal{L}\left\{\psi_n(z)\right\} - j\omega\varepsilon Z^{\text{load}}(z)\psi_n(z)\right]. \tag{4.3}$$

Applying the Galerkin MoM then leads to the generalized system

$$\left(\underline{\underline{Z}} + \underline{\underline{Z}}^{\text{load}}\right)\underline{I} = \underline{F}, \quad \Rightarrow \quad \underline{\underline{A}}\,\underline{I} = \underline{F}, \tag{4.4}$$

where $\underline{\underline{A}}$ is referred to as the "generalized system matrix", and is the sum of the "unloaded" system matrix $\underline{\underline{Z}}$ and the "loading" (or "load") matrix $\underline{\underline{Z}}^{\text{load}}$. In particular, the (m, n)-th element of the impedance matrix $\underline{\underline{Z}}^{\text{load}}$ is

$$Z_{m,n}^{\text{load}} = -j\omega\varepsilon \int\limits_{z=0}^{h} Z^{\text{load}}(z)\psi_m(z)\psi_n(z)dz, \tag{4.5}$$

with $\psi_m(z)$ and $\psi_n(z)$ the m-th and n-th testing and basis function (3.5), respectively. Apart from particular impedance profiles $Z^{\text{load}}(z)$ (e.g., lumped loads, uniformly distributed loads) for which the value of $Z_{m,n}^{\text{load}}$ in (4.5) can be determined analytically, we numerically compute $Z_{m,n}^{\text{load}}$ by a trapezoidal rule, which is consistent with the piecewise-linear expansion functions. The matrix $\underline{\underline{Z}}$ corresponds to the unloaded antenna configuration, while the matrix $\underline{\underline{Z}}^{\text{load}}$ includes the effects of both general impedance distributions along the wire and lumped elements placed at a particular position. In the case of a general impedance distribution along the wire, the matrix $\underline{\underline{Z}}^{\text{load}}$ has only a tri-diagonal form (i.e., the storage required for the $\underline{\underline{Z}}^{\text{load}}$ elements is $3N - 2$ instead of N^2). For lumped elements, the number of non-zero matrix elements is even smaller.

4.2 Lumped or localized loadings

Suppose that the wire has been cut at the position $z = z_L$ and that an impedance has been placed between $z = z_L + \Delta$ and $z = z_L - \Delta$ (i.e., between the two faces of the wire). By

taking the limit for $\Delta \downarrow 0$, the field drop due to the presence of the impedance becomes

$$-Z^{\text{load}}(z)I(z) = -Z^{\text{load}}\delta(z - z_L)I(z) = -Z^{\text{load}}\delta(z - z_L)I(z_L). \tag{4.6}$$

Since Z^{load} is a lumped loading, it is expressed in Ohm (Ω). Substituting the impedance $Z^{\text{load}}(z) = Z^{\text{load}}\delta(z - z_L)$ in (4.5) yields

$$Z_{m,n}^{\text{load}} = -j\omega\varepsilon \int\limits_{z=0}^{h} Z^{\text{load}}\delta(z - z_L)\psi_m(z)\psi_n(z)dz = -j\omega\varepsilon Z^{\text{load}}\psi_m(z_L)\psi_n(z_L), \tag{4.7}$$

for $m, n = 1, \ldots, N$, with

$$\psi_m(z_L) = \begin{cases} 1 + \dfrac{z_L}{\Delta z} - m, & (m-1)\Delta z \leq z_L \leq m\Delta z, \\[2mm] 1 - \dfrac{z_L}{\Delta z} + m, & m\Delta z \leq z_L \leq (m+1)\Delta z, \\[2mm] 0, & \text{otherwise.} \end{cases} \tag{4.8}$$

We observe that, for lumped loadings placed at lattice points, the value $Z_{m,n}^{\text{load}}$ is identical to Z^{load} only if $m = n$. Otherwise the element $Z_{m,n}^{\text{load}}$ is approximated by means of a product of two piecewise-linear functions.

4.3   Dipole antenna with a lumped loading

The developed FORTRAN program GEKMoM has been extended to calculate the current distribution of loaded straight wires.

As an example, we compute the current distribution of a $\lambda/2$ dipole antenna loaded with a lumped element placed at $z_L = 10/156\lambda$. The lumped loading is a series group comprising of a capacitor $C = 12$ pF and an inductor $L = 40$ nH, which means that

$$Z^{\text{load}} = \left(j\omega L + \frac{1}{j\omega C}\right) = j31.106 \ \Omega. \tag{4.9}$$

The dipole has length $h = 0.5$ m, a length-radius ratio of $h/a = 100$ and it is fed by a delta-gap voltage $V(\omega) = V_0 = 1$ V placed in its center, see Fig. 4.1. The calculation is performed by using N basis functions (i.e., $N + 1$ segments) to expand the current distribution. The magnitudes of the currents I computed by GEKMoM and NEC 4.1 are shown and compared in Fig. 4.2.

PSfrag replacements
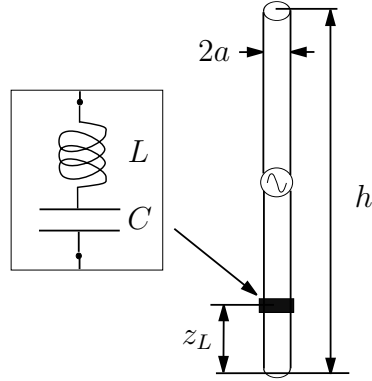
Figure 4.1: *Dipole antenna with a series loading.*

(a)   (b)
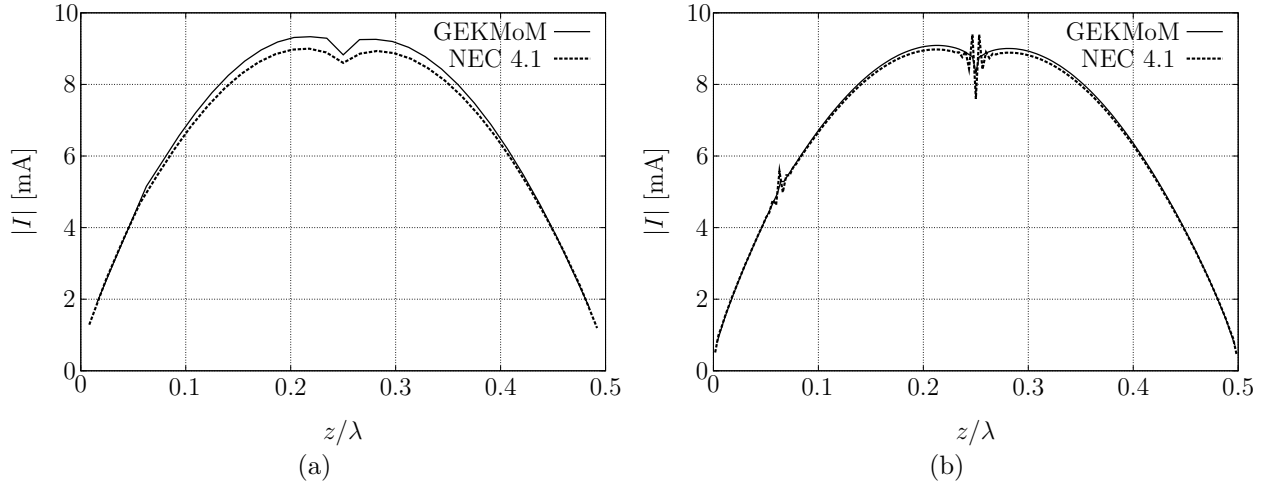
Figure 4.2: *Magnitude of the current distribution versus the position along a loaded $\lambda/2$ dipole, $h/a = 100$, fed by a delta-gap voltage $V_0 = 1$ V in its center. Lumped series element: $L = 40$ nH, $C = 12$ pF. (a)- Using $N = 31$ basis functions; (b)- using $N = 155$ basis functions.*

A good agreement between the two curves is observed in Fig. 4.2-(a) when $N = 31$ basis functions are used. By refining the discretization, using $N = 155$ basis functions the solution computed by NEC 4.1 produces oscillatory results, see Fig. 4.2-(b). The oscillations occur at the position of the lumped loading and at the location of the delta-gap voltage in the center of the wire. As explained in Secs. 3.4.1 and 3.4.2, the erroneous oscillatory behavior of results calculated by NEC 4.1 (dashed line) is probably caused by the ill-posed nature of the reduced kernel formulation used [3].

4.4 Dipole antenna loaded with a resistive profile

In this section, a $\lambda/2$ dipole antenna with $h = 0.5$ m, $h/a = 100$ and a constant resistive loading $Z^{\text{load}}(z) = 1000$ Ω/m for $0 \leq z \leq h$, fed in its center by a delta-gap voltage $V(\omega) = V_0 = 1$ V has been analyzed. We compute the current distribution along the dipole by using N basis functions. The calculated results are compared with those obtained by NEC 4.1. Figure 4.3 shows a good agreement in the current computed with the two methods for $N = 31$ (Fig. 4.3-(a)), while for $N = 155$, the undesired oscillation appears only at the position of the delta gap (Fig. 4.3-(b)) and not along the distributed loading. We can therefore conclude that the oscillatory behavior at the locations of concentrated loadings of results calculated by NEC 4.1 (see Sec. 4.3) is not present when the wire is loaded with a distributed (continuous) impedance profile.
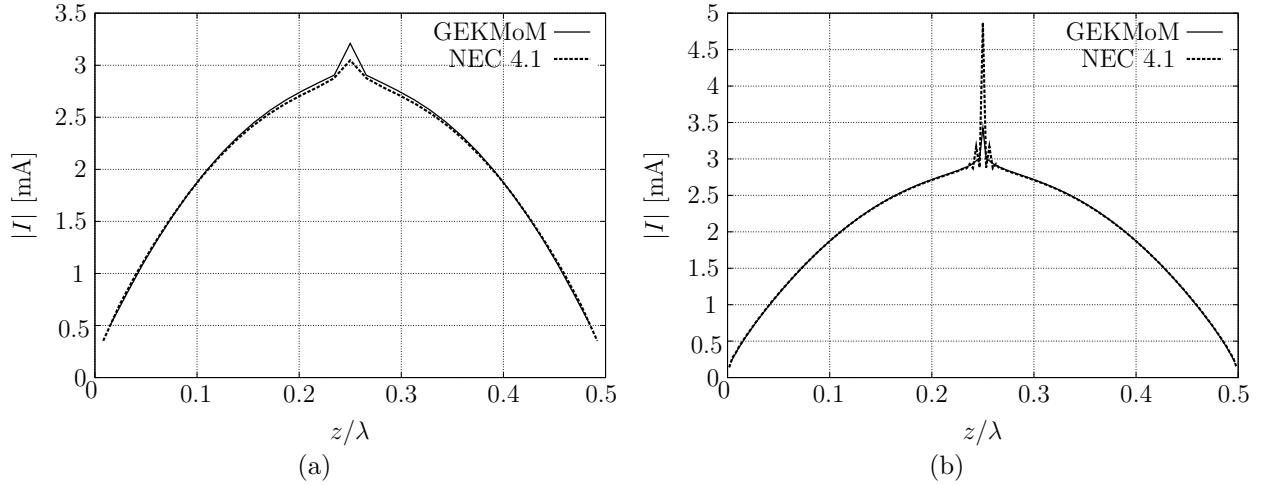
Figure 4.3: *Magnitude of the current distribution versus the position along a loaded $\lambda/2$ dipole, $h/a = 100$, fed by a delta-gap voltage $V_0 = 1$ V in its center. Resistive distributed loading: $Z^{load}(z) = 1000$ Ω/m, for $0 \leq z \leq h$. (a)- Using $N = 31$ basis functions; (b)- using $N = 155$ basis functions.*

4.5 Monopole antenna with a lumped loading

We consider here a PEC monopole antenna of length $h = 15$ cm and radius $a = 0.3$ cm on an infinite PEC ground plane, see Fig. 4.4. The antenna is loaded with a single lumped capacitor $C = 0.80789$ pF placed at a distance $z_L = 6$ cm from the ground plane. This means that $Z^{\text{load}} = -j197$ Ω at 1 GHz. The monopole is fed by a delta-gap voltage $V(\omega) = V_0 = 1$ V at its base. Calculation by GEKMoM of the input admittance Y_{in} is

performed in a frequency range $f \in [1.1, 2.7]$ GHz and compared in Fig. 4.5 with theoretical
and experimental results from [49, Fig. 5.8].
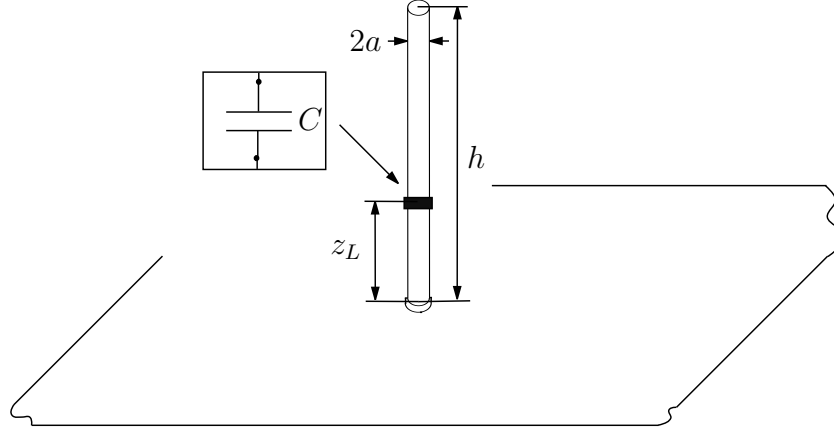
Figure 4.4: *Monopole antenna with capacitive loading over an infinite ground plane.*

Values of G computed by GEKMoM are in good accordance with the theoretical and
experimental values published in [49]. Experimental results of the susceptance B are
better predicted by the theoretical model proposed by Popović et al. [49]. This is most
probably due to the approximation of the excitation region used (i.e., belt generator),
which accurately models the coaxial line used in the experiment [49].

In Fig. 4.6 the conductance G and the susceptance B of the capacitively loaded monopole
versus the frequency are compared with those of the unloaded antenna. To gain some
insight into the influence of the lumped capacitor on the antenna properties, we calculate
the Voltage Standing Wave Ratio (VSWR) from the computed input admittance Y_{in} as

$$\text{VSWR} = \frac{1 + |\Gamma|}{1 - |\Gamma|}, \tag{4.10}$$

where Γ is the reflection coefficient

$$\Gamma = \frac{1 - Z_0 Y_{in}}{1 + Z_0 Y_{in}}, \tag{4.11}$$

and $Z_0 = 50\,\Omega$ is the characteristic impedance of the transmission line. Figure 4.7 shows the
VSWR of the loaded (continuous line) and unloaded (dotted line) monopole as a function
of the frequency. Note that the presence of the loading reduces the VSWR in the frequency
range from 1.1 to 1.4 GHz, thus improving the antenna impedance matching. In this way
the VSWR is less than 3 over the entire band of interest.
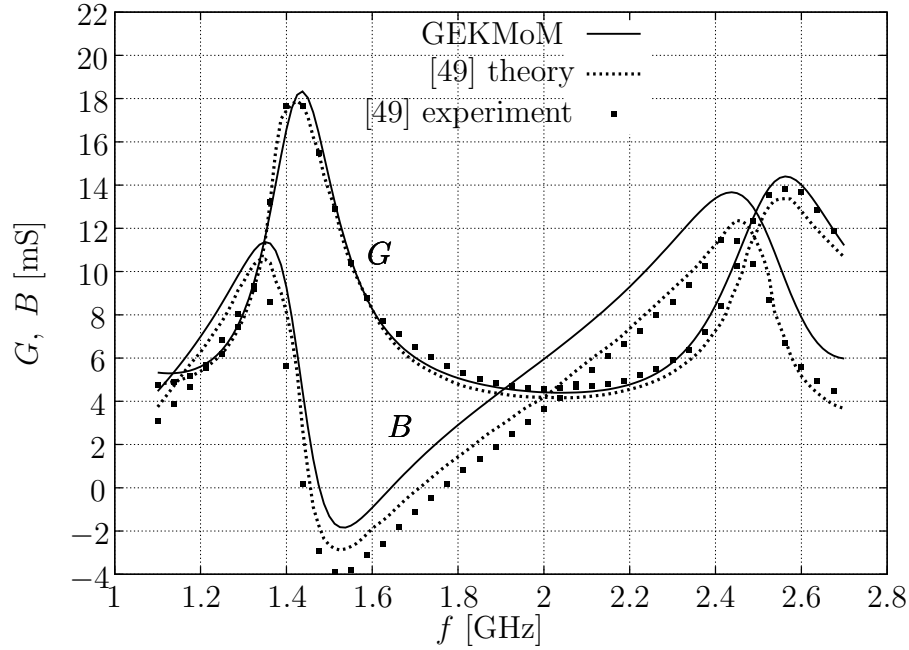
Figure 4.5: *Conductance G and susceptance B of a monopole loaded with a capacitive loading. GEKMoM: continuous line, [49] theory: dotted line, [49] experiment: black boxes. Capacitance C = 0.80789 pF at a distance $z_L = 6$ cm from the ground plane. Length h = 15 cm, radius a = 0.3 cm.*
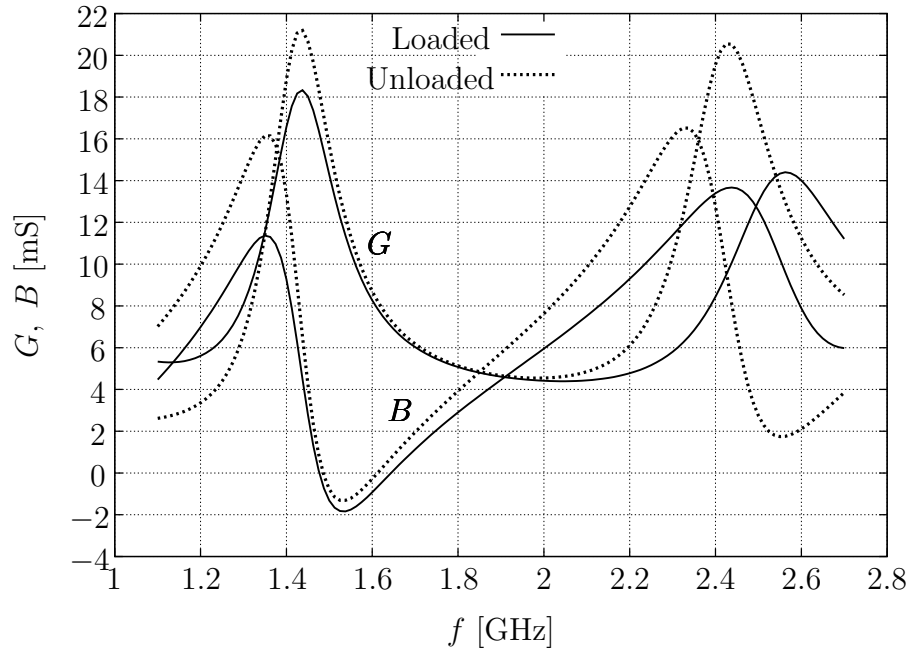
Figure 4.6: *Conductance G and susceptance B compared with the unloaded monopole. Monopole loaded with a capacitive loading C = 0.80789 pF at a distance $z_L = 6$ cm from the ground plane. Length h = 15 cm, radius a = 0.3 cm.*
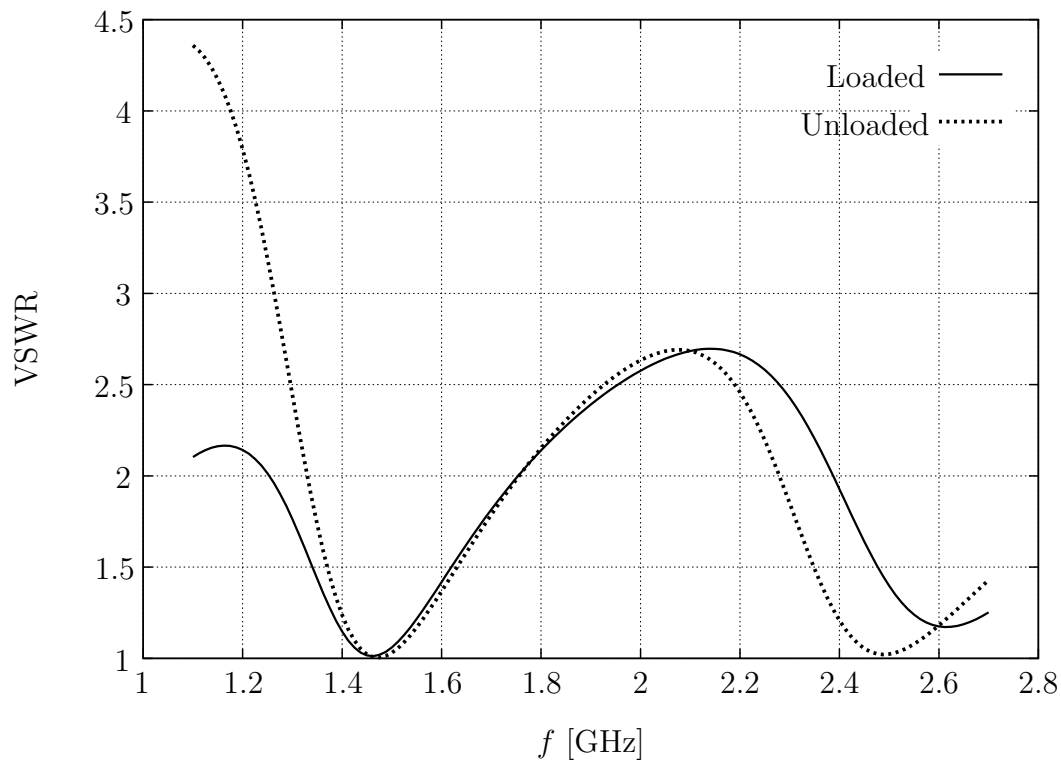
Figure 4.7: *VSWR compared with the unloaded monopole. Monopole loaded with a capacitive loading* $C = 0.80789$ pF *at a distance* $z_L = 6$ cm *from the ground plane. Length* $h = 15$ cm, *radius* $a = 0.3$ cm.

Chapter 5

Natural Frequencies

In this chapter, the numerical method for the analysis of loaded wire antennas has been extended to find the location of the natural frequencies in the complex plane of Laplace's variable s. As extensively described by Baum in the Singularity Expansion Method (SEM) [50–52], natural frequencies constitute a complete description of the electromagnetic behavior of the object. Natural frequencies are obtained as zeros of the determinant of the system matrix and are widely used in the definition of the generated current of the wire by means of the Singularity Expansion Method (SEM) [50–54]. Instead of looking for zeros of the system matrix determinant [54], we use a different search procedure which performs the Singular Value Decomposition (SVD) of the system matrix as described in Section 5.1.1. We study the case of a perfectly conducting wire as well as a wire antenna loaded with different resistive profiles [54] and with a lumped element. As the value of the loading increases, we can generate successive initial estimates of the natural frequencies and obtain a marching-on-in-loading approach.

5.1   Natural Frequencies

For the following derivation it is convenient to introduce the Laplace transform. The one-sided Laplace transform of an arbitrary function $f(t)$ is defined as

$$F(s) \;=\; \int_{t=t_0}^{\infty} f(t) \exp(-st) dt \; , \tag{5.1}$$

where $s = \beta + j\omega$ is a complex variable and where $\omega \geq 0$ is the angular frequency. $f(t)$ is a causal function (i.e., $f(t) = 0$ for $-\infty < t < t_0$) of the real variable t. The function $f(t)$ is assumed to have a behavior such that $F(s)$ exists and is analytic in the right half

$(0 \leq \text{Re}\{s\} < \infty)$ of the complex s plane. The subset of values of s for which the Laplace transform exists is called the region of convergence or the domain of convergence. The corresponding inverse Laplace transformation is given by the Bromwich inversion integral,

$$f(t) = \frac{1}{2\pi j} \int_{s=\beta_0-j\infty}^{\beta_0+j\infty} F(s) \exp(st) ds \ , \tag{5.2}$$

where β_0 is a real number so that the contour path of integration is in the region of convergence of $F(s)$. For a causal function, β_0 must be chosen such that $\beta_0 \geq \text{Re}\{s_\alpha\}$ for every singularity s_α of $F(s)$. If we select $\beta_0 = 0$, and define the frequency f as $f = \omega/2\pi$, the above inverse integral formula becomes identical to the inverse Fourier transformation. The Laplace transform of the thin-wire integro-differential equation (3.1) becomes

$$\left(\partial_z^2 - \frac{s^2}{c^2}\right) \int_{z'=0}^{h} K_E(z - z', s) I(z', s) dz' = -s\varepsilon \left(V(s)\delta(z - z_g) + \widehat{E}_z^i(\mathbf{r}, s)\right), \tag{5.3}$$

where $\mathbf{r} = z\mathbf{i}_z + a\mathbf{i}_r(\phi)$ is a point on the wire mantle and where the exact kernel K_E is

$$K_E(z - z', s) = \frac{1}{2\pi^2} \int_{\varphi=0}^{\pi/2} \frac{\exp\left(-\frac{s}{c}\sqrt{(z - z')^2 + 4a^2 \sin^2 \varphi}\right)}{\sqrt{(z - z')^2 + 4a^2 \sin^2 \varphi}} d\varphi. \tag{5.4}$$

From a mathematical point of view, natural frequencies of a wire are the complex values $s = \beta + j\omega$ for which the homogenous version of equation (5.3)

$$\left(\partial_z^2 - \frac{s^2}{c^2}\right) \int_{z'=0}^{h} K_E(z - z', s) I(z', s) dz' = 0, \tag{5.5}$$

allows nontrivial solution. For these values $s_\alpha = \beta_\alpha + j\omega_\alpha$, a current distribution along the wire may be present even if no excitation is present. Furthermore, since s_α is a natural frequency, we observe that

- because we assume that the medium reacts passively and causally, the real part of a natural frequency should be non-positive, that is $\beta_\alpha \leq 0$;

- singular values s_α occur in conjugate pairs (i.e., $s_\alpha = \beta_\alpha + j\omega_\alpha$ and $s_\alpha^* = \beta_\alpha - j\omega_\alpha$) or are on the real s-axis.

- singular values s_α occur in so-called layers ℓ and are ordered within a layer where m is the order within the layer [53].

To solve the homogenous equation (5.5), we apply the Galerkin Method of Moments (see Sec. 3.1.1). Thus, from (5.5), we write the system matrix equation

$$\underline{\underline{Z}}(s)\underline{I}(s) = \underline{0}, \tag{5.6}$$

where the dependence on the complex variable s is explicit. As described in Sec. 4.1, when the effect of distributed or lumped loadings is taken into account, the system matrix $\underline{\underline{Z}}(s)$ is generalized to $\underline{\underline{A}}(s) = \underline{\underline{Z}}(s) + \underline{\underline{Z}}^{\text{load}}(s)$. Therefore, it follows that natural frequencies of loaded wires are the complex values s for which the homogenous linear system

$$\underline{\underline{A}}(s)\,\underline{I}(s) = 0, \tag{5.7}$$

has nontrivial solution.

5.1.1   Numerical Determination

At this stage, we want to find the values of s such that the matrix $\underline{\underline{A}}$ is singular. The strategy implemented performs, as a first step, the Singular Value Decomposition (SVD) of $\underline{\underline{A}}$

$$\underline{\underline{A}}(s) = \underline{\underline{U}}(s)\underline{\underline{\Sigma}}(s)\underline{\underline{V}}(s)^T, \tag{5.8}$$

where the superscript T indicates the transpose operator. The matrices $\underline{\underline{U}}$ and $\underline{\underline{V}}$ are both orthogonal (in the sense that their columns are orthonormal) and $\underline{\underline{\Sigma}} = \text{diag}(\sigma_1, \sigma_2, ..., \sigma_N)$ is a diagonal matrix with positive or zero elements $\sigma_1 \geq \sigma_2 \geq ... \geq \sigma_N \geq 0$ called singular values. Next, we search for those values $s = s_\alpha$ for which $\sigma_N = 0$. In a numerical iterative scheme that means finding s_α such that σ_N vanishes. An IMSL routine performs the SVD and natural frequencies are found by means of an implemented minimization algorithm based on Powell's modified method [55]. Since natural frequencies occur in conjugate pairs or are on the real axis, as searching region we define $\text{Re}\{s\} \leq 0$, $\text{Im}\{s\} \geq 0$ in the complex s plane. This means that, once M natural frequencies $\{s_\alpha, \alpha = 1, \ldots, M\}$ are determined also their complex conjugate values are known. Moreover, Powell's method requires an initial estimate (i.e., at the iteration step $i = 1$) of natural frequencies. For this initial step, the estimate of the natural frequency s_α corresponds to the first resonant frequency that occurs for an unloaded wire, i.e., $f = c/(2h)$, where h is the length of the wire. The same searching scheme is applied to find the location of natural frequencies for wires loaded with impedance distribution $Z^{\text{load}}(z)$, see Sec. 4.1. As the value of the loading profile $Z^{\text{load}}(z)$ increases, we search for natural frequency trajectories in the complex s-plane. In this case we have implemented an elegant iterative algorithm. A good estimate

of the i-th iteration $Z^{\text{load}}(z) + i\Delta Z^{\text{load}}(z)$ can be obtained by using the natural frequency which corresponds to $Z^{\text{load}}(z) + (i-1)\,\Delta Z^{\text{load}}(z)$. This scheme concept can be regarded as "marching-on-in-loading" [56,57]. The same procedure is applied to find other natural frequencies $\{s_\alpha, \alpha = 2, \dots M\}$. To this end, as first initial estimates for Powell's method, we chose for subsequent approximated resonant frequencies of the unloaded wire (i.e., $f = \dfrac{c}{2h}, \dfrac{3c}{2h}, \dots$).

5.1.2   Residual Matrix evaluation

In this section we derive an expression for the current along the wire in the time domain. To this end, once the wire natural frequencies s_α have been determined, we compute the residue matrix at each of these values. The solution of matrix equation $\underline{\underline{\mathbf{A}}}(s)\,\underline{\mathbf{I}}(s) = \underline{\mathbf{F}}(s)$ can be written as

$$\underline{\mathbf{I}}(s) = \underline{\underline{\mathbf{A}}}(s)^{-1}\underline{\mathbf{F}}(s), \tag{5.9}$$

where $\underline{\mathbf{F}}(s)$ is the known excitation vector in the domain of the complex frequency s. Then, applying the residue theorem [58, Chp. 7], we represent the matrix $\underline{\underline{\mathbf{A}}}^{-1}$ as a sum over all natural frequencies in the complex s plane

$$\underline{\underline{\mathbf{A}}}(s)^{-1} = \underline{\underline{\mathbf{R}}}_0(s) + \sum_{\alpha=-\infty}^{\infty} \frac{\underline{\underline{\mathbf{R}}}_\alpha}{s - s_\alpha}, \tag{5.10}$$

where $\underline{\underline{\mathbf{R}}}_0$ is an entire function of s and $\underline{\underline{\mathbf{R}}}_\alpha$ is the residue matrix of the system at the natural frequency s_α. This residue matrix can be represented as the scalar product of two independent vectors: the natural mode vector (eigenvector or natural current) $\underline{\boldsymbol{\nu}}_\alpha$ and the transpose coupling vector $\underline{\boldsymbol{\mu}}_\alpha^T$ [51]. That is

$$\underline{\underline{\mathbf{R}}}_\alpha = \underline{\boldsymbol{\nu}}_\alpha\,\underline{\boldsymbol{\mu}}_\alpha^T, \tag{5.11}$$

where $\underline{\boldsymbol{\nu}}_\alpha$ and $\underline{\boldsymbol{\mu}}_\alpha$ are the nontrivial solutions of the homogeneous equations

$$\underline{\underline{\mathbf{A}}}(s_\alpha)\,\underline{\boldsymbol{\nu}}_\alpha = \underline{\mathbf{0}}, \qquad \left(\underline{\underline{\mathbf{A}}}^*\right)^T(s_\alpha)\,\underline{\boldsymbol{\mu}}_\alpha = \underline{\mathbf{0}}, \tag{5.12}$$

where $*$ indicates the complex conjugate. The subscript α refers to a particular singular value s_α. Then, for a symmetric system matrix as obtained by applying the Galerkin Method of Moments to the thin-wire equation, where the property $\underline{\boldsymbol{\nu}}_\alpha = \underline{\boldsymbol{\mu}}_\alpha$ is valid, the residue matrix (5.11) can be written as

$$\underline{\underline{\mathbf{R}}}_\alpha = \underline{\boldsymbol{\nu}}_\alpha\,\underline{\boldsymbol{\nu}}_\alpha^T = \underline{\boldsymbol{\mu}}_\alpha\,\underline{\boldsymbol{\mu}}_\alpha^T. \tag{5.13}$$

At this stage it is worth noticing that the entire function $\underline{\underline{\mathbf{R}}}_0(s)$ in (5.10) represents singularities which may occur in the complex s-plane at infinity. For the present study we ignore this contribution and we consider only the singularities in the finite complex plane since singularities at infinity affect only the early-time current and are not important in the time domain solution at later instants [53,54]. Thus, substituting the form (5.13) in (5.10) yields

$$\underline{\underline{\mathbf{A}}}(s)^{-1} = \sum_{\alpha=-\infty}^{\infty} \frac{\boldsymbol{\nu}_\alpha\,\boldsymbol{\nu}_\alpha^T}{s - s_\alpha} = \sum_{\alpha=-\infty}^{\infty} \frac{\boldsymbol{\mu}_\alpha\,\boldsymbol{\mu}_\alpha^T}{s - s_\alpha}. \tag{5.14}$$

Therefore from (5.9), the representation of the wire current in the complex frequency domain is

$$\mathbf{I}(s) = \sum_{\alpha=-\infty}^{\infty} \frac{\boldsymbol{\nu}_\alpha\,\boldsymbol{\nu}_\alpha^T}{s - s_\alpha}\mathbf{F}(s_\alpha) = \sum_{\alpha=-\infty}^{\infty} \frac{\boldsymbol{\mu}_\alpha\,\boldsymbol{\mu}_\alpha^T}{s - s_\alpha}\mathbf{F}(s_\alpha), \tag{5.15}$$

where the excitation vector $\underline{\mathbf{F}}$ is included in the pole residues [52]. Starting from (5.10), we now calculate the residue at the k-th pole. The inverted system matrix $\underline{\underline{\mathbf{A}}}(s)^{-1}$ becomes undefined as s approaches a particular s_α (because the denominator is approaching 0). Multiplying both sides of (5.10) by $(s - s_k)$ and taking the limit $s \to s_k$ gives

$$\lim_{s\to s_k}(s - s_k)\underline{\underline{\mathbf{A}}}(s)^{-1} = \lim_{s\to s_k}(s - s_k)\sum_\alpha \frac{\underline{\underline{\mathbf{R}}}_\alpha}{s - s_\alpha} = \underline{\underline{\mathbf{R}}}_k. \tag{5.16}$$

Defining a small difference δ such that $(s - s_k) = \delta$, from (5.16) we obtained

$$\underline{\underline{\mathbf{R}}}_k = \lim_{\delta\to 0}\delta\,\underline{\underline{\mathbf{A}}}(s_k + \delta)^{-1}. \tag{5.17}$$

From the SVD it follows immediately that the system matrix inverse is

$$\underline{\underline{\mathbf{A}}}^{-1}(s) = \underline{\underline{\mathbf{V}}}(s)\underline{\underline{\boldsymbol{\Sigma}}}^{-1}(s)\underline{\underline{\mathbf{U}}}^T(s). \tag{5.18}$$

Suppose now that

$$\underline{\underline{\mathbf{A}}}(s_k + \delta) \approx \underline{\underline{\mathbf{U}}}(s_k)\mathrm{diag}(\sigma_1, \sigma_2, ..., \sigma_{N-1}, \delta)\underline{\underline{\mathbf{V}}}^T(s_k), \tag{5.19}$$

$$\underline{\underline{\mathbf{A}}}^{-1}(s_k + \delta) \approx \underline{\underline{\mathbf{V}}}(s_k)\mathrm{diag}(1/\sigma_1, 1/\sigma_2, ..., 1/\sigma_{N-1}, 1/\delta)\underline{\underline{\mathbf{U}}}^T(s_k). \tag{5.20}$$

Taking the limit for $\delta \to 0$ then leads to

$$\begin{aligned}
\lim_{\delta\to 0}\delta\underline{\underline{\mathbf{A}}}^{-1}(s_k + \delta) &\approx \underline{\underline{\mathbf{V}}}(s_k)\mathrm{diag}(\delta/\sigma_1, \delta/\sigma_2, ..., \delta/\sigma_{N-1}, 1)\underline{\underline{\mathbf{U}}}^T(s_k) \\
&\approx \underline{\underline{\mathbf{V}}}(s_k)\mathrm{diag}(0, 0, ..., 0, 1)\underline{\underline{\mathbf{U}}}^T(s_k) \\
&= \underline{\underline{\mathbf{R}}}_k.
\end{aligned} \tag{5.21}$$

In conclusion, for each singular value s_α we can evaluate $\underline{\underline{\mathbf{R}}}_\alpha$ by determining the SVD of the system matrix $\underline{\underline{\mathbf{A}}}(s)$, which means

$$\underline{\underline{\mathbf{R}}}_\alpha = \underline{\mathbf{v}}_\alpha \underline{\mathbf{u}}_\alpha^T, \tag{5.22}$$

where $\underline{\mathbf{v}}_\alpha$ and $\underline{\mathbf{u}}_\alpha$ are the N-th columns of the matrices $\underline{\underline{\mathbf{V}}}$ and $\underline{\underline{\mathbf{U}}}$, respectively. Comparing the expression (5.22) with (5.11), we can conclude that the natural current mode and the coupling vector are represented by

$$\underline{\boldsymbol{\nu}}_\alpha = \underline{\mathbf{v}}_\alpha, \qquad \underline{\boldsymbol{\mu}}_\alpha^T = \underline{\mathbf{u}}_\alpha^T, \tag{5.23}$$

and therefore from (5.13) it follows that

$$\underline{\underline{\mathbf{R}}}_\alpha = \underline{\mathbf{v}}_\alpha \underline{\mathbf{v}}_\alpha^T = \underline{\mathbf{u}}_\alpha \underline{\mathbf{u}}_\alpha^T. \tag{5.24}$$

Further, substituting this result in (5.15) leads to

$$\underline{\mathbf{I}}(s) = \sum_{\alpha=-\infty}^{\infty} \frac{\underline{\mathbf{u}}_\alpha \, \underline{\mathbf{u}}_\alpha^T}{s - s_\alpha} \underline{\mathbf{F}}(s_\alpha), \tag{5.25}$$

and thus, applying the inverse Laplace transformation (5.2), the time-domain current expression becomes

$$\underline{\mathbf{i}}(t) = \frac{1}{2\pi j} \int_{s=\beta_0-j\infty}^{\beta_0+j\infty} \sum_{\alpha=-\infty}^{\infty} \frac{\underline{\mathbf{u}}_\alpha \underline{\mathbf{u}}_\alpha^T}{s - s_\alpha} \underline{\mathbf{F}}(s_\alpha) \exp(st) ds. \tag{5.26}$$

Finally, by closing the integral at infinity and applying Cauchy's theorem leads to the real-valued time current

$$\begin{aligned} \underline{\mathbf{i}}(t) &= \underline{\mathbf{u}}_0 \underline{\mathbf{u}}_0^T \underline{\mathbf{F}}(\beta_0) \exp(\beta_0 t) + \left(\sum_{\alpha=-\infty}^{-1} + \sum_{\alpha=1}^{\infty} \right) \underline{\mathbf{u}}_\alpha \underline{\mathbf{u}}_\alpha^T \underline{\mathbf{F}}(s_\alpha) \exp(s_\alpha t) \\ &= \underline{\mathbf{u}}_0 \underline{\mathbf{u}}_0^T \underline{\mathbf{F}}(\beta_0) \exp(\beta_0 t) + 2 \sum_{\alpha=1}^{\infty} \underline{\mathbf{u}}_\alpha \underline{\mathbf{u}}_\alpha^T \underline{\mathbf{F}}(s_\alpha) \cos(\omega_\alpha t) \exp(\beta_\alpha t), \end{aligned} \tag{5.27}$$

valid for $t \geq 0$, where $\underline{\mathbf{u}}_0$ is the vector (5.23) related to a pole $s_0 = \beta_0$ on the real axis in the complex s-plane. If only M conjugate pairs of natural frequencies are considered, the time-domain current (5.27) is approximated as

$$\underline{\mathbf{i}}(t) \approx \underline{\mathbf{u}}_0 \underline{\mathbf{u}}_0^T \underline{\mathbf{F}}(\beta_0) \exp(\beta_0 t) + 2 \sum_{\alpha=1}^{M} \underline{\mathbf{u}}_\alpha \underline{\mathbf{u}}_\alpha^T \underline{\mathbf{F}}(s_\alpha) \cos(\omega_\alpha t) \exp(\beta_\alpha t), \quad t \geq 0. \tag{5.28}$$

5.2   Numerical results

In this section, representative results are shown for an unloaded straight thin wire as well as for thin wires loaded with different impedance profiles. It is worth mentioning that natural frequencies s_α occur in layers ℓ and are ordered within a layer where m represents the order [53]. We have restricted our analysis to the first layer, since it is much closer to the imaginary axis $j\omega$ than other layers. Moreover from the time-domain current expression (5.27) it follows that the effects of natural frequencies with a real part β_α negative and large in magnitude, as for high-layer frequencies, are rapidly damped.

5.2.1   Natural frequencies of a straight thin wire

Following the scheme proposed in Sec. 5.1.1, we compute the natural frequencies of a straight thin wire with $h/a = 200$. Figure 5.1 shows the converging behavior of the natural frequencies in the complex s-plane by increasing the number N of basis functions used for the current expansion.
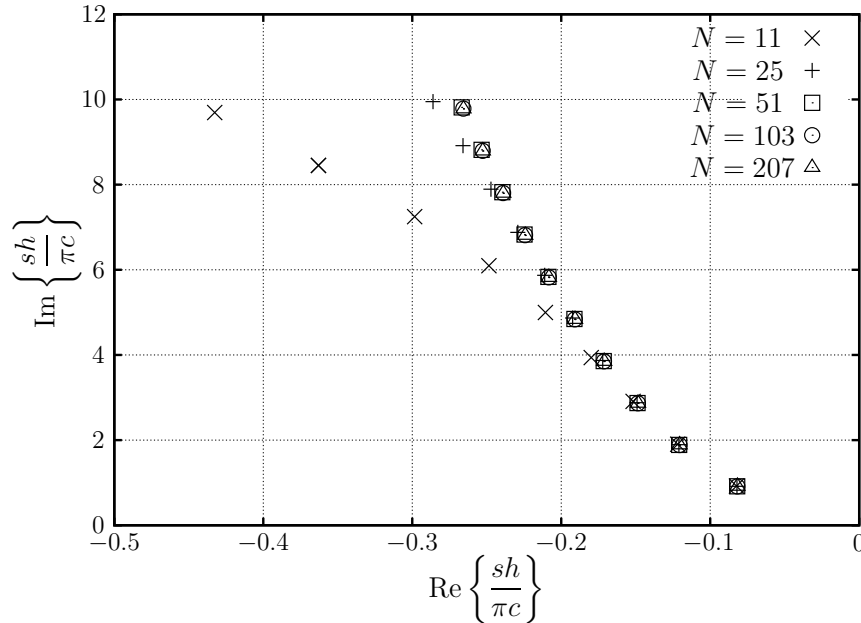
Figure 5.1: *First* 10 *natural frequencies for an unloaded straight thin wire with* $h/a = 200$ *when N basis functions are used in the current expansion.*

In Table 5.1 the first ten pole values are given as calculated by our numerical method for two different discretization number $N = 103$ and $N = 207$, and as obtained by Tesche [54]

and Pearson [59]. Moreover, for these ten values we have evaluated the relative error

$$\zeta = \max\left\{\frac{|s_\alpha - \widetilde{s}_\alpha|}{|s_\alpha|}\right\}_{m=1}^{10}, \tag{5.29}$$

where s_α is the reference value and $\widetilde{s}_\alpha$ is the value as calculated by our numerical scheme. We have computed this error in four different cases:

- reference value s_α given by Tesche [54] and value $\widetilde{s}_\alpha$ calculated when $N = 103$ basis functions are used in the MoM scheme;

- reference value s_α given by Tesche [54] and value $\widetilde{s}_\alpha$ calculated when $N = 207$ basis functions are used in the MoM scheme;

- reference value s_α given by Pearson [59] and value $\widetilde{s}_\alpha$ calculated when $N = 103$ basis functions are used in the MoM scheme;

- reference value s_α given by Pearson [59] and value $\widetilde{s}_\alpha$ calculated when $N = 207$ basis functions are used in the MoM scheme;

For all cases we have found that the error in (5.29) is about 0.01 which means that the first ten natural frequencies as computed by our method agree to about one percent with those in the literature [54, 59].

Table 5.1: *Natural frequencies $(sh)/(\pi c)$ for an unloaded straight thin wire with $h/a = 200$ as calculated by our numerical scheme and as computed by Tesche [54] and Pearson [59].*

m	$N = 103$	$N = 207$	[54]	[59]
1	$-0.082 + j0.913$	$-0.082 + j0.912$	$-0.082 + j0.926$	$-0.082 + j0.924$
2	$-0.121 + j1.886$	$-0.121 + j1.884$	$-0.120 + j1.897$	$-0.120 + j1.908$
3	$-0.149 + j2.866$	$-0.148 + j2.863$	$-0.147 + j2.874$	$-0.146 + j2.900$
4	$-0.171 + j3.850$	$-0.171 + j3.846$	$-0.169 + j3.854$	$-0.169 + j3.882$
5	$-0.191 + j4.836$	$-0.191 + j4.831$	$-0.188 + j4.835$	$-0.187 + j4.878$
6	$-0.208 + j5.824$	$-0.208 + j5.818$	$-0.205 + j5.817$	$-0.204 + j5.864$
7	$-0.224 + j6.813$	$-0.224 + j6.806$	$-0.220 + j6.800$	$-0.219 + j6.863$
8	$-0.239 + j7.803$	$-0.239 + j7.795$	$-0.234 + j7.783$	$-0.234 + j7.854$
9	$-0.253 + j8.794$	$-0.253 + j8.785$	$-0.247 + j8.767$	$-0.247 + j8.847$
10	$-0.266 + j9.786$	$-0.266 + j9.775$	$-0.260 + j9.752$	$-0.259 + j9.850$

In Fig. 5.2, natural frequencies of a straight thin wire are plotted for several wire length-radius ratios h/a. From Fig. 5.2 we observe that, as long as the ratio h/a is increased,

natural frequencies s_α move towards the imaginary axis but their imaginary parts ω_α are almost invariant. Indeed the resonant frequencies of a wire are almost independent of the ratio h/a.
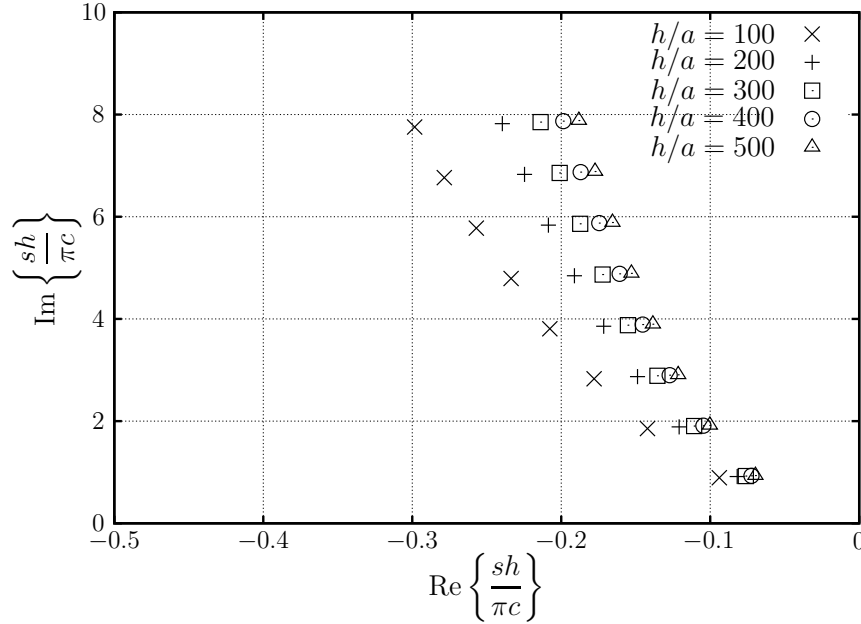
Figure 5.2: *Locations of the first* 8 *natural frequencies of an unloaded thin wire with different length-radius ratios h/a. Number of basis functions used: $N = 51$.*

5.2.2 Natural frequencies of loaded thin wires

As a second example, we have computed the natural frequencies of a wire with $h/a = 200$, loaded with a uniform resistive distribution $Z^{\text{load}}(z) = R_1$. Figure 5.3 shows the trajectories followed by the natural frequencies compared with results from the literature [54]. As the value of R_1 increases, the locations of these frequencies in the complex s-plane move towards the real axis. This means that the contribution of these frequencies to the time-domain current (5.27) attenuates more rapidly since the value β_α is negative and has a large magnitude. The physical explanation of this phenomenon is that the increased resistive loading profile R_1 causes an increased attenuation for the waves traveling along the wire [60]. Focusing on the first natural frequency with $m = 1$, we observe that, as the value of the loading increases, this pole moves towards the real axis to a value whose imaginary part is equal to 0. In this point a double pole (natural frequency) occurs, since natural frequencies occur in conjugate pairs. This means that the natural frequency and its complex conjugate coincide. As the value of the loading is further increased this pair

of natural frequencies splits up again and remains on the negative real s-axis, one natural frequency moving to $-\infty$ and the other to 0. This behavior can be clearly observed in Fig. 5.4, where the first order natural frequencies (i.e., $m = 1$) of a wire with $h/a = 200$ loaded with a linear resistive distribution $Z^{\text{load}}(z) = R_2|z - h/2|/h$ are shown as a function of the constant R_2. In the double pole, as well as for all poles on the real s-axis (occurring for larger values of the load), the corresponding temporal contribution in (5.27) does not exhibit an oscillatory behavior since the imaginary part equals zero.

We have also studied how natural frequencies change for an increasing value of a lumped load with $Z^{\text{load}}(z) = Z^{\text{load}}\delta(z - z_L)$. In Figs. 5.5 and 5.6, we show the first six natural frequencies of a wire with $h/a = 200$ loaded with the lumped resistance $Z^{\text{load}} = R_0$ placed at $z_L = 0.3$ m. The trajectories of the first natural frequency $m = 1$ are shown in Fig. 5.5 for different discretization numbers N. Figure 5.6 shows the trajectories of higher-order natural frequencies s_α. In particular, we observe, as expected, that for higher-order s_α a finer discretization is needed to predict the value with sufficient accuracy. Indeed, higher-order poles (i.e., $m \geq 1$) correspond to higher frequencies (i.e. ω_α), hence, a higher discretization number N is required to converge.
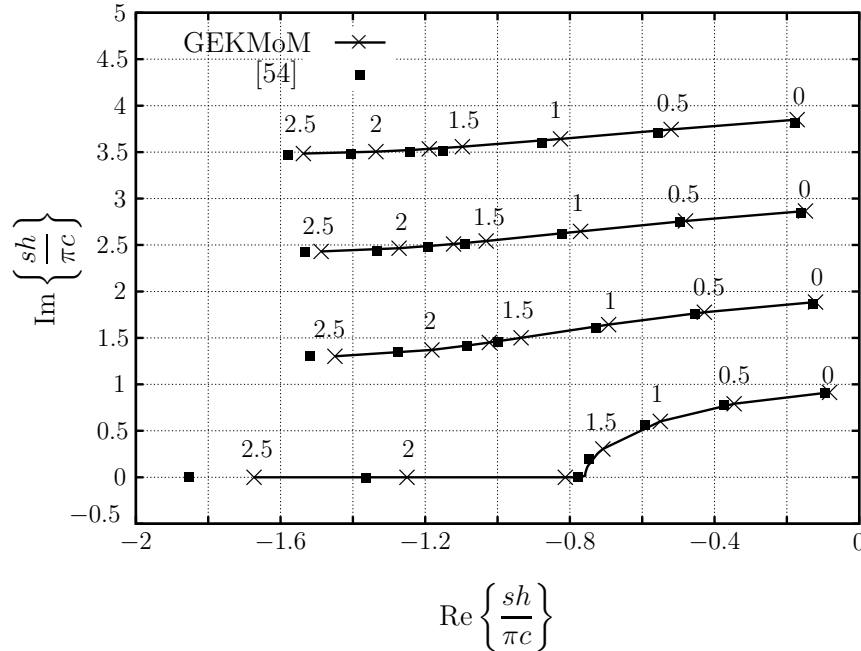
Figure 5.3: *Trajectories of the natural frequencies of a wire with $h/a = 200$, loaded with a uniform resistive distribution $Z^{load}(z) = R_1$ as a function of R_1 in $k\Omega/m$. Discretization number $N = 103$.*
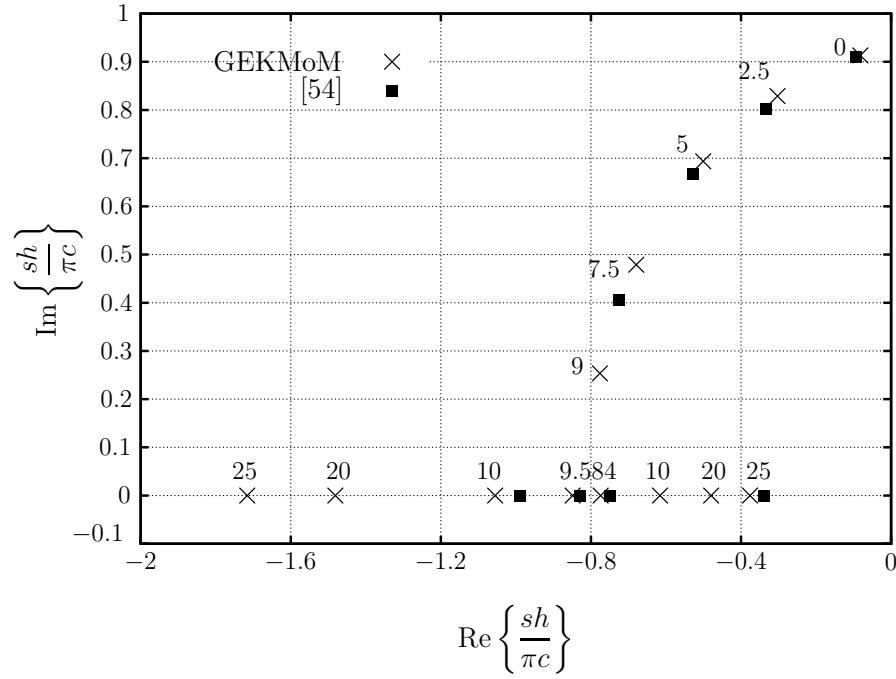
Figure 5.4: *Trajectory followed by the first order natural frequency $m = 1$ of a wire with $h/a = 200$ loaded with a linear resistive distribution $Z^{load}(z) = R_2|z - h/2|/h$ as a function of R_2 in $k\Omega/m$. Discretization number $N = 103$.*
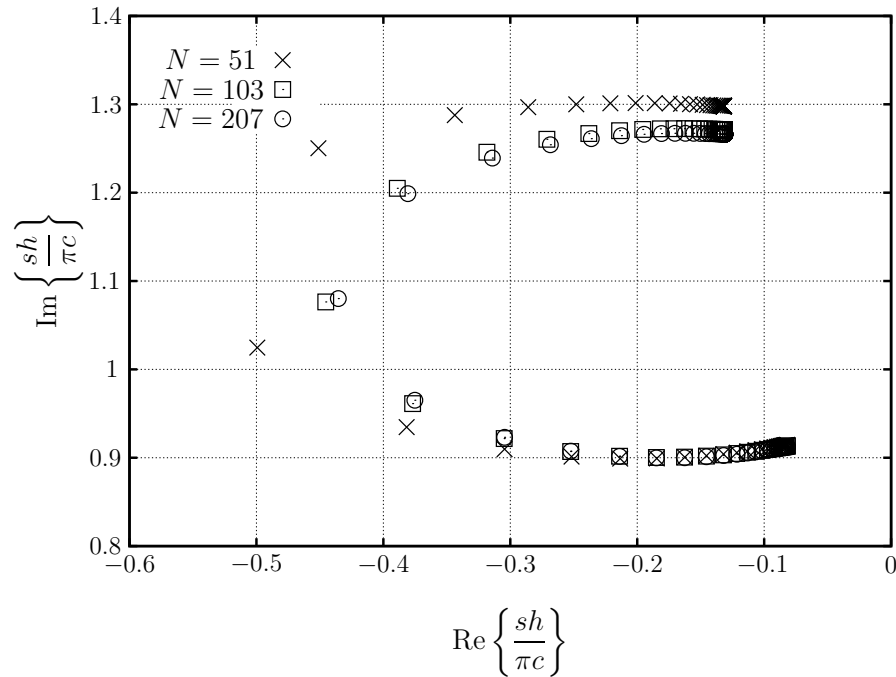
Figure 5.5: *Trajectories followed by the first natural frequency $m = 1$ of a wire with $h/a = 200$ and with a lumped loading placed at $z_L = 0.3$ m as a function of R_0 for different wire segmentation numbers N.*
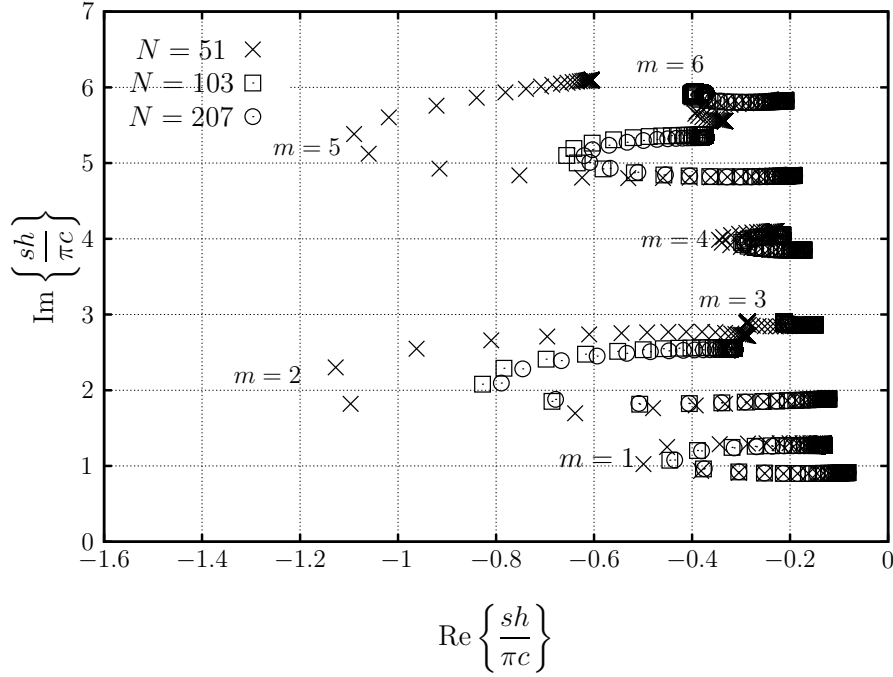
Figure 5.6: *Trajectories of the first* 6 *natural frequencies of a wire with* $h/a = 200$ *and with a lumped loading placed at* $z_L = 0.3$ m *as a function of* R_0 *for different wire segmentation numbers* N.

5.3 Conclusions and discussion

In this chapter we have discussed a method to calculate the natural frequencies of unloaded and loaded wire antennas. Natural frequencies of a wire antenna loaded with different impedance profiles as well as lumped elements are computed applying the Singular Value Decomposition to the generalized MoM matrix together with a suitable search algorithm. The results show how the locations of the poles change in the complex s-plane when some characteristic parameters (e.g., ratio h/a of the wire, discretization number N, etc.) are varied. Since natural frequencies occur in conjugate pairs or are located on the real axis, we have confined the search algorithm to the region $\text{Re}\{s\} \leq 0$, $\text{Im}\{s\} \geq 0$. From this study some interesting observations on the time-domain current can also be made.

By increasing the thickness of an unloaded wire antenna, we have observed that natural frequencies move further away from the $j\omega$ axis. This means that their effect on the time domain current is rapidly damped since their real part increases.

The validation done for an unloaded wire by comparing our results with those found in the literature [54,59] (agreement of about one percent) is a further confirmation of the validity

and robustness of the numerical method implemented.

In particular, we have studied how locations of natural frequencies of a loaded wire vary in the complex s-plane when a resistive impedance $Z^{\text{load}}(z)$ is gradually increased by a step ΔZ^{load}. As the value of the impedance gradually increases, the developed algorithm generates successive initial estimates yielding a marching-on-in-loading approach. From a physical point of view, the increased resistive loading profile causes an increased attenuation for the waves traveling along the wire. This is reflected in a movement of the natural frequencies towards the real axis. Indeed the contribution of these frequencies to the time-domain current attenuates more rapidly since the value β_α is negative and has a larger magnitude.

For higher resistive impedance, the conjugate pairs of natural frequencies move to the real axis and collapse to a value where a double pole occurs yielding the absence of oscillatory behavior of the time domain current expression. As the loading is further increased natural frequencies split, laying on the real axis. In conclusion, since these poles have imaginary part equal to zero, the oscillations in the time-domain current will not be present.

Chapter 6

EM coupling between arbitrarily oriented wires

In previous chapters we have discussed how the current along an unloaded and loaded wire can be evaluated by applying the Galerkin MoM to Pocklington's equation with exact kernel. This was a first step towards the study of the electromagnetic coupling between arbitrary oriented wires. In this case the current along a "source" wire radiates a field which illuminates all the other wires (referred to as "observation" wires). This field induces currents along "observation" wires' surfaces. Efficient and accurate field evaluation is therefore essential to solve electromagnetic coupling between wires especially, when wires are close to each other.

6.1 Introduction

In Sec. 2.2.1, we observed that the field radiated by the total current $I(z')$ induced on the wire can be determined up to $O(a^2)$, where a is the small radius of the wire. The derivation of this result proceeded in two steps. First, for a point $\mathbf{r}'$ on the surface of the wire, the longitudinal and transverse components of the current density were written as

$$J_z(\mathbf{r}') \;=\; \widehat{J}_z(z') + \left(J_z(\mathbf{r}') - \widehat{J}_z(z') \right) = \widehat{J}_z(z') + \Delta J_z(\mathbf{r}'), \tag{6.1}$$

$$J_\phi(\mathbf{r}') \;=\; \widehat{J}_\phi(z') + \left(J_\phi(\mathbf{r}') - \widehat{J}_\phi(z') \right) = \widehat{J}_\phi(z') + \Delta J_\phi(\mathbf{r}'), \tag{6.2}$$

where $\widehat{J}_z(z')$ and $\widehat{J}_\phi(z')$ denote the values averaged over $\phi' \in [0, 2\pi)$. For $\widehat{J}_z(z')$, we have

$$\widehat{J}_z(z') = \frac{I(z')}{2\pi a}, \tag{6.3}$$

where $I(z')$ is the desired total current along the wire. From the closed-form separation-of-variables expression for the current density induced by an incident plane wave [32], [33, pp.481–483], [34], we have

$$\Delta J_z(\mathbf{r}') = O(1), \quad \widehat{J}_\phi(\mathbf{r}') = O(1), \quad \Delta J_\phi(\mathbf{r}') = O(a), \tag{6.4}$$

as $a \downarrow 0$. The second step was to consider an approximation of the distance $|\mathbf{r} - \mathbf{r}'|$ as in (2.44) and carrying out a Taylor expansion (see Sec. 2.2.1). This led to a one-dimensional integral expression of the field radiated by the current $I(z')$ on the wire axis

$$
\begin{aligned}
\mathbf{E}(\mathbf{r}) \;=\; & \frac{1}{j\omega\varepsilon}\frac{1}{4\pi}\int_{z'=0}^{h} I(z')\frac{\exp(-jk|\mathbf{r} - z'\mathbf{i}_z|)}{|\mathbf{r} - z'\mathbf{i}_z|^3}\left\{ -\left[(jk|\mathbf{r} - z'\mathbf{i}_z|)^2 + jk|\mathbf{r} - z'\mathbf{i}_z| + 1\right]\mathbf{i}_z\right. \\
& +\left. \left[3 + 3jk|\mathbf{r} - z'\mathbf{i}_z| + (jk|\mathbf{r} - z'\mathbf{i}_z|)^2\right]\frac{z - z'}{|\mathbf{r} - z'\mathbf{i}_z|^2}\left(\mathbf{r} - z'\mathbf{i}_z\right)\right\} dz' + O(a^2), \tag{6.5}
\end{aligned}
$$

valid when $h \gg a$, $|\mathbf{r} - \mathbf{r}'| \gg a$ and $ka \ll 1$, and referred to as the radiated field thin-wire axis approximation. If we now consider the interaction between two wires, the most efficient evaluation is obtained by using (6.5), and the integral equation with exact kernel for determining the current on the observation wire. This leads to a one-dimensional integral for the transmitting wire, and a two-dimensional integral for receiving wire. The radiated field (6.5) breaks down where the distance between the wires is of $O(a)$ or smaller. In this case, we locally have to use the full two-dimensional integral equation, writing for example the longitudinal component of the surface current as an angular Fourier series

$$J_z(\mathbf{r}') = \sum_{m=-\infty}^{\infty} J_{z,m}(z')\,\exp(jm\phi), \tag{6.6}$$

where $J_{z,0}(z') = \widehat{J}_z(z')$ as defined in (6.3). The resulting analysis would be outside the scope of this thesis. Nevertheless, it is useful to obtain an estimate of the error caused by introducing the computationally efficient form (6.5), and to compare it to the error that is introduced by the space discretization required by the Method of Moments. To this end, we consider the approximations in (6.1), (6.2) and (6.4) as a crude version of the general procedure prescribed by (6.6). This means that we also consider the case with the total current homogeneously distributed along the mantle of the transmitting wire, and compare it with the case where that current is concentrated on the central axis. This should at least give us an indication of the error due to (6.5).

6.2   Electric field radiated by a straight wire

In this section, we consider the total current homogeneously distributed along the mantle of the transmitting wire and we derive a two-dimensional integral expression of the radiated electric field. In this case, as described in Sec. 2.2.1 equation (2.41), the vector potential $\mathbf{A}(\mathbf{r})$ is determined up to $O(a^2)$ by

$$\mathbf{A}(\mathbf{r}) = \mathbf{i}_z \int\limits_{z'=0}^{h} \frac{I(z')}{2\pi} \int\limits_{\phi'=0}^{2\pi} \frac{\exp(-jk|\mathbf{r}-\mathbf{r}'|)}{4\pi|\mathbf{r}-\mathbf{r}'|} d\phi' dz', \tag{6.7}$$

where h is the length of the wire antenna, $\mathbf{r} \in \overline{D}$ (i.e., the region outside the wire), $\mathbf{r} = r\mathbf{i}_r(\phi) + z\mathbf{i}_z$ represents the observation point and $\mathbf{r}' = a\mathbf{i}_r(\phi') + z'\mathbf{i}_z$ represents the source point along the mantle of the wire, Fig. 6.1.
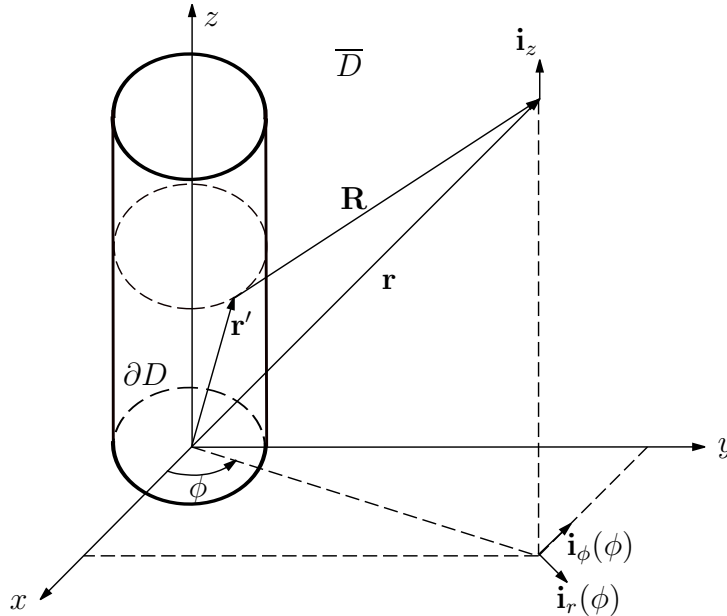
Figure 6.1: *Geometry of the wire.*

The radiated electric field is then evaluated as

$$\mathbf{E}(\mathbf{r}) = \frac{1}{j\omega\varepsilon} \left[k^2 \mathbf{A}(\mathbf{r}) + \nabla \left(\nabla \cdot \mathbf{A}(\mathbf{r}) \right) \right]. \tag{6.8}$$

By a straightforward evaluation of the divergence of the vector potential $\mathbf{A}$, it follows that

$$\nabla \cdot \mathbf{A}(\mathbf{r}) \;=\; \int\limits_{z'=0}^{h} \frac{I(z')}{2\pi} \int\limits_{\phi'=0}^{2\pi} \mathbf{i}_z \cdot \nabla \left(\frac{\exp(-jkR)}{4\pi R} \right) d\phi' dz'$$

$$=\; \int\limits_{z'=0}^{h} \frac{I(z')}{2\pi} \int\limits_{\phi'=0}^{2\pi} (-1 - jkR) \frac{\exp(-jkR)}{4\pi R^3} (z - z') d\phi' dz', \tag{6.9}$$

where $\mathbf{r} - \mathbf{r}' = (r\cos\phi - a\cos\phi')\,\mathbf{i}_x + (r\sin\phi - a\sin\phi')\,\mathbf{i}_y + (z - z')\,\mathbf{i}_z$, resulting in a distance

$$R = |\mathbf{r} - \mathbf{r}'| = \sqrt{(z - z')^2 + (r - a)^2 + 4ra\sin^2\left(\frac{\phi - \phi'}{2}\right)}. \tag{6.10}$$

Next, we determine the gradient

$$\nabla\left\{ (-1 - jkR) \frac{\exp(-jkR)}{4\pi R^3} (z - z') \right\} =$$

$$(\nabla R) \left[\partial_R \left((-1 - jkR) \frac{\exp(-jkR)}{R^3} \right) \right] (z - z') - (1 + jkR) \frac{\exp(-jkR)}{R^3} \mathbf{i}_z =$$

$$\left[3 + 3jkR + (jkR)^2 \right] \frac{\exp(-jkR)}{R^3} \frac{(\mathbf{r} - \mathbf{r}')}{R^2} (z - z') - (1 + jkR) \frac{\exp(-jkR)}{R^3} \mathbf{i}_z. \tag{6.11}$$

The electric field now follows from (6.8) as a function of the total current $I(z')$

$$\mathbf{E}(\mathbf{r}) \;=\; \frac{1}{j\omega\varepsilon} \frac{1}{8\pi^2} \int\limits_{z'=0}^{h} I(z') \int\limits_{\phi'=0}^{2\pi} \frac{\exp(-jkR)}{R^3} \left\{ - \left[(jkR)^2 + jkR + 1 \right] \mathbf{i}_z \right.$$

$$+\; \left. \left[3 + 3jkR + (jkR)^2 \right] \frac{z - z'}{R} \frac{\mathbf{r} - \mathbf{r}'}{R} \right\} d\phi' dz', \tag{6.12}$$

where the points $\mathbf{r}$ and $\mathbf{r}'$ are on the observation and source wire mantles, respectively. Expression (6.12) is referred to as radiated field thin-wire mantle approximation. In this case, besides the integration in z' (present also in (6.5)), an integration in ϕ' has to be carried out in the evaluation of the field (6.12). The numerical implication in terms of CPU time and accuracy of the two approximations (6.5), (6.12) will be further discussed in Sec. 6.3.1. The formulation that follows is applicable in both cases.

The next step in the evaluation of the radiated field for the thin-wire axis and mantle approximations (6.5) and (6.12) is the expansion of the current by means of N rooftop basis functions $\psi_n(z')$

$$I(z') = \sum_{n=1}^{N} I_n \psi_n(z'), \qquad \psi_n(z') = \begin{cases} 1 - \left| \dfrac{z'}{\Delta z} - n \right|, & |z' - n\Delta z| \leq \Delta z, \\ 0, & \text{otherwise,} \end{cases} \tag{6.13}$$

with $\Delta z = h/(N+1)$. Consequently, the field can be seen as a sum of N elementary electric fields radiated by a current along the n-th source (transmitting) wire element (composed of two adjacent segments) and weighted by coefficient terms I_n, hence

$$\mathbf{E}(\mathbf{r}) = \sum_{n=1}^{N} I_n \mathbf{E}_n(\mathbf{r}). \tag{6.14}$$

For the thin-wire axis approximation the expressions of the elementary fields $\mathbf{E}_n$ follow from (6.5)

$$\mathbf{E}_n(\mathbf{r}) = \frac{1}{j\omega\varepsilon}\frac{1}{4\pi} \int\limits_{z'=(n-1)\Delta z}^{(n+1)\Delta z} \psi_n(z') \frac{\exp(-jk|\mathbf{r}-z'\mathbf{i}_z|)}{|\mathbf{r}-z'\mathbf{i}_z|^3} \left\{ -\left[(jk|\mathbf{r}-z'\mathbf{i}_z|)^2 + jk|\mathbf{r}-z'\mathbf{i}_z|\right.\right.$$

$$\left.\left. + 1\right]\mathbf{i}_z + \left[3 + 3jk|\mathbf{r}-z'\mathbf{i}_z| + (jk|\mathbf{r}-z'\mathbf{i}_z|)^2\right] \frac{(z-z')}{|\mathbf{r}-z'\mathbf{i}_z|^2} (\mathbf{r}-\mathbf{r}')\right\} dz', \tag{6.15}$$

and, for the thin-wire mantle approximation from (6.12)

$$\mathbf{E}_n(\mathbf{r}) = \frac{1}{j\omega\varepsilon}\frac{1}{8\pi^2} \int\limits_{z'=(n-1)\Delta z}^{(n+1)\Delta z} \psi_n(z') \int\limits_{\phi'=0}^{2\pi} \frac{\exp(-jkR)}{R^3} \left\{ -\left[(jkR)^2 + jkR + 1\right]\mathbf{i}_z\right.$$

$$\left. + \left[3 + 3jkR + (jkR)^2\right] \frac{(z-z')}{R}\frac{(\mathbf{r}-\mathbf{r}')}{R}\right\} d\phi' dz', \tag{6.16}$$

where the distance R is given by (6.10).

6.3 Mutually coupled wires

As already explained, the computation of electromagnetic coupling between arbitrarily oriented wires is based on the evaluation of the electric field radiated by the current flow of a single wire element (i.e. two adjacent segments). This field induces a current on all other wires, hence the mutual interaction. As a simplification, we consider the coupling between two wires in the configuration depicted in Fig. 6.2. The total field incident on wire 1 can be written as the sum of two parts

$$\mathbf{E}_t^1(\mathbf{r}) = \mathbf{E}_e(\mathbf{r}) + \mathbf{E}^{1,2}(\mathbf{r}), \tag{6.17}$$

where $\mathbf{E}_e(\mathbf{r})$ is the field due to external sources and $\mathbf{E}^{1,2}(\mathbf{r})$ is the induced field on wire 1 due to the current flowing along wire 2. A similar expression can be derived for wire 2

$$\mathbf{E}_t^2(\mathbf{r}) = \mathbf{E}_e(\mathbf{r}) + \mathbf{E}^{2,1}(\mathbf{r}). \tag{6.18}$$

PSfrag replacements
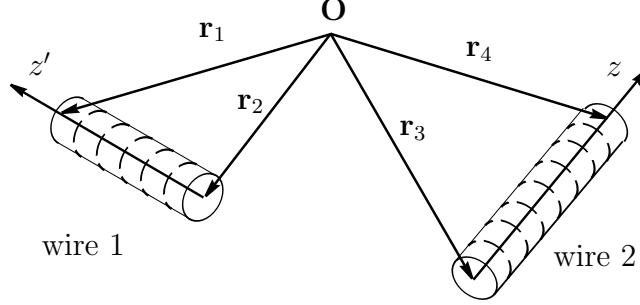
Figure 6.2: *The two wires geometry.*

As can be seen in Fig. 6.2, wire 1 has end points $\mathbf{r}_1$ and $\mathbf{r}_2$ while wire 2 has end points $\mathbf{r}_3$ and $\mathbf{r}_4$. The wires have radius a_1 and a_2, respectively. In particular, following the Method of Moments procedure, the current is expanded by means of N and M rooftop basis functions defined on $N+1$ and $M+1$ segments, respectively. By recalling the elementary field (6.14), we can write the electric field radiated by currents flowing along wire 1 (or wire 2) and incident on wire 2 (or wire 1) as

$$\mathbf{E}^{2,1}(\mathbf{r}) \;=\; \sum_{n=1}^{N} I_n \mathbf{E}_n^{2,1}(\mathbf{r}), \tag{6.19}$$

$$\mathbf{E}^{1,2}(\mathbf{r}) \;=\; \sum_{m=1}^{M} I_m \mathbf{E}_m^{1,2}(\mathbf{r}). \tag{6.20}$$

Combining these results with (6.17) and (6.18), and applying the testing procedure in the Method of Moments, the matrix equation $\underline{\underline{\mathbf{Z}}}\,\underline{\mathbf{I}} = \underline{\mathbf{F}}$ in (3.8) now may be generalized as

$$\begin{bmatrix} \underline{\underline{\mathbf{Z}}}^1 & -\underline{\underline{\mathbf{C}}}^{1,2} \\ -\underline{\underline{\mathbf{C}}}^{2,1} & \underline{\underline{\mathbf{Z}}}^2 \end{bmatrix} \begin{bmatrix} \underline{\mathbf{I}}^1 \\ \underline{\mathbf{I}}^2 \end{bmatrix} = \begin{bmatrix} \underline{\mathbf{F}}_e^1 \\ \underline{\mathbf{F}}_e^2 \end{bmatrix}, \tag{6.21}$$

where each known vector on the right-hand side represents the weighted field of external origin. The diagonal blocks $\underline{\underline{\mathbf{Z}}}^1$ and $\underline{\underline{\mathbf{Z}}}^2$ are referred to as "self matrices" and represent the interaction between segments of the same wire, while the "coupling matrices" $\underline{\underline{\mathbf{C}}}^{1,2}$ and $\underline{\underline{\mathbf{C}}}^{2,1}$ describe the interaction between segments of different wires.

As an example, we consider the (m,n)-th element of matrix $\underline{\underline{\mathbf{C}}}^{2,1}$. A current distribution along two adjacent segments, defined here as the n-th source element of wire 1, radiates an elementary electric field $\mathbf{E}_n^1$ as in (6.15) or (6.16). These elementary fields are known for a reference system where the axis of wire 1 runs along the interval $0 < z < h$, where $h = |\mathbf{r}_2 - \mathbf{r}_1|$ is the length of wire 1. This field impinges on wire 2 and induces a current along each of its segments. In this case, we are interested in the induced current flowing

along the m-th element (composed by two adjacent segments) of wire 2, referred to as the observation element. Assuming that the point $\mathbf{r}'$ on the mantle of wire 1 is known in a reference system local to this wire,

$$\mathbf{r}' = a_1 \cos \phi' \mathbf{i}_{x'} + a_1 \sin \phi' \mathbf{i}_{y'} + z' \mathbf{i}_{z'}, \tag{6.22}$$

as well as the observation point $\mathbf{r}$ on the mantle of wire 2 is known in a reference system local to wire 2,

$$\mathbf{r} = a_2 \cos \phi \mathbf{i}_x + a_2 \sin \phi \mathbf{i}_y + z \mathbf{i}_z, \tag{6.23}$$

the following steps are performed to compute the coupling element $C_{m,n}^{2,1}$.

- With the aid of the translation and rotations formulas in Appendix D.1, the angles θ_1, ϕ_1, χ_1, θ_2, ϕ_2, χ_2 are evaluated by using expressions (D.6), (D.7), (D.12) and (D.13). Then the two transformation matrices $\underline{\mathbf{T}}_1$, $\underline{\mathbf{T}}_2$ (related to wire 1 and wire 2, respectively) are computed as in (D.14).

- Next, consider the observation point $\mathbf{r}$ expressed in Cartesian coordinates with respect to a system local to wire 2

$$\mathbf{r} = x_2 \mathbf{i}_x + y_2 \mathbf{i}_y + z_2 \mathbf{i}_z. \tag{6.24}$$

Its coordinates (x_2, y_2, z_2) are "transformed" to coordinates (x_1, y_1, z_1) with respect to a system local to wire 1

$$\mathbf{r} = x_1 \mathbf{i}_{x'} + y_1 \mathbf{i}_{y'} + z_1 \mathbf{i}_{z'}. \tag{6.25}$$

The transformation which relates these two systems of coordinates can be found in Appendix D.1.

- Then the electric field $\mathbf{E}_n^1(\mathbf{r})$ is computed and expressed in Cartesian coordinates (E_x^1, E_y^1, E_z^1) with respect to a system local to wire 1

$$\mathbf{r} = E_x^1 \mathbf{i}_{x'} + E_y^1 \mathbf{i}_{y'} + E_z^1 \mathbf{i}_{z'}. \tag{6.26}$$

The next step is to transform these coordinates into Cartesian coordinates with respect to a system local to wire 2, see Appendix D.1.

- Finally the integral

$$\int_{z=(m-1)\Delta z_2}^{(m+1)\Delta z_2} \left(1 - \left|\frac{z}{\Delta z_2} - m\right|\right) \int_{\phi=0}^{2\pi} \mathbf{E}_n^1(\mathbf{r}) \cdot \mathbf{i}_z d\phi dz, \tag{6.27}$$

can be evaluated, where $\mathbf{E}_n^1$ is expressed in coordinates with respect to system 2, where the m-th testing function along wire 2 is explicitly defined, and where $\Delta z_2 = |\mathbf{r}_4 - \mathbf{r}_3|/(M+1)$.

Once the elements of matrix $\underline{\underline{\mathbf{C}}}^{2,1}$ have been evaluated, we can fill matrix $\underline{\underline{\mathbf{C}}}^{1,2}$ without any further calculation since by reciprocity the property

$$\underline{\underline{\mathbf{C}}}^{1,2} = \underline{\underline{\mathbf{C}}}^{2,1^T}, \tag{6.28}$$

is satisfied, where T indicates the transpose operator.

Generalizing the problem to the case of P arbitrarily oriented wires, from matrix equation (6.21), we write

$$\begin{bmatrix} \underline{\underline{\mathbf{Z}}}^1 & -\underline{\underline{\mathbf{C}}}^{1,2} & \cdots & -\underline{\underline{\mathbf{C}}}^{1,P} \\ -\underline{\underline{\mathbf{C}}}^{2,1} & \underline{\underline{\mathbf{Z}}}^2 & \cdots & -\underline{\underline{\mathbf{C}}}^{2,P} \\ \vdots & \vdots & \vdots & \vdots \\ -\underline{\underline{\mathbf{C}}}^{P,1} & -\underline{\underline{\mathbf{C}}}^{P,2} & \cdots & \underline{\underline{\mathbf{Z}}}^P \end{bmatrix} \begin{bmatrix} \underline{\mathbf{I}}^1 \\ \underline{\mathbf{I}}^2 \\ \vdots \\ \underline{\mathbf{I}}^P \end{bmatrix} = \begin{bmatrix} \underline{\mathbf{F}}_e^1 \\ \underline{\mathbf{F}}_e^2 \\ \vdots \\ \underline{\mathbf{F}}_e^P \end{bmatrix}. \tag{6.29}$$

Matrices $\underline{\underline{\mathbf{C}}}^{q,p}$, $(p, q = 1, \ldots, P)$ describe the electromagnetic coupling between segments belonging to different wires, while self matrices $\underline{\underline{\mathbf{Z}}}^p$, $(p = 1, \ldots, P)$ take into account the electromagnetic interaction between segments of the same wire. Each known vector $\underline{\mathbf{F}}_e^p$ on the right-hand side represents the external weighted excitation on the p-th wire.

6.3.1 Efficient evaluation of coupling elements

For the case of a single wire, it has already been explained in Sec. 3.2 and in Sec. 3.3, how the elements of the known vector $\underline{\mathbf{F}}$ and of the self matrix $\underline{\underline{\mathbf{Z}}}$ are computed efficiently. Our attention is now therefore focused on the computation of the coupling-matrix elements. Consider the (m, n)-th element of matrix $\underline{\underline{\mathbf{C}}}^{2,1}$. In accordance with the thin-wire axis approximation (6.5), only one integral has to be carried out to calculate the elementary field $\mathbf{E}_n^1$ since the current is on axis (of the the n-th radiating element of wire 1), see (6.15). For the mantle approximation a double integration (6.16) is required since the current flows along the mantle of the radiating element. In both cases, an additional double integral (6.27) has to be computed to determine the mutual interaction between this field and the induced current distribution along the m-th observation element of wire 2. Thus, we summarize the two approaches as:

- 1D+2D integration (i.e., radiating current along wire axis and 2D integral for the "observation" wire);

- $2 \times 2D$ integration (i.e., radiating current along the wire surface and 2D integral for the "observation" wire).

A simple test was performed to compare the two approaches in terms of accuracy and CPU time. We consider two parallel wires of length $h = \lambda/2$ placed at a distance d and illuminated by an incident plane wave $|\mathbf{E}^i| = 1$ V/m as shown in Fig. 6.3. Both wires are subdivided in $N + 1$ segments which means that N rooftop basis functions are defined. Moreover, for both wires, we calculate the root-mean-square (RMS) error

$$\zeta_{\text{cur}} = \sqrt{\frac{\int\limits_{z=0}^{h} \left| I(z) - \widetilde{I}(z) \right|^2 dz}{\int\limits_{z=0}^{h} |I(z)|^2 dz}}, \tag{6.30}$$

where the reference value $I(z)$ is computed by following the second approach (i.e., $2 \times 2D$ integration). The value $\widetilde{I}(z)$ is calculated by following the first approach (i.e., 1D+2D integration). It is worth noticing that the error (6.30) is made in combination with the discretization error introduced by the GEKMoM method already calculated in Sec. 3.4.3.
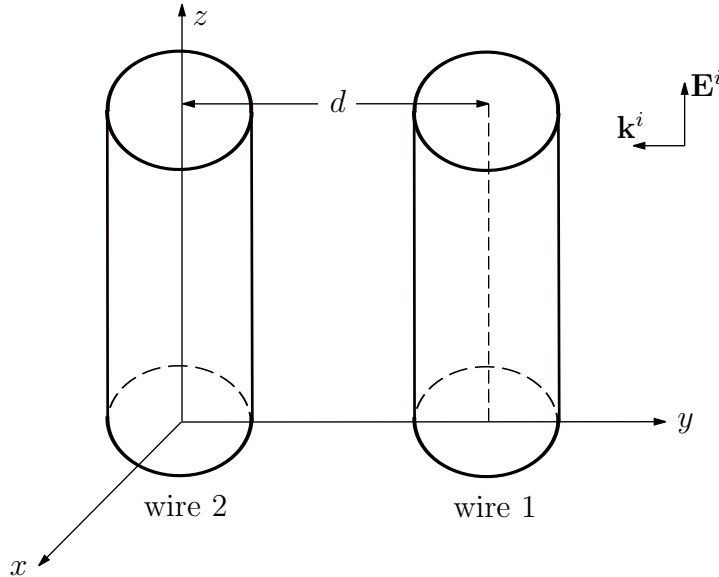
Figure 6.3: *Two parallel wires placed at a distance d illuminated by an incident plane wave.*

The errors ζ_{cur}^1 and ζ_{cur}^2 calculated for the current along wire 1 and along wire 2, respectively, are given in Tables 6.1, 6.2 and 6.3 for two wires with length $h = \lambda/2$ and length-radius ratio $h/a = 100$, $h/a = 30$ and $h/a = 20$, respectively. In all these cases $N = 23$ basis

functions are used. For this discretization number, as depicted in Sec. 3.4.3, we have found that for a single wire the numerical method GEKMoM introduces a discretization error of about $1/N$ for all the length-radius ratios h/a here considered. In particular, in Table 6.4, we report the discretization error for the single wire for the three different ratios h/a.

Table 6.1: *RMS errors ζ^1_{cur}, ζ^2_{cur} and computational cost analysis of two parallel thin wires $h/a = 100$ by varying the distance d.*

$d\ [\lambda]$	ζ^1_{cur}	ζ^2_{cur}	CPU Time ratio $(2 \times 2\text{D}){:}(1\text{D}+2\text{D})$
1	4.7×10^{-5}	4.7×10^{-5}	$14.07 : 1$
0.5	6.5×10^{-5}	6.5×10^{-5}	$14.03 : 1$
0.3	2.3×10^{-4}	2.6×10^{-5}	$13.92 : 1$

Table 6.2: *RMS errors ζ^1_{cur}, ζ^2_{cur} and computational cost analysis of two parallel thin wires $h/a = 30$ by varying the distance d.*

$d\ [\lambda]$	ζ^1_{cur}	ζ^2_{cur}	CPU Time ratio $(2 \times 2\text{D}){:}(1\text{D}+2\text{D})$
1	4.8×10^{-4}	4.8×10^{-4}	$13.95 : 1$
0.5	6.5×10^{-4}	6.5×10^{-4}	$13.93 : 1$
0.3	2.3×10^{-3}	3.0×10^{-4}	$13.84 : 1$

Table 6.3: *RMS errors ζ^1_{cur}, ζ^2_{cur} and computational cost analysis of two parallel thin wires $h/a = 20$ by varying the distance d.*

$d\ [\lambda]$	ζ^1_{cur}	ζ^2_{cur}	CPU Time ratio $(2 \times 2\text{D}){:}(1\text{D}+2\text{D})$
1	1.1×10^{-3}	1.1×10^{-3}	$13.88 : 1$
0.5	1.5×10^{-3}	1.5×10^{-3}	$13.92 : 1$
0.3	5.4×10^{-3}	7.6×10^{-4}	$13.96 : 1$

Table 6.4: *Discretization error for a single $\lambda/2$ wire for three different length-radius ratios h/a as calculated in Sec. 3.4.3.*

N	$h/a = 100$	$h/a = 30$	$h/a = 20$
23	3.97×10^{-2}	2.92×10^{-2}	2.47×10^{-2}

Comparing values in Table 6.4 with those in Tables 6.1, 6.2 and 6.3, we observe that the errors ζ_{cur}^1 and ζ_{cur}^2 introduced by placing the radiating current on the wire axis are always smaller than the discretization error introduced by our numerical method. Moreover, as expected, the thin-wire axis approximation is computationally less expensive than the 2D integration. For the cases studied, a reduction of a factor about 14 in terms of CPU time is obtained.

As a conclusion, the deviation introduced by going from a 2×2D integration to a 1D+2D integration is negligible compared with the discretization error introduced by applying the Method of Moments.

6.3.2   Interpolation technique

In this section we describe a methodology to reduce the computation time required by the straightforward 2×2D approach. To this end, an interpolation technique has been successfully applied to compute the coupling-matrix elements [61,62]. This technique might become useful in all cases where the thin-wire axis approximation breaks down and the full two-dimensional procedure is needed (see Sec. 6.1).

Consider the (m, n)-th element of matrix $\underline{\mathbf{C}}^{2,1}$. To simplify the notation, we will place the radiating n-th element composed by two adjacent segments in the center of a cylindrical coordinate system (ρ', ϕ', z') as shown in Fig. 6.4. Observing that the electric field $\mathbf{E}_n^1$ radiated by a current flow along element n of wire 1 is rotationally symmetric, some considerations have been made. First of all, the observation region of the n-th radiating element can be defined in a plane (ρ', z') with $\rho' > 0$ by points $\rho_{\min}$, $\rho_{\max}$, $z_{\min}$, $z_{\max}$, as depicted in Fig. 6.4. This region contains the projection of the mantle of element m of wire 2 in terms of the coordinates related to wire 1. In order to compute the integral in (6.27), the field $\mathbf{E}_n^1$ is evaluated as in (6.16) on a discrete grid of points within the observation region and then interpolated. For this purpose, we have therefore investigated tabulation and interpolation techniques for the evaluation of the radiated electric field in order to accelerate the computation of coupling matrix elements [63,64]. Even though uniform and
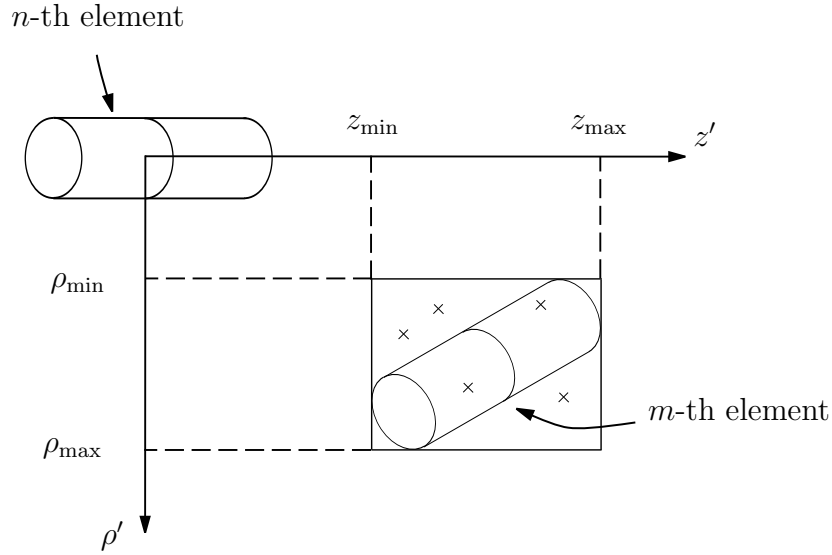
Figure 6.4: *Interpolation area defined to evaluate the electromagnetic interaction between two wire elements.*

random sampling algorithms have been explored, the most efficient technique in choosing points is the one which samples the radiated electric field in a way that follows the behavior of the field. The proposed algorithm is developed based on the following three ideas:

- An interpolation technique is applied to reduce the number of points where the radiated electric field is computed.

- By making use of standard routines a set of points on a non-uniform grid is generated and an interpolation function is then defined. A numerical adaptive multidimensional integration routine [65] has been modified in order to generate a set of points used in a subsequent interpolation step where a piecewise polynomial surface is defined as interpolant function following the method proposed by Renka and Cline [66] (routines E01SAF, E01SBF). In this way, the integration routine will choose the distribution of points according to the behavior of the field $\mathbf{E}_n^1$ which is to be interpolated.

- By subtracting the analytically known point-dipole field from the elementary electric field $\mathbf{E}_n^1$ and by applying the interpolation technique to this difference, the efficiency of the method is improved for a fixed accuracy.

Considering the third point of the list, in order to accelerate the generation of coupling matrices and to control accuracy, further efficiency is gained by observing that the function

to be interpolated is relatively smooth. This term should be quick to evaluate and resemble the (far) field of the n-th radiating element. A function difference $\mathbf{D}_n^1$ is defined as the difference of the field $\mathbf{E}_n^1$ and the electric field $\mathbf{E}^p$ radiated by a point dipole placed in the origin of the coordinate system. Function $\mathbf{E}^p$ behaves asymptotically (i.e., for $R \to \infty$) as $\mathbf{E}_n^1$ and is singular when the distance R vanishes

$$
\begin{aligned}
\mathbf{E}^p(\mathbf{r}) \;=\; & \frac{1}{j\omega\varepsilon} \frac{\Delta z_1}{4\pi} \frac{\exp(-jkR)}{R^3} \left\{ -\left[(jkR)^2 + jkR + 1\right] \mathbf{i}_z \right. \\
& + \left. \left[(jkR)^2 + 3jkR + 3\right] \frac{\mathbf{r}z}{R^2} \right\}, \qquad R = \sqrt{\rho^2 + z^2}.
\end{aligned}
\tag{6.31}
$$

Thanks to these properties, the resulting function $\mathbf{D}_n^1 = \mathbf{E}_n^1 - \mathbf{E}^p$ has a behavior considerably smoother than $\mathbf{E}_n^1$ (and also decreases faster as $R \to \infty$) and is therefore interpolated in a numerically easier way with a higher accuracy. The flow chart in Fig. 6.5 shows the fundamental steps of the proposed algorithm. Our numerical scheme begins by setting a desired accuracy ε with which the elementary radiated electric field (6.16) has to be evaluated. While the adaptive routine [65] numerically integrates the function difference $\mathbf{D}_n^1$, choosing points (ρ_i', z_i') in the observation region $[\rho_{\min}, \rho_{\max}] \times [z_{\min}, z_{\max}]$ following the behavior of this function, the implemented scheme gathers the first N_a points $\{(\rho_i', z_i')\}_{i=1}^{N_a}$. Next, on this non-uniform set of N_a points an interpolated function $\widetilde{\mathbf{D}}_n^1$ is defined by using a NAG routine [66]. To examine the obtained accuracy of $\widetilde{\mathbf{D}}_n^1$ compared to $\mathbf{D}_n^1$ and normalized to the incident field $\mathbf{E}_n^1$, a relative error $\widetilde{\varepsilon}$ has been defined as

$$
\widetilde{\varepsilon} = \frac{|\mathbf{D}_n^1 - \widetilde{\mathbf{D}}_n^1|}{|\mathbf{E}_n^1|}.
\tag{6.32}
$$

The proposed algorithm calculates the error $\widetilde{\varepsilon}$ in N_e points and terminates if $\widetilde{\varepsilon} \leq \varepsilon$ in all points N_e. If the error condition is not met, N_a additional points are added via the integration routine to the previously defined set. An interpolant function is determined on this new grid of $N_a + N_a$ points and the error $\widetilde{\varepsilon}$ is subsequently calculated. Until the error condition is met, the algorithm keeps adding N_a points. Finally, the approximated value of the radiated field is computed as follows

$$
\widetilde{\mathbf{E}}_n^1 = \widetilde{\mathbf{D}}_n^1 + \mathbf{E}^p.
\tag{6.33}
$$

It is worth mentioning that the computational efficiency of the proposed algorithm is strictly related to the number N_a and to the termination condition (i.e., the choice of the N_e points). Based on our numerical experience, we suggest N_a to be in the order of ten and $1 \leq N_e \leq 4$. The N_e points are chosen in anticipation of the subsequent N_a points by the implemented algorithm.
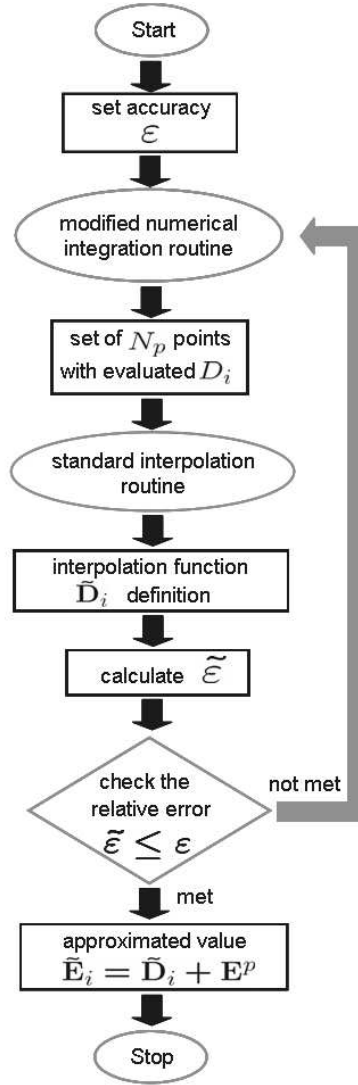
Figure 6.5: *Flow chart of the proposed numerical interpolation algorithm.*

6.3.3   Validation of the interpolation method

To validate the method described in Sec. 6.3.2, first we analyze the configuration of the two parallel wires studied in Sec. 6.3.1. In this case the root-mean-square (RMS) error $\overline{\zeta}_{\mathrm{cur}}$ is calculated as

$$
\overline{\zeta}_{\mathrm{cur}} = \sqrt{\frac{\int\limits_{z=0}^{h} \left| I(z) - \widetilde{I}(z) \right|^2 dz}{\int\limits_{z=0}^{h} \left| I(z) \right|^2 dz}}, \tag{6.34}
$$

where the reference value $I(z)$ is computed by following the second approach (i.e., $2 \times 2D$ integration) while the value $\widetilde{I}(z)$ is calculated by following the interpolation method. Results for a thin wire with length-radius ratio $h/a = 100$ and for thick wires with ratio $h/a = 30$ and $h/a = 20$ are given in Tables 6.5, 6.6 and 6.7, respectively.

Table 6.5: *RMS errors $\overline{\zeta}^1_{cur}$, $\overline{\zeta}^2_{cur}$ and computational cost analysis of two parallel thin wires $h/a = 100$ by varying the distance d.*

$d \, [\lambda]$	$\overline{\zeta}^1_{\text{cur}}$	$\overline{\zeta}^2_{\text{cur}}$	CPU Time ratio $(2 \times 2D):(\text{Interpol.})$
1	2.4×10^{-7}	2.4×10^{-7}	$8.34 : 1$
0.5	2.0×10^{-7}	2.0×10^{-7}	$6.32 : 1$
0.3	1.7×10^{-5}	1.9×10^{-6}	$5.55 : 1$

Table 6.6: *RMS errors $\overline{\zeta}^1_{cur}$, $\overline{\zeta}^2_{cur}$ and computational cost analysis of two parallel thin wires $h/a = 30$ by varying the distance d.*

$d \, [\lambda]$	$\overline{\zeta}^1_{\text{cur}}$	$\overline{\zeta}^2_{\text{cur}}$	CPU Time ratio $(2 \times 2D):(\text{Interpol.})$
1	1.1×10^{-6}	1.1×10^{-6}	$5.99 : 1$
0.5	2.3×10^{-6}	2.3×10^{-6}	$5.66 : 1$
0.3	1.5×10^{-5}	2.0×10^{-6}	$5.07 : 1$

Table 6.7: *RMS errors $\overline{\zeta}^1_{cur}$, $\overline{\zeta}^2_{cur}$ and computational cost analysis of two parallel thin wires $h/a = 20$ by varying the distance d.*

$d \, [\lambda]$	$\overline{\zeta}^1_{\text{cur}}$	$\overline{\zeta}^2_{\text{cur}}$	CPU Time ratio $(2 \times 2D):(\text{Interpol.})$
1	2.7×10^{-6}	2.7×10^{-6}	$5.84 : 1$
0.5	7.1×10^{-6}	7.1×10^{-6}	$4.99 : 1$
0.3	7.1×10^{-5}	1.0×10^{-5}	$4.57 : 1$

We observe that errors $\overline{\zeta}_{\mathrm{cur}}^{1}$ and $\overline{\zeta}_{\mathrm{cur}}^{2}$ are at least two orders of magnitude smaller than the ones computed when the 1D+2D integration approach is considered (see Tables 6.1, 6.2 and 6.3). Moreover, thanks to the interpolation technique, we achieve a reduction of a factor 6 with respect to the straightforward 2×2D integration. This reduction is about half the one achieved with the 1D+2D integration which places the radiating current on the wire axis.

Second, the case of two parallel thin wires of length $h = \lambda/2$ and radius $a = \lambda/1000$, placed at a distance d, is considered. Both wires are subdivided in $N+1$ segments and N rooftop functions are defined. For all the remaining test cases a delta-gap voltage source of 1 V placed in the middle of wire 1 is present. With a desired accuracy $\varepsilon = 10^{-3}$, the computation times required for evaluating the system matrix $\underline{\underline{Z}}$ by the straightforward double 2D integration and by the interpolation method are compared by varying the distance d and the number of expansion functions N. As can be observed in Table 6.8, the interpolation method greatly reduces the CPU time needed to calculate the impedance matrix even in case of a coarse discretization (e.g., $N = 10$). When the two wires are close to each other (e.g., $d \leq 0.1\lambda$) the computation time reduction can be appreciated only by refining the segmentation. As a matter of fact at small distances the function difference $\mathbf{D}_n$ may not be as smooth as when the distances are larger since the source field $\mathbf{E}_n$ differs from the point-dipole field $\mathbf{E}^p$.

Table 6.8: *Computational cost analysis of two parallel thin wires $h/a = 500$ by varying the distance d and the number of expansion functions N. Desired accuracy $\varepsilon = 10^{-3}$.*

d [λ]	CPU Time ratio $(2 \times 2$D Int$)$: (Interp)		
	$N = 68$	$N = 34$	$N = 10$
1	$10.12 : 1$	$10.09 : 1$	$7.00 : 1$
0.5	$10.14 : 1$	$9.34 : 1$	$5.00 : 1$
0.3	$8.72 : 1$	$7.45 : 1$	$3.28 : 1$
0.1	$5.31 : 1$	$1.32 : 1$	$0.046 : 1$

The number of field evaluations using the straightforward 2D integration and using the interpolation method is also analyzed. Figure 6.6 shows how the number of evaluations N_p required for the computation of coupling matrix $\underline{\underline{\mathbf{C}}}^{1,2}$ varies as a function of the desired

accuracy ε for the configuration depicted above of two parallel thin wires at a distance $d/\lambda = 0.5$ and discretized with 35 segments. Figure 6.6 shows that the total number of evaluations for the interpolation method is usually far less than for the integration, which results in a considerable reduction of computation time. Figure 6.6 also shows that increasing the accuracy in computing the electric field corresponds to an increase in the number of field evaluations N_p.
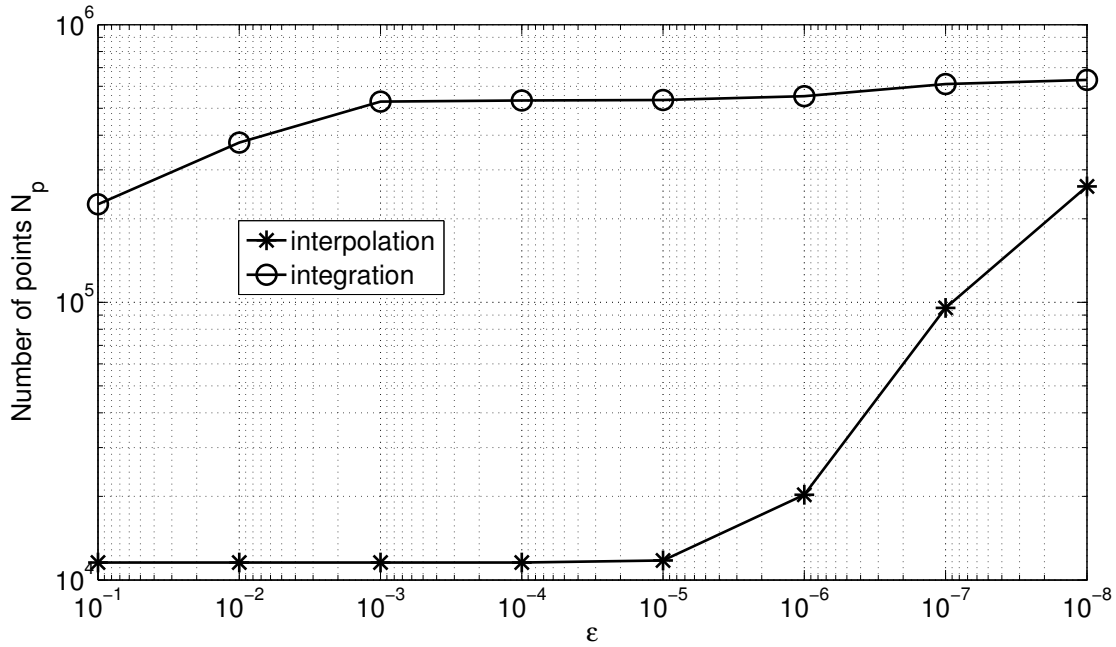
Figure 6.6: *Number of evaluations N_p required for the coupling matrix $\underline{\underline{C}}^{1,2}$ versus the desired accuracy ε for two parallel thin wires of length $h = \lambda/2$ and radius $a = \lambda/1000$ placed at a distance $d/\lambda = 0.5$ and discretized with 35 segments.*

Third, we compare the computation time for the case of two parallel mutually coupled thick wires. In this case $h = \lambda/2$, the radius $a = \lambda/60$, and the wires are equally discretized with $N + 1$ segments. A desired accuracy of $\varepsilon = 10^{-3}$ is defined. Table 6.9 again shows how the proposed method enhances the efficiency of computing coupling matrix elements even for thick wires.

Table 6.9: *Computational cost analysis of two parallel thick wires $h/a = 30$ by varying the distance d and the number of expansion functions N. Desired accuracy $\varepsilon = 10^{-3}$.*

d $[\lambda]$	CPU Time ratio $(2 \times 2D\ Int) : (Interp)$	
	$N = 50$	$N = 20$
1	$10.13 : 1$	$9.29 : 1$
0.5	$10.11 : 1$	$8.49 : 1$
0.3	$8.37 : 1$	$8.04 : 1$
0.1	$0.12 : 1$	$0.18 : 1$

Finally, two arbitrary oriented thin wires with $h_1 = \lambda/2$, $h_2 = 0.2236\lambda$ and radius $a_1 = a_2 = \lambda/1000$ are analyzed. The first and the second wires have end points

$$\mathbf{r}_1 = (0.3, 0.3, 0.5)\lambda, \qquad \mathbf{r}_2 = (0.3, 0.3, 1.0)\lambda, \qquad \text{(wire 1)},$$
$$\mathbf{r}_3 = (0.3, 0.7, 0.5)\lambda, \qquad \mathbf{r}_4 = (0.3, 0.8, 0.7)\lambda, \qquad \text{(wire 2)},$$

respectively. Again the CPU time comparison is carried out for different segmentations with a desired relative error $\varepsilon = 10^{-3}$. Note that the minimum and maximum distances between the two wires are $d_{\min} = 0.4\lambda$, $d_{\max} = 0.64\lambda$, respectively. Results for this case are shown in Table 6.10.

Table 6.10: *Computational cost analysis of two arbitrarily oriented thin wires $h/a = 500$, by varying the number of expansion functions N. Desired accuracy $\varepsilon = 10^{-3}$.*

N	CPU Time ratio $(2 \times 2D\ Int) : (Interp)$
68	$10.83 : 1$
34	$10.83 : 1$
10	$7.07 : 1$

6.4 Conclusions and discussion

In this chapter the electromagnetic coupling between arbitrary oriented wires has been analyzed. Coupling matrix elements are computed by following two different approaches:

- 1D+2D integration (i.e., radiating current along wire axis and 2D integral for the "observation" wire);

- $2 \times 2D$ integration (i.e., radiating current along the wire surface and 2D integral for the "observation" wire),

which are compared in terms of computation time and accuracy.

Results confirm that the thin-wire axis approximation (i.e., 1D+2D integration) is computationally less expensive than the straightforward $2 \times 2D$ integration. For the cases studied, a reduction of a factor about 14 in terms of CPU time is obtained. Moreover, we have observed that the RMS errors introduced by placing the radiating current on the wire axis are much smaller than the discretization error introduced by the GEKMoM numerical method (see Sec. 6.3.1 and Sec. 3.4.3).

For the approach which leaves the current along the mantle of the wire (i.e., $2 \times 2D$ integration) a numerically efficient interpolation algorithm has successfully been developed to reduce the CPU time required by the computation of the coupling-matrix elements. This algorithm might be useful in all cases where the thin-wire axis approximation breaks down and the full two-dimensional procedure is needed (see Sec. 6.1). Within a prescribed accuracy, coupling matrix elements can be computed more efficiently than by straightforward double integrations. This method is developed based on three main ideas elucidated in Sec. 6.3.2.

Numerical examples show that the proposed algorithm results in a reduction of the CPU time of a factor of 6 with respect to the straightforward $2 \times 2D$ integration. This reduction is comparable with the one achieved with the 1D+2D integration which places the radiating current on the wire axis. When the distance between the source and the observation element is small compared to the wavelength (e.g. $d \leq 0.1\lambda$) the smoothness of the function difference deteriorates and the advantages of the interpolation algorithm are lost. This is mainly due to the different behavior of the point-dipole field and the field radiated by a source element in the near-field region.

We can conclude that the deviation introduced by going from a $2 \times 2D$ integration to a 1D+2D integration is negligible compared with the discretization error introduced by applying the Method of Moments.

Chapter 7

Scattering from PEC objects

Until now, we have studied only the interaction between thin wires. As a next step, we want to bring surfaces into our model. To this end, in this chapter, we first consider the scattering of a single surface as such. In Chapter 8, we then arrive at the aim of the thesis, studying the electromagnetic behavior of structures consisting of wires, surfaces and wire-surface junctions. The effort in facing the problem of the scattering of a single surface has been limited to the implementation of existing formulations present in the literature [16, 17]. In this chapter, the problem of the electromagnetic scattering from an open surface is addressed. An Electric Field Integral Equation (EFIE) is introduced where the scattered field is written as a function of the unknown current distribution flowing on the surface. A numerical scheme similar to the one used for the wire-current computation, is followed here to solve the relevant EFIE.

Firstly, the surface of the object is discretized. A possible solution is the one proposed by [2, 67, 68] where a wire grid is used to model surfaces in terms of connected thin wires. Unfortunately, a surface can be modeled accurately only if many wires per wavelength are used (typically 20 wires per wavelength). The latter restricts the application of the wire-grid model. Another possibility is to employ a surface-patch (e.g., square, rectangle, triangle) modeling, which requires less unknowns per square wave length of area. In the modeling of arbitrarily shaped surfaces, planar triangular patches are particularly appropriate. They conform to many geometrical surfaces or boundaries and suitable expansion basis functions can be defined on them [16, 17]. It is noted that the resulting triangles are preferably as uniform in size and shape as possible, since this property may improve the capacity of solving the relevant integral equation [69]. In this thesis we mainly focus on the discretization of the pertinent EFIE, where an in-house developed simple mesh generator is used.

Secondly, the Galerkin Method of Moments (MOM) together with a Conjugate Gradient scheme is applied to solve the Electric Field Integral Equation. Taking advantage of the existing literature [16–19], we have implemented an efficient numerical method by using well-known RWG basis functions defined on triangular patches. Finally an expression for the electric field radiated by a current distribution flowing on the surface of the object is derived and some examples are shown.

7.1   Electric Field Integral Equation (EFIE)

In this section we derive an integral equation for the surface current induced on a perfectly electrically conducting scatterer by an incident electric field. Next, applying the Method of Moments (MoM) to the integral equation found, we derive an expression for each element of the MoM matrix using a particular set of basis and testing functions. This is performed in a similar fashion as described in [16, 70, 71].

We model an arbitrarily shaped open surface S (scatterer) as a perfectly electrically conducting (PEC) object. The unit vector normal to the interface S is represented by $\mathbf{i}_n$. The external medium has permittivity ε and permeability μ. We assume that an electric field $\mathbf{E}^i$, due to an impressed source, is present (in absence of the scatterer). This field is incident on the open surface S and induces surface currents $\mathbf{J}_s$ which radiate a field $\mathbf{E}^s$ expressed by

$$\mathbf{E}^s(\mathbf{r}) = -j\omega\mu\mathbf{A}(\mathbf{r}) + \frac{\nabla\left(\nabla\cdot\mathbf{A}(\mathbf{r})\right)}{j\omega\varepsilon}. \tag{7.1}$$

The vector potential is defined as

$$\mathbf{A}(\mathbf{r}) = \int_S G(\mathbf{r} - \mathbf{r}')\mathbf{J}_S(\mathbf{r}')dS(\mathbf{r}'), \tag{7.2}$$

and the Green's function of the Helmholtz operator in free space is

$$G(\mathbf{r} - \mathbf{r}') = \frac{\exp\left(-jk|\mathbf{r} - \mathbf{r}'|\right)}{4\pi|\mathbf{r} - \mathbf{r}'|}, \tag{7.3}$$

where $k = \omega\sqrt{\varepsilon\mu}$. The source point $\mathbf{r}'$ and the observation point $\mathbf{r}$ are both on the surface S. For the sake of simplicity, from now on, we refer to $dS(\mathbf{r}')$ as dS' and to $dS(\mathbf{r})$ as dS. Substituting expression (7.2) in (7.1), we obtain

$$\mathbf{E}^s(\mathbf{r}) = -j\omega\mu\int_{S'} G(\mathbf{r} - \mathbf{r}')\mathbf{J}_S(\mathbf{r}')dS' + \frac{1}{j\omega\varepsilon}\nabla\left(\nabla\cdot\int_{S'} G(\mathbf{r} - \mathbf{r}')\mathbf{J}_S(\mathbf{r}')dS'\right). \tag{7.4}$$

Next, by enforcing the boundary condition

$$\mathbf{i}_n \times \left(\mathbf{E}^s(\mathbf{r}) + \mathbf{E}^i(\mathbf{r})\right) = \mathbf{0}, \qquad \mathbf{r} \in S, \tag{7.5}$$

we derive the following integro-differential equation for $\mathbf{J}_S(\mathbf{r})$

$$\mathbf{i}_n \times \left[j\omega\mu \int\limits_{S'} G(\mathbf{r} - \mathbf{r}')\mathbf{J}_S(\mathbf{r}')dS' - \frac{1}{j\omega\varepsilon}\nabla \left(\nabla \cdot \int\limits_{S'} G(\mathbf{r} - \mathbf{r}')\mathbf{J}_S(\mathbf{r}')dS' \right) \right] = \mathbf{i}_n \times \mathbf{E}^i(\mathbf{r}), \tag{7.6}$$

valid for $\mathbf{r} \in S$. Equation (7.6) is referred to as the Electric Field Integral Equation (EFIE). For open surfaces (e.g., planar surfaces) this equation is sufficient to determine the unknown surface current $\mathbf{J}_S(\mathbf{r})$. The divergence in the second term on the left-hand side of equation (7.6) is applied along the surface, and represents a differentiation with respect to $\mathbf{r}$. It can be written as

$$\nabla \cdot \left(\int\limits_{S'} G(\mathbf{r} - \mathbf{r}')\mathbf{J}_S(\mathbf{r}')dS' \right) = \int\limits_{S'} (\nabla G(\mathbf{r} - \mathbf{r}')) \cdot \mathbf{J}_S(\mathbf{r}')dS'$$

$$= -\int\limits_{S'} (\nabla' G(\mathbf{r} - \mathbf{r}')) \cdot \mathbf{J}_S(\mathbf{r}')dS' = -\int\limits_{S'} (\nabla_{S'} G(\mathbf{r} - \mathbf{r}')) \cdot \mathbf{J}_S(\mathbf{r}')dS', \tag{7.7}$$

where ∇' expresses differentiation with respect to $\mathbf{r}'$ and $\nabla_{S'}$ indicates that the gradient operator is applied along the surface S'. Before proceeding, we focus on the following integral

$$\int\limits_{S'} \nabla_{S'} \cdot (G(\mathbf{r} - \mathbf{r}')\mathbf{J}_S(\mathbf{r}')) \, dS' = \int\limits_{S'} (\nabla_{S'} G(\mathbf{r} - \mathbf{r}')) \cdot \mathbf{J}_S(\mathbf{r}')dS'$$

$$+ \int\limits_{S'} G(\mathbf{r} - \mathbf{r}') (\nabla_{S'} \cdot \mathbf{J}_S(\mathbf{r}')) \, dS'. \tag{7.8}$$

Since the normal component of $\mathbf{J}_S$ is zero at the surface's boundaries, applying Gauss's theorem to the latter leads to

$$\int\limits_{S'} \nabla_{S'} \cdot (G(\mathbf{r} - \mathbf{r}')\mathbf{J}_S(\mathbf{r}')) \, dS' = \oint\limits_{C'} \mathbf{i}_b \cdot (G(\mathbf{r} - \mathbf{r}')\mathbf{J}_S(\mathbf{r}')) \, d\ell = 0, \tag{7.9}$$

where C' is the contour around the surface S' and $\mathbf{i}_b$ is the unit vector normal to the contour and pointing outward of the contour C'. Therefore, substituting this result in (7.8) yields

$$\int\limits_{S'} (\nabla_{S'} G(\mathbf{r} - \mathbf{r}')) \cdot \mathbf{J}_S(\mathbf{r}')dS' = -\int\limits_{S'} G(\mathbf{r} - \mathbf{r}') (\nabla_{S'} \cdot \mathbf{J}_S(\mathbf{r}')) \, dS'. \tag{7.10}$$

With the aid of the latter, we can simplify expression (7.7) as

$$
\nabla \cdot \left(\int\limits_{S'} G(\mathbf{r} - \mathbf{r}')\mathbf{J}_S(\mathbf{r}')dS' \right) = \int\limits_{S'} G(\mathbf{r} - \mathbf{r}') \left(\nabla_{S'} \cdot \mathbf{J}_S(\mathbf{r}') \right) dS'. \tag{7.11}
$$

Finally, thanks to the previous expression we write equation (7.6) as

$$
j\omega\mu \int\limits_{S'} G(\mathbf{r} - \mathbf{r}')\mathbf{J}_S(\mathbf{r}')dS' - \frac{1}{j\omega\varepsilon}\nabla_S \int\limits_{S'} G(\mathbf{r} - \mathbf{r}') \left(\nabla_{S'} \cdot \mathbf{J}_S(\mathbf{r}') \right) dS' = \mathbf{E}_S^i(\mathbf{r}), \qquad \mathbf{r} \in S,
$$

$$
\tag{7.12}
$$

where $\mathbf{E}_S^i = \mathbf{E}^i - (\mathbf{i}_n \cdot \mathbf{E}^i)\mathbf{i}_n$. In (7.12) we have restricted the equation to the surface components of the field $\mathbf{E}^i$. The gradient ∇ of the second integral on the left-hand side of (7.6) is reduced to a surface gradient ∇_S. The Green's function in (7.3) has a singular behavior when $\mathbf{r}$ approaches $\mathbf{r}'$. Thus, the integrands on the left-hand side of (7.12) are singular when the distance $\mathbf{r} - \mathbf{r}'$ approaches zero. Because of the presence of derivatives appearing in conjunction with a singularity, special care has to be taken in solving this equation and therefore in selecting the expansion functions and the testing procedure in the Method of Moments.

7.1.1   The Rao-Wilton-Glisson (RWG) function

The required set of basis functions should be chosen such that their linear combination can approximate the surface current with an acceptable accuracy. Since surface triangulation is used in discretizing the object under study, local basis functions having triangular patches as support are then chosen.

The well-known Rao-Wilton-Glisson (RWG) functions [16, 17] have these characteristics and are adopted as expansion functions in the Method of Moments. Each basis function $\boldsymbol{\psi}_n^B$ is defined on two adjoining triangles T_n^+ and T_n^- connected through the n-common edge of length ℓ_n as shown in Fig. 7.1. The plus or minus designation of the triangles is determined by choosing the positive surface current direction (associated with the n-common edge) to be from T_n^+ to T_n^-. All points on the RWG function can be designated either by the vector $\mathbf{r}_n^\pm$ with respect to the global coordinate system, or by the vector $\boldsymbol{\rho}_n^\pm$ in $T_n^\pm$ with respect to a coordinate system local to the triangle with origin in vertex $O_n^\pm$.

The n-th RWG function is defined by

$$
\boldsymbol{\psi}_n^B(\mathbf{r}) =
\begin{cases}
\dfrac{\ell_n}{2A_n^+}\boldsymbol{\rho}_n^+, & \mathbf{r} \in T_n^+, \\[2mm]
\dfrac{\ell_n}{2A_n^-}\boldsymbol{\rho}_n^-, & \mathbf{r} \in T_n^-, \\[2mm]
0, & \text{otherwise,}
\end{cases}
\tag{7.13}
$$

where $A_n^\pm$ is the area of triangle $T_n^\pm$.
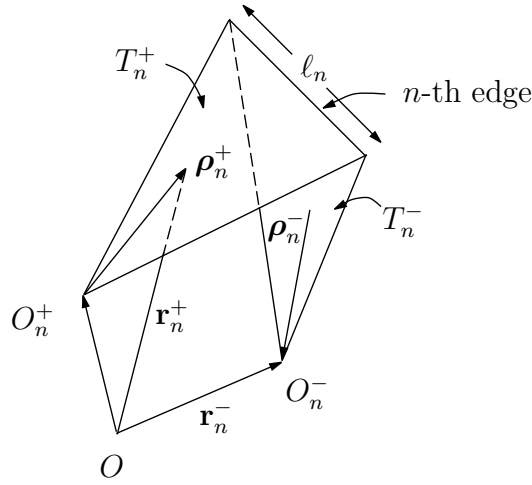
Figure 7.1: *Geometry of the nth RWG basis function.*

The current distribution has a component normal to the common edge ℓ_n, as shown in Fig. 7.2, and no line charges are present along this edge. Moreover, the current has no component normal to the boundary of the surface formed by the triangle pairs T_n^+ and T_n^- and no line charges are present along this boundary.
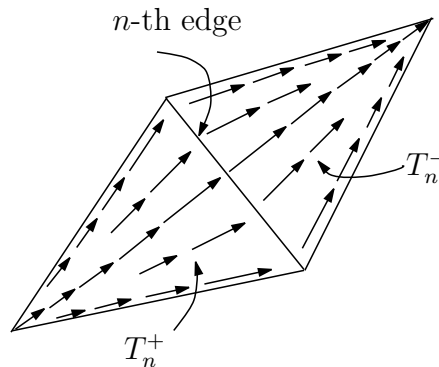
Figure 7.2: *Current flow over the nth RWG basis function from T_n^+ to T_n^-.*

A detailed description of the RWG function together with its properties can be found in [17], which is also summarized in Appendix E.

7.2   Matrix Equation

From the Electric Field Integral Equation (7.12), following a similar numerical scheme as we used for thin wires (see Sec. 3.1.1), we apply the Galerkin Method of Moments expanding the surface current density $\mathbf{J}_S(\mathbf{r}')$ in terms of RWG basis functions as

$$\mathbf{J}_S(\mathbf{r}') = \sum_{n=1}^{N} J_n \boldsymbol{\psi}_n^B(\mathbf{r}'), \tag{7.14}$$

where N is the number of edges not on the surface boundaries (i.e., non-boundary edges). Let us consider the n-th basis function $\boldsymbol{\psi}_n^B$ associated with the n-th non-boundary edge. We recall that the current distribution on this triangular domain has a component normal to the non-boundary edge and flows parallel to the other two edges. Substituting (7.14) in equation (7.12) leads to the approximate equation

$$j\omega\mu \sum_{n=1}^{N} J_n \int_{T_n^+ \cup T_n^-} G(\mathbf{r} - \mathbf{r}') \boldsymbol{\psi}_n^B(\mathbf{r}') dS'$$

$$-\frac{1}{j\omega\varepsilon} \sum_{n=1}^{N} J_n \nabla_S \int_{T_n^+ \cup T_n^-} G(\mathbf{r} - \mathbf{r}') \left(\nabla_{S'} \cdot \boldsymbol{\psi}_n^B(\mathbf{r}') \right) dS' = \mathbf{E}_S^i(\mathbf{r}). \tag{7.15}$$

At this stage, $\mathbf{r}$ can be any point on the surface S. Indeed the previous equation in N unknowns is infinitely overdetermined. To find a solution of (7.15), following the Method of Moments procedure we define the inner product

$$< \mathbf{f}(\mathbf{r}), \mathbf{g}(\mathbf{r}) > = \int_S \mathbf{f}^*(\mathbf{r}) \cdot \mathbf{g}(\mathbf{r}) dS, \tag{7.16}$$

where $\mathbf{f}(\mathbf{r})$ and $\mathbf{g}(\mathbf{r})$ are two general complex vector functions with $\mathbf{r} \in S$. The superscript $*$ indicates the complex conjugate. Now, we choose a finite set of RWG testing functions $\{\boldsymbol{\psi}_m^B\}_{m=1}^N$ with support $T_m^+ \cup T_m^-$ and we take the inner product (7.16) of equation (7.15)

with each $\boldsymbol{\psi}_m^B$. Since RWG functions are real-valued (i.e., $\left(\boldsymbol{\psi}_m^B\right)^* = \boldsymbol{\psi}_m^B$), it yields

$$j\omega\mu \sum_{n=1}^N J_n \int_{T_m^+ \cup T_m^-} \boldsymbol{\psi}_m^B(\mathbf{r}) \cdot \left(\int_{T_n^+ \cup T_n^-} G(\mathbf{r} - \mathbf{r}')\boldsymbol{\psi}_n^B(\mathbf{r}')dS' \right) dS +$$

$$-\frac{1}{j\omega\varepsilon} \sum_{n=1}^N J_n \int_{T_m^+ \cup T_m^-} \boldsymbol{\psi}_m^B(\mathbf{r}) \cdot \left(\nabla_S \int_{T_n^+ \cup T_n^-} G(\mathbf{r} - \mathbf{r}') \left(\nabla_{S'} \cdot \boldsymbol{\psi}_n^B(\mathbf{r}') \right) dS' \right) dS \qquad (7.17)$$

$$= \int_{T_m^+ \cup T_m^-} \boldsymbol{\psi}_m^B(\mathbf{r}) \cdot \mathbf{E}_S^i(\mathbf{r})dS, \qquad \text{with } m = 1, ..., N,$$

where $\boldsymbol{\psi}_n^B$ and $\boldsymbol{\psi}_m^B$ represent the n-th basis and m-th testing RWG function, respectively. A graphical representation of RWG functions is shown in Fig. 7.3.
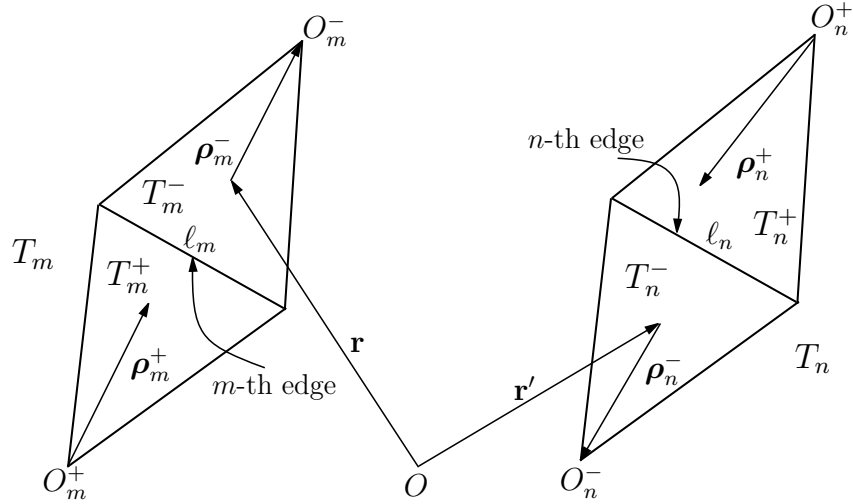
Figure 7.3: *Graphical representation of RWG functions used as basis and testing functions.*

The second integral on the left-hand side with respect to the primed coordinate is a scalar quantity depending solely on $\mathbf{r}$. Thus, applying the property

$$\int_{T_m^+ \cup T_m^-} \boldsymbol{\psi}_m(\mathbf{r}) \cdot \left(\nabla_S \int_{T_n^+ \cup T_n^-} G(\mathbf{r} - \mathbf{r}') \left(\nabla_{S'} \cdot \boldsymbol{\psi}_n(\mathbf{r}') \right) dS' \right) dS =$$

$$- \int_{T_m^+ \cup T_m^-} \left(\nabla_S \cdot \boldsymbol{\psi}_m(\mathbf{r}) \right) \int_{T_n^+ \cup T_n^-} G(\mathbf{r} - \mathbf{r}') \left(\nabla_{S'} \cdot \boldsymbol{\psi}_n(\mathbf{r}') \right) dS'dS, \qquad (7.18)$$

verified in Appendix E.2 for RWG functions, reduces the previous equation (7.17) to

$$
j\omega\mu \sum_{n=1}^{N} J_n \int\limits_{T_m^+ \cup T_m^-} \boldsymbol{\psi}_m^B(\mathbf{r}) \cdot \left(\int\limits_{T_n^+ \cup T_n^-} G(\mathbf{r} - \mathbf{r}') \boldsymbol{\psi}_n^B(\mathbf{r}') dS' \right) dS +
$$

$$
+ \frac{1}{j\omega\varepsilon} \sum_{n=1}^{N} J_n \int\limits_{T_m^+ \cup T_m^-} \left(\nabla_S \cdot \boldsymbol{\psi}_m^B(\mathbf{r}) \right) \int\limits_{T_n^+ \cup T_n^-} G(\mathbf{r} - \mathbf{r}') \left(\nabla_{S'} \cdot \boldsymbol{\psi}_n^B(\mathbf{r}') \right) dS' dS \qquad (7.19)
$$

$$
= \int\limits_{T_m^+ \cup T_m^-} \boldsymbol{\psi}_m^B(\mathbf{r}) \cdot \mathbf{E}_S^i(\mathbf{r}) dS, \qquad \text{with } m = 1, ..., N.
$$

Equation (7.19) can be expressed as a system matrix equation

$$
\underline{\underline{\mathbf{Z}}} \, \underline{\mathbf{I}} = \underline{\mathbf{F}}, \tag{7.20}
$$

where $\underline{\underline{\mathbf{Z}}} = [Z_{m,n}]$ is the $N \times N$ system matrix, $\underline{\mathbf{I}} = [J_n]$ is the unknown vector of current coefficients and $\underline{\mathbf{F}} = [F_n]$ is the known excitation vector. Substituting in equation (7.19) the explicit expression of RWG functions (7.13) and RWG functions' property (see Appendix E)

$$
\nabla_S \cdot \boldsymbol{\psi}_n(\mathbf{r}) = \begin{cases} \dfrac{\ell_n}{A_n^+}, & \mathbf{r} \in T_n^+, \\[2mm] -\dfrac{\ell_n}{A_n^-}, & \mathbf{r} \in T_n^-, \\[2mm] 0, & \text{otherwise,} \end{cases} \tag{7.21}
$$

we can write each matrix element $Z_{m,n}$ as

$$
Z_{m,n} = j\omega\mu \frac{\ell_m \ell_n}{4} \left[\frac{1}{A_m^+ A_n^+} \int\limits_{T_m^+} \int\limits_{T_n^+} \boldsymbol{\rho}_m^+ \cdot \boldsymbol{\rho}_n^+ G(\mathbf{r} - \mathbf{r}') dS' dS \right.
$$

$$
+ \frac{1}{A_m^+ A_n^-} \int\limits_{T_m^+} \int\limits_{T_n^-} \boldsymbol{\rho}_m^+ \cdot \boldsymbol{\rho}_n^- G(\mathbf{r} - \mathbf{r}') dS' dS + \frac{1}{A_m^- A_n^+} \int\limits_{T_m^-} \int\limits_{T_n^+} \boldsymbol{\rho}_m^- \cdot \boldsymbol{\rho}_n^+ G(\mathbf{r} - \mathbf{r}') dS' dS
$$

$$
+ \left. \frac{1}{A_m^- A_n^-} \int\limits_{T_m^-} \int\limits_{T_n^-} \boldsymbol{\rho}_m^- \cdot \boldsymbol{\rho}_n^- G(\mathbf{r} - \mathbf{r}') dS' dS \right] + \tag{7.22}
$$

$$
+ \frac{1}{j\omega\varepsilon} \ell_m \ell_n \left[\frac{1}{A_m^+ A_n^+} \int\limits_{T_m^+} \int\limits_{T_n^+} G(\mathbf{r} - \mathbf{r}') dS' dS - \frac{1}{A_m^+ A_n^-} \int\limits_{T_m^+} \int\limits_{T_n^-} G(\mathbf{r} - \mathbf{r}') dS' dS \right.
$$

$$
\left. - \frac{1}{A_m^- A_n^+} \int\limits_{T_m^-} \int\limits_{T_n^+} G(\mathbf{r} - \mathbf{r}') dS' dS + \frac{1}{A_m^- A_n^-} \int\limits_{T_m^-} \int\limits_{T_n^-} G(\mathbf{r} - \mathbf{r}') dS' dS \right].
$$

The vectors $\boldsymbol{\rho}_m^\pm = \boldsymbol{\rho}_m^\pm(\mathbf{r})$ and $\boldsymbol{\rho}_n^\pm = \boldsymbol{\rho}_n^\pm(\mathbf{r}')$ are defined on $T_m^\pm$ and $T_n^\pm$ and denote the position of the observation and the source points with respect to the vertices $O_m^\pm$ and $O_n^\pm$ opposite to the m-th and n-th non-boundary edge (see Fig. 7.3). Even though the expression (7.22) may seem complicated, since eight integrals are present, we observe that these integrations can be carried out systematically. Indeed the integrals in (7.22) have two different forms, scalar and vectorial respectively:

$$\text{Int}_a = \int\limits_{T} \int\limits_{T'} G(\mathbf{r} - \mathbf{r}') dS' dS, \tag{7.23}$$

$$\text{Int}_b = \int\limits_{T} \int\limits_{T'} \boldsymbol{\rho}_\alpha \cdot \boldsymbol{\rho}_\beta G(\mathbf{r} - \mathbf{r}') dS' dS = \int\limits_{T} \boldsymbol{\rho}_\alpha \cdot \int\limits_{T'} \boldsymbol{\rho}_\beta G(\mathbf{r} - \mathbf{r}') dS' dS, \tag{7.24}$$

where $T = T_m^\pm$, $T' = T_n^\pm$ are the m-th "observation" (test) triangle and the n-th "source" (basis) triangle, respectively. The position vectors $\boldsymbol{\rho}_\alpha = \boldsymbol{\rho}_\alpha(\mathbf{r})$, $\boldsymbol{\rho}_\beta = \boldsymbol{\rho}_\beta(\mathbf{r}')$ denote the "observation" and "source" points with respect to vertices α and β, see Fig. 7.4.
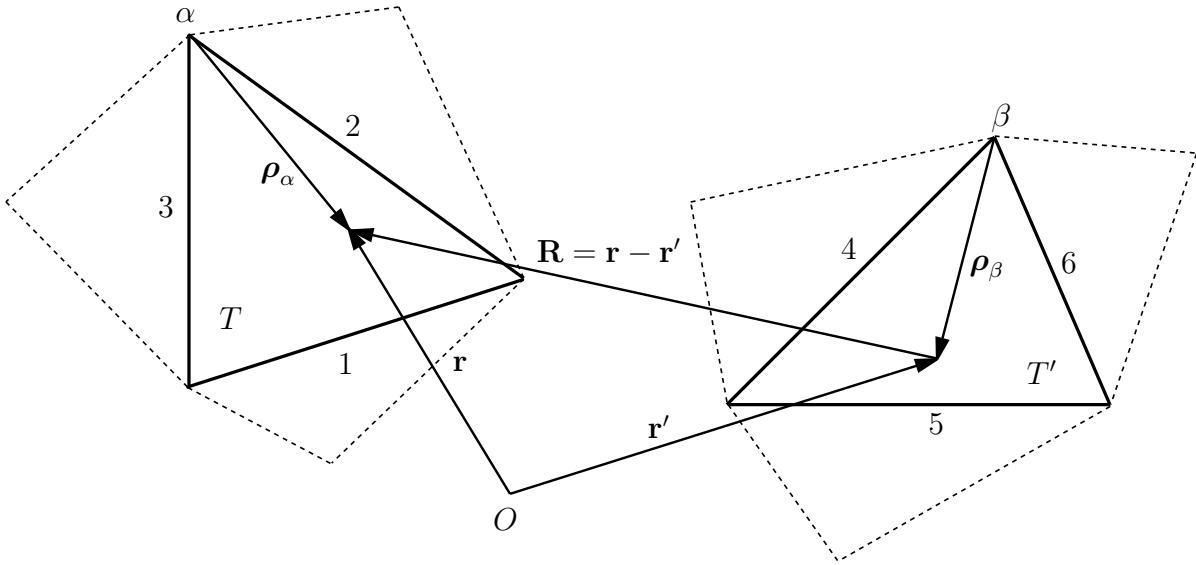
Figure 7.4: *Observation patch T' with associated edges 1, 2, 3 and source patch T with edges 4, 5, 6.*

To determine the integrals (7.23) and (7.24), they are transformed from the global Cartesian coordinate system to a local normalized coordinate system with the coordinate transformation defined in Appendix F.1 [72].

7.3   Efficient evaluation of system matrix elements

Since many triangles are needed when arbitrarily shaped scatterers are analyzed, the resulting number N^2 of matrix entries increases and the filling of the matrix $\underline{\underline{\mathbf{Z}}}$ will dominate the computation time. To minimize the computation time and have a fast algorithm, it is therefore important to efficiently evaluate each matrix element $Z_{m,n}$.

Let us consider pairs of triangular patches rather than pairs of edges. In Fig. 7.4 it is shown that each triangle is formed by three edges which means that three different RWG functions are involved. When a uniform triangular mesh can be applied, it is obvious that some integrals, computed for a certain matrix element and related to a certain triangular patch, can be reused in the determination of other matrix elements. In particular when we deal with open surfaces, all the integrals related to non-boundary patches can be reused, which allows a reduction in CPU time. Moreover, the use of the Galerkin Method of Moments leads to a symmetric system matrix $\underline{\underline{\mathbf{Z}}}$, which results in a CPU time reduction of almost fifty percent, since only the upper triangle matrix elements need to be computed.

7.3.1   Efficient evaluation of integrals

It is well-known that the Green's function $G(\mathbf{r} - \mathbf{r}')$ in (7.3) present in the integral forms (7.23) and (7.24) contains an integrable singularity when the distance $R = |\mathbf{r} - \mathbf{r}'|$ between the source and the observation point vanishes. For this reason, different approaches should be followed depending on the relative position between source triangle T and observation triangle T'. Referring to the integrals (7.23) and (7.24) we distinguish three situations.

- If T and T' coincide, this means that the integration is performed over the self patch and the distance R may become zero. Then, the integrands exhibit a singularity and are unbounded. An analytical integration is mandatory.

- If T and T' share an edge or vertex, the integrands are also unbounded. Therefore, if high accuracy is required, analytical integration of the singular terms is recommended.

- If T and T' are disjoint triangles, then the distance R is never zero and the integrands are bounded. Thus, the integrals Int_a (7.23) and Int_b (7.24) converge and are carried out numerically by a Gaussian quadrature rule over the triangular surface, see Appendix F.2.

To deal with the first two cases, we extract the singularity from the Green's function as follows

$$G(\mathbf{r} - \mathbf{r}') = [G(\mathbf{r} - \mathbf{r}') - G_{\text{sing}}(\mathbf{r} - \mathbf{r}')] + G_{\text{sing}}(\mathbf{r} - \mathbf{r}'). \tag{7.25}$$

The first term on the right-hand side is regular and is computed numerically, while the remaining singular integral is evaluated analytically. We employ the small-argument expansion of $\exp(-jkR)$ to obtain

$$G_{\text{sing}}(\mathbf{r} - \mathbf{r}') = \frac{1}{4\pi R} - \frac{k^2 R}{8\pi}, \qquad \text{with } R = |\mathbf{r} - \mathbf{r}'|. \tag{7.26}$$

The constant value $-jk/(4\pi)$ is not included since it does not depend on R and its contribution to the integration is constant. As suggested in [18], the expansion (7.26) contains two terms. In this way the regular term between brackets of (7.25) has two continuous derivatives at $R = 0$ and can be evaluated accurately with a Gaussian quadrature rule over the triangular surface also for integrals that involve a spatial derivative operating on the Green's function. Substituting the extracted singular term G_{sing} (7.26) into expressions (7.23) and (7.24) leads to the following integral forms

$$\text{Int}_a = \underbrace{\frac{1}{4\pi} \int\limits_{T} \int\limits_{T'} \frac{1}{R} dS' dS}_{=I_1} - \underbrace{\frac{k^2}{8\pi} \int\limits_{T} \int\limits_{T'} R dS' dS}_{=I_3}, \tag{7.27}$$

$$\text{Int}_b = \underbrace{\frac{1}{4\pi} \int\limits_{T} \boldsymbol{\rho}_\alpha \cdot \int\limits_{T'} \boldsymbol{\rho}_\beta \frac{1}{R} dS' dS}_{=I_2} - \underbrace{\frac{k^2}{8\pi} \int\limits_{T} \boldsymbol{\rho}_\alpha \cdot \int\limits_{T'} \boldsymbol{\rho}_\beta R dS' dS}_{=I_4}. \tag{7.28}$$

In case of coincident domains of integrations (i.e., source triangle T is identical to observation triangle T'), the integrals I_1 and I_2 are carried out analytically following the scheme proposed by Arcioni et. al. [19]. The surface integrals over T and T' are rewritten into contour integrals over the triangle boundaries C and C' by means of Stokes' theorem. Analytical expressions for these integrals are calculated in [19] and reported in Appendix F.3 for the sake of completeness. The evaluation of I_3 (7.27) and I_4 (7.28) is performed in two steps: the integral over the source triangle T' is expressed in a closed form via compact formulas as described in [18] and as reported in Appendix F.4. Subsequently, the integration over the observation triangle T is computed via the Gaussian quadrature rule for triangles, see Appendix F.2.

When the triangular patches are joined by an edge or a vertex, the integrand functions in (7.23) and (7.24) are nearly singular. In these cases, for all integrals in (7.27) and (7.28),

we calculate the integrals over the source triangle T' in closed form [18]. The subsequent integral over the observation triangle T is computed with the aid of a Gaussian quadrature rule.

In all other cases, that is when the observation patch T and the source patch T' are disjoint, the integration is carried out numerically employing a Gaussian quadrature rule specific for a triangular domain, see Appendix F.2.

7.4   Electric field radiated by a surface current distribution flowing on a PEC object

In this section we determine the electric field radiated by a surface current distribution $\mathbf{J}_S$ flowing along the surface of a perfectly electrically conducting object.

The electric field for a general volumetric current distribution $\mathbf{J}(\mathbf{r})$ is given by the expression

$$\mathbf{E}(\mathbf{r}) = \frac{1}{j\omega\varepsilon}\left(k^2\mathbf{A} + \nabla\left(\nabla\cdot\mathbf{A}\right)\right), \tag{7.29}$$

where the magnetic vector potential is given by

$$\mathbf{A}(\mathbf{r}) = \int\limits_{V_\infty} G(\mathbf{r}-\mathbf{r}')\mathbf{J}(\mathbf{r}')dV(\mathbf{r}') = \int\limits_{V_\infty} \frac{\exp(-jkR)}{4\pi R}\mathbf{J}(\mathbf{r}')dV(\mathbf{r}'), \qquad R = |\mathbf{r}-\mathbf{r}'|, \tag{7.30}$$

where $\mathbf{J}(\mathbf{r}')$ is the volume current density. In particular, for a current flowing along a surface of an object, the integral in (7.30) becomes a surface integral

$$\mathbf{A}(\mathbf{r}) = \int\limits_{S'} G(\mathbf{r}-\mathbf{r}')\mathbf{J}_S(\mathbf{r}')dS(\mathbf{r}') = \int\limits_{S'} \frac{\exp(-jkR)}{4\pi R}\mathbf{J}_S(\mathbf{r}')dS(\mathbf{r}'), \tag{7.31}$$

where $\mathbf{J}_S(\mathbf{r}')$ is a surface current density. In order to evaluate (7.29), we first have to explicitly determine $\nabla\cdot\mathbf{A}(\mathbf{r})$ and in particular the following differential operator applied to the Green's function

$$\begin{aligned}
\nabla G(\mathbf{r}-\mathbf{r}') &= \nabla\left(\frac{\exp(-jkR)}{4\pi R}\right) = \left[\partial_R\left(\frac{\exp(-jkR)}{4\pi R}\right)\right](\nabla R) \\
&= -(jkR+1)\frac{\exp(-jkR)}{4\pi R^2}\frac{\mathbf{r}-\mathbf{r}'}{R}.
\end{aligned} \tag{7.32}$$

Substituting expression (7.31) in (7.29) yields

$$\mathbf{E}(\mathbf{r}) = \frac{1}{j\omega\varepsilon}\left(k^2\int\limits_{S'} G(\mathbf{r}-\mathbf{r}')\mathbf{J}_S(\mathbf{r}')dS' + \nabla\left(\nabla\cdot\int\limits_{S'} G(\mathbf{r}-\mathbf{r}')\mathbf{J}_S(\mathbf{r}')dS'\right)\right), \tag{7.33}$$

where $dS' = dS(\mathbf{r}')$. Following the same steps (7.7)-(7.11) we can simplify (7.33) to an expression more suitable for numerical evaluation

$$\mathbf{E}(\mathbf{r}) = \frac{1}{j\omega\varepsilon} \left(k^2 \int_S G(\mathbf{r} - \mathbf{r}')\mathbf{J}_S(\mathbf{r}')dS' + \nabla \int_S G(\mathbf{r} - \mathbf{r}') \left(\nabla_{S'} \cdot \mathbf{J}_S(\mathbf{r}') \right) dS' \right). \tag{7.34}$$

The current is now expanded in terms of N RWG basis functions $\boldsymbol{\psi}_n^B(\mathbf{r})$ (see Sec. 7.2) as

$$\mathbf{J}_S(\mathbf{r}') = \sum_{n=1}^{N} J_n \boldsymbol{\psi}_n^B(\mathbf{r}'). \tag{7.35}$$

This leads to the following expressions for the magnetic vector potential

$$\mathbf{A}(\mathbf{r}) = \sum_{n=1}^{N} J_n \int_{T_n^+ \cup T_n^-} \boldsymbol{\psi}_n^B(\mathbf{r}')G(\mathbf{r} - \mathbf{r}')dS' = \sum_{n=1}^{N} J_n \int_{T_n^+ \cup T_n^-} \boldsymbol{\psi}_n^B(\mathbf{r}')\frac{\exp(-jkR)}{4\pi R}dS', \tag{7.36}$$

and for the radiated electric field

$$\mathbf{E}(\mathbf{r}) = \frac{1}{j\omega\varepsilon} \sum_{n=1}^{N} J_n \left(k^2 \int_{T_n^+ \cup T_n^-} \boldsymbol{\psi}_n^B(\mathbf{r}')G(\mathbf{r} - \mathbf{r}')dS' + \nabla \int_{T_n^+ \cup T_n^-} G(\mathbf{r} - \mathbf{r}') \left(\nabla_{S'} \cdot \boldsymbol{\psi}_n^B(\mathbf{r}') \right) dS' \right). \tag{7.37}$$

Writing the explicit RWG function expression (7.13) and its divergence as in (7.21), we write the latter as

$$\mathbf{E}(\mathbf{r}) = \frac{1}{j\omega\varepsilon} \sum_{n=1}^{N} J_n \ell_n \left[k^2 \int_{T_n^+} \frac{1}{2A_n^+}\boldsymbol{\rho}_n^+(\mathbf{r}')G(\mathbf{r} - \mathbf{r}')dS' + k^2 \int_{T_n^-} \frac{1}{2A_n^-}\boldsymbol{\rho}_n^-(\mathbf{r}')G(\mathbf{r} - \mathbf{r}')dS' \right.$$
$$\left. + \nabla \left(\frac{1}{A_n^+} \int_{T_n^+} G(\mathbf{r} - \mathbf{r}')dS' - \frac{1}{A_n^-} \int_{T_n^-} G(\mathbf{r} - \mathbf{r}')dS' \right) \right]. \tag{7.38}$$

Then, with the aid of the differential operator in (7.32), we write the final expression of the radiated electric field as follows

$$\mathbf{E}(\mathbf{r}) = \sum_{n=1}^{N} J_n \frac{\ell_n}{4\pi j\omega\varepsilon} \left[\frac{k^2}{2A_n^+} \int_{T_n^+} \boldsymbol{\rho}_n^+(\mathbf{r}')\frac{\exp(-jkR)}{R}dS' + \frac{k^2}{2A_n^-} \int_{T_n^-} \boldsymbol{\rho}_n^-(\mathbf{r}')\frac{\exp(-jkR)}{R}dS' \right.$$
$$\left. - \frac{1}{A_n^+} \int_{T_n^+} (1 + jkR)(\mathbf{r} - \mathbf{r}')\frac{\exp(-jkR)}{R^3}dS' + \frac{1}{A_n^-} \int_{T_n^-} (1 + jkR)(\mathbf{r} - \mathbf{r}')\frac{\exp(-jkR)}{R^3}dS' \right]. \tag{7.39}$$

The previous expression can be written in terms of the elementary electric field $\mathbf{E}_n(\mathbf{r})$ that is the radiated field by the surface current of the n-th RWG function

$$\mathbf{E}(\mathbf{r}) = \sum_{n=1}^{N} J_n \mathbf{E}_n(\mathbf{r}), \tag{7.40}$$

with

$$\begin{aligned}
\mathbf{E}_n(\mathbf{r}) &= \frac{\ell_n}{4\pi j\omega\varepsilon} \left[\frac{k^2}{2A_n^+} \int_{T_n^+} \boldsymbol{\rho}_n^+(\mathbf{r}')\frac{\exp(-jkR)}{R}dS' + \frac{k^2}{2A_n^-} \int_{T_n^-} \boldsymbol{\rho}_n^-(\mathbf{r}')\frac{\exp(-jkR)}{R}dS' \right. \\
&\quad - \frac{1}{A_n^+} \int_{T_n^+} (1+jkR)(\mathbf{r}-\mathbf{r}')\frac{\exp(-jkR)}{R^3}dS' \\
&\quad \left. + \frac{1}{A_n^-} \int_{T_n^-} (1+jkR)(\mathbf{r}-\mathbf{r}')\frac{\exp(-jkR)}{R^3}dS' \right].
\end{aligned} \tag{7.41}$$

This integral has been evaluated numerically by a seven-point Gaussian quadrature rule for triangles, Appendix F.2.

7.5   Numerical implementation

The numerical method presented has been implemented in a FORTRAN code referred to as Galerkin Method of Moments for Open Surface (GMoMOS) and used for the evaluation of the surface current distribution of open surfaces. As already pointed out, the first step in the discretization process is the generation of the triangular mesh in which N_p planar triangular surfaces, N_v vertices (or nodes) and N_e edges are defined. To this end a simple in-house developed mesh generator is used which is able to generate simple types of triangular meshes as in Fig. 7.5. Focusing on a planar rectangular surface of dimensions $L_x \times L_y$, N_x and N_y rectangular patches are defined along the x and y directions, respectively. Therefore $N_p = 2N_x N_y$ triangles and $N_v = (N_x + 1)(N_y + 1)$ vertices are also given, see Fig. 7.5. To analyze the scattering from open surfaces, the developed computer code needs, as input, information related to the geometrical representation of the surface. In particular the code requires two sets of input data. The first is an indexed list referred to as *vertex matrix* of position vectors in Cartesian coordinates $\mathbf{v}_i = x_i\mathbf{i}_x + y_i\mathbf{i}_y + z_i\mathbf{i}_z$, $i = 1, 2, ..., N_v$ of the i-th vertex with respect to the global coordinate system, where N_v is the total number of vertices. The second set of data is a *patch matrix*

$$\underline{P} = [p_{i,j}], \qquad i = 1, 2, ..., N_p, \; j = 1, 2, 3, \tag{7.42}$$

which gives for each i-th triangle the indices of the three delimiting vertices. The direction of the vector normal to the triangular patch is assigned by the writing order of these indices. We choose this direction such that the normal of all triangles points into the same direction.
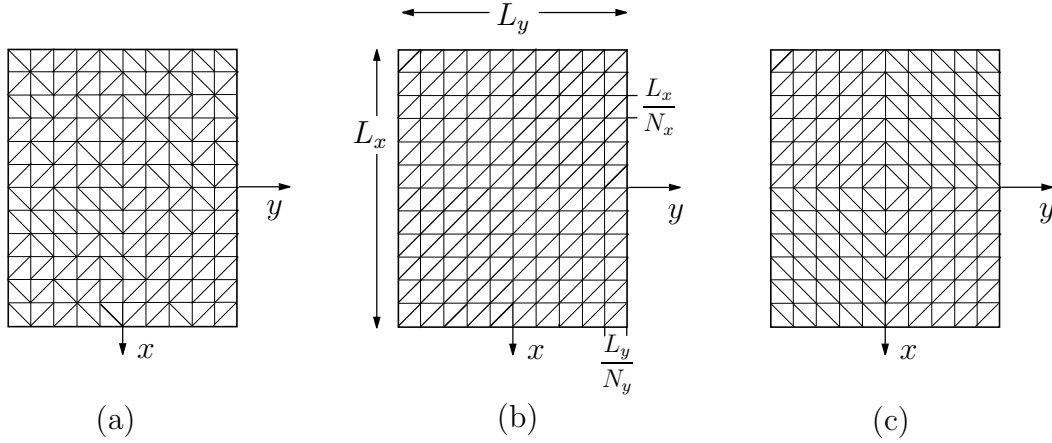
Figure 7.5: *Examples of triangular mesh of a planar surface: (a)- random; (b)- translational diagonal; (c)- rhombic.*

It is important to note that each element $Z_{m,n}$ of the system matrix $\underline{\underline{Z}}$ in equation (7.20) represents the electromagnetic interaction between the RWG testing function defined for the m-th edge and the RWG basis function defined for the n-th edge. This means that the system matrix $\underline{\underline{Z}}$ in (7.20) refers to edges, and the integrals involved in expression (7.22) are evaluated over the surface triangular patches. We therefore found it convenient to introduce a *patch-to-edge matrix*

$$\underline{\underline{F}} = [F_{i,j}], \qquad i = 1, 2, ..., N_p, \ j = 1, 2, 3, \tag{7.43}$$

in which the i-th row corresponds to the i-th triangle and the j-th column indicates the index of its j-th edge together with a $\pm$ sign for the associated current direction. In this way, the system matrix $\underline{\underline{Z}}$ can be filled by calculation of the three integrals associated with each triangle pair (i.e., each RWG function).

Special care has been taken in the implementation of the method to improve the efficiency of the FORTRAN code, as already mentioned. Focusing on the system matrix $\underline{\underline{Z}}$ in (7.20) we observe that off-diagonal elements represent the electromagnetic interaction between non-adjacent triangular patches, while elements belonging to a diagonal "band" describe the mutual interaction between self triangular patches or patches which share an edge or a vertex, see Fig. 7.6. In particular, only off-diagonal elements in the upper-triangular part of the matrix are evaluated. Thanks to the symmetry of the matrix $\underline{\underline{Z}}$, the off-diagonal

elements in the lower part then follow without further calculation. The evaluation of off-diagonal elements involves integrals that are never singular and are numerically calculated by a seven-point Gaussian rule, as described in Sec. 7.3. When the distance between the observation and the source patch becomes large (with respect to the wavelength), a midpoint integration rule could be preferred to the Gaussian rule. In these cases, thanks to a smooth behavior of the integrands within the triangular domains, the use of a midpoint rule could reduce the numerical complexity. However, this procedure is not implemented in our code. The evaluation of diagonal elements requires special attention due to the presence of a singularity, and a different approach is pursued (see Sec. 7.3).

upper off-diagonal part:
non-adjacent triangular patches

lower off-diagonal part:
non-adjacent triangular patches

diagonal band:
self triangular patches or
patches sharing an edge or
a vertex
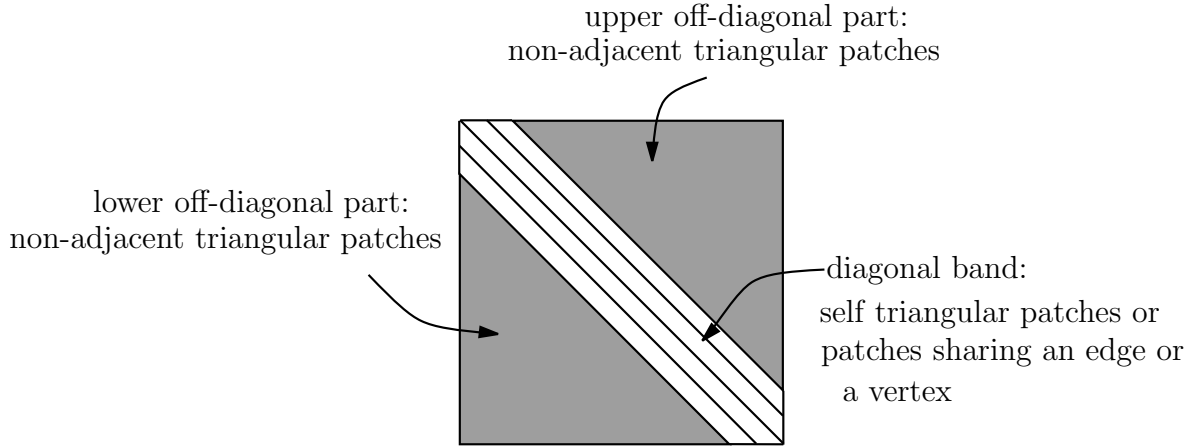
Figure 7.6: *Symmetric matrix* $\underline{\underline{\mathbf{Z}}}$.

Moreover, the evaluation of the matrix $\underline{\underline{\mathbf{Z}}}$ in (7.20) involves mainly two types of errors:

- errors due to the numerical calculation of the integrals (i.e., due to the numerical routine implemented);

- errors due to the geometry discretization (i.e., due to the type of triangular mesh, shape and size of triangles used).

To reduce the errors introduced by the geometrical discretization, triangles should be as uniform as possible in shape and in size, as suggested in [69]. Further, once the current coefficients J_n are evaluated, the FORTRAN code is capable of calculating the electric field radiated in a point $\mathbf{r}$ in the surrounding space.

7.6   Numerical results

In this section, the implemented code GMoMOS has been validated by means of some test cases.

7.6.1   Scattering by a PEC square plate

We consider here a square plate $L_x = L_y$ in free space, illuminated by a normally incident plane wave polarized along x, $|\mathbf{E}^i| = E_x = 1$ V/m, see Fig. 7.7.
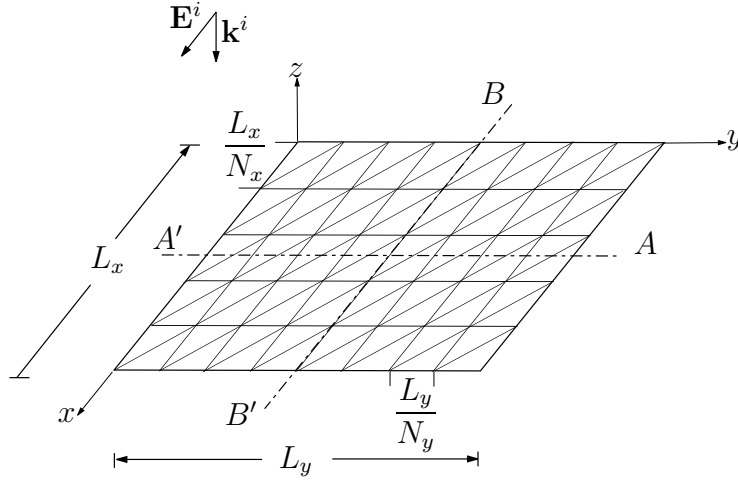
Figure 7.7: *Triangular mesh of a rectangular $L_x \times L_y$ plate.*

We compute the dominant component of the current distribution along the two principal cuts (i.e., cut along AA' and BB', see Fig. 7.7) for a $0.15\lambda \times 0.15\lambda$ and a $\lambda \times \lambda$ square plate, respectively. The evaluated current values are shown in Figs. 7.8 and 7.9 compared with those reported in [16] where both triangular and rectangular patches are used.
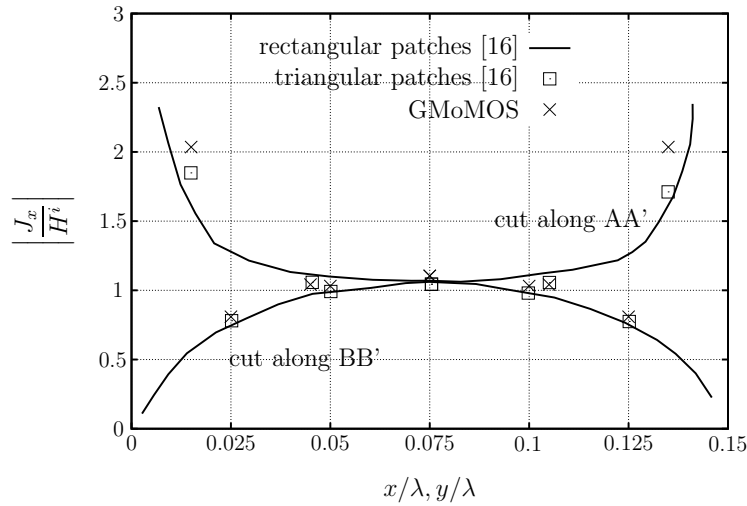
Figure 7.8: *Distribution of the dominant component of current on a $0.15\lambda \times 0.15\lambda$ square flat plate. Incident Plane wave: $|\mathbf{E}^i| = E_x = 1$ V/m, $H^i = |\mathbf{H}^i| = |\mathbf{E}^i|/\zeta_0$ where $\zeta_0 = 120\pi$ Ω is the free-space impedance. Discretization: $N_x = 6$, $N_y = 5$.*
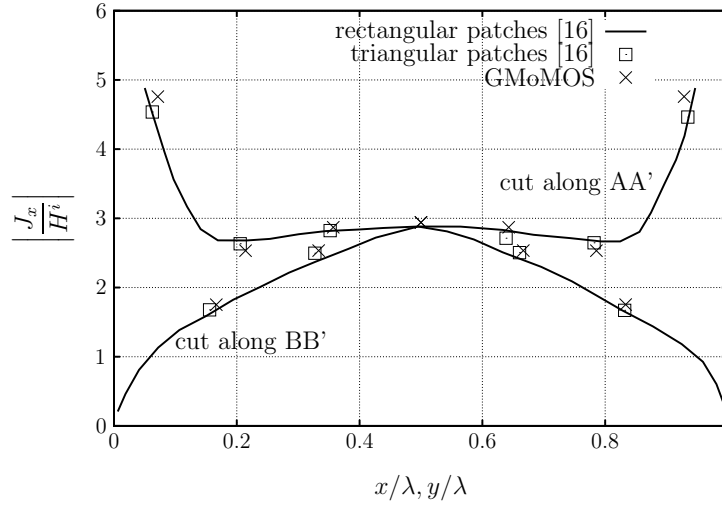
Figure 7.9: *Distribution of the dominant component of current on $\lambda \times \lambda$ square flat plate. Incident Plane wave:* $|\mathbf{E}^i| = E_x = 1$ V/m, $H^i = |\mathbf{H}^i| = |\mathbf{E}^i|/\zeta_0$ *where* $\zeta_0 = 120\pi$ Ω *is the free-space impedance. Discretization:* $N_x = 6$, $N_y = 7$.

These comparisons show a good agreement both for a $0.15\lambda \times 0.15\lambda$ Fig. 7.8 and a $\lambda \times \lambda$ square plate Fig. 7.9.

7.6.2   Induced electric current of a straight thin wire antenna

We consider here the simplest practical antenna, that is a straight thin wire. This antenna is modeled in two different ways: as a thin strip of infinitesimal thickness (Fig. 7.10-(a)) and as a cylindrical straight wire (Fig. 7.10-(b)). For both cases we evaluate the total current flowing along the straight wire antenna and we compare the results. A thin long strip of half a wavelength $(\lambda/2)$ and 0.05 m width is analyzed. A normally incident plane wave $\mathbf{E}^i$, of amplitude $|\mathbf{E}^i| = 1$ V/m and frequency $f = 75$ MHz, polarized along the direction of the antenna axis, impinges on the antenna. The cylindrical thin wire has the same length of $\lambda/2$ and a diameter d such that the lateral surface of the wire is equal to the strip surface (i.e., $d = w/\pi$, w being the strip width). We use 35 segments to discretize this cylindrical antenna and two different meshes (segmentations) for the strip model: $N_x = 35$, $N_y = 1$ and $N_x = 35$, $N_y = 5$, where N_x and N_y are the number of subintervals for the x- and y-coordinates.

The code used for the cylindrical thin wire model gives, as output, the total current distribution in Ampère (A, see Chapter 3), while the code used for the strip model gives the surface current density expressed in A/m. Therefore, in order to compare the results obtained with the two models, a numerical integration along the strip width is carried out

PSfrag replacements

(a)   (b)
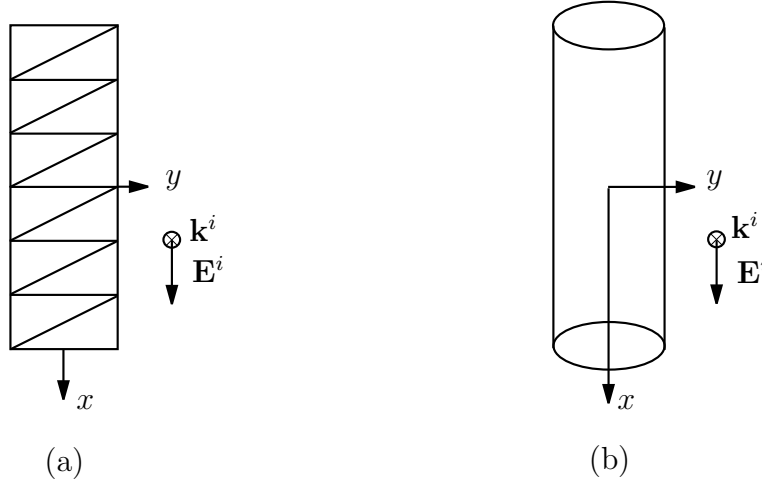
Figure 7.10: *Two different models of a thin-wire antenna: (a)- surface thin-strip model with RWG functions; (b)- cylindrical straight thin wire.*

to estimate its total surface current. Figure 7.11 shows a good agreement in the amplitude and in the phase of the resulting total current flowing along the antenna for the two different models and the different meshes. We can observe that increasing the number of RWG functions used (i.e., from $N_y = 1$ to $N_y = 5$) in the strip model leads to a better agreement in the phase of the current.

(a)   (b)
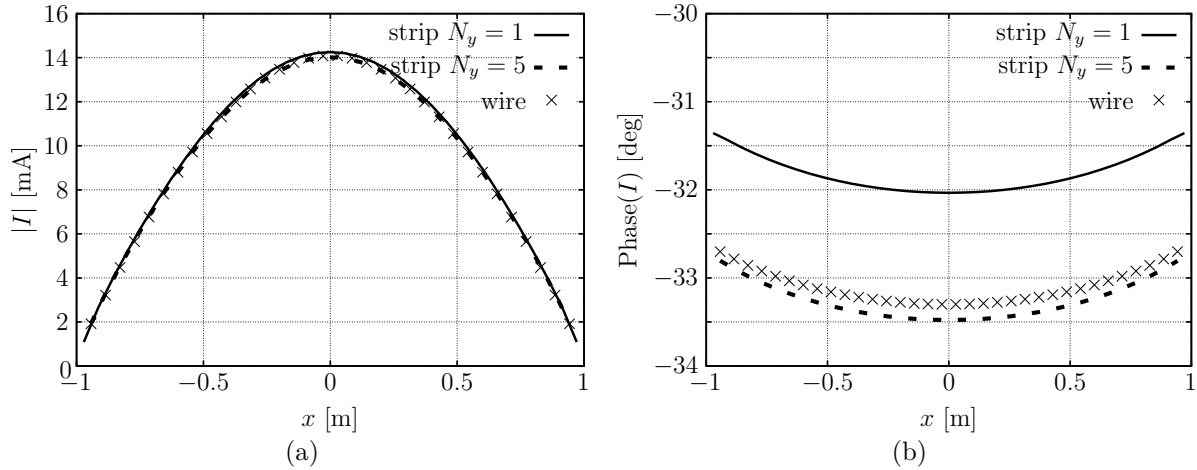
Figure 7.11: *Total current along the strip and along the wire: (a)- magnitude; (b)- phase.*

The strip wire model has also been validated by comparing the surface current density results with those described in the literature [73, pag. 25-28], and reported in Fig. 7.12, while Fig. 7.13 shows results by GMoMOS. For both these qualitative pictures, a lighter color corresponds to a higher current magnitude. To have a more quantitative result, we

have calculated the maximum value in the middle of the strip $J_{x\ \text{MAX}} = 0.2851$ A/m and compared this value with the one reported in [73], $J_{x\ \text{MAX}} = 0.2855$ A/m.
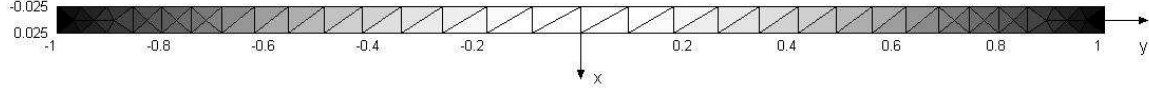
Figure 7.12: *Magnitude of the surface current density along the half-wavelength strip, as in [73]. The x- and y-axes are in meter.*
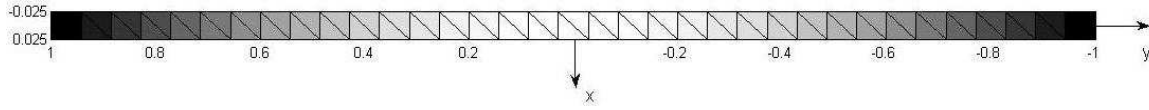
Figure 7.13: *Magnitude of the surface current density along the half-wavelength strip as evaluated by GMoMOS. The dipole strip is modeled using a discretization of $N_x = 35$ and $N_y = 1$. The x- and y-axes are in meter.*

7.6.3   Considerations on RWG functions

At this point, some useful considerations on the way of plotting surface currents seem in order. The surface current density is defined everywhere on the surface and can be evaluated from the current coefficients J_n. In particular, we evaluate the surface current in two different sets of points as shown in Fig. 7.14.

(a)   (b)
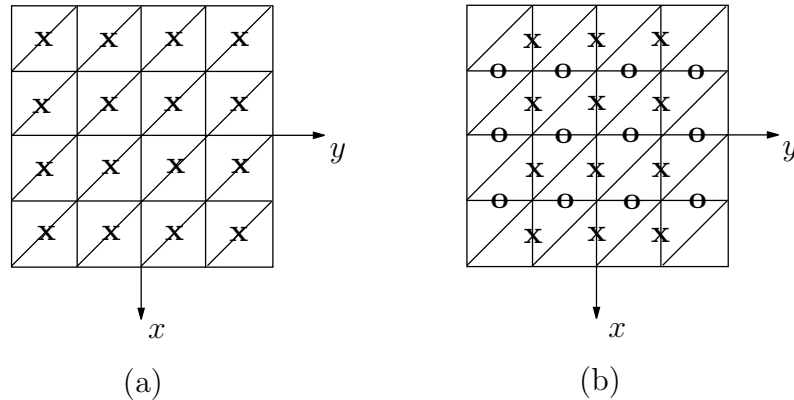
Figure 7.14: *Different sets of points: (a)- points on the diagonal edges (i.e., symbol (x)): points for the evaluation of both J_x and J_y components; (b)- points on the horizontal and vertical edges: points for the evaluation of J_x (i.e., symbol (o)); points for the evaluation of J_y (i.e., symbol (x)).*

The grid points in Fig. 7.14-(a) are located on diagonal edges of the patches. Whereas in Fig. 7.14-(b) the points lie on the horizontal and vertical edges. We study the case of a $\lambda \times \lambda$ square plate excited by a normally incident plane wave, x-polarized ($|\mathbf{E}^i| = E_x = 1$ V/m), discretized with 1058 triangular patches (i.e., $N_x = N_y = 23$), and we plot the x- and y-components of the surface current for the two different grids of points. Figure 7.15 shows the amplitudes of the dominant J_x and non-dominant J_y current components in the sample points on the diagonal edges (Fig. 7.14-(a)). While, in Fig. 7.16, the amplitudes of J_x and J_y are evaluated in the sample points on the horizontal and vertical edges as in Fig. 7.14-(b). In particular, at first glance, Fig. 7.15 shows an incorrect physical behavior near the edge $y = \pm 0.5$ for the non-dominant component J_y (i.e., it seems that this current flows off the surface). However this behavior is not noticeable in the x-component (Fig. 7.15) since this component is one order of magnitude larger than J_y. The explanation for the behavior of J_y in Fig. 7.15 is related to the type of basis functions used (i.e., RWG functions) and to the grid of points chosen to represent the current. Indeed, the grid of points used does not include points on the boundary edges $y = \pm 0.5$ where the current goes to zero. Moreover the root-like behavior of the current along this edge cannot be reproduced by a piecewise-linear approximation given by RWG functions. The computed values are in agreement with the results presented in [70] and in [74] where the Locally Corrected Nyström method has been used as alternative to the Method of Moments. Moreover, we notice that when a different grid of points is used to represent the current, like the one in Fig 7.14-(b), the incorrect behavior in J_y is not present (see Fig. 7.16) because the RWG functions have no component parallel to the edges $y = \pm 0.5$. In the following, more investigations have been done by refining the discretization. In particular, we evaluate the amplitude of the non-dominant current component J_y along the cut $x = 0.28\lambda$ for two different discretizations: $N_x = N_y = 23$ and $N_x = N_y = 41$. The current J_y is calculated for the two different grids of points in Fig. 7.14-(a) and Fig. 7.14-(b) symbol (x). As we can observe in Fig. 7.17, refining the mesh reduces the amplitude of J_y near the edges $y = \pm 0.5$ (e.g., from 0.338 mA/m to 0.252 mA/m) for values of the current in the points of Fig. 7.14-(a). Figure 7.18 shows the amplitude of J_y in the points of Fig. 7.14-(b) when the discretization is refined from $N_x = N_y = 23$ to $N_x = N_y = 41$. In this case the current goes smoothly to zero. Indeed, in the grid points of Fig. 7.14-(a), where the values of the current J_y are calculated, the RWG functions have a component in the y-direction, while in the grid points of Fig. 7.14-(b) no component in the y-direction is present, see Fig. 7.19.

PSfrag replacements

J_x

PSfrag replacements

J_x
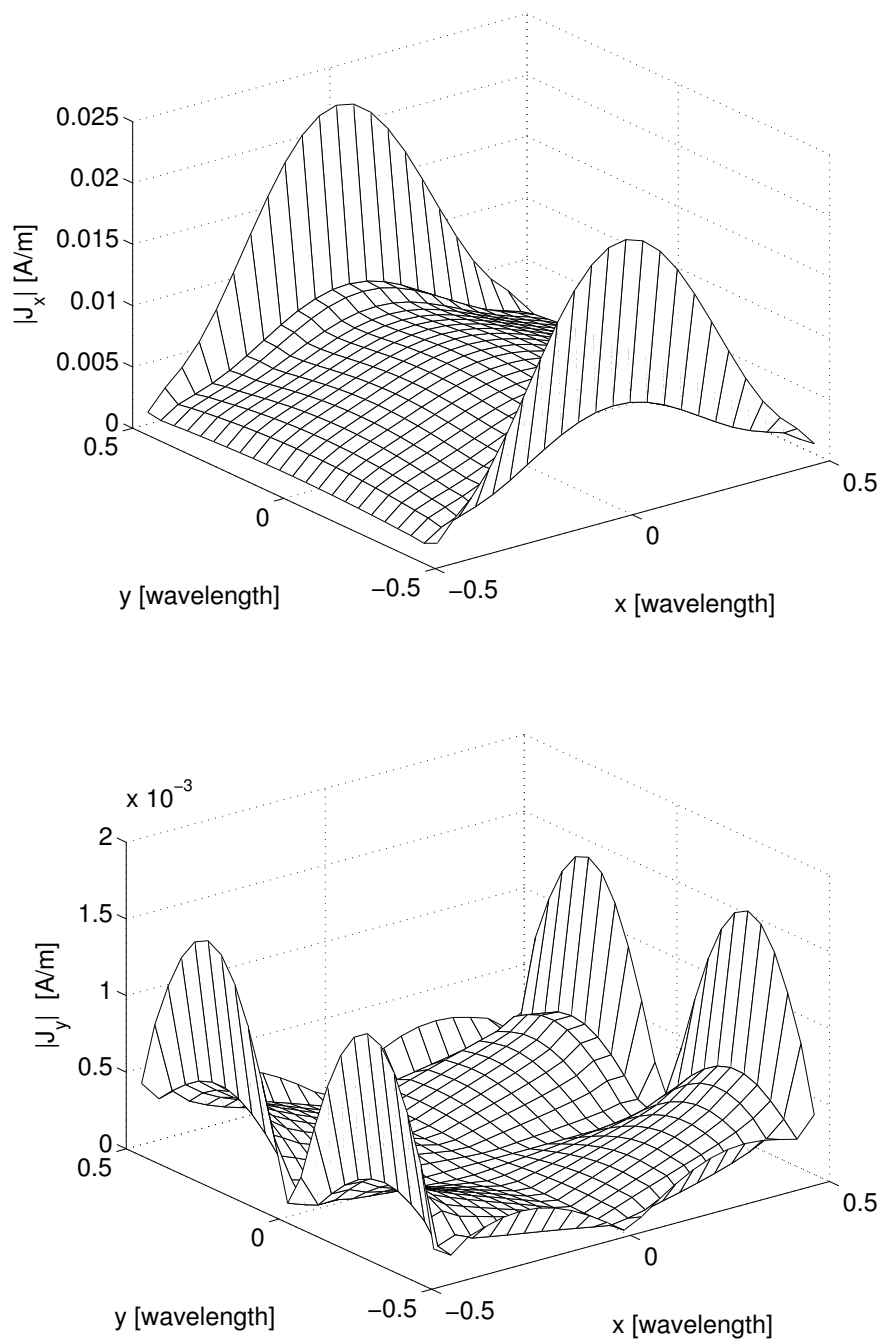
Figure 7.15: *x-component and y-component of surface current distribution in the set of points in Fig. 7.14-(a).*
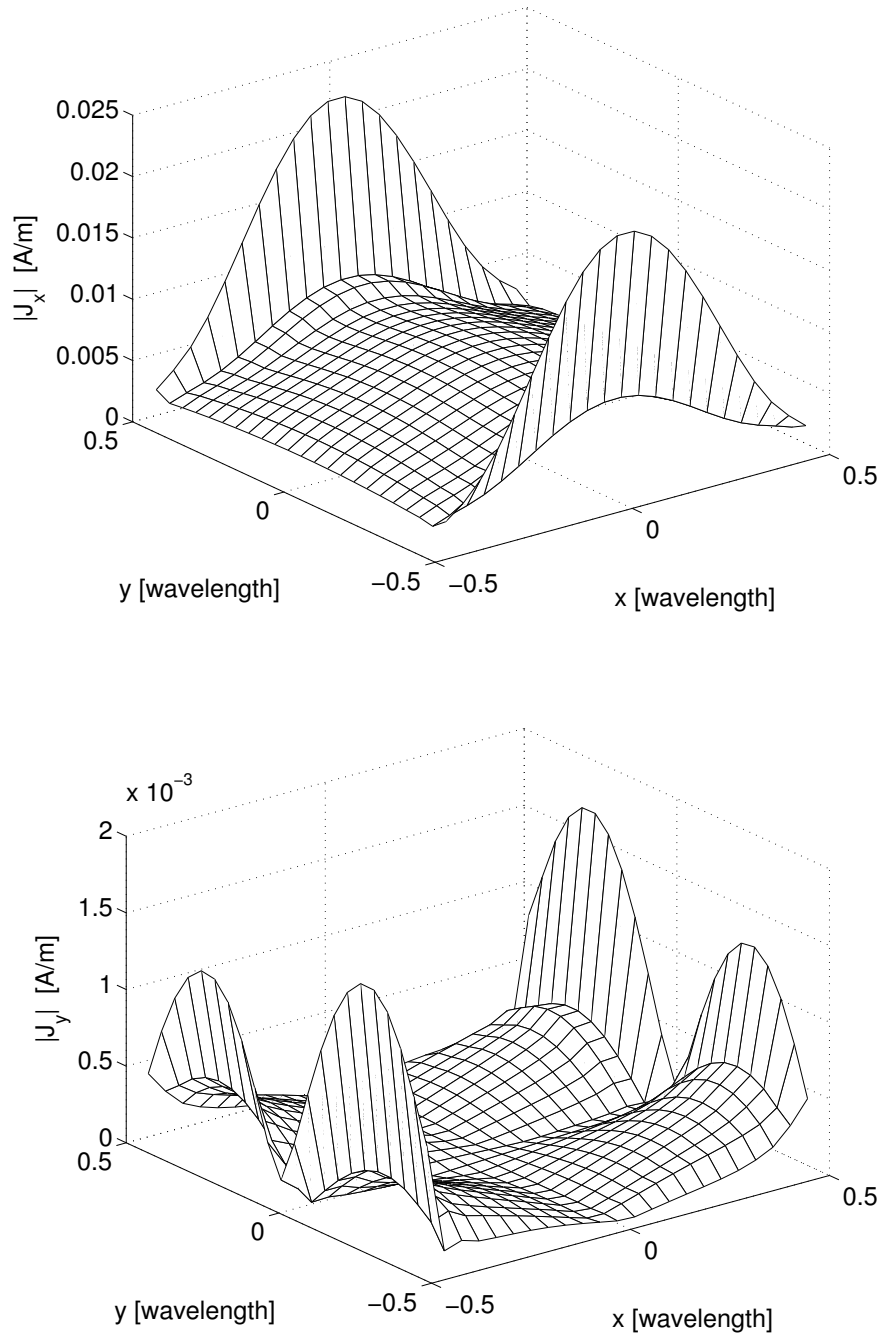
Figure 7.16: *x-component of surface current distribution in the set of points in Fig. 7.14-(b), symbol* (o)*; y-component of surface current distribution in the set of points in Fig. 7.14-(b), symbol* (x)*.*
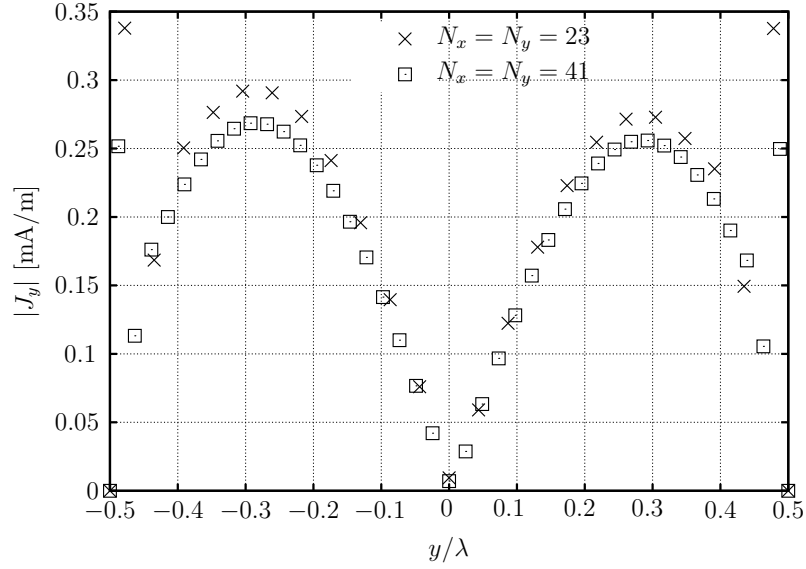
Figure 7.17: J_y component along a cut in $x = 0.28\lambda$ in the set of points of Fig. 7.14-(a), for two different discretizations $N_x = N_y = 23$ and $N_x = N_y = 41$.
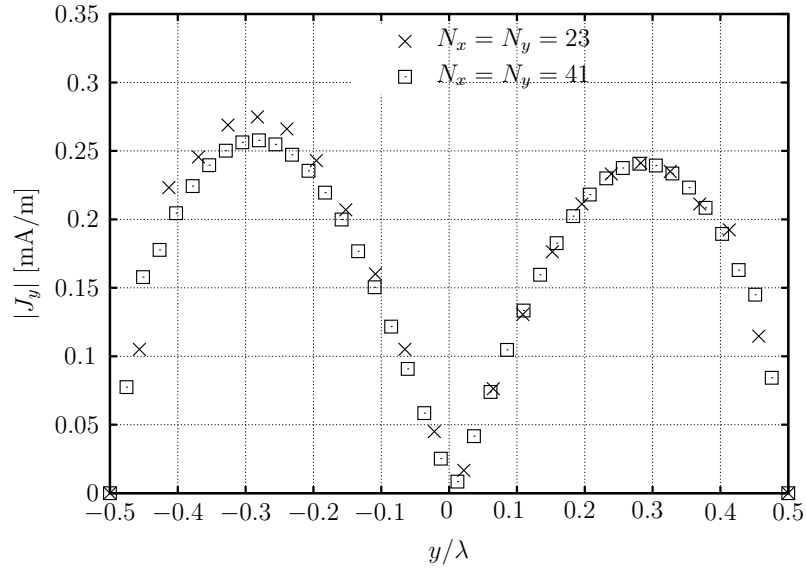
Figure 7.18: J_y component along a cut in $x = 0.28\lambda$ in the set of points of Fig. 7.14-(b) symbol (x), for two different discretizations $N_x = N_y = 23$ and $N_x = N_y = 41$.
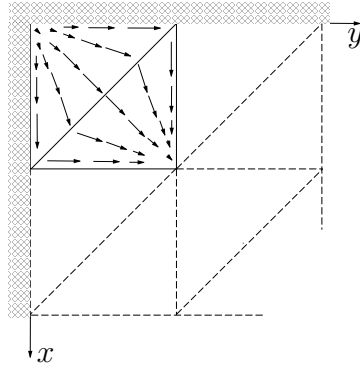
Figure 7.19: *Behavior of RWG edge functions at a boundary edge.*

When an arbitrary polarized incident field is considered, the two components J_x and J_y are of the same order of magnitude and the "non-physical" behavior along the opposite edge (i.e., y and x respectively) is no longer visible. Figures 7.20 and 7.21 show the amplitudes of the two current components J_x and J_y, respectively, when a $\lambda \times \lambda$ square plate illuminated by a plane wave polarized at 45°, $E_x = E_y = \sqrt{2}/2$ V/m is analyzed. A discretization of $N_x = N_y = 23$ (i.e., 1028 triangular patches) is used and the grid of points in Fig. 7.14-(a) are used to plot the current.
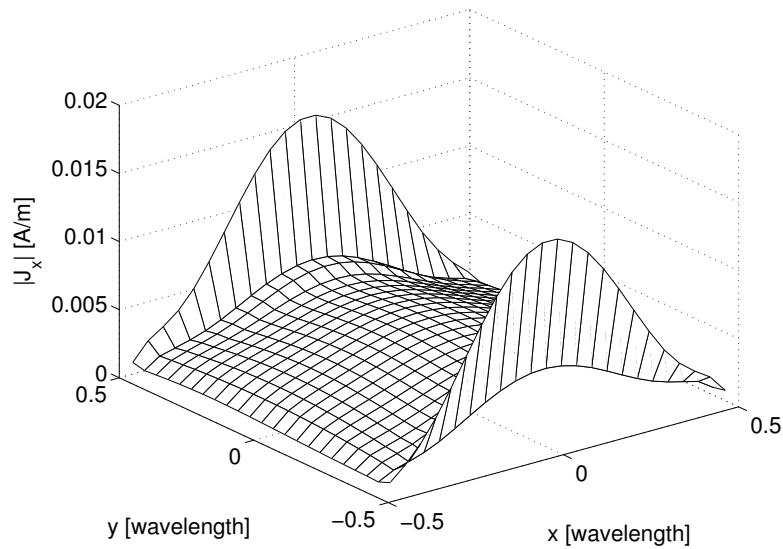
Figure 7.20: *x-component of the surface current distribution in the grid of points of Fig. 7.14-(a).*
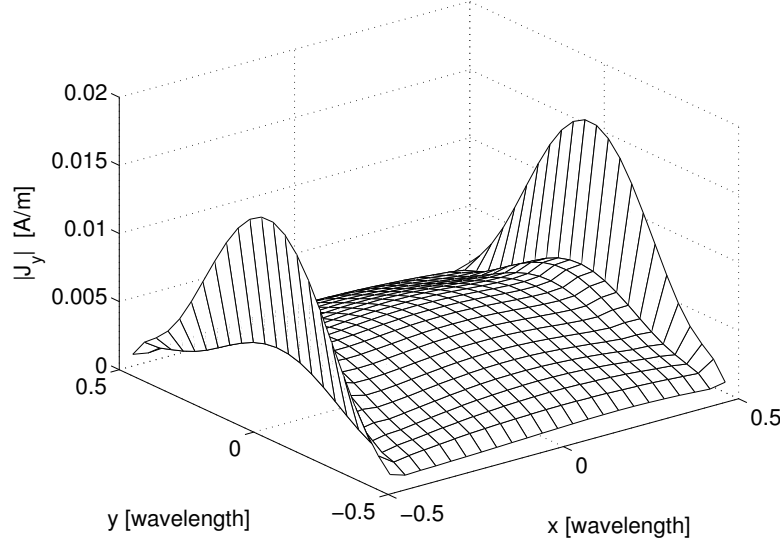
Figure 7.21: *y-component of the surface current distribution in the grid of points of Fig. 7.14-(a).*

We conclude that not only the way electric current distributions are calculated is important, also the way these results are presented requires a careful interpretation.

7.6.4 Field radiated by a current on a PEC rectangular plate

As previously mentioned, the numerical FORTRAN code implemented is capable of computing the electric field radiated by a given surface current J_S in an arbitrary point $\mathbf{r}$ in the surrounding space. To validate the code, we have evaluated the electric field radiated by a $\lambda \times \lambda$ square PEC planar surface (with $\lambda = 1$ m), discretized using a triangular mesh with a rhombic symmetry, see Fig. 7.22. The number of triangles is equal in both directions $N_x = N_y = 16$ and a normally incident plane wave of amplitude $|\mathbf{E}^i| = 1$ V/m polarized in the x-direction illuminates the plate, Fig. 7.22. The configuration is symmetric in both directions. The expected current distribution, however is symmetric in the x-direction and antisymmetric in the y-direction. From the evaluated current coefficients, we calculate the radiated electric field on an observation plane at a distance of 10 cm (i.e., $\lambda/10$) from the square plate (see Sec .7.4). Our results are compared with the ones obtained by running NEC 4.1. It is worth mentioning that NEC models the radiating surface as a wire grid [2] (in this case we use 21 wires parallel to the x-direction and 21 wires parallel to the y-direction spaced with $d_w = \lambda/20$ and with radius $a = d_w/2\pi$), while GMoMOS uses a triangular patch discretization. Figure 7.22 shows the geometry of the problem.

(a)   (b)
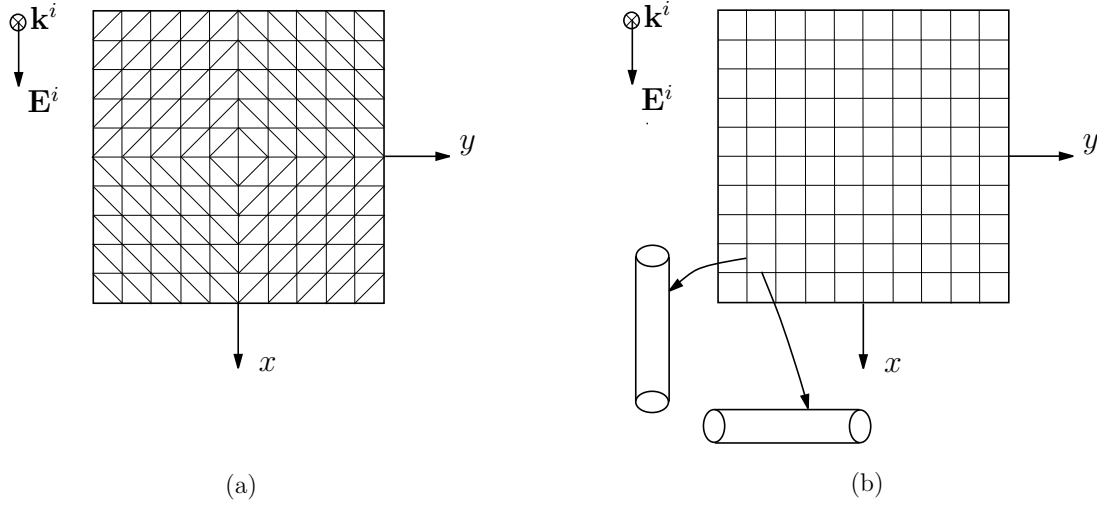
Figure 7.22: *Different discretization: (a)- with triangular patches as in GMoMOS; (b)-with a wire grid as in NEC 4.1.*

Figures 7.23 and 7.24 show results by our numerical method and by NEC 4.1, both for the amplitude and the phase of the dominant component of the radiated field E_x. As can be seen in Figs. 7.25, 7.26 and 7.27, 7.28, a good agreement is also present for the two non-dominant components E_y and E_z of the radiated field. The amplitude of the three components of the field calculated with the two models (GMoMOS and NEC 4.1) are compared and the contour plots of their differences are shown in Figs. 7.29, 7.30 and 7.31. Moreover, we note that for a generic observation point $\mathbf{r}$ in the space outside the surface domain, the electric field, radiated by the current flowing on the surface, should satisfy the property

$$\nabla \cdot \mathbf{E}(\mathbf{r}) = 0, \tag{7.44}$$

which can also be written as

$$\partial_x E_x(\mathbf{r}) + \partial_y E_y(\mathbf{r}) + \partial_z E_z(\mathbf{r}) = 0. \tag{7.45}$$

Choosing an "infinitesimal interval" Δ, a generic observation point $\mathbf{r} \equiv (x_0, y_0, z_0)$, and approximating the derivative in (7.45) as

$$\partial_x E_x \;=\; \frac{E_x(x_0 + \Delta, y_0, z_0) - E_x(x_0 - \Delta, y_0, z_0)}{2\Delta}, \tag{7.46}$$

$$\partial_y E_y \;=\; \frac{E_y(x_0, y_0 + \Delta, z_0) - E_y(x_0, y_0 - \Delta, z_0)}{2\Delta}, \tag{7.47}$$

$$\partial_z E_z \;=\; \frac{E_z(x_0, y_0, z_0 + \Delta) - E_z(x_0, y_0, z_0 - \Delta)}{2\Delta}, \tag{7.48}$$

we have verified that the property (7.44) is satisfied for our results up to the 3-rd decimal and for NEC results up to the 1-st decimal.

(a)   (b)
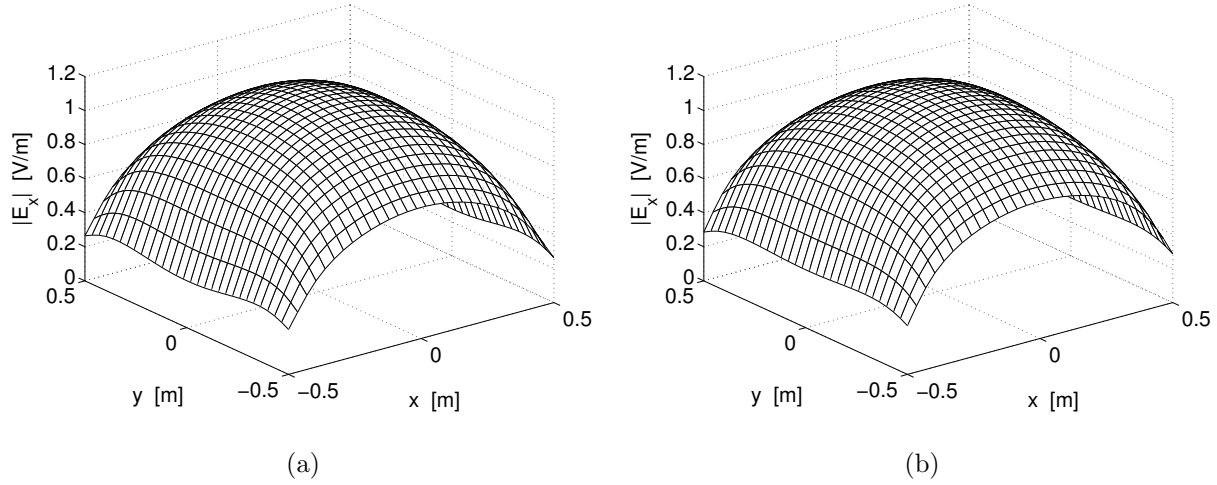
Figure 7.23: *Amplitude of x-component of the radiated electric field as evaluated: (a)- with GMoMOS; (b)- with NEC 4.1.*

(a)   (b)
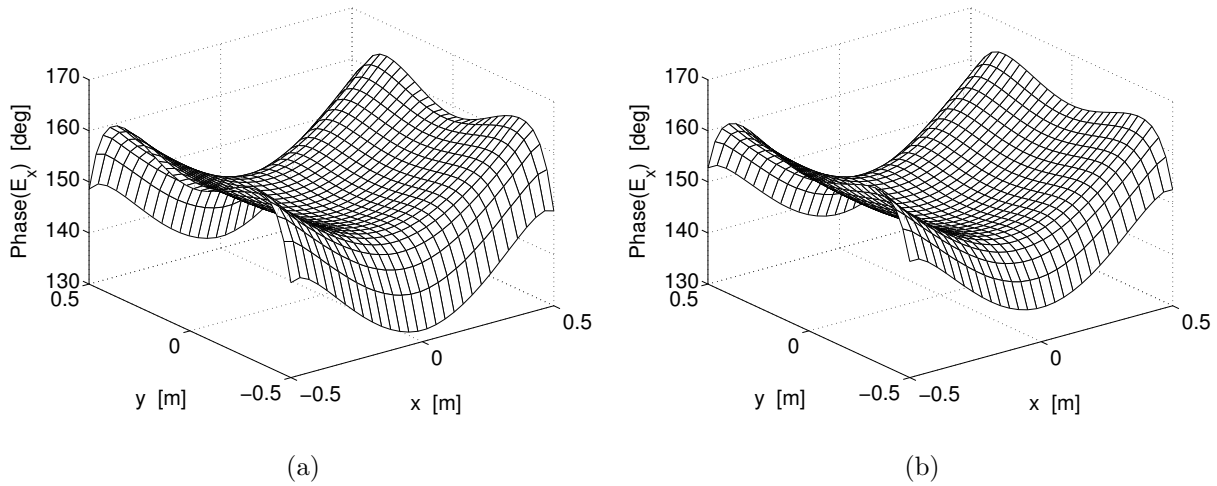
Figure 7.24: *Phase of x-component of the radiated electric field as evaluated: (a)- with GMoMOS; (b)- with NEC 4.1.*

(a)   (b)
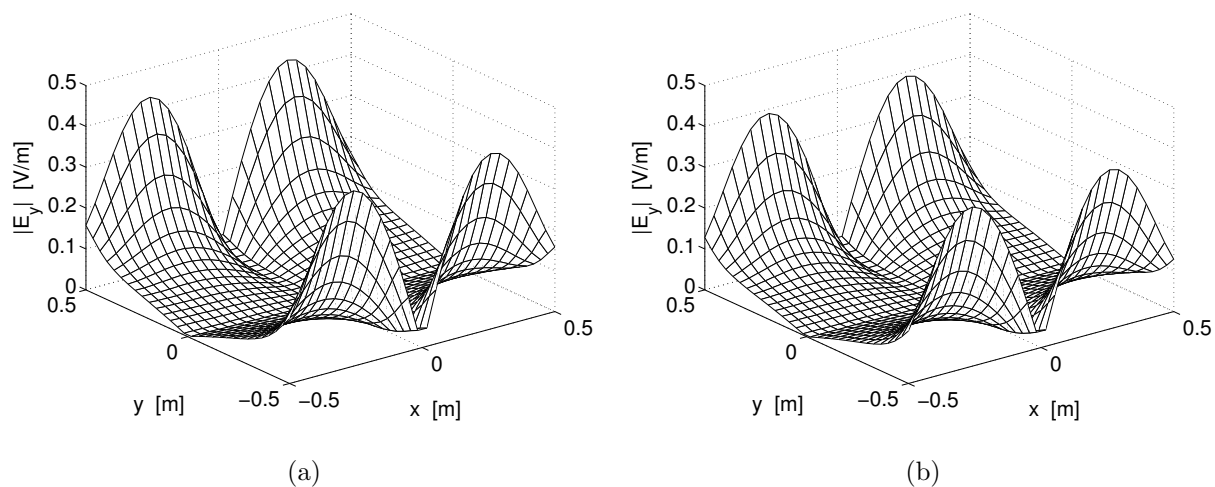
Figure 7.25: *Amplitude of y-component of the radiated electric field as evaluated: (a)- with GMoMOS; (b)- with NEC 4.1.*

(a)   (b)
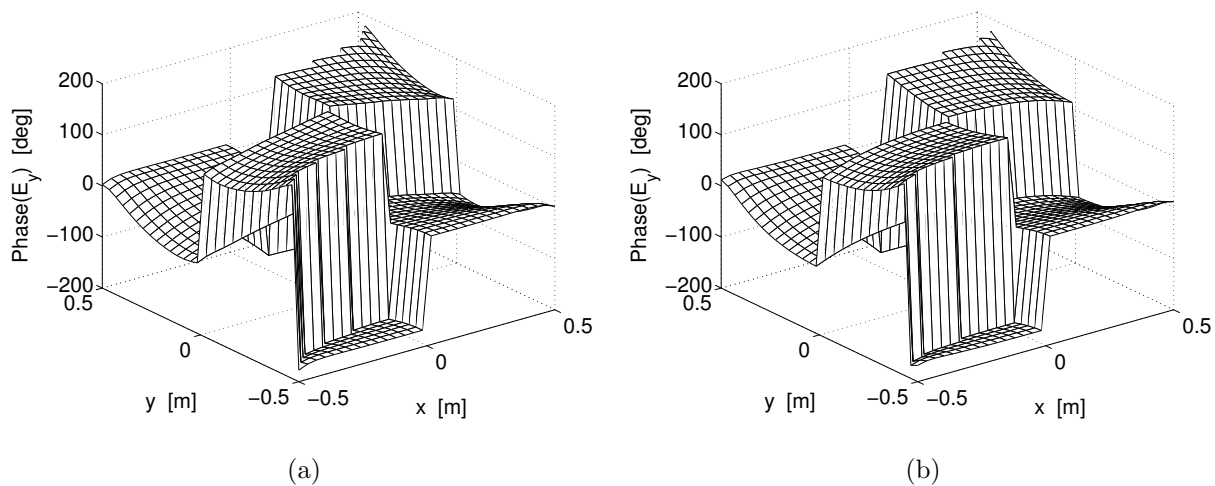
Figure 7.26: *Phase of y-component of the radiated electric field as evaluated: (a)- with GMoMOS; (b)- with NEC 4.1.*

(a)   (b)
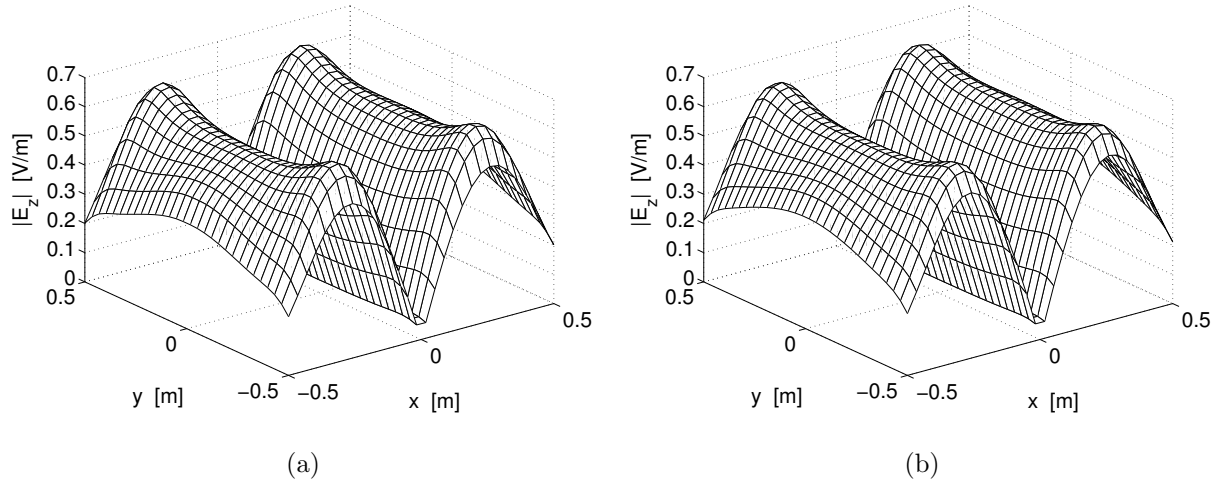
Figure 7.27: *Amplitude of z-component of the radiated electric field as evaluated: (a)- with GMoMOS; (b)- with NEC 4.1.*

(a)   (b)
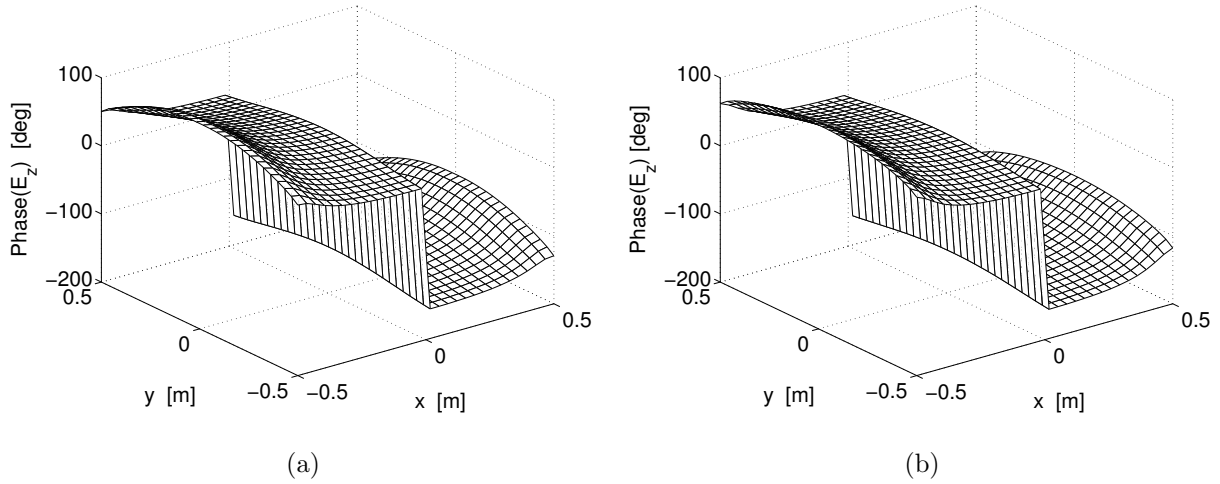
Figure 7.28: *Phase of z-component of the radiated electric field as evaluated: (a)- with GMoMOS; (b)- with NEC 4.1.*
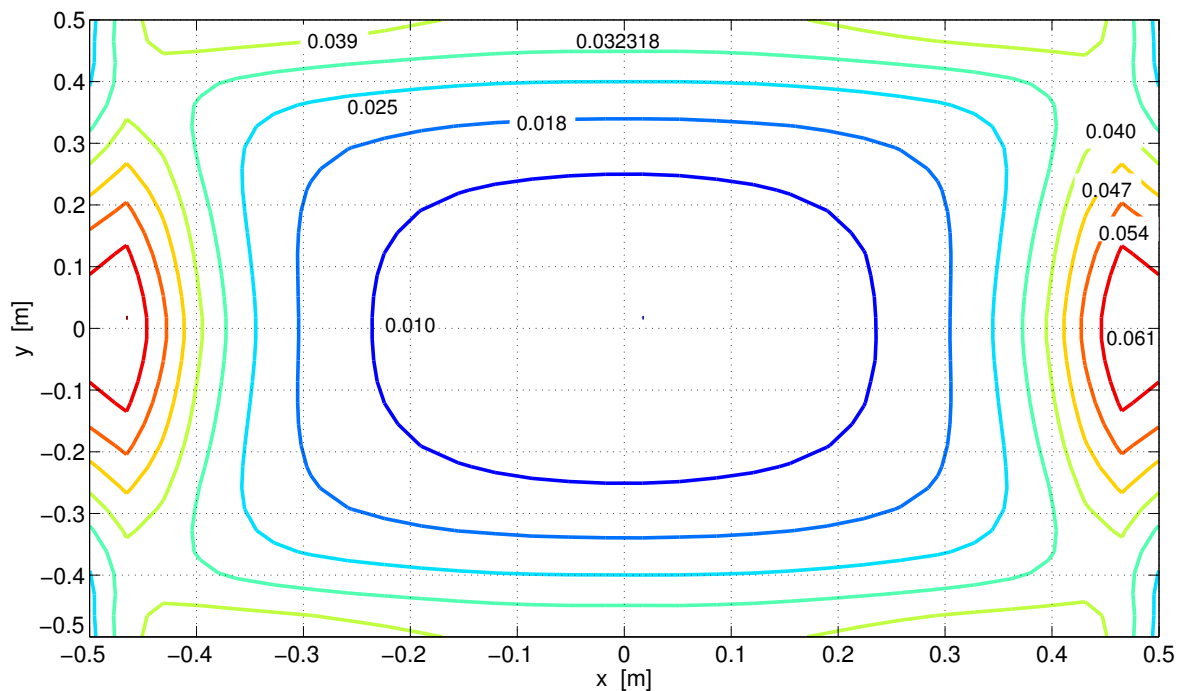
Figure 7.29: *Difference in amplitude of E_x between result by GMoMOS and by NEC 4.1.*
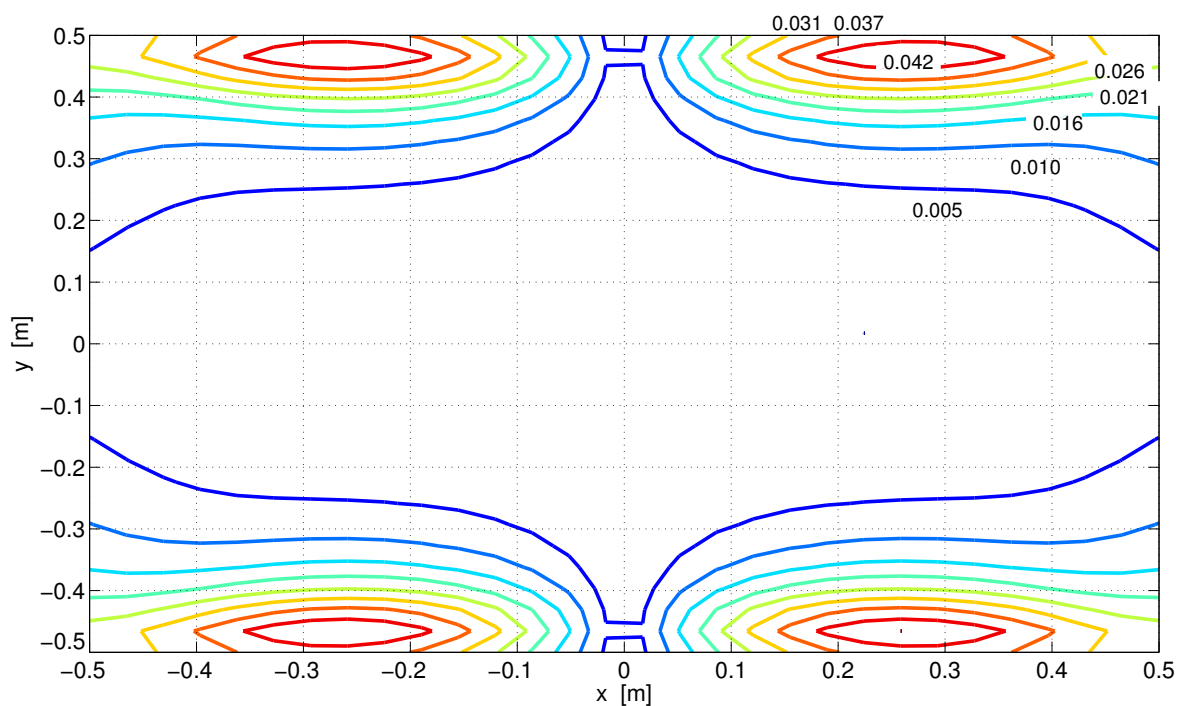
Figure 7.30: *Difference in amplitude of E_y between result by GMoMOS and by NEC 4.1.*
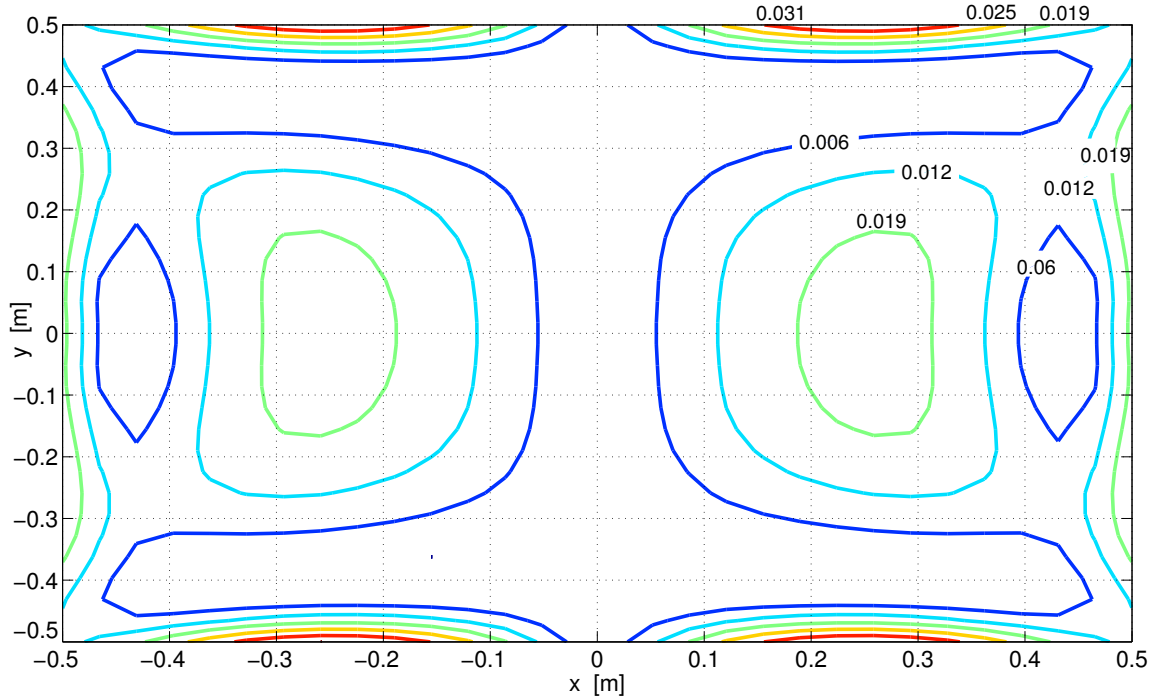
Figure 7.31: *Difference in amplitude of E_z between result by GMoMOS and by NEC 4.1.*

7.7   Conclusions and discussion

In this chapter the problem of electromagnetic scattering by PEC open surfaces with vanishing thickness has been studied. We have discretized the pertinent Electric Field Integral Equation by means of a Galerkin MoM obtaining a system matrix equation. RWG basis functions over a triangular domain have been introduced to expand the unknown surface current. In this case, the evaluation of matrix elements requires the calculation of two times two-fold integrals (on triangular patches) where the integrand exhibits an integrable singularity when the distance between the source and the observation point vanishes. Therefore, in the developed method, we have used different approaches in agreement with the relative position between source and observation triangles (see Sec. 7.3). All singularities are extracted and calculated in closed form and numerical integration is applied only for regular functions.

Moreover, the implementation of the presented numerical method clearly showed that dealing with RWG functions and triangular mesh is a delicate procedure. In fact, depending on the mesh selection, errors are possibly introduced in the evaluation of matrix elements.

Besides, also the way electric current distributions are presented requires a careful interpretation.

The approach is applied to the scattering problems of a PEC square plate and a PEC thin strip illuminated by a plane wave. Comparisons of a surface current density with results in the literature using different computation methods (e.g., NEC) showed good correspondence in both cases. By means of a numerical example (see Sec. 7.6.4), we have shown that once the surface current distribution has been calculated, the implemented numerical scheme is well capable of evaluating the field radiated by this current.

Chapter 8

Modeling of mutual coupling between surfaces and wires

The problem of calculating the current distribution along wire antennas in free space has been solved by defining an Electric Field Integral Equation (EFIE) which makes use of the free-space Green's function and then by solving this equation applying a Galerkin Exact Kernel Method of Moments (see Sec. 2.2.2 and Sec. 3.1). For wire antennas attached to other scattering structures (e.g. planar surfaces), the previous theoretical approach has to be modified. The free-space Green's function can for example be replaced by the Green's function specific for the particular scattering structure which has to be known in an efficient form. Another possible approach retains the free-space Green's function, but expands the currents on attached wires and on scattering structures in a suitable way. In general, the surface patch Method of Moments [20–22] follows the second approach, while the hybridizations between the Method of Moments and the Geometrical Theory of Diffraction (MoM/GTD) are examples of the first approach (Geometrical Theory of Diffraction can be viewed as a high-frequency approximation to the spatial Green's function) [23]. Looking at the present literature related to the full MoM approach, it can be seen that the interaction between a scattering surface and the wire attached to that has been analyzed following different methodologies. For example, in [21, 75, 76] the connection between the monopole and the independently segmented ground plane has been modeled defining a particular junction basis function. In [22], on the other hand, based on the so-called general localized junction model, a specific segmentation technique of wires and plates has been proposed. In this case a good versatility in positioning of the monopole is achieved by re-segmenting the ground plane for each wire attachment position.

We will follow the full MoM methodology, retaining the free-space Green's function we will

model the attachment region by defining a new basis function. In this chapter, we analyze the mutual coupling between arbitrary oriented open surfaces and wires including the case of wires connected to surfaces.

8.1   Electromagnetic coupling between a PEC surface and a PEC wire

In this section, we first recall the expressions of the electric field radiated by a current flowing along a PEC wire and by a current flowing over a PEC open surface as already defined in Sec. 6.2 and in Sec. 7.4. Second, the mutual interaction between these two types of structures is derived: the electric field radiated by the current along a single wire element (i.e., two adjacent segments) is evaluated over the surface of the RWG support (i.e., two triangular patches) and vice versa. Focusing on the wire, as motivated in Secs. 2.2.1 and 6.1, the radiating total current is considered flowing on the wire axis. Moreover, the radiated field can be approximated as (see Sec. 6.2)

$$\mathbf{E}(\mathbf{r}) = \sum_{n=1}^{N} I_n \mathbf{E}_n(\mathbf{r}), \tag{8.1}$$

where the elementary electric field $\mathbf{E}_n(\mathbf{r})$ is

$$\mathbf{E}_n(\mathbf{r}) = \frac{1}{j\omega\varepsilon}\frac{1}{4\pi} \int\limits_{z'=(n-1)\Delta z}^{(n+1)\Delta z} \psi_n(z')\frac{\exp(-jk|\mathbf{r}-z'\mathbf{i}_z|)}{|\mathbf{r}-z'\mathbf{i}_z|^3} \left\{ -\left[(jk|\mathbf{r}-z'\mathbf{i}_z|)^2 + jk|\mathbf{r}-z'\mathbf{i}_z| \right. \right.$$

$$\left. + 1\right]\mathbf{i}_z + \left[3 + 3jk|\mathbf{r}-z'\mathbf{i}_z| + (jk|\mathbf{r}-z'\mathbf{i}_z|)^2\right]\frac{(z-z')}{|\mathbf{r}-z'\mathbf{i}_z|^2}(\mathbf{r}-\mathbf{r}') \right\} dz', \tag{8.2}$$

and I_n are the coefficients of the rooftop (triangular) basis functions $\boldsymbol{\psi}_n^W$

$$\boldsymbol{\psi}_n^W(z') = \psi_n^W(z')\mathbf{i}_z = \begin{cases} \left(1 - \left|\dfrac{z'}{\Delta z} - n\right|\right)\mathbf{i}_z, & |z' - n\Delta z| \leq \Delta z, \\ 0, & \text{otherwise.} \end{cases} \tag{8.3}$$

Expression (8.2) refers to a coordinate system local to the wire, which has its origin at the first wire end point and the z-axis oriented along the wire axis.

As already described in Sec. 7.4, we can express the field radiated by a current flowing on the surface of an object in terms of elementary electric fields $\mathbf{E}_m(\mathbf{r})$ radiated by the m-th current distribution on the support of the m-th RWG function (i.e., $T_m^+ \cup T_m^-$). For the

sake of clarity, we re-write here equations (7.40) and (7.41)

$$\mathbf{E}(\mathbf{r}) = \sum_{m=1}^{M} J_m \mathbf{E}_m(\mathbf{r}), \tag{8.4}$$

$$\mathbf{E}_m(\mathbf{r}) = \frac{\ell_m}{4\pi j\omega\varepsilon} \left[\frac{k^2}{2A_m^+} \int_{T_m^+} \boldsymbol{\rho}_m^+(\mathbf{r}') \frac{e^{-jkR}}{R} dS' + \frac{k^2}{2A_m^-} \int_{T_m^-} \boldsymbol{\rho}_m^-(\mathbf{r}') \frac{e^{-jkR}}{R} dS' \right.$$

$$\left. - \frac{1}{A_m^+} \int_{T_m^+} (1+jkR)(\mathbf{r}-\mathbf{r}') \frac{e^{-jkR}}{R^3} dS' + \frac{1}{A_m^-} \int_{T_m^-} (1+jkR)(\mathbf{r}-\mathbf{r}') \frac{e^{-jkR}}{R^3} dS' \right], \tag{8.5}$$

where a source point $\mathbf{r}'$ is designed by the vector $\boldsymbol{\rho}_m^{\pm}$ in each triangle $T_m^{\pm}$ with respect to a coordinate system local to the triangle $T_m^{\pm}$ (see Fig. 7.1).

In the evaluation of the electromagnetic interaction between wires and surfaces the two expressions (8.2) and (8.5) together with (8.1) and (8.4) are fundamental. In fact this mutual interaction can be described by evaluating the scattered field from a wire on a surface and vice versa.

In the configuration studied, an arbitrary oriented PEC wire and a PEC open surface (object, body) are fed by external sources (i.e., an incident plane wave and/or a delta-gap voltage). In this case a current distribution will be induced on the wire mantle and on the open surface. The total electric field which excites the wire can be written as the sum of two parts:

$$\mathbf{E}_t^W(\mathbf{r}) = \mathbf{E}_e(\mathbf{r}) + \mathbf{E}^{W,B}(\mathbf{r}), \tag{8.6}$$

where $\mathbf{E}_e(\mathbf{r})$ represents the field due to external sources, and $\mathbf{E}^{W,B}(\mathbf{r})$ is the field radiated by a current flowing on the open surface, incident on the wire. A similar expression describes the total electric field incident on the object

$$\mathbf{E}_t^B(\mathbf{r}) = \mathbf{E}_e(\mathbf{r}) + \mathbf{E}^{B,W}(\mathbf{r}), \tag{8.7}$$

where $\mathbf{E}^{B,W}(\mathbf{r})$ is the field radiated by a current flowing on the wire, incident on the open surface. Equations (8.6) and (8.7) describe our problem. These equations are solved by applying the Galerkin Method of Moments.

First, we focus our attention on equation (8.6). After discretizing the wire in $N+1$ segments, we apply the Galerkin Method of Moments defining a set of N rooftop "basis"

and "testing" functions as in (8.3), each overlapping two segments. Hence, the system matrix equation $\underline{\underline{\mathbf{Z}}}\,\underline{\mathbf{I}} = \underline{\mathbf{F}}$ in (3.8) is generalized as follows

$$\underline{\underline{\mathbf{Z}}}^W\,\underline{\mathbf{I}}^W = \underline{\mathbf{F}}_e^W + \underline{\mathbf{F}}^{W,B}, \tag{8.8}$$

where the matrix $\underline{\underline{\mathbf{Z}}}^W$ is the same as $\underline{\underline{\mathbf{Z}}}$ and the vector $\underline{\mathbf{F}}_e^W$ represents the contribution due to the external excitation on the wire as in expression (3.10). The vector $\underline{\mathbf{F}}^{W,B}$ represents how the electric field radiated by a current on the open surface is electromagnetically coupled with the wire

$$\underline{\mathbf{F}}^{W,B} = \begin{bmatrix} \left\langle \boldsymbol{\psi}_1^W, \widehat{\mathbf{E}}^{W,B} \right\rangle \\ \left\langle \boldsymbol{\psi}_2^W, \widehat{\mathbf{E}}^{W,B} \right\rangle \\ \vdots \\ \left\langle \boldsymbol{\psi}_N^W, \widehat{\mathbf{E}}^{W,B} \right\rangle \end{bmatrix}. \tag{8.9}$$

The inner product defined in (3.7) is used. Consistently with the formulation of the thin-wire integral equation in Sec. 2.2.2, $\widehat{\mathbf{E}}^{W,B}$ denotes values averaged over $\phi \in [0, 2\pi)$

$$\widehat{\mathbf{E}}^{W,B} = \frac{1}{2\pi} \int\limits_{\phi=0}^{2\pi} \mathbf{E}^{W,B} d\phi, \tag{8.10}$$

where $\mathbf{E}^{W,B}$ is the field radiated by a current on an open surface and incident on the wire. Second, the same steps will be followed in the evaluation of the contribution of the induced electric field from the wire to the open surface. In this case, no field averaging is required. In fact the total current is considered on the axis of the radiating wire as explained in Secs. 6.1 and 6.3.1. Thus, from (8.7), discretizing the surface in triangular patches where M RWG functions are defined, and applying the Galekin MoM, we find the following system matrix equation $\underline{\underline{\mathbf{Z}}}\,\underline{\mathbf{I}} = \underline{\mathbf{F}}$ from (7.20)

$$\underline{\underline{\mathbf{Z}}}^B\,\underline{\mathbf{I}}^B = \underline{\mathbf{F}}_e^B + \underline{\mathbf{F}}^{B,W}. \tag{8.11}$$

The vector $\underline{\mathbf{F}}^{B,W}$ represents how the electric field radiated by the wire current is coupled to the surface current of the object

$$\underline{\mathbf{F}}^{B,W} = \begin{bmatrix} \left\langle \boldsymbol{\psi}_1^B, \mathbf{E}^{B,W} \right\rangle \\ \left\langle \boldsymbol{\psi}_2^B, \mathbf{E}^{B,W} \right\rangle \\ \vdots \\ \left\langle \boldsymbol{\psi}_M^B, \mathbf{E}^{B,W} \right\rangle \end{bmatrix}. \tag{8.12}$$

The inner product defined in (7.16) is used. The functions $\left\{\boldsymbol{\psi}_m^B\right\}_{m=1}^M$ are the RWG "testing" functions defined in Sec. 7.1.1 and M is the number of non-boundary edges used in the surface discretization. The other vector $\underline{\mathbf{F}}_e^B$ represents the contribution due to the external excitation on the open surface (see Sec. 7.2). Vectors $\underline{\mathbf{F}}^{W,B}$ in (8.9) and $\underline{\mathbf{F}}^{B,W}$ in (8.12) can also be written as functions of the unknown current vectors $\underline{\mathbf{I}}^B$ and $\underline{\mathbf{I}}^W$

$$\underline{\mathbf{F}}^{W,B} = \underline{\underline{\mathbf{C}}}^{W,B}\underline{\mathbf{I}}^B, \qquad \underline{\mathbf{F}}^{B,W} = \underline{\underline{\mathbf{C}}}^{B,W}\underline{\mathbf{I}}^W. \tag{8.13}$$

Finally, from (8.8) and (8.11), together with (8.13), a general system of equations may be elegantly written as $\underline{\underline{\mathbf{Z}}}\underline{\mathbf{I}} = \underline{\mathbf{F}}$ or more explicitly as

$$\begin{bmatrix} \underline{\underline{\mathbf{Z}}}^B & -\underline{\underline{\mathbf{C}}}^{B,W} \\ -\underline{\underline{\mathbf{C}}}^{W,B} & \underline{\underline{\mathbf{Z}}}^W \end{bmatrix} \begin{bmatrix} \underline{\mathbf{I}}^B \\ \underline{\mathbf{I}}^W \end{bmatrix} = \begin{bmatrix} \underline{\mathbf{F}}_e^B \\ \underline{\mathbf{F}}_e^W \end{bmatrix}. \tag{8.14}$$

The matrices $\underline{\underline{\mathbf{Z}}}^B$ and $\underline{\underline{\mathbf{Z}}}^W$ are referred to as self matrices, while the off-diagonal matrices $\underline{\underline{\mathbf{C}}}^{B,W}$ and $\underline{\underline{\mathbf{C}}}^{W,B}$ are referred to as coupling matrices and describe the interaction between a wire and a surface and vice versa. In particular, in the evaluation of $\underline{\underline{\mathbf{C}}}^{B,W}$, we consider the field radiated by the total current on the wire axis incident on the open surface. This leads to a one-dimensional integral in transmission and a two-dimensional integral for reception. For each element $C_{m,n}^{B,W}$ the field (8.2) radiated by the n-th source element (i.e., two adjacent segments) is calculated on the m-th observation element of the conducting surface (i.e., two adjacent triangular patches). For the calculation of $\underline{\underline{\mathbf{C}}}^{W,B}$, we consider the field radiated by a surface current distribution incident on the wire mantle. This yields a two-dimensional integral in transmission and a two-dimensional integral for reception. In this case, for each element $C_{n,m}^{W,B}$, the field (8.5) radiated by the m-th source element of the conducting surface (i.e., two adjacent triangular patches) is calculated on the wire mantle of n-th observation element (i.e., two adjacent segments). Thanks to the Galerkin MoM applied, the matrix $\underline{\underline{\mathbf{Z}}}$ in (8.14) holds the symmetry property. Therefore, each element $C_{m,n}^{B,W}$ is equal to $C_{n,m}^{W,B}$, (i.e., $\underline{\underline{\mathbf{C}}}^{W,B} = \left(\underline{\underline{\mathbf{C}}}^{B,W}\right)^T$). Thus, aiming at an efficient computational method in terms of CPU time, only the elements of $\underline{\underline{\mathbf{C}}}^{B,W}$ are calculated since a 1D+2D integration is required instead of a 2×2D integration needed for the computation of $\underline{\underline{\mathbf{C}}}^{W,B}$. Then, the matrix $\underline{\underline{\mathbf{C}}}^{W,B}$ is filled in, without any further calculation.

When more than one wire is present in the environment, we have to take into account the electromagnetic interaction between each wire and the surface as well as the interaction between the wires. Therefore, for the case of P arbitrary oriented wires, the system matrix equation (8.14) may be generalized to

$$
\begin{bmatrix}
\underline{\underline{\mathbf{Z}}}^{B} & -\underline{\underline{\mathbf{C}}}^{B,W_1} & -\underline{\underline{\mathbf{C}}}^{B,W_2} & \cdots & -\underline{\underline{\mathbf{C}}}^{B,W_P} \\
-\underline{\underline{\mathbf{C}}}^{W_1,B} & \underline{\underline{\mathbf{Z}}}^{W_1} & -\underline{\underline{\mathbf{C}}}^{W_1,W_2} & \cdots & -\underline{\underline{\mathbf{C}}}^{W_1,W_P} \\
-\underline{\underline{\mathbf{C}}}^{W_2,B} & -\underline{\underline{\mathbf{C}}}^{W_2,W_1} & \underline{\underline{\mathbf{Z}}}^{W_2} & \cdots & -\underline{\underline{\mathbf{C}}}^{W_2,W_P} \\
\vdots & \vdots & \vdots & \vdots & \vdots \\
-\underline{\underline{\mathbf{C}}}^{W_P,B} & -\underline{\underline{\mathbf{C}}}^{W_P,W_1} & -\underline{\underline{\mathbf{C}}}^{W_P,W_2} & \cdots & \underline{\underline{\mathbf{Z}}}^{W_P}
\end{bmatrix}
\begin{bmatrix}
\underline{\mathbf{I}}^{B} \\
\underline{\mathbf{I}}^{W_1} \\
\underline{\mathbf{I}}^{W_2} \\
\vdots \\
\underline{\mathbf{I}}^{W_P}
\end{bmatrix}
=
\begin{bmatrix}
\underline{\mathbf{F}}_e^{B} \\
\underline{\mathbf{F}}_e^{W_1} \\
\underline{\mathbf{F}}_e^{W_2} \\
\vdots \\
\underline{\mathbf{F}}_e^{W_P}
\end{bmatrix}.
\tag{8.15}
$$

In a similar fashion, multiple surfaces may be introduced.

8.1.1 Evaluation of the elements $C_{m,n}^{B,W}$

Now we consider the m,n-th element $C_{m,n}^{B,W}$ of the surface-wire matrix $\underline{\underline{\mathbf{C}}}^{B,W}$ which expresses the interaction from the n-th wire element current on the m-th triangular element. As explained, the current flows along the wire axis. From equation (8.2), valid in a local "wire coordinate system", we know the elementary electric field radiated by a current along the n-th wire element. First, we determine the image $\mathbf{E}_n^{''}(\mathbf{r})$ of $\mathbf{E}_n(\mathbf{r})$ by applying the proper transformation formulas from the wire coordinate system to the global coordinate system as defined in Appendix D. Second, we evaluate the inner product

$$
C_{m,n}^{B,W} = \int\limits_{T_m^+ \cup T_m^-} \boldsymbol{\psi}_m^B(\mathbf{r}) \cdot \mathbf{E}_n^{''}(\mathbf{r}) dS,
\tag{8.16}
$$

where $\mathbf{r}$ is restricted to the support of the RWG function $\boldsymbol{\psi}_m^B$ (i.e., $\mathbf{r} \in (T_m^+ \cup T_m^-)$) defined in (7.13) and reported here for the sake of clarity

$$
\boldsymbol{\psi}_n^B(\mathbf{r}) =
\begin{cases}
\dfrac{\ell_n}{2A_n^+}\boldsymbol{\rho}_n^+, & \mathbf{r} \in T_n^+, \\
\dfrac{\ell_n}{2A_n^-}\boldsymbol{\rho}_n^-, & \mathbf{r} \in T_n^-, \\
0, & \text{otherwise,}
\end{cases}
\tag{8.17}
$$

Finally, substituting this expression in (8.16) leads to

$$
C_{m,n}^{B,W} = \frac{\ell_m}{2A_m^+}\int\limits_{T_m^+}\boldsymbol{\rho}_m^+(\mathbf{r}) \cdot \mathbf{E}_n^{''}(\mathbf{r})dS + \frac{\ell_m}{2A_m^-}\int\limits_{T_m^-}\boldsymbol{\rho}_m^-(\mathbf{r}) \cdot \mathbf{E}_n^{''}(\mathbf{r})dS.
\tag{8.18}
$$

8.2 Attachment of wires to the surface

In the problem of computing the current distribution along wires and surfaces, including the case where wires are connected to the surface, it is convenient to define a special basis

function (attachment mode) which describes the current flow from the mantle of the wire to the surface and vice versa. In this way an accurate evaluation of the electric current distribution is ensured. The attachment mode is defined over a wire segment and a small planar surface region around that segment. In [76,77], an attachment mode suited to RWG surface basis functions is proposed. It consists of a wire segment and a set of triangular patches sharing a common vertex (i.e., the connection point). Although this attachment basis function satisfies the desirable properties of RWG functions being free of charge accumulation, the surface current around a junction is not always uniformly distributed, being strictly dependent on the shape of triangular patches involved in the attachment.

Here a different basis function for the attachment region is proposed. The configuration studied consists of a perfectly electrically conducting wire perpendicularly attached to a perfectly electrically conducting planar surface (object, body). An incident field is present and/or a delta gap voltage source feeds the wire. This problem may be easily generalized to the case of more than one wire or more surfaces.

8.2.1   Definition of the junction basis function

In this section we define the basis function associated with wires attached to a surface. For ease of implementation, we assume that the wire is perpendicularly connected to the surface, and that a wire-to-surface junction exists only at triangular patch vertices (which can always be achieved by a proper triangulation). Moreover, a circular symmetry is assumed at the attachment point, see Fig. 8.1. The surface is meshed with triangular patches and a linear segmentation of the wire mantle is assumed. As already discussed in Sec. 3.1.1 and Sec. 7.1.1, basis functions suitable for representing currents induced on wires and on the surface of objects are rooftop and RWG functions, respectively.

For a general wire-to-surface junction on a structure as illustrated in Fig. 8.1, the attachment mode is built up of two parts, namely a disk S^{aD} on the surface and a segment S^{aW} on the wire. A local circularly cylindrical coordinate system (r, ϕ, z) with origin in the junction point is defined. In order to be suited for representing the current in the neighborhood of a junction, an attachment basis function has to satisfy the following properties:

- it guarantees the proper $1/r$ behavior of the body surface current density in the vicinity of the attachment point;

- it meets the Kirchhoff current continuity requirement: namely, the surface disk current equals the wire current at the wire base (i.e., $r = a$, $z = 0$, with a the radius of the wire);

- it vanishes at a distance $r = b$ from the attachment vertex;

- finally, it should be free of charge accumulation. This means that the integral of its surface divergence (which is proportional to the surface charge density) vanishes.

PSfrag replacements
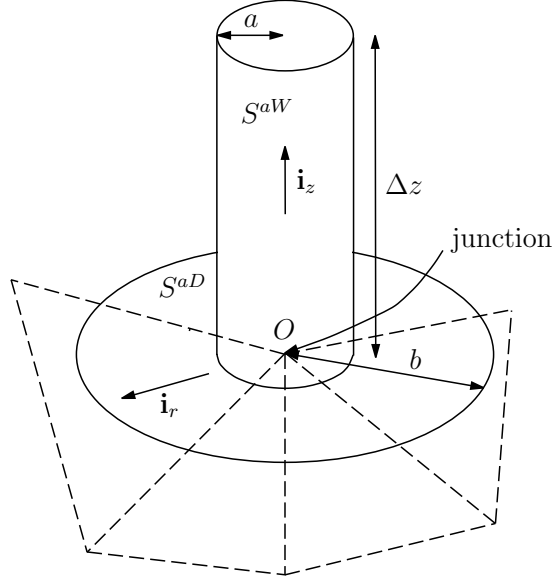
Figure 8.1: *Geometrical parameters associated with the wire-to-surface junction.*

Thus, the attachment mode $\overline{\boldsymbol{\psi}}^a$ is given by

$$\overline{\boldsymbol{\psi}}^a(\mathbf{r}) = \begin{cases} \overline{\boldsymbol{\psi}}^{aW}(\mathbf{r}), & \mathbf{r} \in S^{aW}, \\ \overline{\boldsymbol{\psi}}^{aD}(\mathbf{r}), & \mathbf{r} \in S^{aD}, \\ 0, & \text{otherwise}, \end{cases} \tag{8.19}$$

with

$$\overline{\boldsymbol{\psi}}^{aW}(\mathbf{r}) = \frac{1}{2\pi a}\left(1 - \frac{z}{\Delta z}\right)\delta(r-a)\mathbf{i}_z, \qquad 0 \leq z \leq \Delta z, \tag{8.20}$$

and

$$\overline{\boldsymbol{\psi}}^{aD}(\mathbf{r}) = \begin{cases} 0, & 0 \leq r < a, \\ \dfrac{1}{2\pi(b-a)}\left(\dfrac{r-b}{r}\right)\delta(z)\mathbf{i}_r, & a \leq r \leq b, \\ 0, & r \geq b. \end{cases} \tag{8.21}$$

In this case $\overline{\boldsymbol{\psi}}^a$ express a volume density. The superscript a indicates the attachment basis function. The vector $\mathbf{i}_z$ is an outward-directed unit vector on the attachment segment, Δz

is the segment length, $\mathbf{i}_r$ is a unit vector on the disk surface directed away from the wire, r is the radial coordinate on the disk, b is the outer disk radius and a is the radius of the wire. For the attachment mode $\overline{\boldsymbol{\psi}}^a$ (8.19) all the properties previously mentioned have been verified. We can also express the attachment mode function as a surface density:

$$\boldsymbol{\psi}^a(\mathbf{r}) = \begin{cases} \dfrac{1}{2\pi a}\left(1 - \dfrac{z}{\Delta z}\right)\mathbf{i}_z, & r = a, & 0 \le z \le \Delta z, \\[3mm] \dfrac{1}{2\pi(b-a)}\left(\dfrac{r-b}{r}\right)\mathbf{i}_r, & a \le r \le b, & z = 0, \\[3mm] 0, & \text{otherwise.} \end{cases} \tag{8.22}$$

Moreover, its surface divergence which is proportional to the surface charge density, is

$$\nabla_S \cdot \boldsymbol{\psi}^a(\mathbf{r}) = \begin{cases} -\dfrac{1}{2\pi a \Delta z}, & r = a, & 0 \le z \le \Delta z, \\[3mm] \dfrac{1}{2\pi(b-a)r}, & a \le r \le b, & z = 0. \end{cases} \tag{8.23}$$

The function has been chosen such that no charge is accumulated in the attachment region (the integral of its surface divergence on the wire-to-surface transition area vanishes).

A similar attachment mode is used in [24] to model the connection between a feeding probe and a patch in microstrip antennas, and in [78] where the radiation from wires attached to bodies of revolution is studied. Tests in the literature [20, 78] show that excellent results can be obtained if b is chosen properly. Usually this means that the disk diameter must be taken to be the width of a surface triangular patch edge.

In conclusion, the volume current density over the attachment region can be written as

$$\mathbf{J}^a(\mathbf{r}) = I^a \overline{\boldsymbol{\psi}}^{aW}(\mathbf{r}) + I^a \overline{\boldsymbol{\psi}}^{aD}(\mathbf{r}), \tag{8.24}$$

or

$$\mathbf{J}^a(\mathbf{r}) = \begin{cases} I^a \dfrac{1}{2\pi a}\left(1 - \dfrac{z}{\Delta z}\right)\delta(r-a)\mathbf{i}_z, & 0 \le z \le \Delta z, \\[3mm] I^a \dfrac{1}{2\pi(b-a)}\left(\dfrac{r-b}{r}\right)\delta(z)\mathbf{i}_r, & a \le r \le b, \end{cases} \tag{8.25}$$

where I^a is the unknown current coefficient for the attachment region. This means that for each wire-to-surface junction, only one new unknown is introduced. Having applied the

Method of Moments to the attachment problem, we can write the volume current density on the wire as

$$\mathbf{J}^W(\mathbf{r}) \approx \frac{1}{2\pi a} \sum_{n=1}^{N} I_n^W \delta(r-a) \boldsymbol{\psi}_n^W(\mathbf{r}) + I^a \overline{\boldsymbol{\psi}}^{aW}(\mathbf{r}), \tag{8.26}$$

and the volume current density on the surface involved in the attachment as

$$\mathbf{J}^B(\mathbf{r}) \approx \sum_{m=1}^{M} I_m^B \delta(z) \boldsymbol{\psi}_m^B(\mathbf{r}) + I^a \overline{\boldsymbol{\psi}}^{aD}(\mathbf{r}), \tag{8.27}$$

where N, M are the total number of wire current unknowns and surface current unknowns, respectively. Moreover, coefficients I_n^W and I^a have the dimension of a current (i.e., A) while coefficients I_m^B have the dimension of a surface current density (i.e., A/m).

8.2.2   Testing procedure

When a wire is attached to a surface, expressions (8.6) and (8.7) for the total electric field exciting the wire and the body are extended as follows

$$\mathbf{E}_t^W(\mathbf{r}) = \mathbf{E}_e(\mathbf{r}) + \mathbf{E}^{W,B}(\mathbf{r}) + \mathbf{E}^{W,a}(\mathbf{r}), \tag{8.28}$$

$$\mathbf{E}_t^B(\mathbf{r}) = \mathbf{E}_e(\mathbf{r}) + \mathbf{E}^{B,W}(\mathbf{r}) + \mathbf{E}^{B,a}(\mathbf{r}), \tag{8.29}$$

where $\mathbf{E}^{W,a}(\mathbf{r})$ is the field radiated by the junction current and incident on the wire and $\mathbf{E}^{B,a}(\mathbf{r})$ is the field radiated by the junction current and incident on the surface. Moreover, considering the total electric field incident on the attachment region adds an extra equation to the previous two

$$\mathbf{E}_t^a(\mathbf{r}) = \mathbf{E}_e(\mathbf{r}) + \mathbf{E}^{a,B}(\mathbf{r}) + \mathbf{E}^{a,W}(\mathbf{r}). \tag{8.30}$$

Equations (8.28)-(8.30) give a complete description of the problem.

Following the Method of Moments, we apply the testing procedure using the Galerkin formulation. This means that in the attachment region we use the same weighting function $\boldsymbol{\psi}^a(\mathbf{r})$ used as expansion basis function. Once the inner product is carried out for equations (8.28)-(8.30), the system matrix equation (3.8) can be generalized to

$$\underline{\underline{\mathbf{Z}}}\,\underline{\mathbf{I}} = \underline{\mathbf{F}}, \qquad \Rightarrow \qquad \begin{cases} \underline{\underline{\mathbf{Z}}}^B\,\underline{\mathbf{I}}^B &=& \underline{\mathbf{F}}_e^B &+& \underline{\mathbf{F}}^{B,W} &+& \underline{\mathbf{F}}^{B,a}, \\ \underline{\underline{\mathbf{Z}}}^W\,\underline{\mathbf{I}}^W &=& \underline{\mathbf{F}}_e^W &+& \underline{\mathbf{F}}^{W,B} &+& \underline{\mathbf{F}}^{W,a}, \\ \underline{\underline{\mathbf{Z}}}^a\,\underline{\mathbf{I}}^a &=& \underline{\mathbf{F}}_e^a &+& \underline{\mathbf{F}}^{a,B} &+& \underline{\mathbf{F}}^{a,W}. \end{cases} \tag{8.31}$$

The vector $\underline{\mathbf{F}}^{W,a}$ represents the electric field radiated by the attachment current distribution calculated on the mantle of the wire

$$
\underline{\mathbf{F}}^{W,a} = \begin{bmatrix} \left\langle \boldsymbol{\psi}_1^W, \widehat{\mathbf{E}}^{W,a} \right\rangle \\ \left\langle \boldsymbol{\psi}_2^W, \widehat{\mathbf{E}}^{W,a} \right\rangle \\ \vdots \\ \left\langle \boldsymbol{\psi}_N^W, \widehat{\mathbf{E}}^{W,a} \right\rangle \end{bmatrix},
\tag{8.32}
$$

where N is the number of wire unknowns and where $\boldsymbol{\psi}_n^W$ with $n = 1, \dots, N$ are the triangular (rooftop) functions defined in (8.3). Consistently with the thin-wire formulation (see Sec. 2.2.2), we have defined the averaged electric field radiated by the current on the attachment region and incident on the wire as

$$
\widehat{\mathbf{E}}^{W,a} = \frac{1}{2\pi} \int\limits_{\phi=0}^{2\pi} \mathbf{E}^{W,a} d\phi.
\tag{8.33}
$$

The vector $\underline{\mathbf{F}}^{B,a}$ represents the contribution on the surface due to the field radiated by the "attachment" current

$$
\underline{\mathbf{F}}^{B,a} = \begin{bmatrix} \left\langle \boldsymbol{\psi}_1^B, \mathbf{E}^{B,a} \right\rangle \\ \left\langle \boldsymbol{\psi}_2^B, \mathbf{E}^{B,a} \right\rangle \\ \vdots \\ \left\langle \boldsymbol{\psi}_M^B, \mathbf{E}^{B,a} \right\rangle \end{bmatrix},
\tag{8.34}
$$

where M is the number of non-boundary edges in the surface discretization and $\boldsymbol{\psi}_m^B$ with $m = 1, \dots, M$ are the RWG "testing" functions as defined in Sec. 7.2. The other two vectors $\underline{\mathbf{F}}^{a,W}$, $\underline{\mathbf{F}}^{a,B}$, in equation (8.31), take into account the contribution on the attachment region due to the field radiated by the wire and the surface current, respectively

$$
\underline{\mathbf{F}}^{a,W} = \begin{bmatrix} \left\langle \boldsymbol{\psi}^a, \mathbf{E}^{a,W} \right\rangle \end{bmatrix},
\tag{8.35}
$$

$$
\underline{\mathbf{F}}^{a,B} = \begin{bmatrix} \left\langle \boldsymbol{\psi}^a, \mathbf{E}^{a,B} \right\rangle \end{bmatrix},
\tag{8.36}
$$

in which $\boldsymbol{\psi}^a$ is the attachment basis function as defined in (8.22). In conclusion, when only one wire is attached to one surface, equation (8.31) is elegantly written as a system matrix equation $\underline{\underline{\mathbf{Z}}}\,\underline{\mathbf{I}} = \underline{\mathbf{F}}$

$$
\begin{bmatrix} \underline{\underline{\mathbf{Z}}}^B & -\underline{\underline{\mathbf{C}}}^{B,W} & -\underline{\underline{\mathbf{C}}}^{B,a} \\ -\underline{\underline{\mathbf{C}}}^{W,B} & \underline{\underline{\mathbf{Z}}}^W & -\underline{\underline{\mathbf{C}}}^{W,a} \\ -\underline{\underline{\mathbf{C}}}^{a,B} & -\underline{\underline{\mathbf{C}}}^{a,W} & \underline{\underline{\mathbf{Z}}}^a \end{bmatrix} \begin{bmatrix} \underline{\mathbf{I}}^B \\ \underline{\mathbf{I}}^W \\ \underline{\mathbf{I}}^a \end{bmatrix} = \begin{bmatrix} \underline{\mathbf{F}}_e^B \\ \underline{\mathbf{F}}_e^W \\ \underline{\mathbf{F}}_e^a \end{bmatrix}.
\tag{8.37}
$$

In particular, the newly defined vector $\underline{\mathbf{F}}_e^a$ and the matrix $\underline{\underline{\mathbf{Z}}}^a$ contains only one element while matrices $\underline{\underline{\mathbf{C}}}^{B,a}$, $\underline{\underline{\mathbf{C}}}^{W,a}$, consist of a column of M and N elements, respectively. Reciprocally, matrices $\underline{\underline{\mathbf{C}}}^{a,B}$, $\underline{\underline{\mathbf{C}}}^{a,W}$ consist of one row of M and N elements, respectively.

8.2.3 Expressions for the elements of matrix $\underline{\underline{\mathbf{Z}}}$

Restricting ourselves to the case of only one wire attached to the surface, by looking at system matrix equation (8.37), we observe that only 6 of 9 sub-matrices need to be calculated because of the symmetry in $\underline{\underline{\mathbf{Z}}}$, that means $\underline{\underline{\mathbf{C}}}^{W,B} = \left(\underline{\underline{\mathbf{C}}}^{B,W}\right)^T$, $\underline{\underline{\mathbf{C}}}^{a,B} = \left(\underline{\underline{\mathbf{C}}}^{B,a}\right)^T$ and $\underline{\underline{\mathbf{C}}}^{a,W} = \left(\underline{\underline{\mathbf{C}}}^{W,a}\right)^T$. For the evaluation of self matrices $\underline{\underline{\mathbf{Z}}}^B$ and $\underline{\underline{\mathbf{Z}}}^W$ we refer to Secs. 7.3 and 3.3, and for the evaluation of coupling matrices $\underline{\underline{\mathbf{C}}}^{B,W}$ and $\underline{\underline{\mathbf{C}}}^{W,B}$ we refer to Sec. 8.1. We are therefore left with the computation of matrices $\underline{\underline{\mathbf{C}}}^{B,a}$, $\underline{\underline{\mathbf{C}}}^{W,a}$, and with $\underline{\underline{\mathbf{Z}}}^a$ and $\underline{\mathbf{F}}_e^a$, which consist of only one element. In the following we derive their explicit forms and we outline how they can be evaluated.

Expression for the element $\underline{Z}^a$

As previously mentioned, the matrix $\underline{\underline{\mathbf{Z}}}^a$ contains only one element that can be expressed as

$$
\begin{aligned}
Z^a = {} & j\omega\mu \int\limits_{S^{aW}\cup S^{aD}} \boldsymbol{\psi}^a(\mathbf{r}) \cdot \left(\int\limits_{S^{aW}\cup S^{aD}} G(\mathbf{r}-\mathbf{r}')\boldsymbol{\psi}^a(\mathbf{r}')dS' \right) dS \\
& - \frac{1}{j\omega\epsilon} \int\limits_{S^{aW}\cup S^{aD}} \boldsymbol{\psi}^a(\mathbf{r}) \cdot \left(\nabla_S \int\limits_{S^{aW}\cup S^{aD}} G(\mathbf{r}-\mathbf{r}') \left(\nabla_{S'} \cdot \boldsymbol{\psi}^a(\mathbf{r}')\right) dS' \right) dS,
\end{aligned} \tag{8.38}
$$

where $\boldsymbol{\psi}^a$ is the attachment function in (8.22) and the gradient operator $\nabla_{S'}$ applies to the primed coordinates. We verify that the following property

$$
\begin{aligned}
& - \int\limits_{S^{aW}\cup S^{aD}} \boldsymbol{\psi}^a(\mathbf{r}) \cdot \left(\nabla_S \int\limits_{S^{aW}\cup S^{aD}} G(\mathbf{r}-\mathbf{r}') \left(\nabla_{S'} \cdot \boldsymbol{\psi}^a(\mathbf{r}')\right) dS' \right) dS = \\
& \int\limits_{S^{aW}\cup S^{aD}} \left(\nabla_S \cdot \boldsymbol{\psi}^a(\mathbf{r})\right) \int\limits_{S^{aW}\cup S^{aD}} G(\mathbf{r}-\mathbf{r}') \left(\nabla_{S'} \cdot \boldsymbol{\psi}^a(\mathbf{r}')\right) dS'dS,
\end{aligned} \tag{8.39}
$$

is valid since the wire-to-surface junction function $\boldsymbol{\psi}^a$ vanishes at the contour boundaries of the attachment region $S^{aW} \cup S^{aD}$. Therefore from (8.38), writing $\boldsymbol{\psi}^a$ explicitly as in (8.22), together with the property (8.23) and using the fact that the wire is attached

perpendicularly to the surface (i.e., $\boldsymbol{\psi}^{aD} \cdot \boldsymbol{\psi}^{aW} = 0$) yields

$$
Z^a = j\omega\mu\frac{1}{4\pi^2}\left[\int\limits_{z=0}^{\Delta z}\int\limits_{\phi=0}^{2\pi}\int\limits_{z'=0}^{\Delta z}\int\limits_{\phi'=0}^{2\pi} G(\mathbf{r}-\mathbf{r}')\left(1-\frac{z'}{\Delta z}\right)\left(1-\frac{z}{\Delta z}\right)d\phi'dz'd\phi dz\right]_{\{r=r'=a\}}
$$

$$
+j\omega\mu\frac{1}{4\pi^2(b-a)^2}\left[\int\limits_{r=a}^{b}\int\limits_{\phi=0}^{2\pi}\int\limits_{r'=a}^{b}\int\limits_{\phi'=0}^{2\pi} G(\mathbf{r}-\mathbf{r}')(r'-b)(r-b)\mathbf{i}_{r'}(\phi')\cdot\mathbf{i}_r(\phi)d\phi'dr'd\phi dr\right]_{\{z=z'=0\}}
$$

$$
+\frac{1}{j\omega\epsilon}\frac{1}{4\pi^2\Delta z^2}\left[\int\limits_{z=0}^{\Delta z}\int\limits_{\phi=0}^{2\pi}\int\limits_{z'=0}^{\Delta z}\int\limits_{\phi'=0}^{2\pi} G(\mathbf{r}-\mathbf{r}')d\phi'dz'd\phi dz\right]_{\{r=r'=a\}}
$$

$$
-\frac{1}{j\omega\epsilon}\frac{1}{4\pi^2(b-a)\Delta z}\left[\int\limits_{z=0}^{\Delta z}\int\limits_{\phi=0}^{2\pi}\int\limits_{r'=a}^{b}\int\limits_{\phi'=0}^{2\pi} G(\mathbf{r}-\mathbf{r}')d\phi'dr'd\phi dz\right]_{\{r=a,\ z'=0\}}+
$$

$$
+\frac{1}{j\omega\epsilon}\frac{1}{4\pi^2(b-a)^2}\left[\int\limits_{r=a}^{b}\int\limits_{\phi=0}^{2\pi}\int\limits_{r'=a}^{b}\int\limits_{\phi'=0}^{2\pi} G(\mathbf{r}-\mathbf{r}')d\phi'dr'd\phi dr\right]_{\{z=z'=0\}}
$$

$$
-\frac{1}{j\omega\epsilon}\frac{1}{4\pi^2(b-a)\Delta z}\left[\int\limits_{r=a}^{b}\int\limits_{\phi=0}^{2\pi}\int\limits_{z'=0}^{\Delta z}\int\limits_{\phi'=0}^{2\pi} G(\mathbf{r}-\mathbf{r}')d\phi'dz'd\phi dr\right]_{\{z=0,\ r'=a\}}. \tag{8.40}
$$

We observe that these six four-fold integrals have a 2π-periodic integrand. All integrands depend on $\varphi = \phi - \phi'$ and thus for a generic function f, the following is valid

$$
\int\limits_{\phi=0}^{2\pi}\int\limits_{\phi'=0}^{2\pi} f(\phi-\phi')d\phi d\phi' = 2\pi\int\limits_{\varphi=0}^{2\pi} f(\varphi)d\varphi. \tag{8.41}
$$

Using this result in (8.40) reduces the four-fold integrals to three-fold integrals of five different forms. The first two are

$$
\int\limits_{z=0}^{\Delta z}\int\limits_{z'=0}^{\Delta z}\int\limits_{\varphi=0}^{2\pi} G(\mathbf{r}-\mathbf{r}')\left(1-\frac{z'}{\Delta z}\right)\left(1-\frac{z}{\Delta z}\right)d\varphi dz'dz, \tag{8.42}
$$

$$
\int\limits_{z=0}^{\Delta z}\int\limits_{z'=0}^{\Delta z}\int\limits_{\varphi=0}^{2\pi} G(\mathbf{r}-\mathbf{r}')d\varphi dz'dz, \tag{8.43}
$$

where $R = |\mathbf{r} - \mathbf{r}'| = \sqrt{(z - z')^2 + 4a^2 \sin^2(\varphi/2)}$, with $\mathbf{r}$ and $\mathbf{r}'$ located on the wire attachment surface S^{aW}. Moreover the next two different forms are

$$\int\limits_{r=a}^{b} \int\limits_{r'=a}^{b} \int\limits_{\varphi=0}^{2\pi} G(\mathbf{r} - \mathbf{r}')(r' - b)(r - b)\cos\varphi d\varphi dr' dr, \tag{8.44}$$

$$\int\limits_{r=a}^{b} \int\limits_{r'=a}^{b} \int\limits_{\varphi=0}^{2\pi} G(\mathbf{r} - \mathbf{r}')d\varphi dr' dr, \tag{8.45}$$

where $|\mathbf{r} - \mathbf{r}'| = \sqrt{r^2 + r'^2 - 2rr'\cos\varphi}$, where $\mathbf{r}$ and $\mathbf{r}'$ are located on the wire attachment disk S^{aD}. Finally, the last type of integral

$$\int\limits_{z=0}^{\Delta z} \int\limits_{r'=a}^{b} \int\limits_{\varphi=0}^{2\pi} G(\mathbf{r} - \mathbf{r}')d\varphi dr' dz, \qquad \text{with } |\mathbf{r} - \mathbf{r}'| = \sqrt{r'^2 + a^2 - 2ar'\cos\varphi + z^2}, \tag{8.46}$$

occurs when $\mathbf{r} \in S^{aW}$ and $\mathbf{r}' \in S^{aD}$ or vice versa $\mathbf{r} \in S^{aD}$ and $\mathbf{r}' \in S^{aW}$

$$\int\limits_{r=a}^{b} \int\limits_{z'=0}^{\Delta z} \int\limits_{\varphi=0}^{2\pi} G(\mathbf{r} - \mathbf{r}')d\varphi dz' dr, \qquad \text{with } |\mathbf{r} - \mathbf{r}'| = \sqrt{r^2 + a^2 - 2ar\cos\varphi + z'^2}. \tag{8.47}$$

From reciprocity, we note that integrals (8.46) and (8.47) are identical.

Expression for the elements $\underline{C}^{B,a}$

The generic m-th element $C_m^{B,a}$ represents the effect of the current distribution along the attachment region on the m-th RWG surface element. This element is defined as follows

$$\begin{aligned}
C_m^{B,a} &= -j\omega\mu \int\limits_{T_m^+ \cup T_m^-} \boldsymbol{\psi}_m^B(\mathbf{r}) \cdot \left(\int\limits_{S^{aW} \cup S^{aD}} G(\mathbf{r} - \mathbf{r}')\boldsymbol{\psi}^a(\mathbf{r}')dS' \right) dS \\
&+ \frac{1}{j\omega\epsilon} \int\limits_{T_m^+ \cup T_m^-} \boldsymbol{\psi}_m^B(\mathbf{r}) \cdot \left(\nabla_S \int\limits_{S^{aW} \cup S^{aD}} G(\mathbf{r} - \mathbf{r}')\left(\nabla_{S'} \cdot \boldsymbol{\psi}^a(\mathbf{r}')\right)dS' \right) dS.
\end{aligned} \tag{8.48}$$

A relation similar to (7.18) is valid for the equation (8.48). Thus, writing the attachment function $\boldsymbol{\psi}^a$ as the sum of the two contributions $\boldsymbol{\psi}^{aW}$ and $\boldsymbol{\psi}^{aD}$ in (8.22) leads to

$$
\begin{aligned}
C_m^{B,a} &= -j\omega\mu \int\limits_{T_m^+\cup T_m^-} \boldsymbol{\psi}_m^B(\mathbf{r}) \cdot \left(\int\limits_{S^{aW}} G(\mathbf{r}-\mathbf{r}')\boldsymbol{\psi}^{aW}(\mathbf{r}')dS' \right) dS \\
&\quad - \frac{1}{j\omega\epsilon} \int\limits_{T_m^+\cup T_m^-} \left(\nabla_S \cdot \boldsymbol{\psi}_m^B(\mathbf{r})\right) \int\limits_{S^{aW}} G(\mathbf{r}-\mathbf{r}')\left(\nabla_{S'}\cdot\boldsymbol{\psi}^{aW}(\mathbf{r}')\right) dS'dS \\
&\quad - j\omega\mu \int\limits_{T_m^+\cup T_m^-} \boldsymbol{\psi}_m^B(\mathbf{r}) \cdot \left(\int\limits_{S^{aD}} G(\mathbf{r}-\mathbf{r}')\boldsymbol{\psi}^{aD}(\mathbf{r}')dS' \right) dS \\
&\quad - \frac{1}{j\omega\epsilon} \int\limits_{T_m^+\cup T_m^-} \left(\nabla_S \cdot \boldsymbol{\psi}_m^B(\mathbf{r})\right) \int\limits_{S^{aD}} G(\mathbf{r}-\mathbf{r}')\left(\nabla_{S'}\cdot\boldsymbol{\psi}^{aD}(\mathbf{r}')\right) dS'dS.
\end{aligned}
\tag{8.49}
$$

We focus now on the first term of (8.49). Using the fact that the wire is perpendicularly connected to the surface means that the first term on the right-hand side vanishes. Using the explicit expression (7.13) of the RWG function, and of $\boldsymbol{\psi}^a$ (8.22) and using the properties (7.21) and (8.23), we can write equation (8.49) as

$$
\begin{aligned}
C_m^{B,a} &= -\frac{1}{j\omega\epsilon}\frac{\ell_m}{2\pi\Delta z}\left(\frac{1}{A_m^-}\left[\int\limits_{T_m^-}\int\limits_{z'=0}^{\Delta z}\int\limits_{\phi'=0}^{2\pi} G(\mathbf{r}-\mathbf{r}')dz'd\phi'dS \right]_{\{r'=a\}} + \right. \\
&\quad \left. -\frac{1}{A_m^+}\left[\int\limits_{T_m^+}\int\limits_{z'=0}^{\Delta z}\int\limits_{\phi'=0}^{2\pi} G(\mathbf{r}-\mathbf{r}')dz'd\phi'dS \right]_{\{r'=a\}} \right) + \\
&\quad -j\omega\mu\frac{\ell_m}{4\pi(b-a)}\left(\frac{1}{A_m^+}\left[\int\limits_{T_m^+}\int\limits_{r'=a}^{b}\int\limits_{\phi'=0}^{2\pi} G(\mathbf{r}-\mathbf{r}')(r'-b)\mathbf{i}_r(\phi')\cdot\boldsymbol{\rho}_m^+(\mathbf{r})dr'd\phi'dS \right]_{\{z'=0\}} + \right. \\
&\quad \left. +\frac{1}{A_m^-}\left[\int\limits_{T_m^-}\int\limits_{r'=a}^{b}\int\limits_{\phi'=0}^{2\pi} G(\mathbf{r}-\mathbf{r}')(r'-b)\mathbf{i}_r(\phi')\cdot\boldsymbol{\rho}_m^-(\mathbf{r})dr'd\phi'dS \right]_{\{z'=0\}} \right) + \\
&\quad -\frac{1}{j\omega\epsilon}\frac{\ell_m}{2\pi(b-a)}\left(\frac{1}{A_m^+}\left[\int\limits_{T_m^+}\int\limits_{r'=a}^{b}\int\limits_{\phi'=0}^{2\pi} G(\mathbf{r}-\mathbf{r}')dr'd\phi'dS \right]_{\{z'=0\}} + \right.
\end{aligned}
$$

$$-\frac{1}{A_m^-}\left[\int\limits_{T_m^-}\int\limits_{r'=a}^{b}\int\limits_{\phi'=0}^{2\pi} G(\mathbf{r}-\mathbf{r}')dr'd\phi'dS\right]_{\{z'=0\}}\right). \tag{8.50}$$

We observe that the computation of each coupling matrix element requires the calculation of six different four-fold integrals of three different forms

$$\int\limits_{T}\int\limits_{z'=0}^{\Delta}\int\limits_{\phi'=0}^{2\pi} G(\mathbf{r}-\mathbf{r}')dz'd\phi'dS, \qquad \mathbf{r}' = a\cos\phi'\mathbf{i}_x + a\sin\phi'\mathbf{i}_y + z'\mathbf{i}_z, \tag{8.51}$$

$$\int\limits_{T}\int\limits_{r'=a}^{b}\int\limits_{\phi'=0}^{2\pi} G(\mathbf{r}-\mathbf{r}')(r'-b)\mathbf{i}_r(\phi')\cdot\boldsymbol{\rho}(\mathbf{r})dr'd\phi'dS, \quad \mathbf{r}' = r'\cos\phi'\mathbf{i}_x + r'\sin\phi'\mathbf{i}_y, \tag{8.52}$$

$$\int\limits_{T}\int\limits_{r'=a}^{b}\int\limits_{\phi'=0} G(\mathbf{r}-\mathbf{r}')dr'd\phi'dS, \quad \mathbf{r}' = r'\cos\phi'\mathbf{i}_x + r'\sin\phi'\mathbf{i}_y, \tag{8.53}$$

where $T = T_m^\pm$ is a generic triangular patch and $\boldsymbol{\rho}$ denotes the position of the observation point $\mathbf{r}$ in the triangle T, $\mathbf{r} = r\cos\phi\mathbf{i}_x + r\sin\phi\mathbf{i}_y$, see Fig. 8.2.
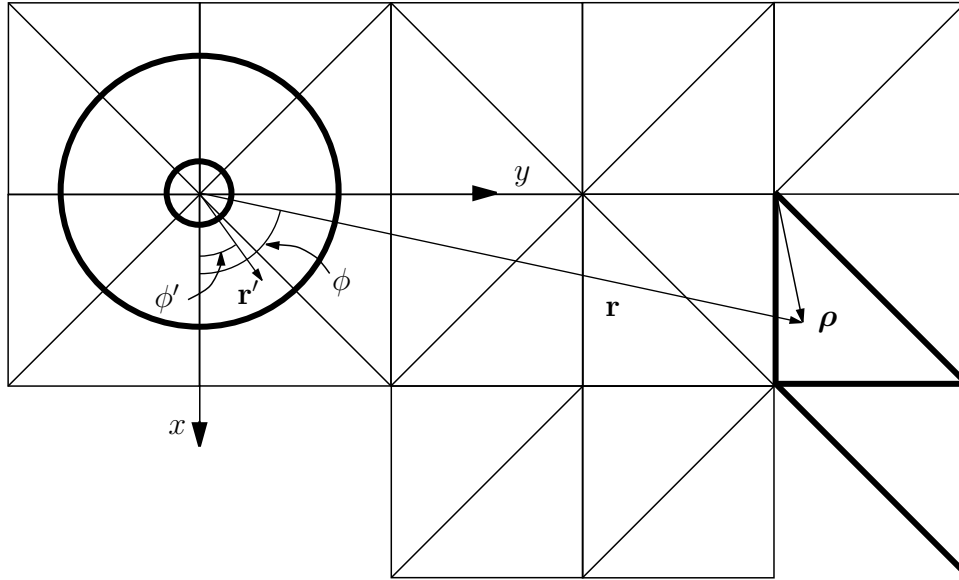
Figure 8.2: *Geometry of the attachment problem on the (x, y)-plane.*

Expression for the elements of $\underline{C}^{W,a}$

In this case the n-th coupling element $C_n^{W,a}$ represents the effect of the current distribution along the wire-to-surface attachment on the n-th rooftop element and it has the following

expression

$$
C_n^{W,a} = -j\omega\mu \frac{1}{2\pi} \int\limits_{z=(n-1)\Delta z}^{(n+1)\Delta z} \boldsymbol{\psi}_n^W(z) \cdot \left(\int\limits_{\phi=0}^{2\pi} \int\limits_{S^{aW}\cup S^{aD}} G(\mathbf{r}-\mathbf{r}')\boldsymbol{\psi}^a(\mathbf{r}')dS' \right) d\phi dz
$$

$$
+ \frac{1}{j\omega\epsilon} \frac{1}{2\pi} \int\limits_{z=(n-1)\Delta z}^{(n+1)\Delta z} \boldsymbol{\psi}_n^W(z) \cdot \left(\int\limits_{\phi=0}^{2\pi} \nabla_S \int\limits_{S^{aW}\cup S^{aD}} G(\mathbf{r}-\mathbf{r}') \left(\nabla_{S'} \cdot \boldsymbol{\psi}^a(\mathbf{r}') \right) dS' \right) d\phi dz. \quad (8.54)
$$

The second integral term on the right-hand side of (8.54) can be written as

$$
\frac{1}{j\omega\epsilon} \frac{1}{2\pi} \int\limits_{z=(n-1)\Delta z}^{(n+1)\Delta z} \int\limits_{\phi=0}^{2\pi} \boldsymbol{\psi}_n^W(z) \cdot \left(\nabla_S \int\limits_{S^{aW}\cup S^{aD}} G(\mathbf{r}-\mathbf{r}') \left(\nabla_{S'} \cdot \boldsymbol{\psi}^a(\mathbf{r}') \right) dS' \right) d\phi dz. \quad (8.55)
$$

Moreover, since the n-th triangular function $\boldsymbol{\psi}_n^W$ (8.3) vanishes at the contour boundaries of the surface S_n^W, the following property is valid

$$
\int\limits_{z=(n-1)\Delta z}^{(n+1)\Delta z} \int\limits_{\phi=0}^{2\pi} \boldsymbol{\psi}_n^W(z) \cdot \left(\nabla_S \int\limits_{S^{aW}\cup S^{aD}} G(\mathbf{r}-\mathbf{r}') \left(\nabla_{S'} \cdot \boldsymbol{\psi}^a(\mathbf{r}') \right) dS' \right) d\phi dz =
$$

$$
- \int\limits_{z=(n-1)\Delta z}^{(n+1)\Delta z} \int\limits_{\phi=0}^{2\pi} \left(\nabla_S \cdot \boldsymbol{\psi}_n^W(z) \right) \int\limits_{S^{aW}\cup S^{aD}} G(\mathbf{r}-\mathbf{r}') \left(\nabla_{S'} \cdot \boldsymbol{\psi}^a(\mathbf{r}') \right) dS'dS. \quad (8.56)
$$

Therefore, from (8.54), writing the attachment function in terms of $\boldsymbol{\psi}^{aW}$ and $\boldsymbol{\psi}^{aD}$ we obtain

$$
\begin{aligned}
C_n^{W,a} =\ & -j\omega\mu \frac{1}{2\pi} \int\limits_{z=(n-1)\Delta z}^{(n+1)\Delta z} \int\limits_{\phi=0}^{2\pi} \int\limits_{S^{aW}} G(\mathbf{r}-\mathbf{r}')\boldsymbol{\psi}_n^W(\mathbf{r}) \cdot \boldsymbol{\psi}^{aW}(\mathbf{r}')dS'd\phi dz \\
& -j\omega\mu \frac{1}{2\pi} \int\limits_{z=(n-1)\Delta z}^{(n+1)\Delta z} \int\limits_{\phi=0}^{2\pi} \int\limits_{S^{aD}} G(\mathbf{r}-\mathbf{r}')\boldsymbol{\psi}_n^W(\mathbf{r}) \cdot \boldsymbol{\psi}^{aD}(\mathbf{r}')dS'd\phi dz \\
& -\frac{1}{j\omega\epsilon} \frac{1}{2\pi} \int\limits_{z=(n-1)\Delta z}^{(n+1)\Delta z} \int\limits_{\phi=0}^{2\pi} \left(\nabla_S \cdot \boldsymbol{\psi}_n^W(\mathbf{r}) \right) \int\limits_{S^{aW}} G(\mathbf{r}-\mathbf{r}') \left(\nabla_{S'} \cdot \boldsymbol{\psi}^{aW}(\mathbf{r}') \right) dS'd\phi dz \\
& -\frac{1}{j\omega\epsilon} \frac{1}{2\pi} \int\limits_{z=(n-1)\Delta z}^{(n+1)\Delta z} \int\limits_{\phi=0}^{2\pi} \left(\nabla_S \cdot \boldsymbol{\psi}_n^W(\mathbf{r}) \right) \int\limits_{S^{aD}} G(\mathbf{r}-\mathbf{r}') \left(\nabla_{S'} \cdot \boldsymbol{\psi}^{aD}(\mathbf{r}') \right) dS'd\phi dz. \quad (8.57)
\end{aligned}
$$

Using the fact that the wire is perpendicularly connected to the surface, with the aid of (8.22), (8.23) and of the explicit expressions (8.3) of the n-th triangular function, we write the coupling matrix element (8.57) as

$$
C_n^{W,a} = -j\omega\mu\frac{1}{4\pi^2}\left[\int\limits_{z=(n-1)\Delta z}^{(n+1)\Delta z}\int\limits_{\phi=0}^{2\pi}\int\limits_{z'=0}^{\Delta z}\int\limits_{\phi'=0}^{2\pi} G(\mathbf{r}-\mathbf{r}')\left(1-\frac{z'}{\Delta z}\right)\times\right.
$$

$$
\left.\left(1-\left|\frac{z}{\Delta z}-n\right|\right)d\phi'dz'd\phi dz\right]_{\{r=r'=a\}} +
$$

$$
+\frac{1}{j\omega\epsilon}\frac{1}{4\pi^2\Delta z^2}\left[\int\limits_{z=(n-1)\Delta z}^{n\Delta z}\int\limits_{\phi=0}^{2\pi}\int\limits_{z'=0}^{\Delta z}\int\limits_{\phi'=0}^{2\pi} G(\mathbf{r}-\mathbf{r}')d\phi'dz'd\phi dz\right]_{\{r=r'=a\}}
$$

$$
-\frac{1}{j\omega\epsilon}\frac{1}{4\pi^2\Delta z^2}\left[\int\limits_{z=n\Delta z}^{(n+1)\Delta z}\int\limits_{\phi=0}^{2\pi}\int\limits_{z'=0}^{\Delta z}\int\limits_{\phi'=0}^{2\pi} G(\mathbf{r}-\mathbf{r}')d\phi'dz'd\phi dz\right]_{\{r=r'=a\}}
$$

$$
-\frac{1}{j\omega\epsilon}\frac{1}{4\pi^2(b-a)\Delta z}\left[\int\limits_{z=(n-1)\Delta z}^{n\Delta z}\int\limits_{\phi=0}^{2\pi}\int\limits_{r'=a}^{b}\int\limits_{\phi'=0}^{2\pi} G(\mathbf{r}-\mathbf{r}')d\phi'dr'd\phi dz\right]_{\{r=a,\ z'=0\}}
$$

$$
+\frac{1}{j\omega\epsilon}\frac{1}{4\pi^2(b-a)\Delta z}\left[\int\limits_{z=n\Delta z}^{(n+1)\Delta z}\int\limits_{\phi=0}^{2\pi}\int\limits_{r'=a}^{b}\int\limits_{\phi'=0}^{2\pi} G(\mathbf{r}-\mathbf{r}')d\phi'dr'd\phi dz\right]_{\{r=a,\ z'=0\}}. \tag{8.58}
$$

Observing that all the integrands in (8.58) depend on $\varphi=\phi-\phi'$, we reduce the four-fold integrals in (8.58) to three-fold integrals. Moreover, looking at the previous expression, we recognize three different types of integrals

$$
\int\limits_{z=(n-1)\Delta z}^{(n+1)\Delta z}\int\limits_{z'=0}^{\Delta z}\int\limits_{\varphi=0}^{2\pi} G(\mathbf{r}-\mathbf{r}')\left(1-\frac{z'}{\Delta z}\right)\left(1-\left|\frac{z}{\Delta z}-n\right|\right)d\varphi dz'dz,
$$

$$
|\mathbf{r}-\mathbf{r}'| = \sqrt{(z-z')^2+4a^2\sin^2(\varphi/2)}, \tag{8.59}
$$

$$
\int\limits_{z=z_1}^{z_2}\int\limits_{z'=0}^{\Delta z}\int\limits_{\varphi=0}^{2\pi} G(\mathbf{r}-\mathbf{r}')d\varphi dz'dz, \qquad |\mathbf{r}-\mathbf{r}'| = \sqrt{(z-z')^2+4a^2\sin^2(\varphi/2)}, \tag{8.60}
$$

$$
\int\limits_{z=z_1}^{z_2}\int\limits_{r'=a}^{b}\int\limits_{\varphi=0}^{2\pi} G(\mathbf{r}-\mathbf{r}')d\varphi dr'dz, \qquad |\mathbf{r}-\mathbf{r}'| = \sqrt{r'^2+a^2-2r'a\cos\varphi+z^2}, \tag{8.61}
$$

where the integration boundaries z_1 and z_2 can assume the values $z_1 = (n - 1)\Delta z$ and $z_2 = n\Delta z$, or $z_1 = n\Delta z$ and $z_2 = (n + 1)\Delta z$. Note that the integral (8.59) is similar to (8.42), while the integrals (8.60) and (8.61) are identical to (8.43) and (8.46), respectively, except for the integration boundaries.

8.2.4 Evaluation of the matrix $\underline{\mathbf{Z}}$

In the previous section, the expressions for the elements of the matrix $\underline{\underline{\mathbf{Z}}}$ are given in (8.40), (8.50) and in (8.58). The computation of these elements requires the integration of nine different forms which are listed in Appendix G.1. We observe that these integrals contain the Green's function of the Helmholtz operator, $G(\mathbf{r} - \mathbf{r}')$, which exhibits a singularity when the distance $|\mathbf{r} - \mathbf{r}'|$ approaches zero. In this case, special attention should be taken in the the numerical evaluation of all the integrals. For this reason, we followed different approaches depending on the relative position between the source point $\mathbf{r}' \in S^{aW} \cup S^{aD}$ and the observation point $\mathbf{r}$ over the triangular patch T_m or over the wire segment surface or over $S^{aW} \cup S^{aD}$. We distinguish three different situations:

- when $\mathbf{r}' \in S^{aW}$ and $\mathbf{r}$ is on the first wire segment surface, the integrand exhibits a singular behavior and we follow the strategy already developed for the single wire. The singular term is extracted and analytically integrated, see Sec. 3.3, equation (3.35). Also when $\mathbf{r}' \in S^{aW}$ and $\mathbf{r}$ is on the triangular patch T_m sharing a vertex with the attachment point, the integrand is unbounded (i.e. exhibits a singular behavior). In this case a series expansion of the Green's function for the Helmholtz operator in cylindrical coordinates has been introduced for the calculation of the integral (see Appendix G.1);

- when $\mathbf{r}' \in S^{aW}$ and $\mathbf{r}$ is on the wire surface but is not on the mantle of the first segment then the integrand is bounded and we perform a numerical integration;

- for all the other cases a brute-force numerical integration is performed by means of an adaptive multidimensional routine [65] .

Details on treatments of singular cases are discussed in Appendix G.1. Numerical and analytical techniques are introduced in order to calculate the matrix elements with a computer program in an accurate way. For ease of implementation, we discretize the attachment region with a triangular mesh as shown in Fig. 8.3.

PSfrag replacements
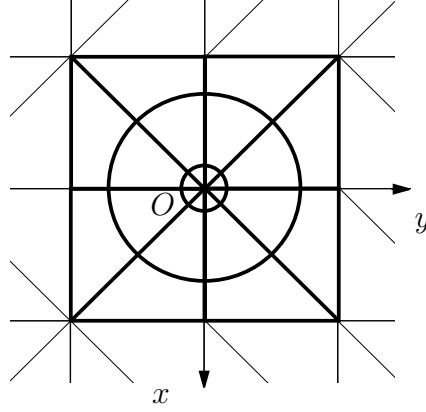
Figure 8.3: *Symmetric mesh configuration in the attachment region.*

At first sight, this simplification may appear as a limitation in positioning the attached wire only at the surface mesh points. In reality, a proper mesh can be generated starting from the attachment point, thus, the connection point can be located everywhere on the surface. An advantage of the inherent symmetry is related to the evaluation of the coupling element $C_m^{B,a}$. The required four-fold integrations (8.50) over the patches involved in the attachment need to be carried out only once over one triangular patch. In fact, the integrations over the patches sharing a vertex with the attachment point will provide the same result. From the expression (8.50) it follows that for those RWG functions defined on triangle pairs involved in the attachment (i.e., both triangles T_m^+ and T_m^- sharing a vertex with the attachment point), the coupling element $C_m^{B,a}$ vanishes. Thus, in the numerical implementation, the computation of these terms can be omitted, which saves CPU time.

8.2.5   Calculation of the vector $\underline{\mathbf{F}}_e^a$

As we have already pointed out, the vector $\underline{\mathbf{F}}_e^a$ on the right-hand side of equation (8.37) has only one element and it represents the contribution due to weighted external excitation (i.e., an incident plane wave and/or a delta-gap voltage) on the attachment region. It is defined as

$$F_e^a = \left\langle \boldsymbol{\psi}^a(\mathbf{r}), V(\omega)\delta(z - z_g)\mathbf{i}_z + \mathbf{E}^i(\mathbf{r}) \right\rangle = \int_{S^{aW} \cup S^{aD}} \boldsymbol{\psi}^a(\mathbf{r}) \cdot \left(V\delta(z - z_g)\mathbf{i}_z + \mathbf{E}^i(\mathbf{r}) \right) dS, \quad (8.62)$$

where S^{aW} and S^{aD} are the wire and the disk regions involved in the attachment. Substituting the explicit expression of the attachment function $\boldsymbol{\psi}^a$ as in (8.22) leads to

$$
\begin{aligned}
F_e^a &= \frac{1}{2\pi} \left[\int\limits_{z=0}^{\Delta z} \int\limits_{\phi=0}^{2\pi} \left(1 - \frac{z}{\Delta z}\right) \left(V(\omega)\delta(z - z_g)\mathbf{i}_z + \mathbf{E}^i(\mathbf{r})\right) \cdot \mathbf{i}_z d\phi dz \right]_{\{r=a\}} \\
&+ \frac{1}{2\pi(b-a)} \left[\int\limits_{r=a}^{b} \int\limits_{\phi=0}^{2\pi} (r - b) \left(V(\omega)\delta(z - z_g)\mathbf{i}_z + \mathbf{E}^i(\mathbf{r})\right) \cdot \mathbf{i}_r(\mathbf{r}) d\phi dr \right]_{\{z=0\}}.
\end{aligned} \tag{8.63}
$$

The first two-fold integral, where $\mathbf{r} = a\cos\phi\mathbf{i}_x + a\sin\phi\mathbf{i}_y + z\mathbf{i}_z$ belongs to the wire attachment region S^{aW}, and, for an incident plane wave can be calculated analytically. While the two-fold integral where $\mathbf{r} = r\cos\phi\mathbf{i}_x + r\sin\phi\mathbf{i}_y$ is on S^{aD}, is carried out numerically with an adaptive multidimensional routine [65]. Explicit expressions of these integrals are given in Appendix G.2.

8.3   Numerical results

The method outlined in Sec. 8.1 and Sec. 8.2 has been implemented in a FORTRAN computer code referred to as GEKMoM+ which is able to calculate the current on the perfectly electrically conducting surface (PEC) and along the PEC wire including the case of a wire perpendicularly connected to a planar surface. Several test cases have been run to validate the code.

8.3.1   Coupling between a thin wire and a PEC square plate

We consider a thin wire of length $\lambda/2$ with a radius $a = 0.001\lambda$, placed centrally and parallel at a distance d from a square surface of dimensions $\lambda \times \lambda$. The structure is excited by a normally incident plane wave, x-polarized, with an amplitude of $|\mathbf{E}^i| = 1$ V/m and $\lambda = 1$ m. This configuration is depicted in Fig. 8.4. The wire current computed is compared with the one obtained by using the commercial software NEC 4.1 [2]. It is important to underline that our numerical scheme discretizes the planar surface with patches, $N_x = N_y = 16$, which means that $N_p = 512$ triangular patches are used. With NEC, we use a wire grid of 21 wires parallel to the x-direction and 21 wires parallel to the y-direction spaced with $d_w = \lambda/20$ and with radius $a = d_w/2\pi$, designed following the guidelines in [2]. The wire current is expanded with $N = 35$ basis functions in both schemes.
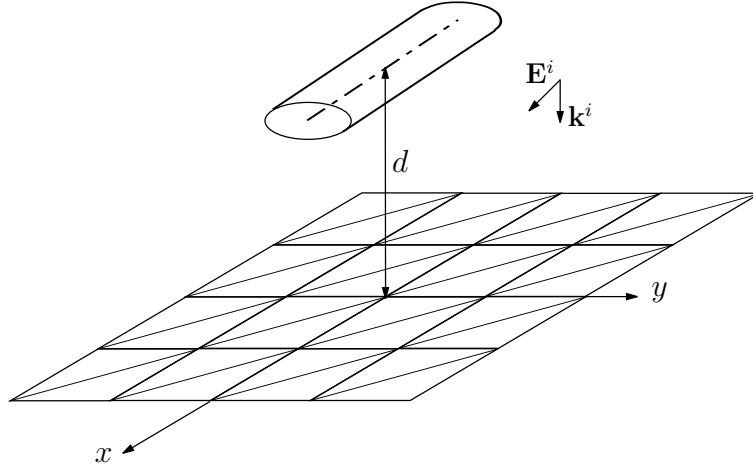
Figure 8.4: *Geometry of the configuration.*

A good agreement between the wire current computed by using the described numerical scheme (named as "GEKMoM+") and NEC 4.1, is shown in Fig. 8.5 when the wire and the surface are placed at a distance $d = 0.3\lambda$. Figure 8.6 shows the amplitude of the x-component of the surface current distribution together with its contour plot calculated using GEKMoM+.
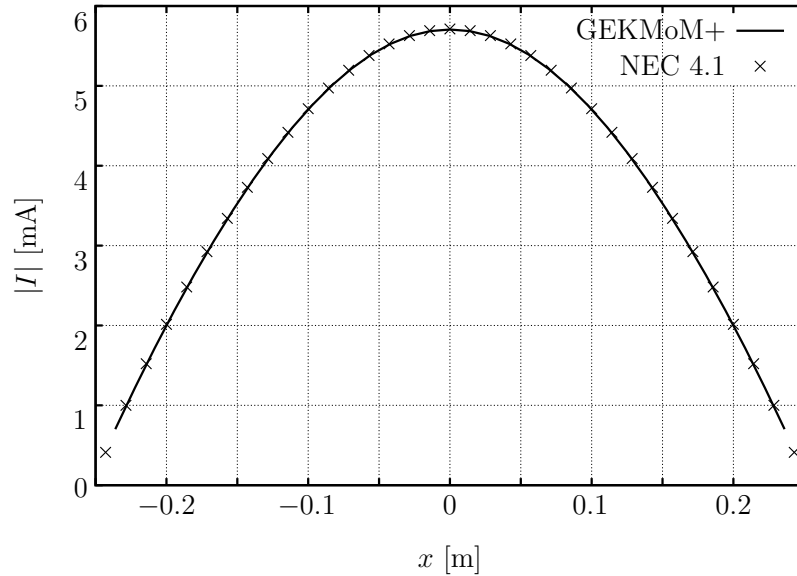
Figure 8.5: *Magnitude of the total current along the thin wire placed at a distance $d = 0.3\lambda$ from the square plate.*
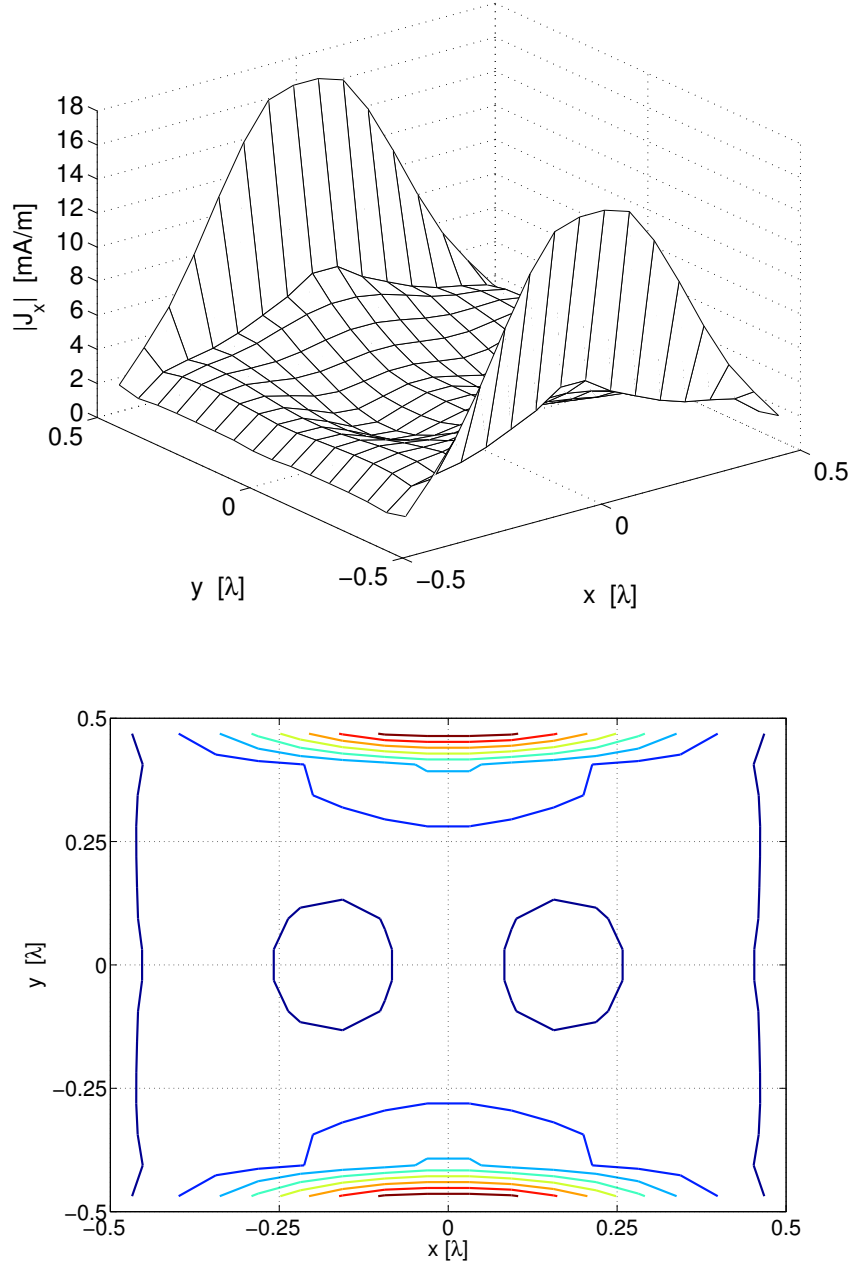
Figure 8.6: *Surface current distribution and contour plot of $|J_x|$ on the square plate placed at a distance $d = 0.3\lambda$ from the thin wire.*

Next we investigate what happens when the distance between the wire and the surface is reduced to 0.1λ. In this case the mutual interaction between the two objects is stronger. The amplitude of the x-component of the surface current distribution together with its contour plot is depicted in Fig. 8.7. For the sake of comparison we report in Fig. 8.8 the

results of the planar surface without the wire.
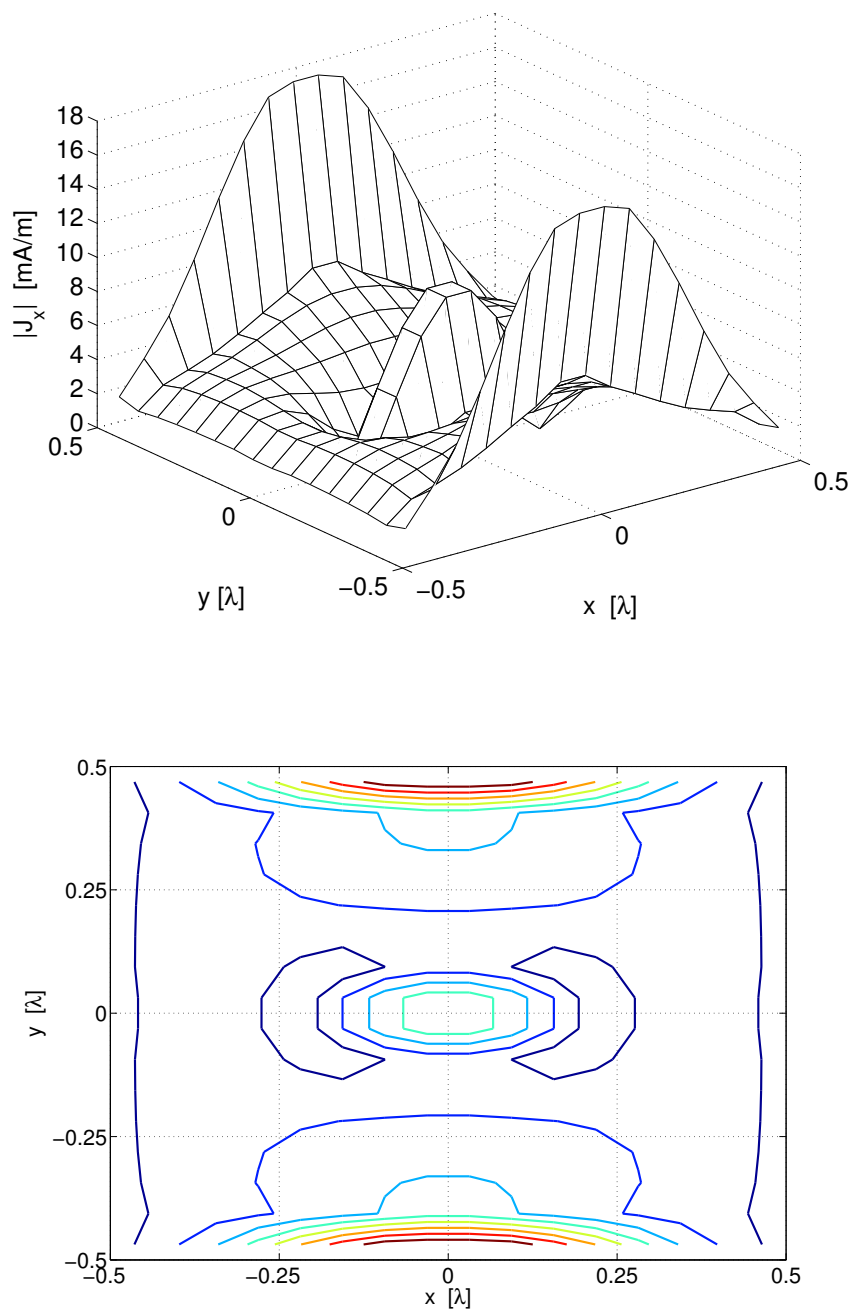
Figure 8.7: *Surface current distribution and contour plot of $|J_x|$ on the square plate placed at a distance $d = 0.1\lambda$ from the thin wire.*
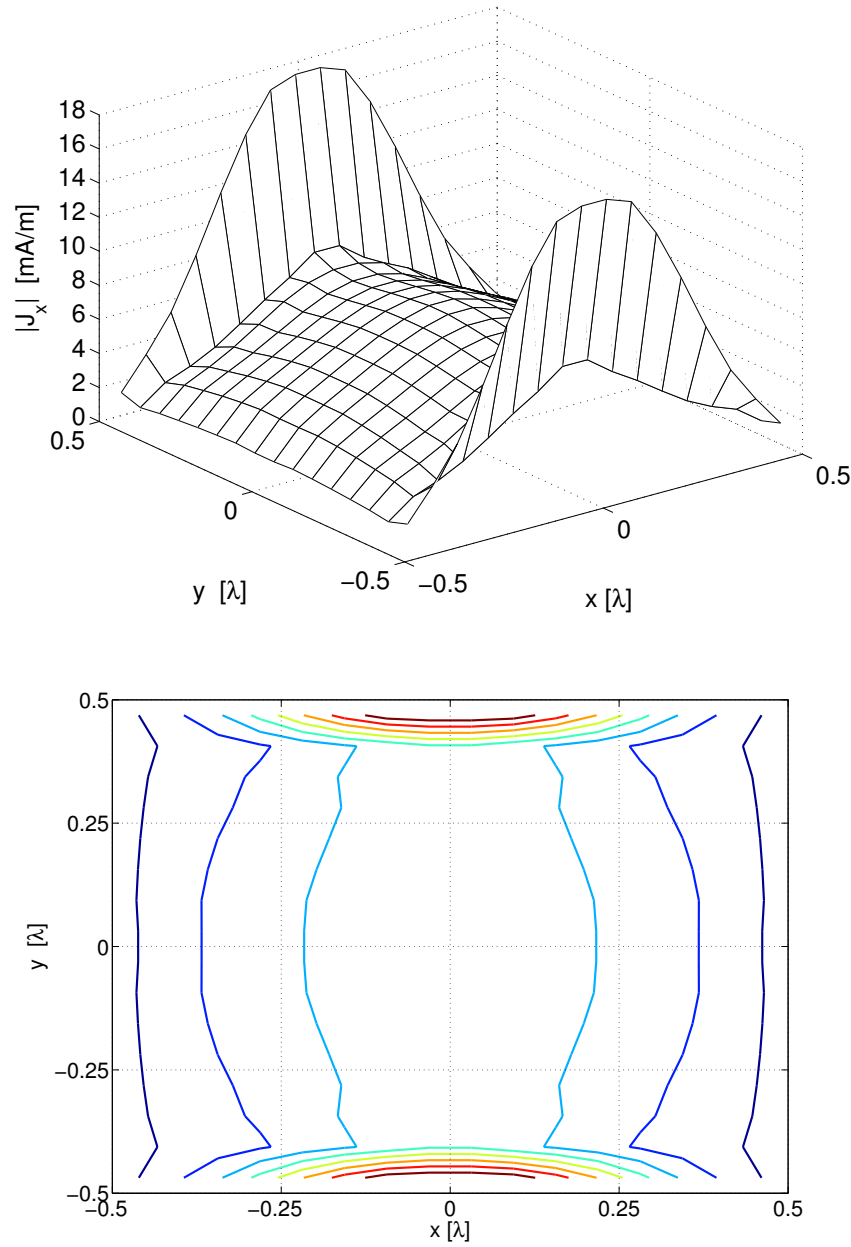
Figure 8.8: *Surface current distribution and contour plot of $|J_x|$ on the square plate without the wire.*

As additional case we compute the current distribution on the square plate when the wire is asymmetrically located (see Fig. 8.9). In Figs. 8.10 and 8.11, the absolute value of the x-components of the resulting currents are shown together with their contour plots for two different distances d.
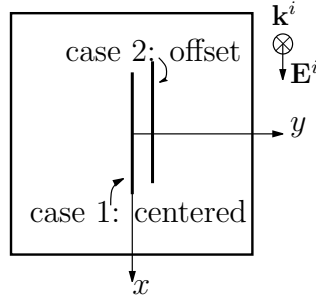
Figure 8.9: *Centered and offset configurations. Offset in x-direction:* 0.05λ, *offset in y-direction:* 0.1λ.
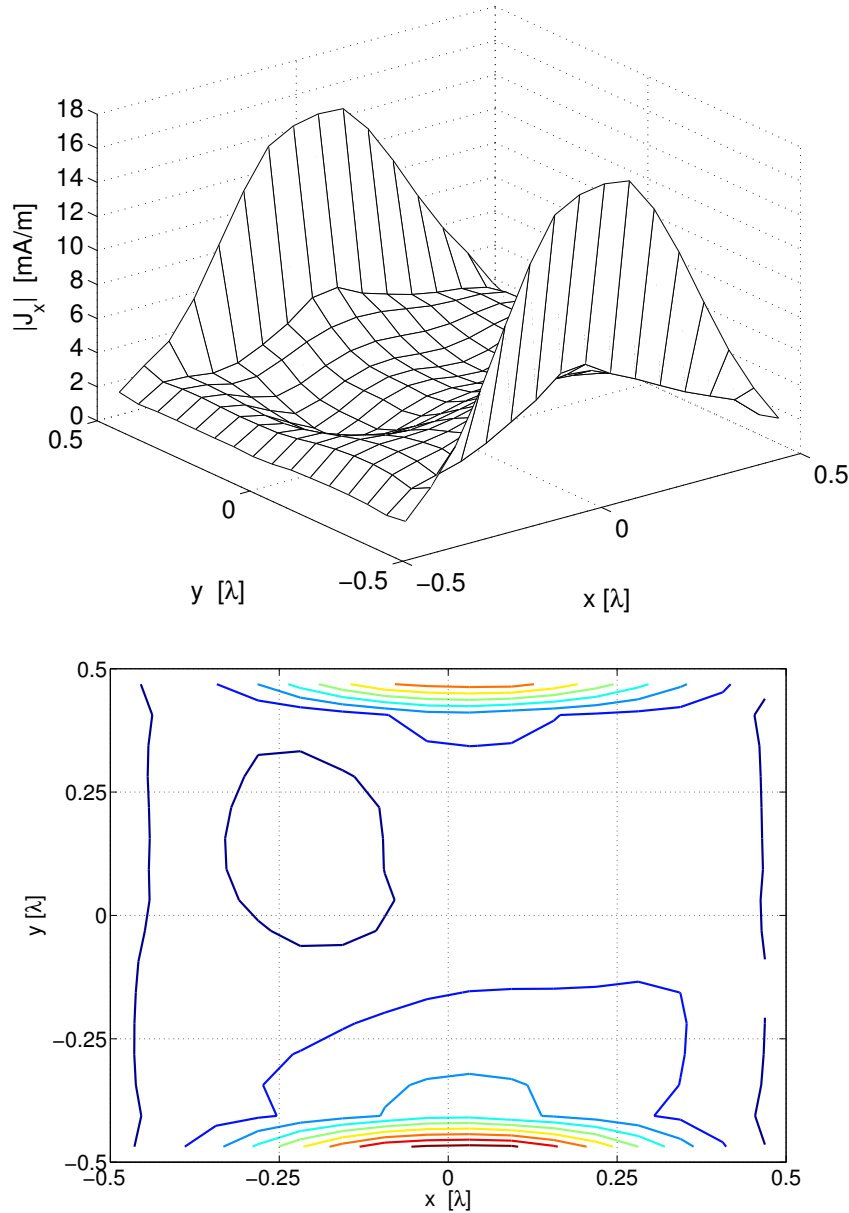
Figure 8.10: *Surface current distribution and contour plot of* $|J_x|$ *on the square plate placed at a distance* $d = 0.3\lambda$ *from the thin wire asymmetrically placed.*
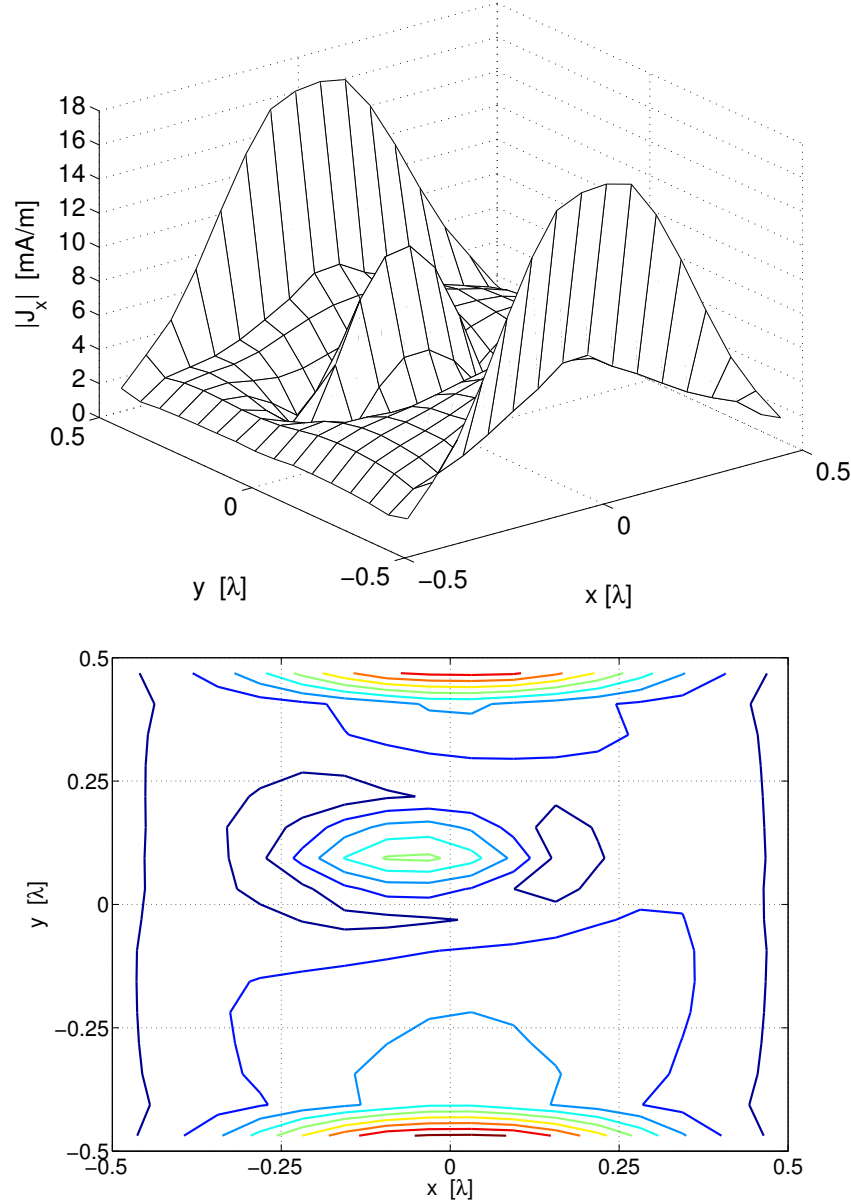
Figure 8.11: *Surface current distribution and contour plot of $|J_x|$ on the square plate placed at a distance $d = 0.1\lambda$ from the thin wire asymmetrically placed.*

Further the wire current for varying d is analyzed. In particular, from Fig. 8.12, we notice that decreasing the distance between the wire and the planar surface corresponds to a reduction in the amplitude of the wire current distribution (to the extreme case of a current equal to zero), as physically expected from image theory. In both cases the wire current distribution has an invariant shape.

(a)   (b)
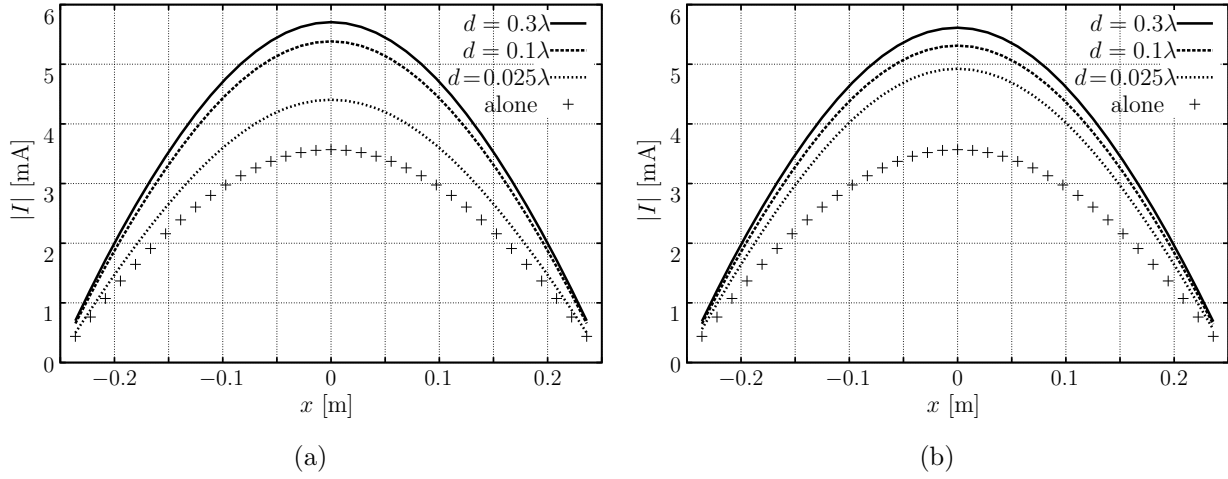
Figure 8.12: *Comparison between the total current magnitude along the wire in presence of the square plate at different distances and for the thin wire without the surface: (a)-centered configuration; (b)- offset configuration.*

As further test, we calculate the total current along the same thin-wire antenna (i.e., $h = \lambda/2$, radius $a = 0.001\lambda$) fed by a delta-gap voltage in its center. This antenna is placed centrally and parallel at a distance $d = 0.3\lambda$ from a $L \times L$ square plate, Fig. 8.13-(a). We consider three different plate dimensions: $L = 0.75\lambda$, 1λ and 1.75λ, discretized with $N_x = N_y = 12$, 16 and 28, respectively. The wire current is expanded with $N = 35$ basis functions. Moreover, we analyze this scattering problem also applying the image theory, referred to as "infinite ground plane". In this case the problem is analyzed by placing a virtual image wire at a distance d below the interface as depicted in Fig. 8.13-(b) [79].

(a)   (b)
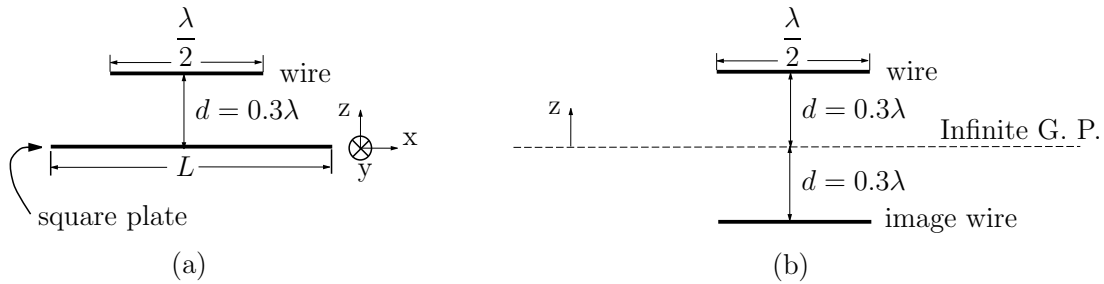
Figure 8.13: *Geometry of the configuration: (a)- $\lambda/2$ wire and L square plate; (b)- source wire and image (virtual) wire as follows from image theory [79].*

Figures 8.14 and 8.15 show the wire current amplitude and phase for different plate dimensions, respectively. Enlarging the surface dimensions from $L = 0.75\lambda$ to $L = 1.75\lambda$, we observe, as expected, that the wire current approaches that found when an infinite ground

plane (continuous line) is considered. As a matter of fact, the length of the wire becomes smaller compared to the planar surface and the effect of the finite dimensions of the plate are less noticeable in agreement with the image theory.
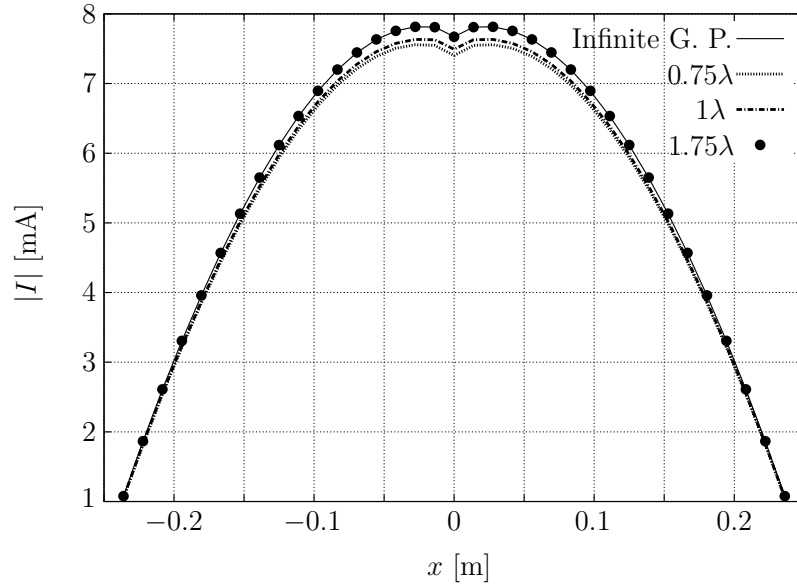
Figure 8.14: *Magnitude of the total current along a thin wire fed by a delta-gap voltage. The wire is placed at a distance $d = 0.3\lambda$ from the square plate.*
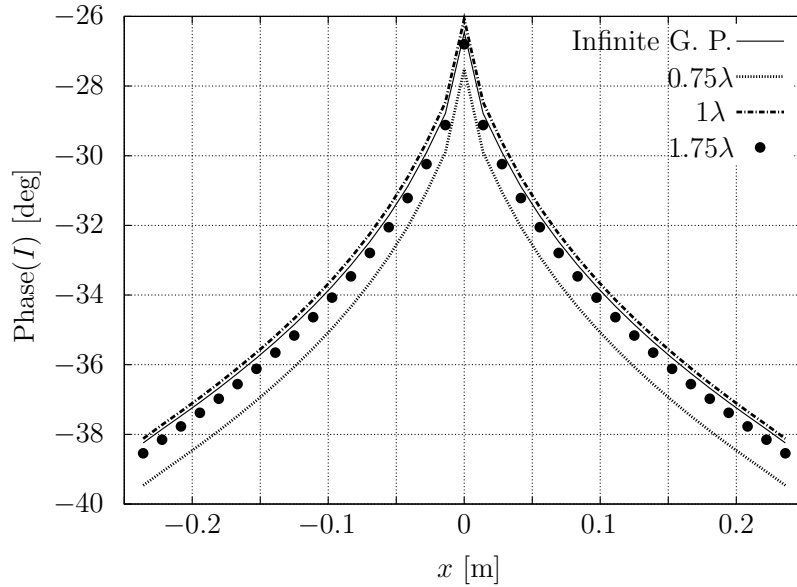
Figure 8.15: *Phase of the total current along a thin wire fed by a delta-gap voltage. The wire is placed at a distance $d = 0.3\lambda$ from the square plate.*

8.3.2 Coupling between a thin strip and a thin wire

In this section we investigate the electromagnetic coupling present between two parallel thin wires due to an incident plane wave. To validate the numerical code GEKMoM+, this configuration is modeled in two different ways as depicted in Fig. 8.16.
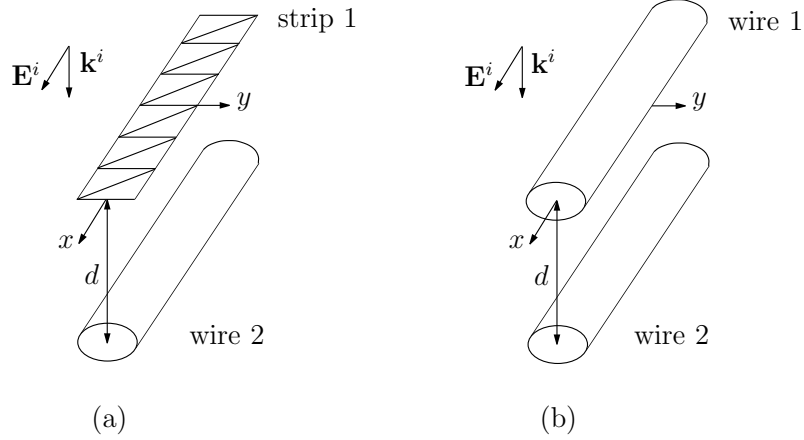
Figure 8.16: *Geometry of the configuration: (a)- wire* 1 *modeled as a surface thin-strip and wire* 2 *as a cylindrical straight thin wire; (b)- two cylindrical straight thin wires.*

As the reference configuration we consider two cylindrical straight wires (wire-wire model) already validated in Chapter 6. GEKMoM+ is applied to a perfectly conducting thin strip of infinitesimal thickness and width $w = 0.05$ m coupled with a cylindrical straight wire (strip-wire model) and results are compared with the ones for the reference configuration. The incident electric field is taken to be a normally incident plane wave with the electric field vector parallel to the x-axis and with an amplitude of $|\mathbf{E}^i| = 1$ V/m and a frequency of $f = 75$ MHz. The two wires of length $\lambda/2$ are placed at a distance $d = 3$ m. The first wire, wire 1, has the same length as the strip and has a diameter d such that the lateral surface of the wire is equal to the strip surface (i.e., $d = w/\pi$, where w is the strip width). The two wires in the wire-wire model have been discretized with 35 segments, while two different meshes are used for the strip-wire model: $N_x = 35$, $N_y = 1$ and $N_x = 35$, $N_y = 5$, where N_x and N_y denote the discretization numbers along the x- and y-directions. For the sake of comparison, we refer the reader to Fig. 7.11, where the current along the straight thin wire without the surface has been shown. For both models we evaluate the total current flowing along the two wire antennas and we compare the results. Figure 8.17 shows the current along wire 1 which is modeled in two different ways: as a strip and as a cylinder. In this case, as already explained in Sec. 7.6.2, when the strip-wire model is used, the output of the numerical code is expressed in terms of a surface current density

and therefore an integration in the transverse direction is needed to compare the results with the ones obtained with the wire-wire model. The current along wire 2, modeled as a straight thin cylinder, is depicted in Fig. 8.18. Even with a coarse strip discretization ($N_y = 1$) in the strip-wire model, we observe a good agreement in the magnitude of the current for both cases. We observe that the GEKMoM+ code is able to reproduce the correct behavior of the current with a relative error of 0.03.
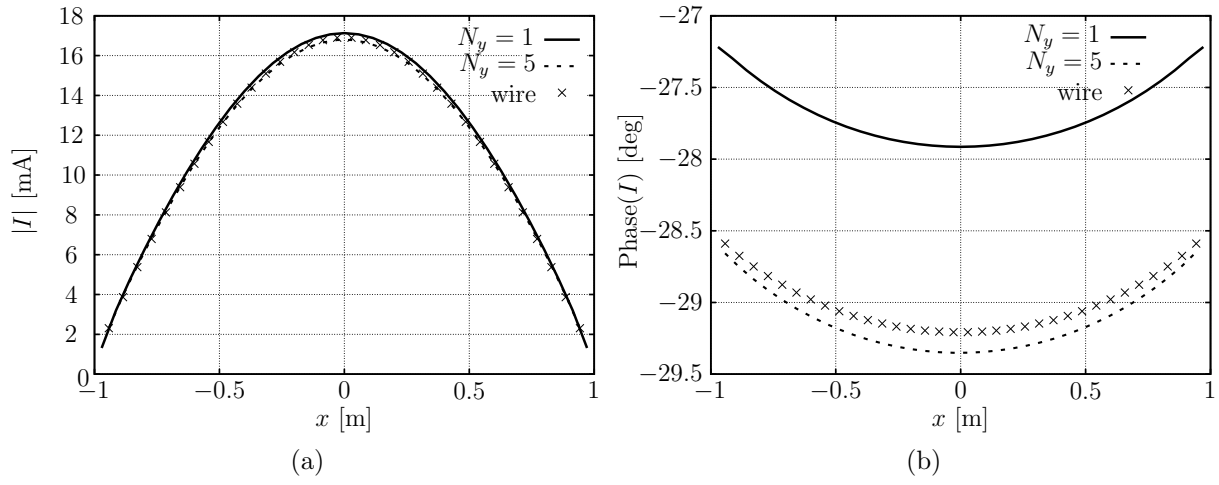
Figure 8.17: *Total current along dipole* 1*: (a)- magnitude; (b)- phase.*
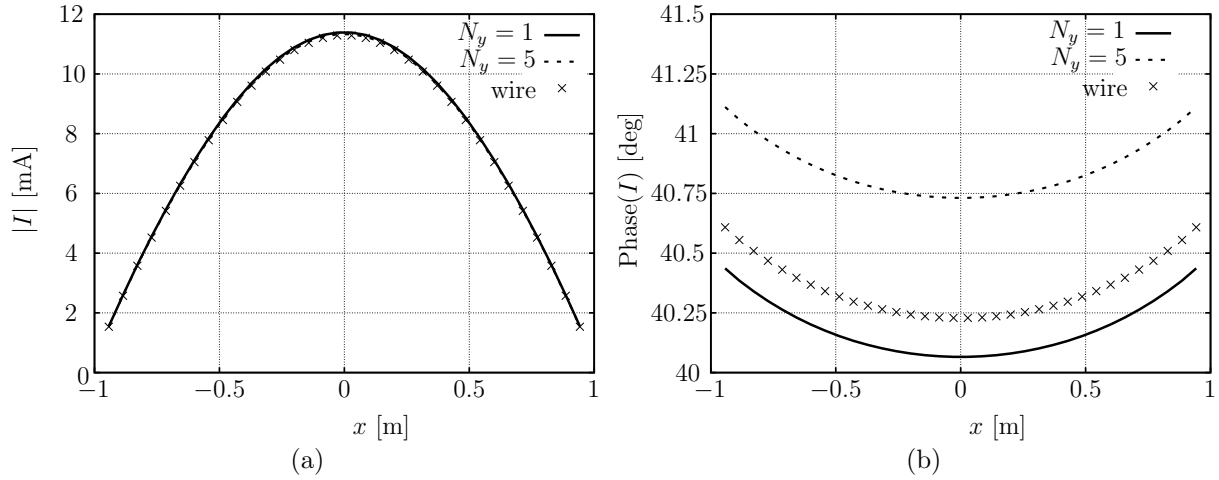
Figure 8.18: *Total current along dipole* 2*: (a)- magnitude; (b)- phase.*

8.3.3 Wire antenna perpendicularly mounted on a finite PEC square plate

We consider a wire antenna (monopole) orthogonally connected to the center of a $1.4\lambda \times 1.4\lambda$ square ground plane. The monopole has radius $a = 1$ mm and is fed by a delta-gap voltage $V = 1$ V at its base. We compute the input impedance of this monopole. First, the wire current is approximated by means of $N = 4$ rooftop functions. Results computed with GEKMoM+ by varying the number M of RWG functions are shown in Fig. 8.19-(a) for the resistance R and in Fig. 8.19-(b) for the input reactance X versus the length h of the monopole. Focusing on the ground plane discretization, we observe that stepping from a mesh size of 0.35λ (i.e., $M = 40$) to 0.14λ (i.e., $M = 280$) does not affect the input impedance values significantly, see Fig. 8.19.

Second, the surface current on the ground plane is approximated by means of $M = 176$ RWG functions while the number N of rooftop functions varies. From the input impedance values in Fig. 8.20 we can conclude that the method converges for the example described. Moreover, in Figs. 8.21 and 8.22, the input impedance values (i.e., R and X) are compared with the ones computed by considering an infinite ground plane and applying image theory (see [79]), and with similar analysis found in the literature [20]. In this case $M = 280$ RWG functions and $N = 4$ rooftop functions are used to discretize the surface current and the wire current, respectively. According to image theory, we analyze a dipole of length $2h$ in free space, discretized with $N_{\mathrm{dip}} = 2N$ triangular basis functions. From the dipole impedance values (i.e., R_{dip} and X_{dip}) we obtain those of the monopole as $R_{\mathrm{mon}} = R_{\mathrm{dip}}/2$, $X_{\mathrm{mon}} = X_{\mathrm{dip}}/2$.

Results are given in Figs. 8.21-(a) and 8.22-(a) for the numerical scheme presented (GEKMoM+), and in Figs. 8.21-(b) and 8.22-(b) as obtained in the literature [20]. Comparing results for a $1.4\lambda \times 1.4\lambda$ ground plane (continuous line) with those for an infinite ground plane (black circles), we observe a good agreement particularly for a decreasing length of the dipole. Indeed, the ground plane becomes large compared with the length of the dipole in agreement with the image theory. From our results, we calculate a relative error

$$\varepsilon_{\mathrm{R}} = \frac{|R_{\mathrm{infGP}} - R_{\mathrm{GP}}|^2}{|R_{\mathrm{infGP}}|^2}, \qquad \varepsilon_{\mathrm{X}} = \frac{|X_{\mathrm{infGP}} - R_{\mathrm{GP}}|^2}{|X_{\mathrm{infGP}}|^2}, \tag{8.64}$$

for the resistance R and reactance X, where R_{infGP}, X_{infGP} are the values for infinite ground plane (image theory) and R_{GP}, X_{GP} are those for a $1.4\lambda \times 1.4\lambda$ ground plane. Reducing the monopole length from 0.3λ to 0.1λ we obtain a reduction in the relative error ε_{R} from 0.0145 to 0.0054 and in the relative error ε_{X} from 0.0788 to 0.0002.
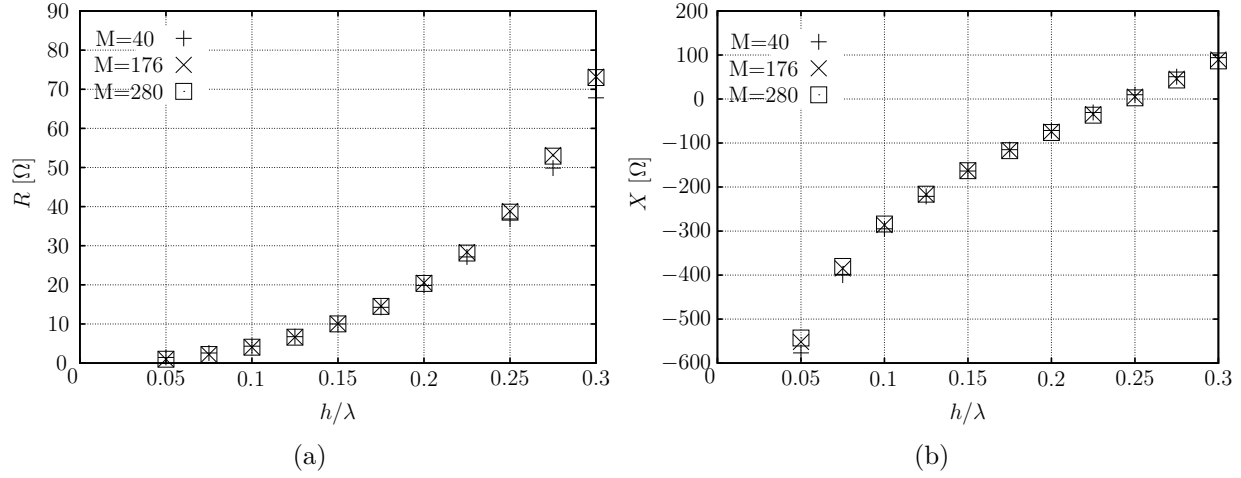
Figure 8.19: *Input impedance of a monopole mounted in the center of a $1.4\lambda \times 1.4\lambda$ square ground plane versus the monopole length by varying the number M of RWG functions used: (a)- resistance R; (b)- reactance X.*
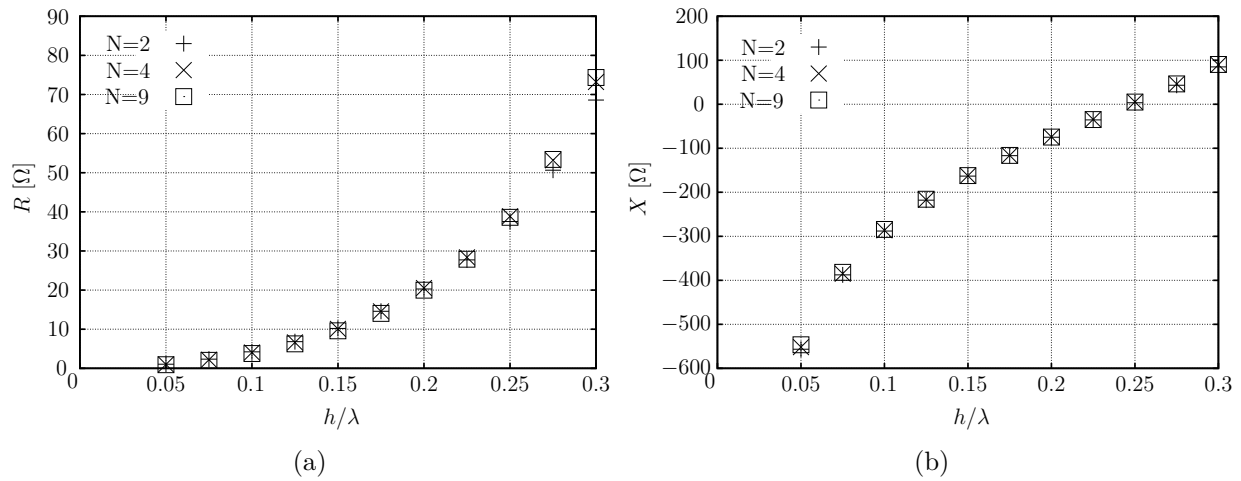
Figure 8.20: *Input impedance of a monopole mounted in the center of a $1.4\lambda \times 1.4\lambda$ square ground plane versus the monopole length by varying the number N of rooftop functions used: (a)- resistance R; (b)- reactance X.*

(a)   (b)
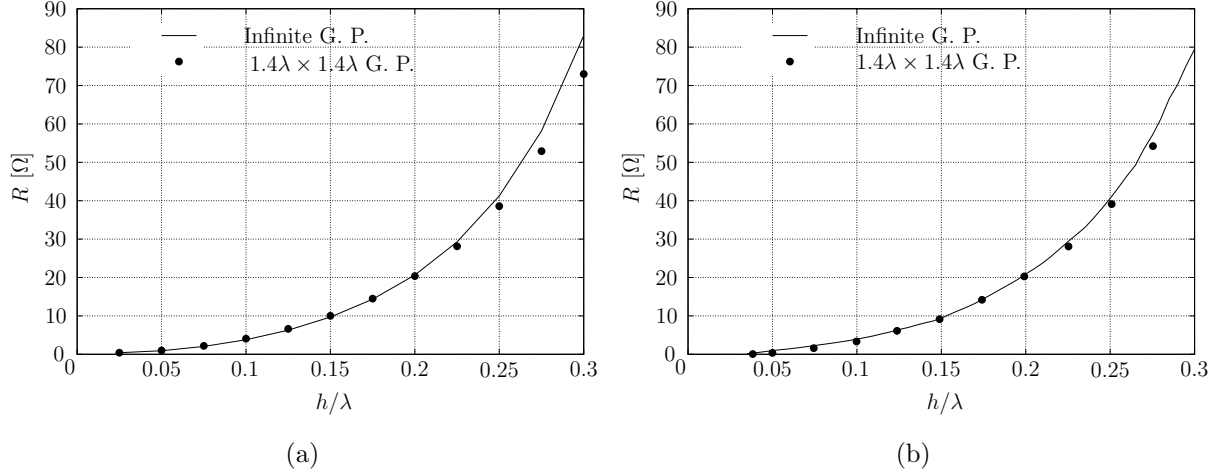
Figure 8.21: *Input resistance R of a monopole mounted in the center of a $1.4\lambda \times 1.4\lambda$ square ground plane versus the monopole length, computed by using the attachment mode and by considering the plane infinite: (a)- results from GEKMoM+; (b)- results from [20].*

(a)   (b)
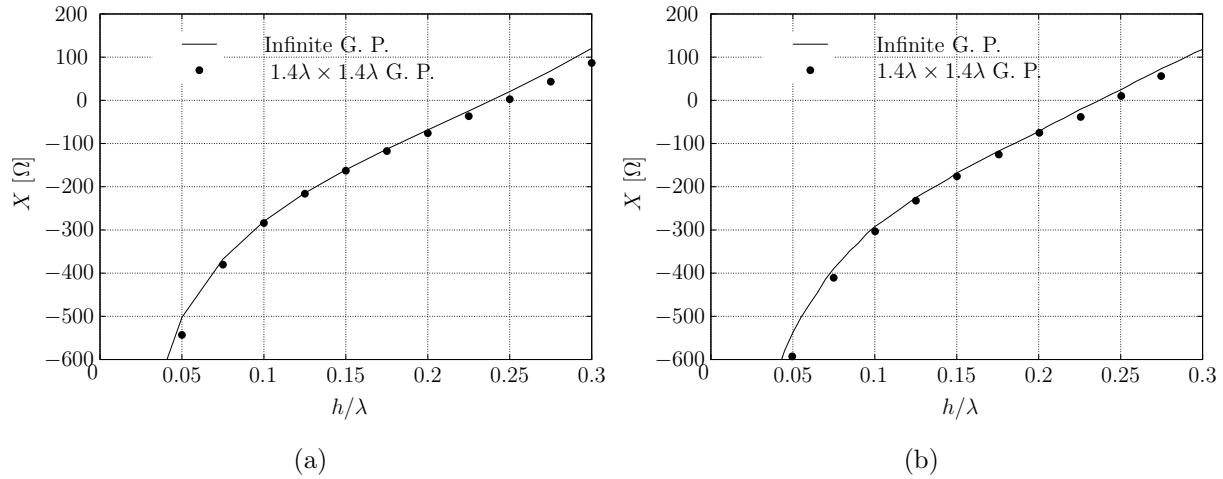
Figure 8.22: *Input reactance X of a monopole mounted in the center of a $1.4\lambda \times 1.4\lambda$ square ground plane versus the monopole length, computed by using the attachment mode and by considering the plane infinite. (a)- results from GEKMoM+; (b)- results from [20].*

As a second test case, we consider a monopole antenna perpendicularly mounted in the center of a finite square PEC plate with dimensions 0.914 m×0.914 m. The wire antenna has length $h = 0.421$ m and has radius $a = 0.8$ mm. We compute the input admittance of this monopole in the frequency range 140–220 MHz. Figure 8.23 shows results obtained with our code (GEKMoM+) and measurements and results from the literature [20]. The calculation was performed with $N = 4$ rooftop functions for the wire and with $M = 40$ RWG functions for the square plate.
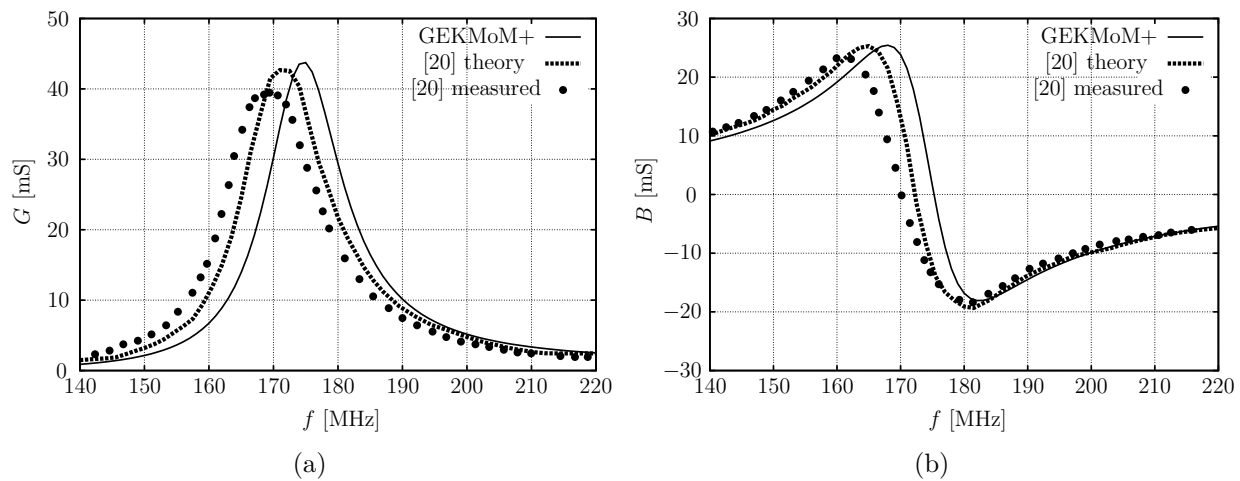
Figure 8.23: *Input admittance of a* 0.421 m *monopole mounted in the center of a square finite plane with dimensions* 0.914 m×0.914 m *versus the frequency: (a)- conductance G; (b)- susceptance B.*

8.4   Conclusions and discussion

In this chapter, we have proposed a numerical method to analyze the electromagnetic coupling between wire antennas and open surfaces. The connection between wires and surfaces has been theoretically investigated and a numerical treatment of the attachment has been analyzed by introducing a proper attachment basis function. The current is considered flowing continuously along the mantle of the wire to the surface and vice versa. The carefully designed attachment mode in combination with the Galerkin MoM formulation leads to nine types of four-fold integrals. Moreover, in case of coincident source and observation points the integrands exhibit a singular behavior. Using analytical techniques, we have accounted for all weakly singular integrands and their four-dimensional integrals have been reduced to a lower dimension. This complexity reduction is reflected in reduction of

computation time involved in integral evaluations. For ease of implementation we made two basic simplifications:

- the attachment region has been discretized with a symmetrical triangular mesh;

- wires are orthogonally attached to the surface.

As described in Sec. 8.2.4, thanks to the symmetric configuration used, the four-fold integrals associated with a certain test and expansion triangle pair involved in the attachment can be used up to eight times (eight triangles are involved in the attachment). The advantage of a more efficient filling of the MoM-matrix due to the use of the "nice" symmetric configuration (Fig. 8.3) can always be achieved by defining a proper surface mesh.

The simplification of having a wire perpendicularly attached to the surface may be generalized as follows. We may think of a first short wire with an end connected orthogonally to a surface and joined with the other end to an arbitrarily tilted second wire.

Although the GEKMoM+ code is not fully optimized, the introduction of a special attachment basis function in combination with the Galerkin MoM does not lead to computational problems. As further development, the implementations of dedicated (ad-hoc) routines to evaluate integrals involved in the attachment may be required to increase the efficiency of the proposed method.

Chapter 9

Design of a loaded monopole by using an evolved PSO algorithm

Over the years, wire antennas have been widely used in many communication systems. Their various fields of application require a specific design of wide-band antennas. Moreover, conventional antennas operating at low frequencies have very large dimensions. In naval applications where antennas operate in VHF (30–300 MHz) and/or UHF (300 MHz– 3 GHz) frequency bands, particular miniaturizing techniques are needed to design small efficient antennas [80,81]. Loading wire antennas with resonant traps, as for instance RLC parallel circuits, is one possible way to obtain broadband performance. In particular, inductors and capacitors guarantee a multi-resonant frequency system while resistors permit achieving wide-band characteristics [80]. In the design of such kind of antennas, the different loading configurations (positions, RLC values) play a crucial role in achieving the required performance in terms of gain and VSWR. An accurate electromagnetic model of the antenna configuration is essential in the design of such a loaded antenna system. To this end, the developed Galerkin MoM code suitable for the analysis of wire antenna structures is embedded in a Particle Swarm Optimization (PSO) algorithm. In this way, we obtain a synthesis program by means of a stochastic optimization technique.

The choice of using a stochastic optimization technique, as Particle Swarm Optimization, is mainly due to its ability to converge to a global minimum together with its simplicity and robustness. Indeed compared to deterministic algorithms (e.g., gradient-based techniques), stochastic algorithms are very useful tools for optimization problems involving a space of solutions with a large amount of local minima. Stochastic optimization techniques are less inclined to converge to a local minimum than deterministic optimization methods [82]. On the other hand, stochastic algorithms require many more forward computations, and

therefore it is important to use efficient antenna modeling in combination with them.

In Section 9.1.1 the PSO mechanism is briefly described and a possible modification to increase the efficiency in terms of convergence is provided in Sec. 9.1.2. The MoM/PSO is applied to a wide-band wire antenna design in Sec. 9.2, where a tailored scheme to enhance efficiency is introduced for the computation of matrix elements, see Sec. 9.2.2. Finally, in Sec. 9.2.3 the relevant results are discussed and compared with those obtained with a Genetic Algorithm (GA) approach.

9.1   Particle Swarm Optimization algorithm

Particle Swarm Optimization (PSO) is a rather new optimization technique, which was developed by Kennedy and Eberhart [83] in 1995. The full merit of the introduction of this stochastic evolutionary algorithm into the electromagnetic community is due to Rahmat-Samii [84] who successfully applied this technique to antenna design.

9.1.1   Conventional PSO

A particle swarm optimizer is a population-based stochastic optimization algorithm that emulates the social behavior of a swarm of bees looking for the most fertile feeding location [84]. In a PSO system, a swarm of individuals (called "agents" or "particles") fly through the search space. Each particle represents a candidate solution to the optimization problem. The position of a particle is influenced both by the best position visited by itself (that is its historical experience) and by the position of the best particle in its neighborhood. As in Genetic Algorithms (GA) a key element of PSO is the definition of a "fitness function" that accurately quantifies the quality of candidate solutions. Recent results in the literature show that PSO is generally faster, more robust and performs better than GA, especially when the dimension of the problem increases [26].

A problem that requires the simultaneous optimization of P parameters varying in a reasonable range of values can be defined on a P-dimensional bounded space where the optimal solution has to be found. In a standard PSO algorithm we define a collection of M agents that change their positions iteratively within this P-dimensional space. In particular, for each agent the updated step in each dimension $p \in [1, P]$ is specified according to

$$x_p(t + \Delta t) = x_p(t) + v_p(t)\Delta t, \qquad (9.1)$$

where the initial position $x_p(0)$ is randomly defined while $v_p(t)$ represents the p-th component of the agent velocity. As will be explained in Sec. 9.1.2, the implemented rule

for velocity update is a key issue for high performance PSO. The conventional stochastic iterative equation, valid for each p-th component of the agent velocity, describes the PSO mechanism [84] and reads

$$v_p(t + \Delta t) = wv_p(t) + c_1 r_{p,1}(t) \left[p_{\text{best},p} - x_p(t) \right] + c_2 r_{p,2}(t) \left[g_{\text{best},p} - x_p(t) \right]. \tag{9.2}$$

The first right-hand side term in equation (9.2) represents the inertial agent tendency to maintain the previous direction, where w is referred to as "inertial weight". The other two terms are pulling toward the best position p_{best} ever found by the m-th agent and the best position g_{best} found by any particle, respectively. Increasing the value of w will increase the speed of the particles, which results in more exploration (g_{best}) and less exploitation (p_{best}).

The constant coefficients c_1 and c_2 are the "cognitive" and the "social" rate, respectively, whereas $r_{p,1}$ and $r_{p,2}$ are two random numbers uniformly distributed within the range $[0, 1]$. This means that c_1 is a factor determining how much the particle is influenced by the memory of its best location, while c_2 is a factor determining how much the particle is influenced by the rest of the swarm. Increasing the value of c_1 will encourage the exploration of the solution space since each particle moves towards his own p_{best}. Increasing the value of c_2 will encourage the exploitation of the supposed global maximum g_{best}.

Positions $p_{\text{best},p}$ and $g_{\text{best},p}$ depend strongly on the chosen fitness function that is used to test each agent performance.

9.1.2 Modified PSO for convergence improvement

The PSO capability to converge to the global optimum and its velocity of convergence strongly depend on the weighting factors w, c_1, c_2 in equation (9.2). In particular, high w values encourage the tendency of the algorithm to expand the search space or, equivalently, its ability to explore new areas. It results in a global search attitude. Realizing the importance of the exploration to find a good seed at the beginning, we have defined w as a decreasing function in the first N_w iteration steps, starting from a high value of w [28]. Noticing that the balance between global and local search through the course of run is critical to the convergence of the algorithm, we have decided to vary both the cognitive and social rate. To be more specific, at certain instants, we set c_1 and c_2 to a high and a low value respectively, recovering their initial values after a pre-defined number of iterations ($N_c - N_w$). This procedure, called modified or extended PSO, is applied to encourage exploration compared to exploitation both at instant N_w and when a stagnation in a local minimum occurs.

9.2   Application of Particle Swarm Optimization to wide-band wire antenna design

The adopted procedure is based on a parametrical description of an antenna model where possible parameters are antenna dimensions and/or positions and values of lumped embedded loadings. The PSO algorithm is therefore used to synthesize a suitable configuration which meets the specifications. Each agent is a set of the mentioned parameters that represents a particular antenna model. The performance of each particle is measured by using a fitness/objective function defined according to the antenna requirements. As a matter of fact, the fitness function provides the link between the optimization algorithm and the physical problem (i.e., the antenna characteristics). However defining this function is not a trivial task. In general, since more than one characteristic has to be optimized simultaneously (e.g., gain, reflection coefficient), the fitness function should exhibit a functional dependence relative to the importance of each one of these characteristics. The classical way to solve this class of multi-objective optimization is to define a function as

$$F = k_1 F_1 + k_2 F_2 + \cdots + k_Q F_Q, \tag{9.3}$$

where $k_1, \ k_2, \ldots, k_Q$ are weighting coefficients that define the importance of each objective function $F_1, \ F_2, \ldots, \ F_Q$ with respect to the others. One example of fitness function will be discussed in detail in Sec. 9.2.1 for the proposed antenna design.

9.2.1   Antenna design problem

As a preliminary design, a monopole of a fixed length h, loaded with parallel RLC lumped circuits and fed through a matching network is considered (see Fig. 9.1). To guarantee broadband characteristics in terms of VSWR and gain, positions and values of the embedded loads as well as matching network elements are the parameters to be optimized [82]. We design a 1.75 m monopole loaded with five RLC groups. The monopole is placed over an infinite ground plane at $z = 0$, it has radius $a = 0.5$ cm and the lumped elements, positioned at height h_i, vary in the ranges $0 < R_{pi} < 1500\ \Omega$, $0 < L_{pi} < 3\ \mu$H and $0 < C_{pi} < 200\ p$F. The i-th resistance R_{pi}, inductance L_{pi}, and capacitance C_{pi} are in parallel as shown in Fig. 9.1. The constraints for the matching network components are $0 < L_s < 2\ \mu$H, $0 < L_p < 2\ \mu$H and $0 < C_p < 50\ p$F, whereas the transformer ratio is in the interval $1 < n_2/n_1 < 5$. Reasonable requirements are a system gain G_s in the horizontal plane ($\theta = 90°$) greater than $G_0 = -5$ dBi and a VSWR < 3.5 in a 30–450 MHz frequency band. Therefore, on the whole, the space of solutions has $P = 24$ dimensions,
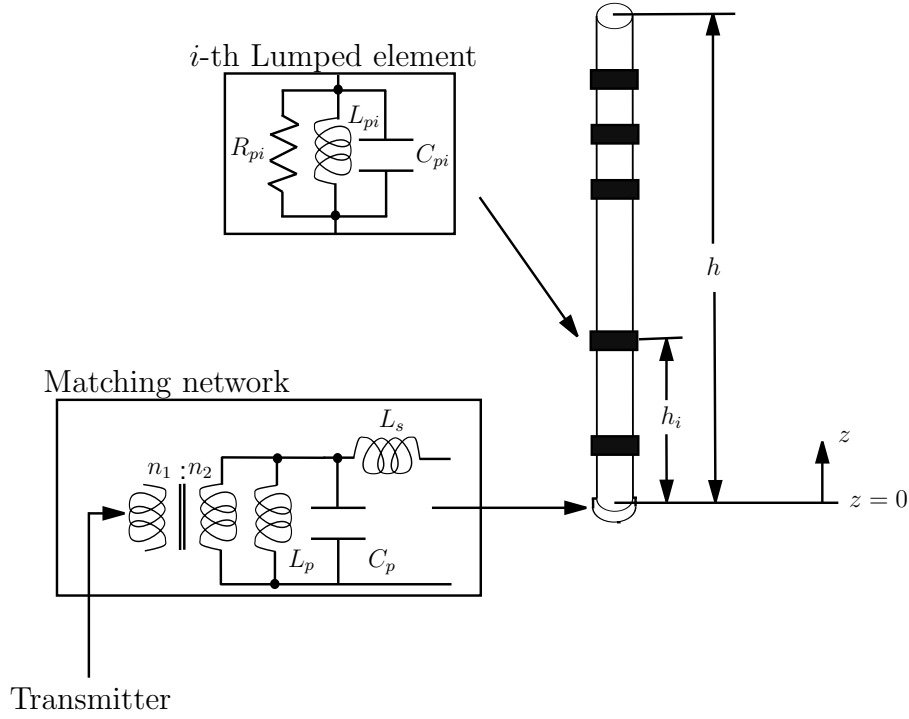
Figure 9.1: *Loaded monopole antenna with its matching network structure.*

which means that 24 parameters have to be optimized. These specifically are: values and positions of 5 lumped loadings (i.e., $4 \times 5 = 20$), and 4 values related to the matching network components and transformer. Moreover, a set of $N_f = 84$ uniformly distributed frequencies f_i, $i = 1, \ldots, N_f$ have been considered in the band of interest. We have chosen a population of $M = 32$ agents for the PSO and, in the Method of Moments analysis, we have approximated the monopole current by $N = 31$ basis functions (i.e., 32 segments). The infinite ground plane has been accounted for by applying the image theory [79].

From the calculated current I in the feeding point $z = 0$, the antenna input impedance Z_{in} is computed as

$$Z_{\text{in}} = V_0/I(0), \tag{9.4}$$

where $V_0 = 1$ V is the voltage in the feeding point. Consequently, the reflection coefficient at the matching network input port is determined as

$$\Gamma_s = \frac{1 - Z_0/Z_s}{1 + Z_0/Z_s}, \tag{9.5}$$

where $Z_0 = 50\,\Omega$ and Z_s is the impedance at the matching network input port (see Fig. 9.2) given by

$$Z_s = \left(\frac{1}{Z_{\text{in}} + j\omega L_s} + j\omega C_p + \frac{1}{j\omega L_p} \right)^{-1}. \tag{9.6}$$

The VSWR of the system can now be calculated as

$$\text{VSWR} = \frac{1 + |\Gamma_s|}{1 - |\Gamma_s|}. \tag{9.7}$$

Consequently, the system gain G_s is determined as

$$G_s = G_a + 10\log_{10}\left(1 - |\Gamma_s|^2\right), \tag{9.8}$$

where the gains G_a and G_s are expressed in dBi. In this way, the antenna and the matching network are optimized simultaneously rather than in two subsequent steps [85].
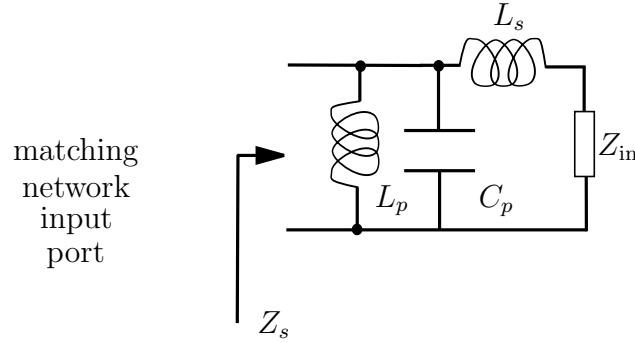
Figure 9.2: *Impedance Z_s at the matching network input port.*

As discussed in Sec. 9.2, the choice of the fitness function is probably the most important factor affecting the success of the optimization and therefore the performance of the final design. To reflect the design goals on the gain and VSWR, the following fitness function has been minimized

$$F = k_1 F_g + k_2 F_s + k_3 F_{\text{VSWR}}, \tag{9.9}$$

where k_1, k_2 and k_3 are weighting constants. The first term F_g expresses a penalty when the system gain G_s in the horizontal plane is smaller than the minimum requested value G_0 for each frequency f_i, $i \in [1, N_f]$

$$F_g = \sum_{i=1}^{N_f} \left(G_0 - G_s(f_i, \theta = 90°)\right)^3 \mathcal{H}\left(f_i\right), \tag{9.10}$$

where the cubic emphasizes the penalty when $G_s \leq G_0$ [82]. The function $\mathcal{H}(f_i)$ in (9.10) is a step function

$$\mathcal{H}(f_i) = \begin{cases} 1 & G_s(f_i, \theta = 90°) \leq G_0, \\ 0 & G_s(f_i, \theta = 90°) > G_0, \end{cases} \tag{9.11}$$

which ensures that the penalty F_g vanishes when $G_s > G_0$.

The smoothness of the antenna gain G_a in the horizontal plane [82] versus frequency is insured by the second term F_s in the fitness function (9.9)

$$F_s = \sum_{i=1}^{N_f-1} \left| G_a\left(f_{i+1}, \theta = 90°\right) - G_a\left(f_i, \theta = 90°\right) \right|^2. \tag{9.12}$$

However, since F_s depends on the number N_f of frequencies used, the smoothness behavior of G_a can be achieved only if N_f is chosen such that the set of f_i frequencies densely cover the frequency band of interest.

Finally, the third term F_{VSWR} in (9.9) has been added to emphasize solutions having a VSWR < 3.5

$$F_{\text{VSWR}} = \sum_{i=1}^{N_f} \left(|\Gamma_s(f_i)| - |\overline{\Gamma}| \right) \mathcal{V}(f_i), \tag{9.13}$$

where $\Gamma_s(f_i)$ is the reflection coefficient at the matching network input port and $\overline{\Gamma}$ corresponds to a goal (VSWR $= 3.5$). Function F_{VSWR} in (9.13) expresses a penalty when $|\Gamma_s|$ is greater than the maximum allowed value $|\overline{\Gamma}|$ for each frequency f_i, $i \in [1, N_f]$. Besides, the step function $\mathcal{V}$ ensures that this penalty vanishes when $|\Gamma_s| < |\overline{\Gamma}|$

$$\mathcal{V}(f_i) = \begin{cases} 1 & |\Gamma_s(f_i)| \geq |\overline{\Gamma}|, \\ 0 & |\Gamma_s(f_i)| < |\overline{\Gamma}|. \end{cases} \tag{9.14}$$

To avoid the PSO algorithm to run indefinitely a maximum number of iterations is fixed at 10000. Nevertheless, a stop criterion has been introduced to terminate the PSO procedure when all agents have reached (within a fixed tolerance) the same position in the solution space.

9.2.2 Efficiency improvement in the numerical scheme GEKMoM

The PSO-based antenna design procedure described in the previous sections calls for the evaluation of a fitness function for each of the M agents for all the N_f frequencies of interest in each iteration step. This means that at each iteration, M monopole structures

with different loadings have to be analyzed by using the Galerkin Method of Moments developed in Chapter 3. Even though this analysis is relatively simple, a direct application of the GEKMoM embedded in the PSO algorithm would result in a very expensive procedure in terms of computation time. Indeed, each agent that represents a loaded monopole configuration, requires the computation of the full system matrix $\underline{\underline{\mathbf{A}}} = \underline{\underline{\mathbf{Z}}} + \underline{\underline{\mathbf{Z}}}^{\text{load}}$ and the solution of the associated linear system equation as described in Sec. 4.1. Assume that the monopole current has been expanded by means of N basis functions. The symmetric Toeplitz matrix $\underline{\underline{\mathbf{Z}}}$, which depicts the unloaded antenna configuration, demands the evaluation of N elements involving two-fold integrals (see equation (3.12) in Sec. 3.1.1). This calculation is computationally expensive. The effects of the loadings are included in the tri-diagonal matrix $\underline{\underline{\mathbf{Z}}}^{\text{load}}$ comprising not more that $3N - 2$ elements which are rapidly evaluated since they are known in an analytic form. Therefore, for all the N_f frequencies of interest, $4N - 2$ matrix elements have to be computed and, subsequently, the linear system $\underline{\underline{\mathbf{A}}}\,\underline{\mathbf{I}} = \underline{\mathbf{F}}$ in (4.4) has to be solved. In this case solving this system is far less time consuming than constructing the "unloaded" matrix $\underline{\underline{\mathbf{Z}}}$.

Since the unloaded monopole does not vary as the PSO evolves, we notice that the calculation of the unloaded matrix elements can be performed only once (before the first $i = 1$ iteration step) for all the frequencies of interest and stored in an array. At the i-th iteration step (with $i \geq 1$), the m-th agent will require only the efficient computation of the loading matrix $\underline{\underline{\mathbf{Z}}}^{\text{load}}$ for all the frequencies of interest. Typically for $N = 31$ basis functions and $N_f = 84$ frequencies, we reduce the CPU time up to a factor of 20.

9.2.3   Results and comparison

In this section results relevant to the antenna design problem described in Sec. 9.2.1 are discussed and compared with those obtained with a Genetic Algorithm (GA) approach [82]. The PSO combined with GEKMoM solver converges to a design whose load values (R_{pi}, L_{pi}, C_{pi}) and positions with respect to ground (h_i) (see Fig. 9.1) are reported in Table 9.1. The matching network results in $L_s = 0.072\ \mu$H, $L_p = 1.358\ \mu$H, $C_p = 1.372\ p$F and $n_2/n_1 = 1.917$.

The gain of the antenna system and the VSWR behavior with respect to the frequency are shown in Figs. 9.3 and 9.4 (continuous line), respectively. In the same figures our results are compared with those obtained in [82] by using a genetic algorithm (dashed line). We observe that PSO and the GA optimizer converge to solutions having similar performance in terms of gain and VSWR.

In Fig. 9.5 the effectiveness of our modified PSO algorithm is demonstrated. The fitness behavior versus the iteration steps obtained by using $M = 32$ agents both for the modified (continuous line) and conventional (dashed line) PSO are plotted. As apparent from Fig. 9.5 in the interval $[N_1 = 16, N_c = 60]$ the algorithm stagnates in a local minimum. Indeed, it results in a smooth behavior of the fitness function.

Table 9.1: *Load positions and RLC values of the designed monopole antenna.*

Load	h_i [cm]	R_{pi} [Ω]	L_{pi} [μH]	C_{pi} [pF]
1	49.736	1256	0.4	0.4
2	70.107	134	0.05	3
3	87.556	201	0.5	8
4	91.936	546	1.4	68
5	134.610	607	0.9	126

PSfrag replacements
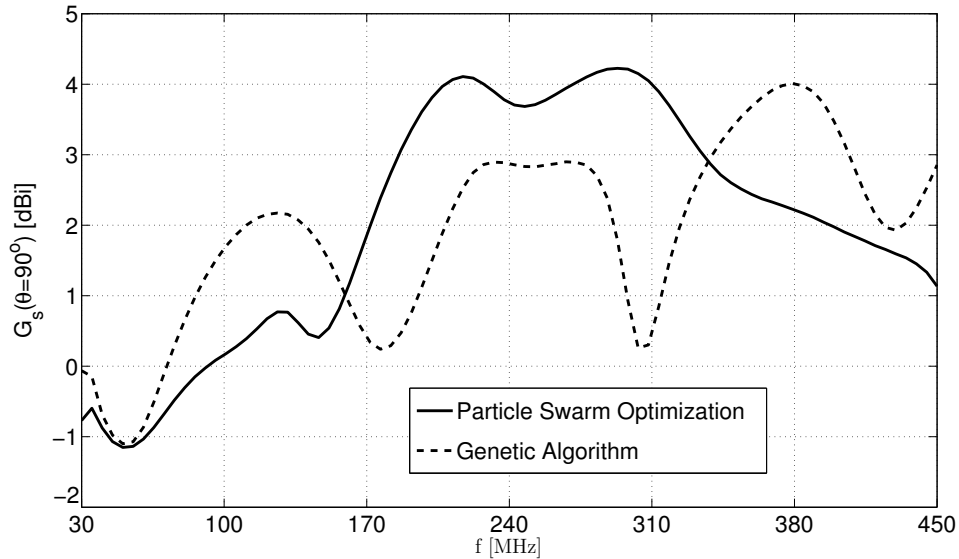
Figure 9.3: *Gain of the monopole-matching network system: results computed by using PSO (continuous line) and GA optimizer (dashed line) [82].*
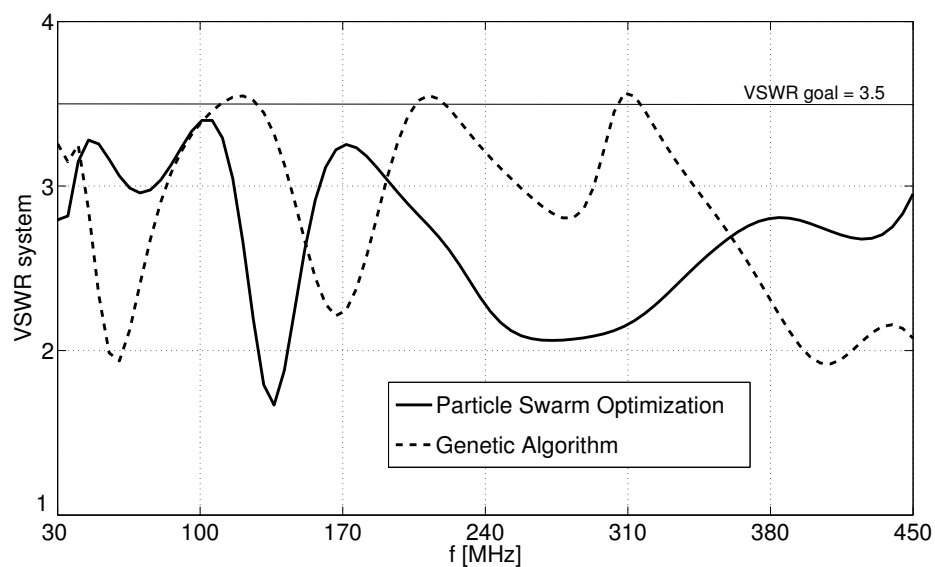
Figure 9.4: *VSWR at the input port of the matching network: results computed by using PSO (continuous line) and GA optimizer (dashed line) [82].*
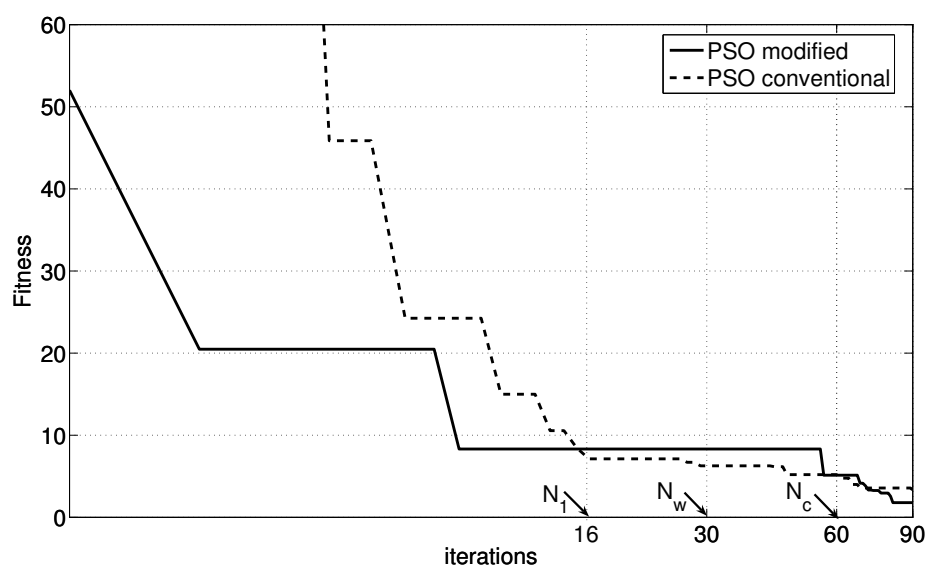
Figure 9.5: *Fitness behavior of the modified PSO (continuous line) and the conventional PSO (dashed line) versus the iteration steps in the initial 90 iterations.*

Figure 9.6 shows that starting from step $N_2 = 79$ the modified PSO converges to an optimum solution faster than the conventional PSO. This improvement results from the c_1 and c_2 variation procedure described in Sec. 9.1.2.
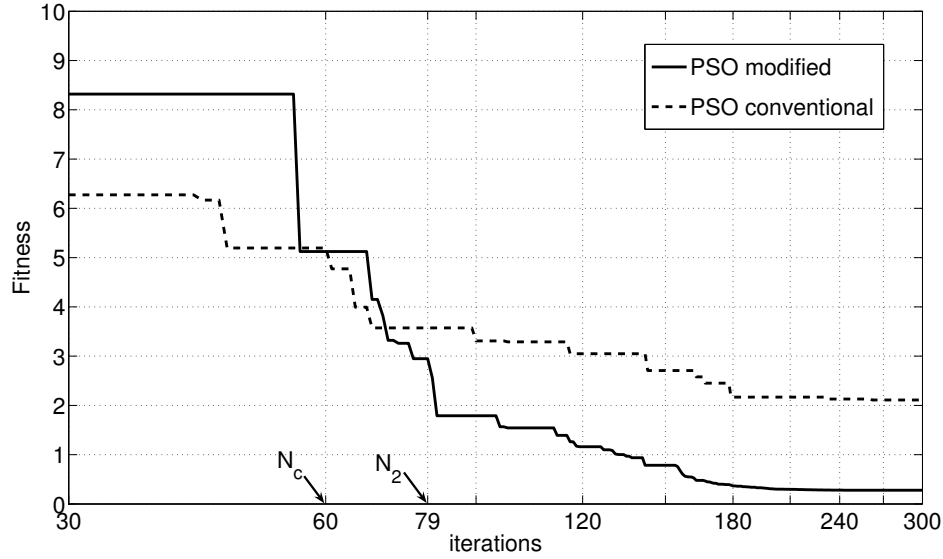
Figure 9.6: *Zoom for iteration steps $i \geq 30$ of the fitness behavior of the modified PSO (continuous line) and the conventional PSO (dashed line) versus the iteration steps.*

Further, we have run different optimizations with the same fitness function (9.9) and same design specifications to investigate how the described PSO algorithm is able to reproduce the same solution. The antenna parameters obtained by the five different optimizations are reported in Table 9.2 ordered by h_i and the gain system and the VSWR behavior versus the frequency are shown in Figs. 9.7 and 9.8. Moreover, Figs. 9.9 and 9.10 show the convergence rate of the five different optimizations. From Table 9.2, we observe that the five optimization runs converge to different values and position of loadings. Nevertheless, antenna performances are within the specified requirements for all the cases as reported in Figs. 9.7 and 9.8. This means that since the gain and the VSWR of the system are within the specifications, the contribution given by F_s (9.12) in the fitness function (9.9) is still to be optimized, assuring a smoothness behavior of the gain versus frequency. Finally the effectiveness of the presented modified PSO (see Sec. 9.1.2) is evident in Figs. 9.9 and 9.10, where no stagnation is observed.

Table 9.2: *Load positions and RLC values of the designed monopole antenna in five optimization runs.*

	run 1	run 2	run 3	run 4	run 5
h_1 [cm]	49.736	47.336	48.874	10.164	48.606
R_{p1} [Ω]	1256	1392	1422	383	1473
L_{p1} [μH]	0.4	0.32	0.35	2.69	0.35
C_{p1} [pF]	0.4	0.75	0.3	108	0.4
h_2 [cm]	70.107	70.678	71.392	37.049	72.397
R_{p2} [Ω]	134	295	291	1497	248
L_{p2} [μH]	0.05	0.77	0.77	0.18	0.76
C_{p2} [pF]	3	0.186	0.2	1.1	0.7
h_3 [cm]	87.556	97.564	89.224	103.905	94.433
R_{p3} [Ω]	201	702	978	557	452
L_{p3} [μH]	0.5	2.16	0.98	1.52	0.5
C_{p3} [pF]	8	118	96	95	164
h_4 [cm]	91.936	98.038	91.345	118.842	98.755
R_{p4} [Ω]	546	625	149	593	291
L_{p4} [μH]	1.4	1.297	2.3	1.74	0.77
C_{p4} [pF]	68	76	39	147	138
h_5 [cm]	134.610	100.145	94.7	121.458	169.94
R_{p5} [Ω]	607	1060	1196	502.5	814
L_{p5} [μH]	0.9	2.94	0.71	1.38	1.7
C_{p5} [pF]	126	46	124	1.3	40
L_s [μH]	0.072	0.044	0.076	0.079	1.857
L_p [μH]	1.358	1.977	1.206	0.95	0.078
C_p [pF]	1.372	0.356	1.527	1.546	1.444
n_2/n_1	1.917	1.896	2.008	1.92	2.024
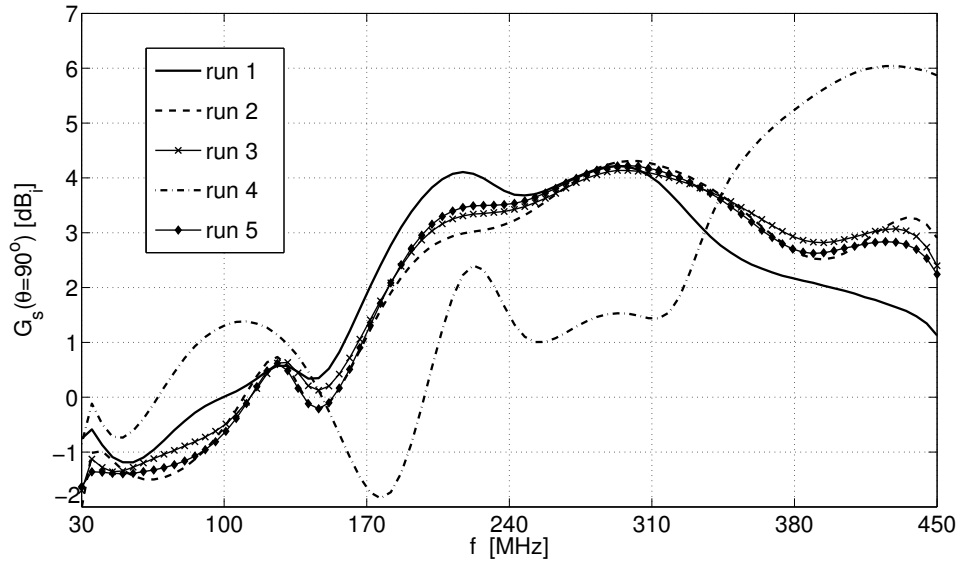
Figure 9.7: *Gain of the monopole-matching network system: results computed by using the GEKMoM for five different optimization runs.*
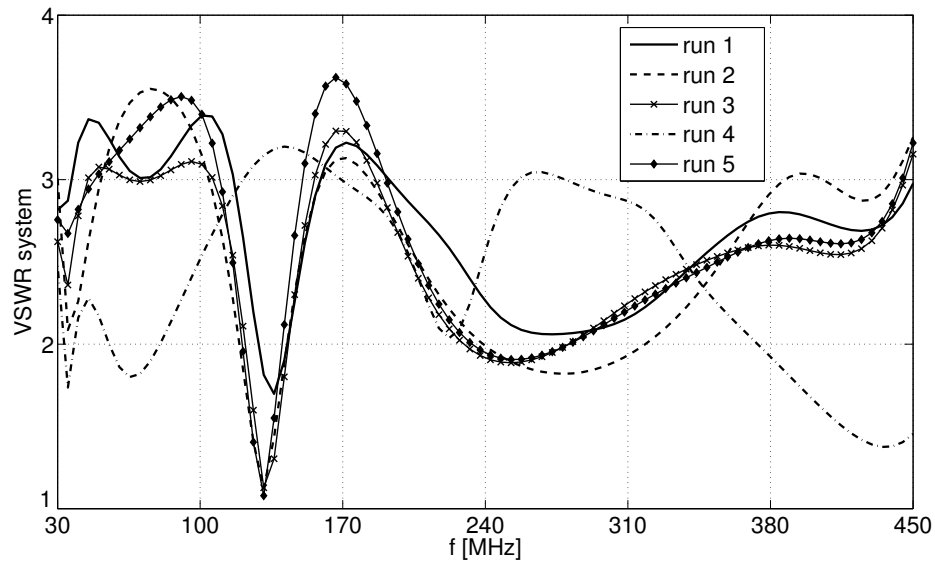
Figure 9.8: *VSWR at the input port of the matching network: results computed by using the GEKMoM for five different optimization runs.*
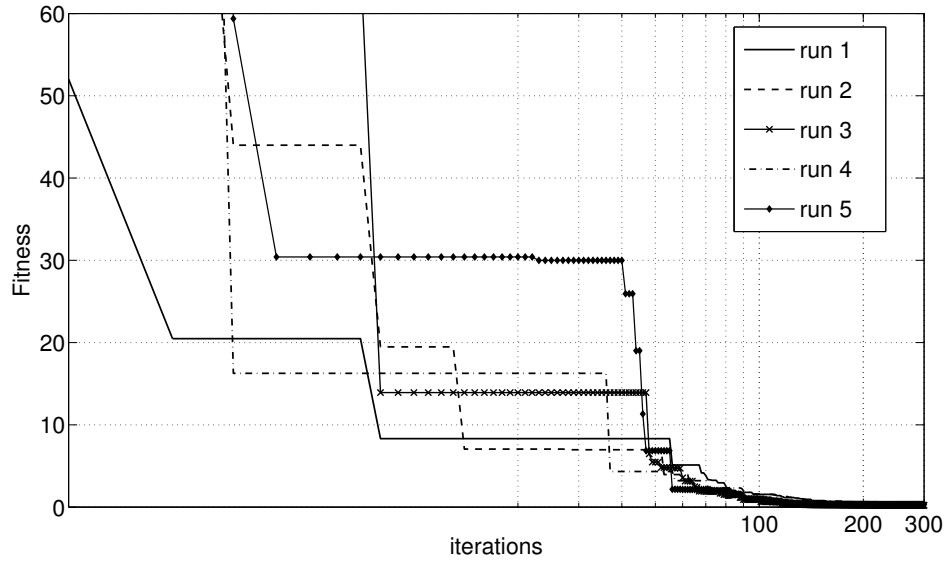
Figure 9.9: *Fitness behavior of the modified PSO versus the iteration steps for five different optimization runs.*
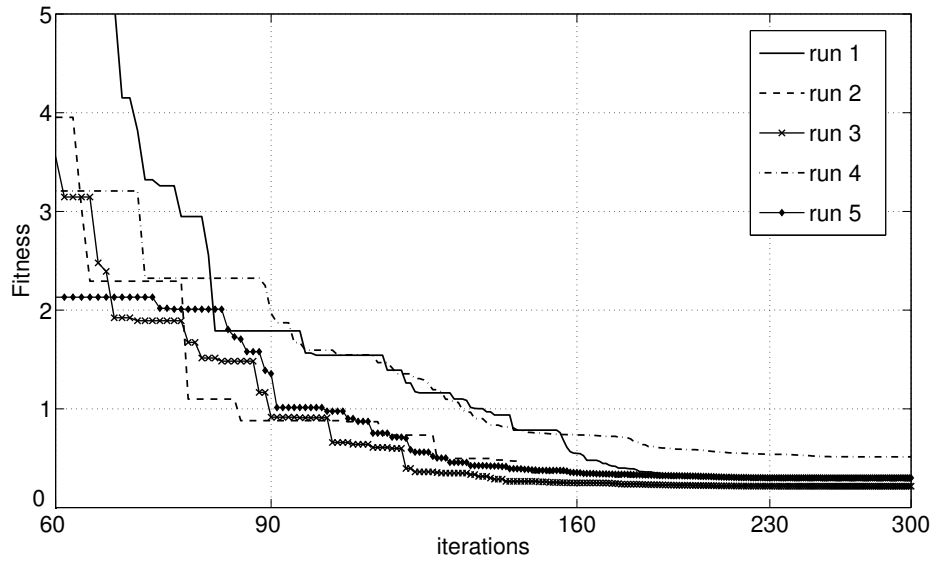
Figure 9.10: *Zoom for iteration steps $i \geq 60$ of the fitness behavior of the modified PSO versus the iteration steps for five different optimization runs.*

It is worth mentioning that, in the PSO algorithm implemented so far, the trajectories of a population of M particles vary in a P-dimensional space of continuous variables. As an alternative, the PSO can also operate in a space of discrete variables. To show the applica-

bility of this PSO option, the same monopole design is studied when the lumped loadings can be placed only at the lattice positions. Since the monopole antenna is discretized with $N + 1$ segments, we restrict the locations of lumped loading to the interconnections between two adjacent segments. In this case loading positions are specified by discrete variables instead of by continuous ones, and the evolution of the swarm (i.e., of the PSO algorithm) is confined in a "discrete" space of solutions. The optimization algorithm converges to a design whose matching network components are $L_s = 0.065$ μH, $L_p = 1.795$ μH, $C_p = 2.068$ pF and the transformer ratio is $n_2/n_1 = 1.682$. Positions and values of RLC loadings are summarized in Table 9.3. Figures 9.11 and 9.12 show the performance in terms of gain and VSWR of the designed system (i.e., antenna and matching network).

Table 9.3: *Load positions and RLC values of the designed monopole antenna.*

Load	n-th segment	h_i [cm]	R_{pi} [Ω]	L_{pi} [μH]	C_{pi} [pF]
1	1	5.469	940	2.39	170.47
2	9	49.219	1428	0.34	0.26
3	16	87.5	399	1.16	3.68
4	25	136.719	297	0.54	197.47
5	29	158.594	161	1.93	50.75
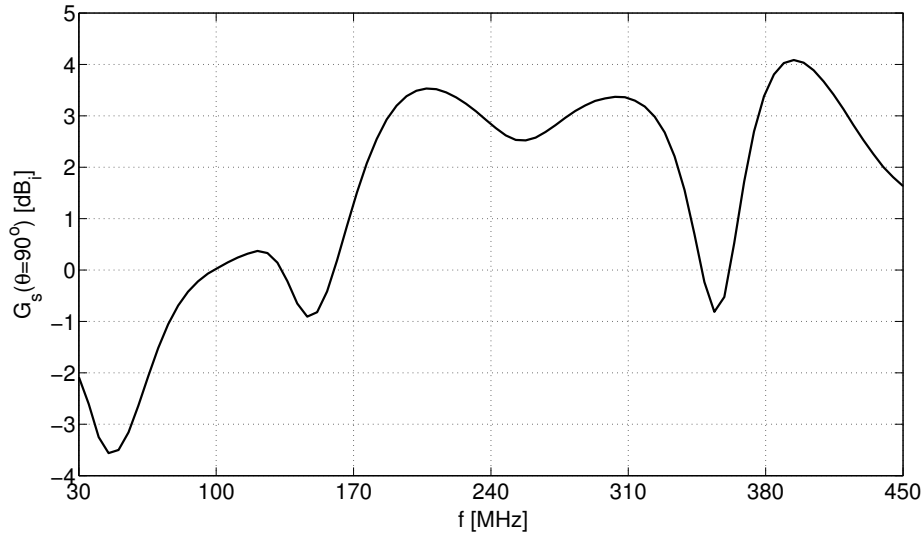
Figure 9.11: *Gain of the monopole-matching network system: results computed by using the GEKMoM (with fixed loadings' locations) embedded in a discrete version of the PSO algorithm.*
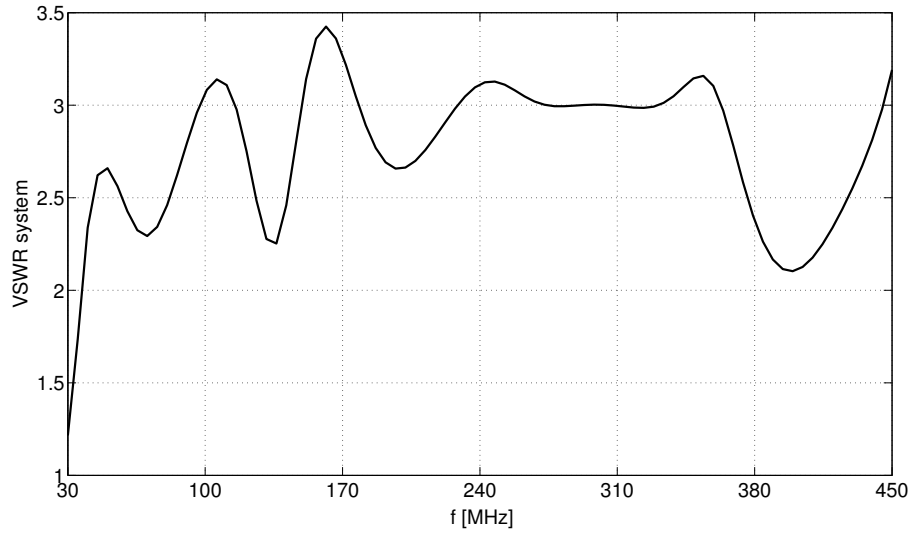
Figure 9.12: *VSWR at the input port of the matching network: results computed by using the GEKMoM (with fixed loadings' locations) embedded in a discrete version of the PSO algorithm.*

9.3 Conclusions and discussion

In this chapter we have discussed an optimization method for the design of broad-band wire antennas. To this end, the full-wave MoM code (GEKMoM) implementation (see Chapter 3) has been embedded in a Particle Swarm Optimization algorithm. In particular, values and positions of the RLC loadings are considered as optimization parameters in the design of a fixed-length loaded monopole over a ground plane. Requirements in terms of system gain and VSWR have been specified.

To enhance efficiency of the proposed GEKMoM/PSO algorithm, a tailored scheme is introduced for the computation of matrix elements. For the practical design studied, a computation time reduction of a factor 20 is achieved.

Further, as discussed in Sec. 9.1.2, we have proposed an improved methodology relevant to the velocity update of the particle swarm algorithm. Results show a convergence improvement of the optimization algorithm without suffering from local minima stagnation. Results obtained by the GEKMoM/PSO algorithm have been compared with those by Genetic Algorithm (GA) [82]. Both optimization approaches are stochastic evolutionary methods based on a population of candidate solutions. By using a PSO algorithm we gain in terms of simplicity and robustness. Indeed, the PSO method is simply based on updating the particles velocity.

Besides, thanks to the particle swarm versatility, a "discrete" version of the GEKMoM/PSO has been implemented. In this case, since optimization parameters (e.g., loadings' locations) can take only discrete values, the particles trajectories change in a discrete space. Compared with the continuous case, the space of solutions is restricted.

Even though stochastic algorithms are particularly effective in handling a large number of optimization parameters, our results show that the particle swarm procedure is not very repeatable. This is mainly due to the solution space, which contains many local minima. Moreover, the swarm may prematurely converge to a solution (a set of parameters). This means that small variations in the parameter values can cause large variations in the performance (e.g., gain, VSWR) of the monopole. A sensitivity study can be done by looking at derivatives of gain and VSWR with respect to each parameter.

The complementarity of stochastic and deterministic approaches suggests as improvement to this optimization procedure, a hybridization of the two methods as possible solution to these problems. Indeed, hybridization refers to combining different approaches to benefit from the advantages of each approach.

Chapter 10

Conclusions and recommendations

In this thesis an efficient Galerkin Method of Moments (MoM) has been described to calculate the electric current distribution along wire antennas as well as on planar surfaces including wire-to-surface junctions. The theoretical formulation presented has been implemented in a FORTRAN computer language program which has been successfully validated with results from the literature. The key elements of this electromagnetic modeling tool, each one corresponding to a FORTRAN module, are:

- **arbitrarily oriented loaded wires**,

- **open surfaces**,

- **connection of wires with surfaces**.

For all three above mentioned key elements, an Electric Field Integral Equation (EFIE) is introduced where the scattered field is written as a function of the unknown current distribution (flowing along arbitrarily oriented loaded wires, or on open surfaces or on wire-to-surface junctions). Next, the pertinent equation is discretized applying a Galerkin Method of Moments and leading to a relevant system matrix equation ($\underline{\underline{Z}}\underline{I} = \underline{F}$). Thanks to the Galerkin method, the MoM matrix $\underline{\underline{Z}}$ holds the symmetry property. Each element of $\underline{\underline{Z}}$ expresses the influence of a current along a "source" element on an "observation" element. An element should be read here as the support of a basis function defined to approximate the current flowing along wires, open surfaces or wire-to-surface junctions. Typically, the complete set of interactions requires the computation of four-dimensional integrals. Moreover, matrix elements belonging to the diagonal, so-called self terms, represent the electromagnetic interaction between coincident source and observation elements. In this case, integrands may show a singular behavior and special care has to be taken

in their numerical integration to guarantee a good numerical accuracy and limit the CPU time.

First, for a straight thin wire, we have formulated the two most important thin-wire equations: the Pocklington equation with exact and with reduced kernel. The Pocklington equation with exact kernel is used as a basis for further discretization applying a Galerkin Method of Moments. We have discussed a way to efficiently calculate elements of the resulting system matrix by performing a singularity extraction and a Landen transform. The numerical method described has been implemented in the first software module referred to as **GEKMoM**. By means of numerical examples we have demonstrated that, when the number of expansion functions is increased, the exact kernel formulation gives stable and converging results, whereas, due to its ill-posed nature the reduced kernel does not. Moreover, a root-mean-square (RMS) error has been defined to study the accuracy of the discretization method implemented. We have observed that when the number of expansion functions is doubled, this RMS error is halved.

Further, we have extended the analysis to loaded wires and we have discussed the electromagnetic interaction between two or more wires having different orientation. Generally speaking, when coupling between wires is studied, two possible approaches are investigated. In fact, the current along a "source" wire radiates an electric field which illuminates all other "observation" wires. In particular, this radiating current can be considered flowing along the wire axis or along its mantle. In the first case a single one-dimensional integration along the wire axis is required to evaluate the radiated field (so called thin-wire far-field approximation), while in the second case, an additional integration along the wire mantle is also needed, which increases the complexity to a two-dimensional integration. These two theoretical approaches are implemented in two numerical programs which are compared in terms of computation time and accuracy. Results have confirmed that the thin-wire far-field approximation is computationally less expensive than the straightforward two-dimensional integration. Moreover, we have observed that root-mean-square errors introduced by placing the radiating current on the wire axis are usually smaller than the discretization error introduced by the GEKMoM numerical method. For the approach that assumes the current along the mantle of the wire, a numerically efficient interpolation algorithm has been developed to reduce the required CPU time. Numerical examples have demonstrated that the proposed interpolation algorithm results in a reduction of the CPU time comparable with the one achieved with the thin-wire far-field approximation.

The numerical method (GEKMoM) has been extended to determine natural frequencies of loaded straight wires. Typically, the Singularity Expansion Method (SEM) [50–52] provides a convenient mean for characterizing the electromagnetic behavior of loaded wires in terms of natural frequencies. For simple geometries these complex natural frequencies are generally computed by searching for the zeros of the MoM matrix determinant. Observing that natural frequencies correspond to complex frequencies for which the system matrix is singular, we have presented a numerical algorithm that calculates these values by performing a Singular Value Decomposition (SVD) of the system matrix. This scheme represents an attractive alternative to the commonly used approaches since SVD produces in addition to the natural frequencies much additional information useful to characterize the time-domain current distribution (eg., residual matrix, natural current mode, etc.). Moreover, for resistively loaded wires, we have shown how the location of these poles vary in the complex plane for an increasing value of the load. A marching-on-in loading approach has been presented and successfully validated. For increased resistive loads, waves traveling along the wire are much more attenuated. In fact, as expected, results showed that a conjugate pair of natural frequencies moves towards the real axis and collapses to a single value (i.e., a double pole occurs). As the loading is further increased this pair splits up and remains on the negative real s-axis, one natural frequency moving to $-\infty$ and the other to 0. This overall study is also beneficial to additionally validate our numerical method.

Taking advantage of the existing literature [16–19], we have shown an efficient numerical method to calculate the current distribution on open surfaces. In particular, the open scatterer has been discretized by means of a triangular mesh, and well-known RWG functions are used to approximate the surface current. Also in this case, the evaluation of MoM matrix elements involves the calculation of integrals with integrable singularities in the integrands. In the developed method, all singularities are extracted and the resulting integrals are calculated in closed form; numerical integration is applied only to regular functions. For open surfaces, the software module developed has been named **GMoMOS**. Results showed the delicacy of dealing with RWG functions and a triangular mesh. Indeed, depending on the mesh selection, the evaluation of matrix elements introduces errors. It is expected that uniformity in size and shape of randomly distributed triangles will be beneficial to reduce these errors.

Further, we have proposed a numerical method to analyze the electromagnetic coupling between wire antennas and open surfaces. The connection between wires and surfaces

has been theoretically investigated and a numerical treatment of the attachment has been proposed by introducing a proper attachment basis function. With respect to the connection between wires and surfaces, including the carefully designed attachment mode into the Galerkin MoM formulation leads to nine types of four-dimensional integrals. Moreover, in case of coincident source and observation points the integrands exhibit a singular behavior. Using analytical techniques, we have accounted for all integrable singularities, reducing the four-dimensional integrals to a lower dimension. This reduction in numerical complexity corresponds to a reduction of computation time. Besides, the numerical method described has been implemented in the software module referred to as **GEKMoM+**. Even though the code is not fully optimized, results prove the success of the proposed method. Implementations of dedicated (ad-hoc) routines for integral evaluations may enhance the efficiency of the proposed numerical treatment. This research has also increased our experience in dealing with the attachment mode in the sense that we are aware of conditions that the special basis function should meet and of the implications for a further numerical treatment.

Having all the previously mentioned key modules at our disposal, we have studied a practical design problem. The developed tool constitutes a valuable starting point for the synthesis and design of HF-VHF antennas widely used in naval communication applications. To this end, the antenna analysis software (GEKMoM) has been embedded into an Particle Swarm Optimization (PSO) algorithm. This stochastic algorithm searches for an antenna that best meets the desired antenna performance as defined in a fitness function. Moreover, we have described a tailored scheme to enhance efficiency in the computation of matrix elements for the proposed GEKMoM/PSO algorithm. Further, owing the versatility of the PSO, a "discrete" version of GEKMoM/PSO has been successfully implemented; this resulted in a reduction of the problem's complexity (i.e., a smaller space of solutions). We have observed that the solution of the particle-swarm procedure is not very repeatable. This is mainly due to the large solution space, which contains many local minima. Improvements may be achieved through a hybridization between evolutionary (stochastic) and deterministic optimization methods.

As a continuation of this work, our code should be validated by means of experimental results. We would pursuit the manufacturing of a loaded monopole to be tested as benchmark. Moreover, with respect to future implementation it is recommended to include tapered and curved wires as well as connections between wires. These are missing key elements to analyze more complex structures as for instance kite antennas, whip antennas

and folded monopoles.

Several measures can be suggested to reduce the CPU time, which makes the numerical code even more efficient and useful for synthesis and design of wire antennas installed in complex environments. If the design of antennas to be installed on conducting surfaces (i.e., antennas performance on board of navy ships) is considered, the use of an **inter-polation algorithm** might be beneficial to gain efficiency in the optimization process, drastically reducing the time to compute the wire-surface coupling matrices. Research towards the feasibility of this application could be pursued. Nevertheless, when a large number of parameters is considered, the increased optimization time could become a show-stopper. Indeed the convergence of the optimizer to a good solution is limited by the huge space of solutions. Moreover, we would consider **preserving the matrix elements that are not affected by a design change**. For example, a small change in the position of the antenna installation will keep most interactions unaffected, and therefore only a small number of matrix elements needs to be updated. However this interesting idea would lead to a significant CPU time reduction only if the mesh generator used is aware of our desire to keep most of the matrix elements untouched and acts accordingly.

Appendix A

Transverse component of the vector potential

We start writing the expression (2.38) of the transverse component $\mathbf{A}_T$ of the vector potential

$$\mathbf{A}_T(\mathbf{r},\omega) = \int\limits_{z'=0}^{h}\int\limits_{\phi'=0}^{2\pi} J_\phi(\mathbf{r}',\omega)G(\mathbf{r}-\mathbf{r}',\omega)\mathbf{i}_\phi(\phi')ad\phi'dz'. \tag{A.1}$$

In Cartesian components (A.1) becomes

$$\begin{aligned}
\mathbf{A}_T(\mathbf{r},\omega) &= A_x(\mathbf{r},\omega)\mathbf{i}_x + A_y(\mathbf{r},\omega)\mathbf{i}_y \\
&= \int\limits_{z'=0}^{h}\int\limits_{\phi'=0}^{2\pi} J_\phi(\mathbf{r}',\omega)G(\mathbf{r}-\mathbf{r}',\omega)\cos\phi'\mathbf{i}_x ad\phi'dz' \\
&+ \int\limits_{z'=0}^{h}\int\limits_{\phi'=0}^{2\pi} J_\phi(\mathbf{r}',\omega)G(\mathbf{r}-\mathbf{r}',\omega)\sin\phi'\mathbf{i}_y ad\phi'dz'. \tag{A.2}
\end{aligned}$$

Further, we write the transverse components of the current density as in Sec. 2.2.1

$$J_\phi(\mathbf{r}',\omega) = \widehat{J}_\phi(z',\omega) + \Delta J_\phi(\mathbf{r}',\omega), \tag{A.3}$$

and the Green's function as

$$G(\mathbf{r}-\mathbf{r}',\omega) = \widehat{G}(z-z',\omega) + \Delta G(\mathbf{r}-\mathbf{r}',\omega), \tag{A.4}$$

Now, we substitute (A.3) and (A.4) in (A.2) and for simplicity we consider the x-component in (A.2). This results in

$$
\begin{aligned}
A_x(\mathbf{r},\omega) \;=\; & \int_{z'=0}^{h}\int_{\phi'=0}^{2\pi} \widehat{J}_\phi(z',\omega)\widehat{G}(z-z',\omega)\cos\phi' a\,d\phi'dz' \\[2mm]
& + \int_{z'=0}^{h}\int_{\phi'=0}^{2\pi} \Delta J_\phi(\mathbf{r}',\omega)\widehat{G}(z-z',\omega)\cos\phi' a\,d\phi'dz' \\[2mm]
& + \int_{z'=0}^{h}\int_{\phi'=0}^{2\pi} \widehat{J}_\phi(z',\omega)\Delta G(\mathbf{r}-\mathbf{r}',\omega)\cos\phi' a\,d\phi'dz' \\[2mm]
& + \int_{z'=0}^{h}\int_{\phi'=0}^{2\pi} \Delta J_\phi(\mathbf{r}',\omega)\Delta G(\mathbf{r}-\mathbf{r}',\omega)\cos\phi' a\,d\phi'dz'.
\end{aligned}
\tag{A.5}
$$

Analogously a similar expression can be derived for A_y in (A.2). From the closed-form separation-of-variables expression for the current density induced by an incident plane wave we have that $\widehat{J}_\phi(z',\omega) = O(1)$ and $\Delta J_\phi(\mathbf{r}',\omega) = O(a)$ [32], [33, pp.481–483], [34]. Moreover $\Delta G(\mathbf{r}-\mathbf{r}',\omega) = O(a)$. The first leading term of $\mathbf{A}_T$ in (A.5) is of order $O(a)$ and it is organized such that the integral over ϕ' reduces to zero. The other terms are of order $O(a^2)$ or smaller. Therefore, it follows that $\mathbf{A}_T \approx 0$ up to a second-order accuracy $O(a^2)$

$$
\mathbf{A}_T = O(a^2).
\tag{A.6}
$$

Appendix B

Radiated field thin-wire axis approximation.

The field radiated by a surface current $\mathbf{J}_S$ along the wire can be written as a function of the vector potential $\mathbf{A}$

$$\mathbf{E}(\mathbf{r}, \omega) = \frac{1}{j\omega\varepsilon} \left[k^2 \mathbf{A}(\mathbf{r}, \omega) + \nabla\left(\nabla \cdot \mathbf{A}(\mathbf{r}, \omega)\right) \right], \tag{B.1}$$

where $\mathbf{A}$ assumes the form

$$\mathbf{A}(\mathbf{r}, \omega) = \int\limits_{z'=0}^{h} \int\limits_{\phi'=0}^{2\pi} \frac{\exp(-jk|\mathbf{r} - \mathbf{r}'|)}{4\pi|\mathbf{r} - \mathbf{r}'|} \mathbf{J}_S(\mathbf{r}', \omega) a\, d\phi'\, dz', \tag{B.2}$$

with the source point $\mathbf{r}'$ on the surface of the wire, and the observation point $\mathbf{r}$ in the volume outside the wire. We note that since the exact expression (B.2) and the approximation (2.45) found in Sec. 2.2.1 and rewritten in (B.3) are both integral representations for the solutions to the three-dimensional homogenous wave equation, we take the gradients of the approximate expression as approximations for gradients of the exact expression. The one-dimensional expression of the vector potential as a function of the current $I(z', \omega)$ along the axis of the wire is here given as

$$\mathbf{A}(\mathbf{r}, \omega) = \mathbf{i}_z \int\limits_{z'=0}^{h} \frac{\exp(-jk|\mathbf{r} - z'\mathbf{i}_z|)}{4\pi|\mathbf{r} - z'\mathbf{i}_z|} I(z', \omega)\, dz', \tag{B.3}$$

where a second-order error is neglected (see Sec. 2.2.1). First, we determine the operator $\nabla \cdot \mathbf{A}$. To this end, we write

$$
\begin{aligned}
\nabla \left(\frac{\exp(-jkR)}{R} dz' \right) &= \left[\partial_R \left(\frac{\exp(-jkR)}{R} \right) \right] (\nabla R) \\
&= (-jkR - 1) \frac{\exp(-jkR)}{R^2} \frac{\mathbf{r} - z'\mathbf{i}_z}{R},
\end{aligned}
\tag{B.4}
$$

where $R = |\mathbf{r} - z'\mathbf{i}_z|$. Therefore substituting (B.4) in (B.3) leads to

$$
\nabla \cdot \mathbf{A}(\mathbf{r}, \omega) = \frac{1}{4\pi} \int_{z'=0}^{h} (-jkR - 1) \frac{\exp(-jkR)}{R^3} (z - z') I(z', \omega) dz'.
\tag{B.5}
$$

Second, we determine the gradient

$$
\begin{aligned}
&\nabla \left[(-jkR - 1) \frac{\exp(-jkR)}{R^3} (z - z') \right] \\
&= (\nabla R) \left[\partial_R \left((-jkR - 1) \frac{\exp(-jkR)}{R^3} \right) \right] (z - z') + (-jkR - 1) \frac{\exp(-jkR)}{R^3} \mathbf{i}_z \\
&= \left[3 + 3jkR + (jkR)^2 \right] \frac{\exp(-jkR)}{R^3} \frac{\mathbf{r} - z'\mathbf{i}_z}{R} (z - z') + (-jkR - 1) \frac{\exp(-jkR)}{R^3} \mathbf{i}_z. \quad \text{(B.6)}
\end{aligned}
$$

Subsequently, substituting (B.6) and (B.3) in (B.1) yields the one-dimensional integral expression of the radiated field for a current flowing on the wire axis

$$
\begin{aligned}
\mathbf{E}(\mathbf{r}) &= \frac{1}{j\omega\varepsilon} \frac{1}{4\pi} \int_{z'=0}^{h} I(z') \frac{\exp(-jk|\mathbf{r} - z'\mathbf{i}_z|)}{|\mathbf{r} - z'\mathbf{i}_z|^3} \left\{ - \left[(jk|\mathbf{r} - z'\mathbf{i}_z|)^2 + jk|\mathbf{r} - z'\mathbf{i}_z| + 1 \right] \mathbf{i}_z \right. \\
&\quad + \left. \left[3 + 3jk|\mathbf{r} - z'\mathbf{i}_z| + (jk|\mathbf{r} - z'\mathbf{i}_z|)^2 \right] \frac{z - z'}{|\mathbf{r} - z'\mathbf{i}_z|^2} (\mathbf{r} - z'\mathbf{i}_z) \right\} dz'.
\end{aligned}
\tag{B.7}
$$

We referred to expression (B.7) as the radiated field thin-wire axis approximation.

Appendix C

Analytical parts for the thin-wire equation and Landen transform

C.1 Known excitation: incident plane wave

In this section we give the analytical expression of the known excitation element on the right-hand side of matrix equation (3.8) in Sec. 3.1.1. Starting from equation (3.19)

$$F_m = j\omega\varepsilon E_{0\theta}\sin\theta_i J_0(ak^i\sin\theta_i)\int\limits_{z=(m-1)\Delta z}^{(m+1)\Delta z}\psi_m(z)\exp\left(jzk^i\cos\theta_i\right)dz, \tag{C.1}$$

where J_0 is the first-kind Bessel function. We recall here the expression of the testing function ψ_m

$$\psi_m(z) = \psi_0\left(z - m\Delta z\right) = \begin{cases} 1 - \left|\dfrac{z}{\Delta z} - m\right|, & \left|\dfrac{z}{\Delta z} - m\right| < 1, \\ 0, & \text{otherwise.} \end{cases} \tag{C.2}$$

Thus, applying the change of variable z in $x = z/\Delta z - m$ to (C.1) yields

$$F_m = -j\omega\varepsilon\Delta z E_{0z} J_0(ak^i\sin\theta_i)\int\limits_{x=-1}^{1}\psi_0(x\Delta z)\exp\left(-jk_z^i(x+m)\Delta z\right)dx, \tag{C.3}$$

where $E_{0z} = -E_{0\theta}\sin\theta_i$ and $k_z^i = -k^i\cos\theta_i$. The evaluation of the integral

$$A_m = \int\limits_{x=-1}^{1}\psi_0(x\Delta z)\exp\left(-jk_z^i(x+m)\Delta z\right)dx, \tag{C.4}$$

is carried out as follows

$$
\begin{aligned}
A_m &= \int\limits_{x=-1}^{0} (1+x)\exp\left(-jk_z^i \Delta z(x+m)\right) dx + \int\limits_{x=0}^{1} (1-x)\exp\left(-jk_z^i \Delta z(x+m)\right) dx \\
&= -2\frac{\cos(k_z^i)-1}{(\Delta z k_z^i)^2}\exp\left(-jk_z^i m\Delta z\right).
\end{aligned}
\tag{C.5}
$$

For a normally incident plane wave (i.e., $k_z^i = 0$), applying a Taylor expansion around $k_z^i = 0$ to (C.5), leads to $A_m = 1$. For wires with $ak^i \ll 1$, the first-kind Bessel function J_0 is approximated by means of series expansion as $J_0(ak^i \sin\theta_i) \approx 1$ and the forcing element F_m in (C.1) can be evaluated as

$$
F_m = \begin{cases} -j\omega\varepsilon\Delta z E_{0z}, & k_z^i = 0, \\ 2j\omega\varepsilon E_{0z}\dfrac{\cos(k_z^i \Delta z)-1}{{k_z^i}^2 \Delta z}\exp\left(-jk_z^i m\Delta z\right), & \text{otherwise.} \end{cases}
\tag{C.6}
$$

C.2   Landen transform method

In this section we describe the Landen transform method in a similar fashion as in [1]. This method has been used in the evaluation of the real part F_1 (3.46) of the exact kernel K_E as introduced in Sec. 3.3.1. One of the most known forms of the Landen transform is the following

$$
(1+q_1)\int\limits_{0}^{\alpha}\frac{d\varphi_1}{\sqrt{1-q_1^2 \sin^2\varphi_1}} = 2\int\limits_{0}^{\beta}\frac{d\varphi}{\sqrt{1-q^2 \sin^2\varphi}},
\tag{C.7}
$$

where

$$
0 \le q = \frac{2\sqrt{q_1}}{1+q_1} \Leftrightarrow q_1 = \frac{1-\sqrt{1-q^2}}{1+\sqrt{1-q^2}}, \qquad q_1 \sin\alpha = \sin(2\beta - \alpha).
\tag{C.8}
$$

The transform may be proven by carrying out the substitution (see [86, pp. 250–251])

$$
\tan\varphi_1 = \frac{\sin(2\varphi)}{q_1 + \cos(2\varphi)}, \qquad \text{or}\quad q_1 \sin\varphi_1 = \sin(2\varphi - \varphi_1).
\tag{C.9}
$$

We start from the expression of the complete elliptic integral of the first kind [39, eq. 17.3.1]

$$
K^{\text{ell}}(q) = \int\limits_{0}^{\pi/2}\frac{d\varphi}{\sqrt{1-q^2 \sin^2\varphi}} = \int\limits_{0}^{1}\frac{dt}{\sqrt{(1-t^2)(1-q^2 t^2)}}, \qquad \text{with}\quad 0 \le q < 1,
\tag{C.10}
$$

where we carried out the substitution $\sin \varphi = t$. Now we introduce the change of variables

$$t = \frac{(1 + q_1)z}{1 + q_1 z^2}, \qquad \text{where} \quad q_1 = \frac{1 - \sqrt{1 - q^2}}{1 + \sqrt{1 - q^2}} \Leftrightarrow q = \frac{2\sqrt{q_1}}{1 + q_1}. \tag{C.11}$$

Then it follows that

$$dt = \frac{(1 + q_1)(1 - q_1 z^2)}{(1 + q_1 z^2)^2} dz, \tag{C.12}$$

or

$$\frac{dt}{\sqrt{(1 - t^2)(1 - q^2 t^2)}} = \frac{(1 + q_1)dz}{\sqrt{(1 - z^2)(1 - q_1^2 z^2)}}. \tag{C.13}$$

Subsequently,

$$\int_0^\tau \frac{dt}{\sqrt{(1 - t^2)(1 - q^2 t^2)}} = (1 + q_1) \int_0^\eta \frac{dz}{\sqrt{(1 - z^2)(1 - q_1^2 z^2)}}, \tag{C.14}$$

where $\tau = (1 + q_1)\eta/(1 + q_1 \eta^2)$. In the special case $\tau = \eta = 1$ the integral (C.10) may be rewritten as

$$K^{\text{ell}}(q) = (1 + q_1)K^{\text{ell}}(q_1), \tag{C.15}$$

which is a special case of (C.7) with $\alpha = \pi$ and $\beta = \pi/2$. Therefore, the complete elliptic integral is computed by employing the Landen transform. From the substitution

$$q_1 = \frac{1 - \sqrt{1 - q^2}}{1 + \sqrt{1 - q^2}} \Leftrightarrow q = \frac{2\sqrt{q_1}}{1 + q_1}, \tag{C.16}$$

it follows that $0 < q_1 < q$. Successive application of this transform results in a sequence of values q_n which converges quadratically to 0, see [87]. Since $K^{\text{ell}}(0) = \pi/2$, the complete elliptic integral may be obtained from the following algorithm:

$$q_0 = q$$
$$F = \frac{\pi}{2}$$
$$n = 0$$
$$\text{do while } 1 + q_n > 1$$
$$\qquad n = n + 1$$
$$\qquad q_n = \frac{1 - \sqrt{1 - q_{n-1}^2}}{1 + \sqrt{1 - q_{n-1}^2}}$$
$$\qquad F = F(1 + q_n)$$
$$\text{enddo}$$

After this algorithm is carried out, F contains an approximation of $K^{\text{ell}}(q)$. A similar routine may be followed for the numerical evaluation of integral F_1 in (3.46), Sec. 3.3.1. The function F_1, reported here for the sake of clarity

$$F_1(\widetilde{\lambda}, \widetilde{\nu}) = \int\limits_0^{\pi/2} \frac{\cos(\widetilde{\nu}\widetilde{R})}{\widetilde{R}} d\varphi, \tag{C.17}$$

is a special case of the integral

$$\overline{K}^{\text{ell}}(q) = \int\limits_0^{\pi/2} \frac{g(\sin\varphi)}{\sqrt{1 - q^2 \sin^2\varphi}} d\varphi = \int\limits_0^1 \frac{g(t)}{\sqrt{(1 - t^2)(1 - q^2 t^2)}} dt, \tag{C.18}$$

where

$$q = \frac{1}{\sqrt{1 + \widetilde{\lambda}}}, \qquad g(t) = q \cos\left(\frac{\widetilde{\nu}}{q}\sqrt{1 - q^2 t^2}\right). \tag{C.19}$$

The scaled variables $\widetilde{\lambda}$ and $\widetilde{\nu}$ are defined in (3.37). The following algorithm has been developed and implemented in a FORTRAN code. We start with the initial values

$$q_0 = \frac{1}{\sqrt{1 + \widetilde{\lambda}^2}}, \tag{C.20}$$

$$F_1 = q_0, \tag{C.21}$$

$$n = 0, \tag{C.22}$$

and we proceed computing the following quantities

$$n = n + 1, \tag{C.23}$$

$$q_n = \frac{1 - \sqrt{1 - q_{n-1}^2}}{1 + \sqrt{1 - q_{n-1}^2}}, \tag{C.24}$$

$$F_1 = F_1 \cdot (1 + q_n), \tag{C.25}$$

while the condition $(1 + q_n) > 1$ is satisfied. During the algorithm, the values of the sequence of Landen parameters q_ℓ with $\ell = 0, 1, ..., n$ (C.24) are stored in an array and are used for the evaluation of the final integral

$$F_1 = F_1 \cdot \int\limits_{\varphi=0}^{\pi/2} g_n(\sin\varphi) d\varphi. \tag{C.26}$$

This integration is carried out with a composite trapezoidal rule, where the function $g_n(\sin\varphi)$ is evaluated recursively as follows

$$g_\ell(t) = g_{\ell-1}\left(\frac{(1+q_\ell)t}{1+q_\ell t^2}\right), \qquad \ell = 1, 2, ..., n, \tag{C.27}$$

where $t = \sin\varphi$ and the initial value at $\ell = 0$ is

$$g_0(t) = q_0\cos\left(\frac{\widetilde{\nu}}{q_0}\sqrt{1-q_0^2 t^2}\right). \tag{C.28}$$

The convergence is guaranteed since the sequence of values q_n converges quadratically to zero.

C.3   Analytical expression for integral I_2

In this section we give the analytical expressions of integral I_2 in (3.35) for the different types of polynomials P. We consider the constituting element Z_ℓ^E in (3.30), for which the polynomial is $P(s) = 1 - s$. The following integration has to be carried out:

$$I_2^E(\overline{\theta}) = \int_{s=0}^{1}(1-s)K_{\text{sing}}((s+\overline{\theta})\Delta z)ds, \tag{C.29}$$

where $\overline{\theta} = \pm\ell$ with $\ell = 0, 1, \ldots, N-1$. By applying a change of variable $x = (s+\overline{\theta})\Delta z$ and by writing the explicit expression of K_{sing} (3.51), we obtain

$$
\begin{aligned}
I_2^E(\overline{\theta}) &= \frac{1}{4\pi^2 a\Delta}\int_{x=x_1}^{x_2}\left(1-\frac{x}{\Delta z}+\overline{\theta}\right)\left(-\ln|x|+|x|-1\right)dx\\
&= \frac{1}{4\pi^2 a\Delta}\left[(1+\overline{\theta})\,x\left(\frac{|x|}{2}-\ln|x|\right)-\frac{1}{2\Delta}x^2\left(\frac{2|x|}{3}-\ln|x|-\frac{1}{2}\right)\right]_{x_1}^{x_2}, \tag{C.30}
\end{aligned}
$$

where x_1 and x_2 are found from distinguishing between the following five cases:

condition	x_1	x_2
$\overline{\theta} < -1 - 1/\Delta z$	$I_2^E = 0$	
$-1/\Delta z - 1 < \overline{\theta} < -1/\Delta z$	-1	$\Delta z(1+\overline{\theta})$
$-1/\Delta z < \overline{\theta} < 1/\Delta z - 1$	$\overline{\theta}\Delta z$	$\Delta z(1+\overline{\theta})$
$1/\Delta z - 1 < \overline{\theta} < 1/\Delta z$	$\overline{\theta}\Delta z$	1
$\overline{\theta} > 1/\Delta z$	$I_2^E = 0$	

Subsequently, for the constituting element Z_ℓ^M in (3.32), we have to evaluate the following integral

$$
\begin{aligned}
I_2^M(\overline{\theta}) &= \int_{s=0}^{1} K_{\text{sing}}((s+\overline{\theta})\Delta z)(\frac{s^2}{2} - s^2 + \frac{2}{3})ds + \int_{s=1}^{2} K_{\text{sing}}((s+\overline{\theta})\Delta z)\frac{(2-s)^3}{6}ds \\
&= \underbrace{\frac{1}{4\pi^2 a\Delta z} \int_{x=x_1}^{x_2} (-\ln|x| + |x| - 1) \left(\frac{2}{3} - \left(\frac{x}{\Delta z} - \overline{\theta}\right)^2 + \frac{1}{2}\left(\frac{x}{\Delta z} - \overline{\theta}\right)^3\right) dx}_{=I_2^{M1}} + \\
&+ \underbrace{\frac{1}{24\pi^2 a\Delta} \int_{x=x_1}^{x_2} (-\ln|x| + |x| - 1) \left(2 - \left(\frac{x}{\Delta z} - \overline{\theta}\right)\right)^3 dx}_{=I_2^{M2}} = I_2^{M1} + I_2^{M2},
\end{aligned}
$$

(C.31)

where the same change of the variable $x = (s+\overline{\theta})\Delta z$ has been used as before. Therefore, focusing on the first integral I_2^{M1} (i.e., when s belongs to the interval $0 \leq s \leq 1$), and carrying out the analytical integration results in

$$
\begin{aligned}
I_2^{M1}(\overline{\theta}) &= \frac{1}{4\pi^2 a\Delta z} \int_{x=x_1}^{x_2} (-\ln|x| + |x| - 1) \left(\frac{2}{3} - \left(\frac{x}{\Delta z} - \overline{\theta}\right)^2 + \frac{1}{2}\left(\frac{x}{\Delta z} - \overline{\theta}\right)^3\right) dx \\
&= \frac{1}{4\pi^2 a\Delta} \left[\alpha x \left(\frac{|x|}{2} - \ln|x|\right) + \frac{\beta x^2}{2}\left(\frac{2|x|}{3} - \ln|x| - \frac{1}{2}\right)\right]_{x_1}^{x_2} + \\
&+ \frac{1}{4\pi^2 a\Delta} \left[\frac{\gamma x^3}{3}\left(\frac{3|x|}{4} - \ln|x| - \frac{2}{3}\right) + \frac{\delta x^4}{4}\left(\frac{4|x|}{5} - \ln|x| - \frac{3}{4}\right)\right]_{x_1}^{x_2},
\end{aligned}
$$

(C.32)

with

$$
\begin{aligned}
\alpha &= \frac{2}{3} - \overline{\theta}^2 - \frac{\overline{\theta}^3}{2}, \\
\beta &= \frac{\overline{\theta}}{\Delta}(2 + \frac{3}{2}\overline{\theta}), \\
\gamma &= -\frac{1}{\Delta^2}\left(1 + \frac{3}{2}\overline{\theta}\right), \\
\delta &= \frac{1}{2\Delta^3}.
\end{aligned}
$$

(C.33)

The five different values of x_1 and x_2 are now given by

condition	x_1	x_2
$\overline{\theta} < -1 - 1/\Delta z$	$I_2^{M1} = 0$	
$-1/\Delta z - 1 < \overline{\theta} < -1/\Delta z$	-1	$\Delta z(1 + \overline{\theta})$
$-1/\Delta z < \overline{\theta} < 1/\Delta z - 1$	$\overline{\theta}\Delta z$	$\Delta z(1 + \overline{\theta})$
$1/\Delta z - 1 < \overline{\theta} < 1/\Delta z$	$\overline{\theta}\Delta z$	1
$\overline{\theta} > 1/\Delta z$	$I_2^{M1} = 0$	

For the second integration I_2^{M2} (i.e., interval is $1 < s \leq 2$) we have

$$
\begin{aligned}
I_2^{M2}(\overline{\theta}) &= \frac{1}{24\pi^2 a\Delta z} \int_{x=x_1}^{x_2} \left(-\ln|x| + |x| - 1\right) \left(2 - \left(\frac{x}{\Delta z} - \overline{\theta}\right)\right)^3 dx \\
&= \frac{1}{24\pi^2 a\Delta z} \left[\alpha x \left(\frac{|x|}{2} - \ln|x|\right) + \frac{\beta x^2}{2}\left(\frac{2|x|}{3} - \ln|x| - \frac{1}{2}\right)\right]_{x_1}^{x_2} + \\
&+ \frac{1}{24\pi^2 a\Delta z} \left[\frac{\gamma x^3}{3}\left(\frac{3|x|}{4} - \ln|x| - \frac{2}{3}\right) + \frac{\delta x^4}{4}\left(\frac{4|x|}{5} - \ln|x| - \frac{3}{4}\right)\right]_{x_1}^{x_2},
\end{aligned}
$$

(C.34)

with

$$
\begin{aligned}
\alpha &= \left(2 + \overline{\theta}\right)^3, \\
\beta &= -\frac{3}{\Delta z}\left(2 + \overline{\theta}\right)^2, \\
\gamma &= \frac{3}{\Delta z^2}\left(2 + \overline{\theta}\right), \\
\delta &= -\frac{1}{\Delta z^3}.
\end{aligned}
$$

(C.35)

In this case the following table summarizes the five different integration intervals.

condition	x_1	x_2
$\overline{\theta} < -2 - 1/\Delta z$	$I_2^{M2} = 0$	
$-1/\Delta z - 2 < \overline{\theta} < -1/\Delta z - 1$	-1	$\Delta z(2 + \overline{\theta})$
$-1/\Delta z - 1 < \overline{\theta} < 1/\Delta z - 2$	$(1 + \overline{\theta})\Delta z$	$\Delta z(2 + \overline{\theta})$
$1/\Delta z - 2 < \overline{\theta} < 1/\Delta z - 1$	$(1 + \overline{\theta})\Delta z$	1
$\overline{\theta} > 1/\Delta z - 1$	$I_2^{M2} = 0$	

Appendix D

Coordinate Transformations

D.1 Transformation formulas

A point P can be identified by a vector $\mathbf{r}$ expressed in terms of the global coordinates

$$\mathbf{r} = x\mathbf{i}_x + y\mathbf{i}_y + z\mathbf{i}_z, \tag{D.1}$$

and by a vector $\mathbf{r}'$ expressed in terms of the local coordinates

$$\mathbf{r}' = x'\mathbf{i}_{x'} + y'\mathbf{i}_{y'} + z'\mathbf{i}_{z'}, \tag{D.2}$$

where the global $(\mathbf{i}_x, \mathbf{i}_y, \mathbf{i}_z)$ and local $(\mathbf{i}_{x'}, \mathbf{i}_{y'}, \mathbf{i}_{z'})$ coordinate systems are depicted in Fig. D.1. We describe here all the steps to obtain the transformation formulas to transform (x, y, z) to (x', y', z') and vice versa. These can be summarized as follows.

- Translate the local coordinate system such that its origin is in the origin of the global coordinate system.

- Rotate the local system about the z-axis such that the image $\mathbf{i}_{z'}^{(1)}$ of $\mathbf{i}_{z'}$ is in the (x, z)-plane with $x \geq 0$.

- Rotate the local system about the y-axis such that the image $\mathbf{i}_{z'}^{(2)}$ of $\mathbf{i}_{z'}^{(1)}$ is on the positive z-axis.

- Rotate the local system about the z-axis such that the image $\mathbf{i}_{x'}^{(3)}$ of $\mathbf{i}_{x'}^{(2)}$ is on the positive x-axis.

First we write the unit vectors $\mathbf{i}_{z'}$, $\mathbf{i}_{x'}$ in global Cartesian coordinates

$$\mathbf{i}_{z'} = x_z\mathbf{i}_x + y_z\mathbf{i}_y + z_z\mathbf{i}_z, \tag{D.3}$$

$$\mathbf{i}_{x'} = x_x\mathbf{i}_x + y_x\mathbf{i}_y + z_x\mathbf{i}_z. \tag{D.4}$$
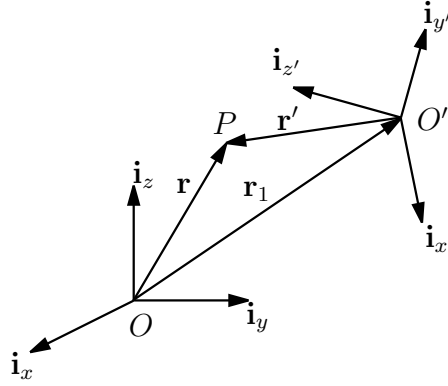
Figure D.1: *Global and local coordinate systems.*

We now translate the local coordinate system such that the origins of the two coordinate systems coalesce. This is a simple translation over the vector $-\mathbf{r}_1$, see Fig. D.1. For the subsequent steps we will write $\mathbf{i}_{z'}$ in Cartesian components in both Cartesian and spherical coordinates

$$\mathbf{i}_{z'} = x_z \mathbf{i}_x + y_z \mathbf{i}_y + z_z \mathbf{i}_z = \sin\theta\cos\phi\, \mathbf{i}_x + \sin\theta\sin\phi\, \mathbf{i}_y + \cos\theta\, \mathbf{i}_z, \tag{D.5}$$

where the angles θ, ϕ are defined as follows

$$\sin\theta = \sqrt{x_z^2 + y_z^2}, \qquad \cos\theta = z_z, \tag{D.6}$$

$$\sin\phi = \frac{y_z}{\sqrt{x_z^2 + y_z^2}}, \qquad \cos\phi = \frac{x_z}{\sqrt{x_z^2 + y_z^2}}. \tag{D.7}$$

In the first step we carry out a rotation about the z-axis such that the image $\mathbf{i}_{z'}^{(1)}$ of $\mathbf{i}_{z'}$ is in the (x, z)-plane with $x \geq 0$. The upper index represents the number of rotations that has been carried out thus far. This rotation can be written as

$$\begin{pmatrix} x_z^{(1)} \\ y_z^{(1)} \\ z_z^{(1)} \end{pmatrix} = \begin{pmatrix} \cos\phi & \sin\phi & 0 \\ -\sin\phi & \cos\phi & 0 \\ 0 & 0 & 1 \end{pmatrix} \begin{pmatrix} x_z \\ y_z \\ z_z \end{pmatrix}. \tag{D.8}$$

In the second step we carry out a rotation about the y-axis such that the image $\mathbf{i}_{z'}^{(2)}$ of $\mathbf{i}_{z'}^{(1)}$ is on the positive z-axis. This rotation is written as

$$\begin{pmatrix} x_z^{(2)} \\ y_z^{(2)} \\ z_z^{(2)} \end{pmatrix} = \begin{pmatrix} \cos\theta & 0 & -\sin\theta \\ 0 & 1 & 0 \\ \sin\theta & 0 & \cos\theta \end{pmatrix} \begin{pmatrix} x^{(1)} \\ y^{(1)} \\ z^{(1)} \end{pmatrix}. \tag{D.9}$$

Applying these two rotations to the unit vector $\mathbf{i}_{x'}$, we find its image $\mathbf{i}_{x'}^{(2)}$ as follows

$$
\begin{pmatrix} x_x^{(2)} \\ y_x^{(2)} \\ z_x^{(2)} \end{pmatrix} = \begin{pmatrix} \cos\theta\cos\phi & \cos\theta\sin\phi & -\sin\theta \\ -\sin\phi & \cos\phi & 0 \\ \sin\theta\cos\phi & \sin\theta\sin\phi & \cos\theta \end{pmatrix} \begin{pmatrix} x_x \\ y_x \\ z_x \end{pmatrix}.
\tag{D.10}
$$

The final step is to rotate about the z-axis such that the image $\mathbf{i}_{x'}^{(3)}$ of $\mathbf{i}_{x'}^{(2)}$ is on the positive x-axis

$$
\begin{pmatrix} x_x^{(3)} \\ y_x^{(3)} \\ z_x^{(3)} \end{pmatrix} = \begin{pmatrix} \cos\chi & \sin\chi & 0 \\ -\sin\chi & \cos\chi & 0 \\ 0 & 0 & 1 \end{pmatrix} \begin{pmatrix} x_x^{(2)} \\ y_x^{(2)} \\ z_x^{(2)} \end{pmatrix},
\tag{D.11}
$$

in which the angle χ is calculated from

$$
\sin\chi = -x_x\sin\phi + y_x\cos\phi,
\tag{D.12}
$$
$$
\cos\chi = x_x\cos\theta\cos\phi + y_x\cos\theta\sin\phi - z_x\sin\theta.
\tag{D.13}
$$

The composition of the three rotations results in the following transformation matrix

$$
\underline{\underline{T}} = \begin{pmatrix} \cos\chi\cos\theta\cos\phi - \sin\chi\sin\phi & \cos\chi\cos\theta\sin\phi + \sin\chi\cos\phi & -\cos\chi\sin\theta \\ -\sin\chi\cos\theta\cos\phi - \cos\chi\sin\phi & -\sin\chi\cos\theta\sin\phi + \cos\chi\cos\phi & \sin\chi\sin\theta \\ \sin\theta\cos\phi & \sin\theta\sin\phi & \cos\theta \end{pmatrix}.
$$
$$
\tag{D.14}
$$

In conclusion, knowing the vector $\mathbf{r}_1 = x_1\mathbf{i}_x + y_1\mathbf{i}_y + z_1\mathbf{i}_z$ and the global coordinates (x, y, z) of a point P, we determine its local coordinates (x', y', z') as

$$
\begin{pmatrix} x' \\ y' \\ z' \end{pmatrix} = \underline{\underline{T}} \begin{pmatrix} x - x_1 \\ y - y_1 \\ z - z_1 \end{pmatrix}.
\tag{D.15}
$$

The inverse transformation, which transforms the local coordinates (x', y', z') in the global (x, y, z), can be written as

$$
\begin{pmatrix} x \\ y \\ z \end{pmatrix} = \underline{\underline{T}}^T \begin{pmatrix} x' \\ y' \\ z' \end{pmatrix} + \begin{pmatrix} x_1 \\ y_1 \\ z_1 \end{pmatrix},
\tag{D.16}
$$

where $\underline{\underline{T}}^T = \underline{\underline{T}}^{-1}$ thanks to the orthogonality property of matrix $\underline{\underline{T}}$.

D.2   Arbitrary oriented wires

For a wire with end points $\mathbf{r}_1$ and $\mathbf{r}_2$, defined in a global coordinate system, we would like to calculate the electric field at the position $\mathbf{r}$ in the direction $\mathbf{v}_0$ given the expression of the electric field for a wire along the interval $0 < z < h$ as in equation (6.12) valid in a coordinate system local to the wire.

Firstly we define a coordinate system $(\mathbf{i}_{x'},\ \mathbf{i}_{y'},\ \mathbf{i}_{z'})$ local to the wire in the following way:

$$\mathbf{i}_{z'} = \frac{\mathbf{r}_2 - \mathbf{r}_1}{|\mathbf{r}_2 - \mathbf{r}_1|} = \frac{x_2 - x_1}{|\mathbf{r}_2 - \mathbf{r}_1|}\mathbf{i}_x + \frac{y_2 - y_1}{|\mathbf{r}_2 - \mathbf{r}_1|}\mathbf{i}_y + \frac{z_2 - z_1}{|\mathbf{r}_2 - \mathbf{r}_1|}\mathbf{i}_z, \tag{D.17}$$

where $(\mathbf{i}_x,\ \mathbf{i}_y,\ \mathbf{i}_z)$ are the unit vectors of the global coordinate system, as depicted in Fig. D.2. Then we determine unit vectors $\mathbf{i}_{x'}$, $\mathbf{i}_{y'}$ such that $\mathbf{i}_{x'} \cdot \mathbf{i}_{z'} = 0$ and $\mathbf{i}_{y'} = \mathbf{i}_{z'} \times \mathbf{i}_{x'}$. The way to calculate the field is to translate and rotate the wire such that it extends along the z-axis from 0 to h and the local unit vector $\mathbf{i}_{x'}$ is on the positive x-axis of the global coordinate system as described in the previous section. Then we use the same translation and rotations to find the images $\mathbf{r}'$ and $\mathbf{v}_0'$ of the vectors $\mathbf{r}$ and $\mathbf{v}_0$ in the local coordinate system. Next we calculate the electric field in the direction $\mathbf{v}_0'$.
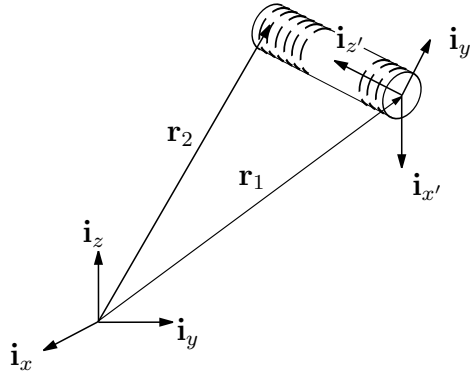
Figure D.2: *The global coordinate system $(\mathbf{i}_x, \mathbf{i}_y, \mathbf{i}_z)$ and the arbitrarily oriented wire with its local coordinate system $(\mathbf{i}_{x'}, \mathbf{i}_{y'}, \mathbf{i}_{z'})$.*

Once the transformation matrix $\underline{\underline{T}}$ has been determined (D.14), having defined an arbitrary point $\mathbf{r}$ and the wire end point $\mathbf{r}_1$ as

$$\begin{align}
\mathbf{r} &= x\mathbf{i}_x + y\mathbf{i}_y + z\mathbf{i}_z, \tag{D.18}\\
\mathbf{r}_1 &= x_1\mathbf{i}_x + y_1\mathbf{i}_y + z_1\mathbf{i}_z, \tag{D.19}
\end{align}$$

we can determine the image $\mathbf{r}'$ of point $\mathbf{r}$ in a coordinate system local to the wire by applying equation (D.15). For the direction vector $\mathbf{v}_0$, it is crucial that the translation

over $-\mathbf{r}_1$ is not carried out. Hence the image $\mathbf{v}_0'$ of $\mathbf{v}_0$ is

$$
\begin{pmatrix} v_{0x}' \\ v_{0y}' \\ v_{0z}' \end{pmatrix} = \underline{\underline{T}} \begin{pmatrix} v_{0x} \\ v_{0y} \\ v_{0z} \end{pmatrix}.
\tag{D.20}
$$

If we define the electric field in $\mathbf{r}$ in the original coordinate system as $\mathbf{E}(\mathbf{r})$ and the electric field in $\mathbf{r}'$ in the transformed one as $\mathbf{E}'(\mathbf{r}')$, then we end up with

$$
\mathbf{v}_0 \cdot \mathbf{E}(\mathbf{r}) = \mathbf{v}_0' \cdot \mathbf{E}(\mathbf{r}').
\tag{D.21}
$$

Appendix E

The Rao-Wilton-Glisson function

E.1   Description

In this appendix we summarize the main properties of the well-known RWG functions [17] extensively used in Chapter 7. Figure E.1 shows a possible set of triangles, edges and vertices for a closed surface (Fig. E.1-(a)) and for a open surface (e.g., a planar surface, Fig. E.1-(b)).
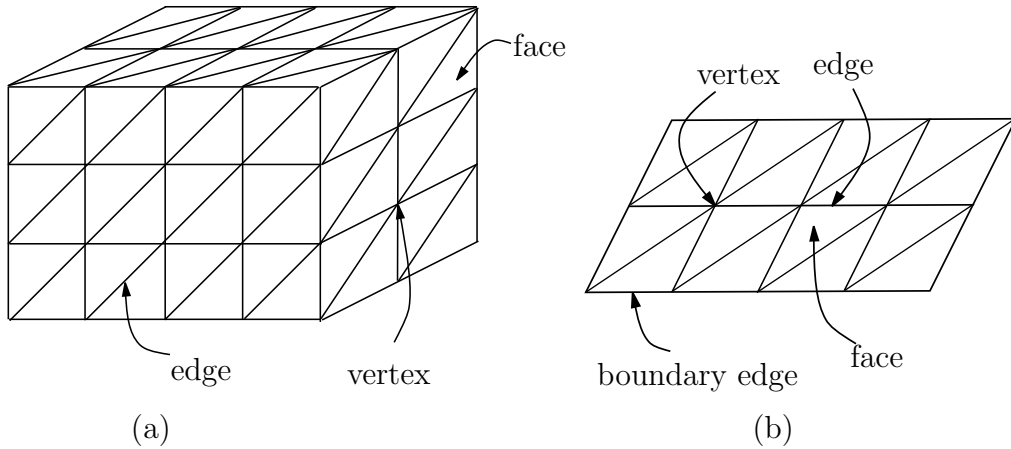
Figure E.1: *(a)- Closed surface of a box approximated by triangular patches. (b)- Planar surface modeled by triangular patches, where a boundary edge is shown.*

The use of RWG functions as expansion functions, is therefore related to the usability of a relatively good mesh generator. As already mentioned (Sec. 7.5), an in-house simple mesh generator has been developed to discretize structures like planar surfaces.

We recall here briefly the expression of an n-th RWG function

$$
\boldsymbol{\psi}_n^B(\mathbf{r}) = \begin{cases}
\dfrac{\ell_n}{2A_n^+}\boldsymbol{\rho}_n^+, & \mathbf{r} \in T_n^+, \\[2mm]
\dfrac{\ell_n}{2A_n^-}\boldsymbol{\rho}_n^-, & \mathbf{r} \in T_n^-, \\[2mm]
0, & \text{otherwise,}
\end{cases}
\tag{E.1}
$$

defined on two adjoining triangles T_n^+ and T_n^- connected through the n-th common edge of length ℓ_n as shown in Fig. E.2-(a). Points on the RWG function can be designated either by the position vectors $\mathbf{r}_n^{\pm}$ with respect to the global origin O, or with the position vectors $\boldsymbol{\rho}_n^{\pm}$ in $T_n^{\pm}$ with respect to triangular vertices $O_n^{\pm}$. $A_n^{\pm}$ is the area of triangle $T_n^{\pm}$ and ℓ_n is the length of the common edge.
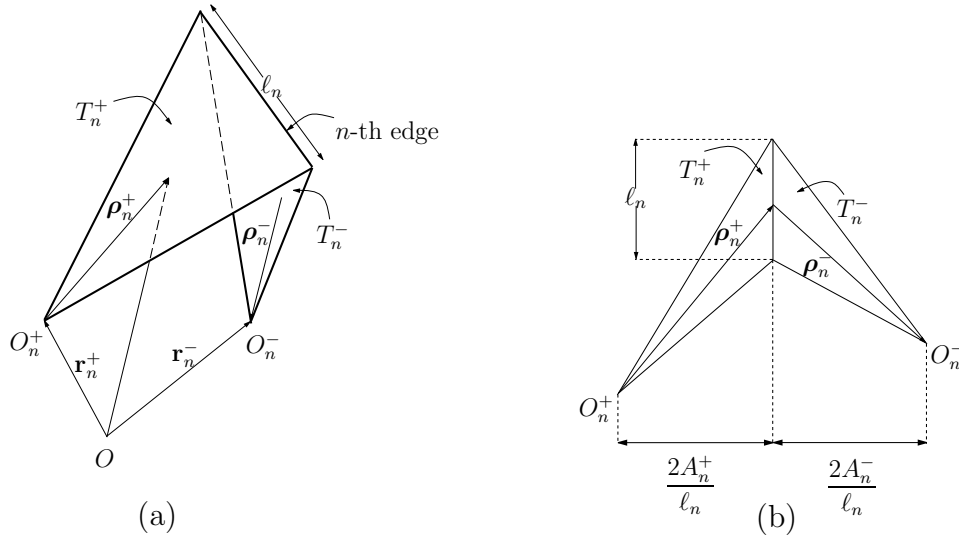
Figure E.2: *(a)- Local coordinates associated with an edge. (b)- Geometry for the normal component at the common edges.*

Now we will describe the main properties of the RWG basis function $\boldsymbol{\psi}_n(\mathbf{r})$.

1. The normal component of the current is continuous across the common edge, and the currents have no component normal to the boundary of the surface formed by $T_n^+ \cup T_n^-$. Consequently, no line charges are present along the common (interior) edge and along the outer boundary of the RWG function. Moreover the surface divergence in $T_n^{\pm}$ of $\boldsymbol{\psi}_n(\mathbf{r})$, which is proportional to the surface charge density associated with

the triangle patch, is

$$
\nabla_S \cdot \boldsymbol{\psi}_n(\mathbf{r}) = \begin{cases} \dfrac{\ell_n}{A_n^+}, & \mathbf{r} \in T_n^+, \\[2mm] -\dfrac{\ell_n}{A_n^-}, & \mathbf{r} \in T_n^-, \\[2mm] 0, & \text{otherwise.} \end{cases}
\tag{E.2}
$$

Hence, we can conclude that the surface charge density is constant within a single triangle and the total charge associated with the triangle pair T_n^+, T_n^- is zero (i.e., the integral of the surface divergence on the triangle pair vanishes).

2. The normal component on the boundary of $T_n^+ \cup T_n^-$ is zero, which facilitates the evaluation of the $\nabla_S \cdot$ term in the integral equation (7.17) as discussed in Appendix E.2.

3. The moment of $\boldsymbol{\psi}_n(\mathbf{r})$ is given by $\left(A_n^+ + A_n^-\right) \boldsymbol{\psi}_n(\mathbf{r})^{\text{avg}}$, which is determined as (see also Fig. E.3)

$$
\left(A_n^+ + A_n^-\right) \boldsymbol{\psi}_n(\mathbf{r})^{\text{avg}} \equiv \int\limits_{T_n^+ \cup T_n^-} \boldsymbol{\psi}_n(\mathbf{r}) dS = \frac{\ell_n}{2} \left(\boldsymbol{\rho}_n^{c+} + \boldsymbol{\rho}_n^{c-}\right) = \ell_n \left(\mathbf{r}_n^{c+} - \mathbf{r}_n^{c-}\right),
\tag{E.3}
$$

where $\boldsymbol{\rho}_n^{c\pm}$ is the vector between the free vertex and the centroid of $T_n^{\pm}$, with $\boldsymbol{\rho}_n^{c+}$ directed toward and $\boldsymbol{\rho}_n^{c-}$ directed away from the common edge ℓ_n. The vector from the global origin O to the centroid of $T_n^{\pm}$ is represented by $\mathbf{r}_n^{c\pm}$.
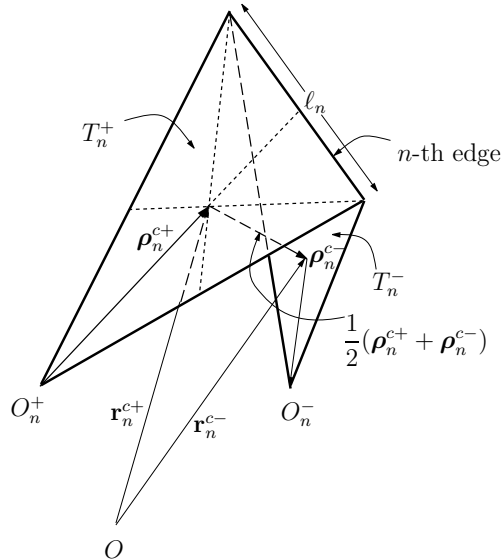
Figure E.3: *Coordinates for calculating centroids and moment of RWG function.*

E.2   Employing the properties

Thanks to the properties of the RWG functions, we will now prove an important result which simplifies the expression (7.17). For the sake of clarity we rewrite here the second term on the left-hand side of (7.17)

$$\int\limits_{T_m^+ \cup T_m^-} \boldsymbol{\psi}_m(\mathbf{r}) \cdot \left(\nabla_S \int\limits_{T_n^+ \cup T_n^-} G(\mathbf{r}, \mathbf{r}') \left(\nabla_{S'} \cdot \boldsymbol{\psi}_n(\mathbf{r}') \right) dS' \right) dS. \tag{E.4}$$

With the definition of the function $p(\mathbf{r})$ as

$$p(\mathbf{r}) = \int\limits_{T_n^+ \cup T_n^-} G(\mathbf{r}, \mathbf{r}') \left(\nabla_{S'} \cdot \boldsymbol{\psi}_n(\mathbf{r}') \right) dS', \tag{E.5}$$

the expression (E.4) becomes

$$\int\limits_{T_m^+ \cup T_m^-} \left(\nabla_S \, p(\mathbf{r}) \right) \cdot \boldsymbol{\psi}_m(\mathbf{r}) dS, \tag{E.6}$$

where the surface gradient operates directly on $p(\mathbf{r})$. Thanks to RWG properties, the integral in (E.5) can be simplified to

$$\int\limits_{T_m^+ \cup T_m^-} \left(\nabla_S p(\mathbf{r}) \right) \cdot \boldsymbol{\psi}_m(\mathbf{r}) dS = - \int\limits_{T_m^+ \cup T_m^-} p(\mathbf{r}) \nabla_S \cdot \boldsymbol{\psi}_m(\mathbf{r}) dS, \tag{E.7}$$

where the surface divergence is applied to the basis function $\boldsymbol{\psi}_n(\mathbf{r})$.

PROOF : The integral with respect to the primed coordinate in (E.4) is a scalar depending solely on $\mathbf{r}$, for which the property (E.7) holds. With the aid of the vector identity $\nabla \cdot (p\mathbf{A}) = \mathbf{A} \cdot \nabla p + p\nabla \cdot \mathbf{A}$ it follows that

$$\int\limits_{T_m^+ \cup T_m^-} \left(\nabla_S p(\mathbf{r}) \right) \cdot \boldsymbol{\psi}_m(\mathbf{r}) dS = \int\limits_{T_m^+ \cup T_m^-} \nabla_S \cdot \left(p(\mathbf{r}) \boldsymbol{\psi}_m(\mathbf{r}) \right) dS - \int\limits_{T_m^+ \cup T_m^-} p(\mathbf{r}) \nabla_S \cdot \boldsymbol{\psi}_m(\mathbf{r}) dS. \tag{E.8}$$

Applying Gauss' theorem now results in

$$\int\limits_{T_m^+ \cup T_m^-} \nabla_S \cdot \left(p(\mathbf{r}) \boldsymbol{\psi}_m(\mathbf{r}) \right) dS = \oint\limits_C \mathbf{i}_b \cdot \left(p(\mathbf{r}) \boldsymbol{\psi}_m(\mathbf{r}) \right) d\ell, \tag{E.9}$$

where C is the contour around the surface $T_m^+ \cup T_m^-$ and where $\mathbf{i}_b$ is the unitary vector normal to the contour, pointing outward of the contour. Since the RWG function

$\boldsymbol{\psi}_m(\mathbf{r})$ has no components normal to the outer boundary (in this case the contour C), it follows that

$$\oint_C \mathbf{i}_b \cdot (p(\mathbf{r})\boldsymbol{\psi}_m(\mathbf{r}))\, d\ell = 0. \tag{E.10}$$

Thus the property in (E.7) is demonstrated and therefore can be applied to the second term on the left-hand side of equation (7.17):

$$\int_{T_m^+ \cup T_m^-} \boldsymbol{\psi}_m(\mathbf{r}) \cdot \left(\nabla_S \int_{T_n^+ \cup T_n^-} G(\mathbf{r},\mathbf{r}')\left(\nabla_{S'} \cdot \boldsymbol{\psi}_n(\mathbf{r}')\right) dS' \right) \cdot \boldsymbol{\psi}_m(\mathbf{r}) dS =$$
$$- \int_{T_m^+ \cup T_m^-} (\nabla_S \cdot \boldsymbol{\psi}_m(\mathbf{r})) \int_{T_n^+ \cup T_n^-} G(\mathbf{r},\mathbf{r}')\left(\nabla_{S'} \cdot \boldsymbol{\psi}_n(\mathbf{r}')\right) dS' dS. \tag{E.11}$$

Appendix F

Integration over a triangular surface

F.1 Normalized area local coordinates

To determine the surface integrals related to the test and basis RWG function (7.13) and
(E.1) it is convenient to use a local coordinate system for each triangle. The triangle T_n
with area A_n is subdivided into three sub-triangles of areas A_1, A_2, A_3, respectively, see
Fig. F.1.
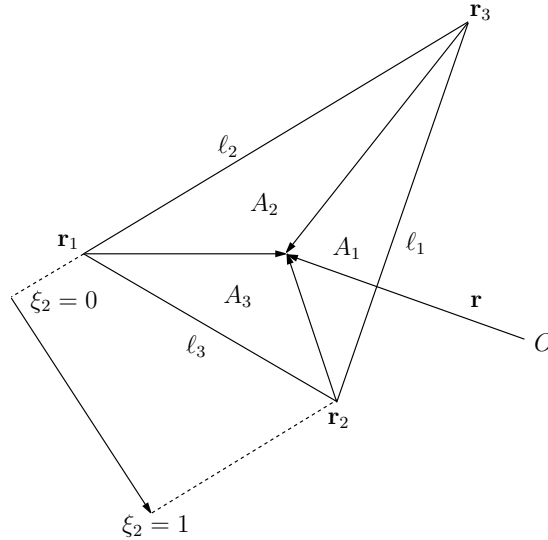
Figure F.1: *The subdivision of triangle T_n in sub-triangles for the definition of the normalized area local coordinates.*

The normalized area coordinates (also referred to as barycentric coordinates) are defined

as

$$\xi_1 = \frac{A_1}{A_n}, \qquad \xi_2 = \frac{A_2}{A_n}, \qquad \xi_3 = \frac{A_3}{A_n}, \tag{F.1}$$

where A_1, A_2, A_3 satisfy the relation

$$A_1 + A_2 + A_3 = A_n, \tag{F.2}$$

and therefore $\xi_1 + \xi_2 + \xi_3 = 1$ is valid. The position of a point in the triangle T_n is given by

$$\mathbf{r} = \xi_1\mathbf{r}_1 + \xi_2\mathbf{r}_2 + \xi_3\mathbf{r}_3 = \xi_1\mathbf{r}_1 + \xi_2\mathbf{r}_2 + (1 - \xi_1 - \xi_2)\,\mathbf{r}_3. \tag{F.3}$$

In the triangle T_n, all the three coordinates vary between zero and one; in particular at the corners $\mathbf{r}_1$, $\mathbf{r}_2$ and $\mathbf{r}_3$, the area coordinates ξ_1, ξ_2 and ξ_3 take the values $(1, 0, 0)$, $(0, 1, 0)$ and $(0, 0, 1)$, respectively. As a consequence, the surface integral of a function $g(\mathbf{r})$ over the triangle T_n becomes

$$\int_{T_n} g(\mathbf{r})dS = 2A_n \int_{\xi_1=0}^{1} \int_{\xi_2=0}^{1-\xi_1} g\left(\xi_1\mathbf{r}_1 + \xi_2\mathbf{r}_2 + (1 - \xi_1 - \xi_2)\,\mathbf{r}_3\right) d\xi_2 d\xi_1, \tag{F.4}$$

where the factor $2A_n$ is the Jacobian.

F.2 Gaussian quadrature rule

This section describes the Gaussian quadrature integration rule which can be applied in local normalized area coordinates (see Appendix F.1). The integration of a function $g(\xi_1, \xi_2)$ over the triangle is performed using Gaussian quadrature such that

$$2A_n \int_{\xi_1=0}^{1} \int_{\xi_2=0}^{1-\xi_1} g(\xi_1, \xi_2)d\xi_2 d\xi_1 \approx A_n \sum_{n=1}^{N_G} w_n g(\xi_{1n}, \xi_{2n}). \tag{F.5}$$

Here, A_n is the area of the n-th triangular patch, N_G is the number of quadrature points. The coordinates of the sample points $(\xi_{1n}, \xi_{2n}, \xi_{3n})$ and the weighting coefficients w_n in (F.5) are given in Table F.1 for $N_G = 7$ and can be found in [88, pag.358].

n	ξ_{1n}	ξ_{2n}	ξ_{3n}	w_n
1	0.333333333333333	0.333333333333333	0.333333333333333	0.112500000000000
2	0.059715871789770	0.470142064105115	0.470142064105115	0.066197076394253
3	0.470142064105115	0.059715871789770	0.470142064105115	0.066197076394253
4	0.470142064105115	0.470142064105115	0.059715871789770	0.066197076394253
5	0.797426985353087	0.101286507323456	0.101286507323456	0.062969590272414
6	0.101286507323456	0.797426985353087	0.101286507323456	0.062969590272414
7	0.101286507323456	0.101286507323456	0.797426985353087	0.062969590272414

Table F.1: *Gaussian points and weighting factors for integration over the triangle T_n,* $\xi_{1n} \geq 0$, $\xi_{2n} \geq 0$, $\xi_{3n} = 1 - \xi_{1n} - \xi_{2n} \geq 0$.

F.3 Analytic part of the integral over the self patch

In this section, the analytical expressions of integrals I_1 and I_2 in (7.27), (7.28) (rewritten here for the sake of completeness)

$$I_1 = \frac{1}{4\pi} \int\limits_T \int\limits_{T'} \frac{1}{R} dS' dS, \tag{F.6}$$

$$I_2 = \frac{1}{4\pi} \int\limits_T \boldsymbol{\rho}_\alpha \cdot \int\limits_{T'} \boldsymbol{\rho}_\beta \frac{1}{R} dS' dS, \tag{F.7}$$

are given as found in [19] for coincident triangles $T = T'$. Consider two generic coplanar triangles T and T'. In this case, the vectors $\mathbf{R} = \mathbf{r} - \mathbf{r}'$, $\boldsymbol{\rho}_\alpha$ and $\boldsymbol{\rho}_\beta$ lie in the same plane of the triangles (see Fig. F.2) and the following identity holds

$$\frac{1}{R} = -\nabla_S \cdot \nabla_{S'} R. \tag{F.8}$$

By applying Stokes' theorem, the authors of [19] transform the two double-surface integrals (F.6), (F.7) in double-line integrals. In the case of coincident triangles, analytical expressions are found and are repeated here:

$$I_1 = -\frac{1}{3\pi} A^2 \left(\frac{1}{a} \ln\left(1 - \frac{a}{p}\right) + \frac{1}{b} \ln\left(1 - \frac{b}{p}\right) + \frac{1}{c} \ln\left(1 - \frac{c}{p}\right) \right). \tag{F.9}$$
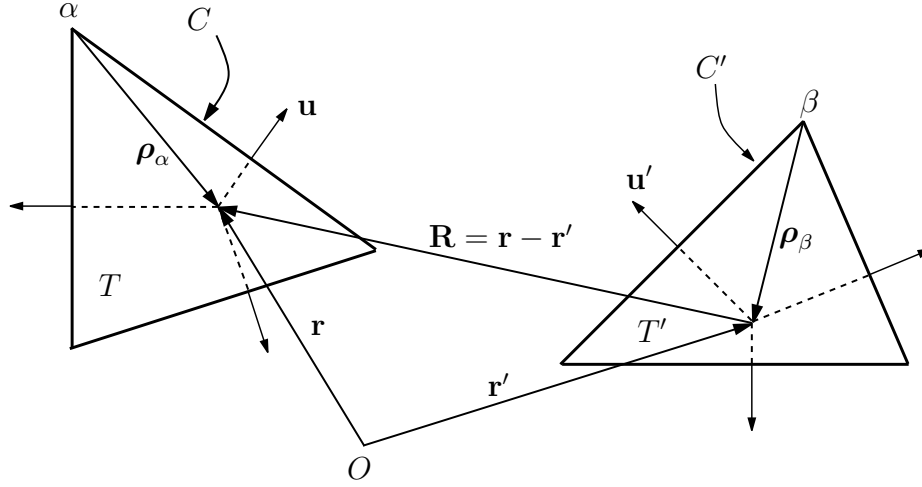
Figure F.2: *Geometrical quantities associated to triangle T and T'.*

Case of vertex $\alpha = \beta$: a is the length of the edge opposite to vertex α

$$
\begin{aligned}
I_2 &= \frac{1}{4\pi} \int_T \boldsymbol{\rho}_\alpha \cdot \int_{T'} \boldsymbol{\rho}_\beta \frac{1}{R} dS' dS \\
&= \frac{A^2}{120\pi} \left[\left(10 + 3\frac{c^2 - a^2}{b^2} - 3\frac{a^2 - b^2}{c^2} \right) a - \left(5 - 3\frac{a^2 - b^2}{c^2} - 2\frac{b^2 - c^2}{a^2} \right) b \right. \\
&\quad - \left(5 + 3\frac{c^2 - a^2}{b^2} + 2\frac{b^2 - c^2}{a^2} \right) c + \left(a^2 - 3b^2 - 3c^2 - 8\frac{A^2}{a^2} \right) \frac{2}{a} \ln\left(1 - \frac{a}{p} \right) \\
&\quad + \left(a^2 - 2b^2 - 4c^2 + 6\frac{A^2}{b^2} \right) \frac{4}{b} \ln\left(1 - \frac{b}{p} \right) \\
&\quad \left. + \left(a^2 - 4b^2 - 2c^2 + 6\frac{A^2}{c^2} \right) \frac{4}{c} \ln\left(1 - \frac{c}{p} \right) \right].
\end{aligned}
\tag{F.10}
$$

Case of vertex $\alpha \neq \beta$: a is the length of the edge between vertices α and β

$$
\begin{aligned}
I_2 &= \frac{A^2}{240\pi} \left[\left(-10 + \frac{c^2 - a^2}{b^2} - \frac{a^2 - b^2}{c^2} \right) a + \left(5 + \frac{a^2 - b^2}{c^2} - 6\frac{b^2 - c^2}{a^2} \right) b \right. \\
&\quad + \left(5 - \frac{c^2 - a^2}{b^2} + 6\frac{b^2 - c^2}{a^2} \right) c + \left(2a^2 - b^2 - c^2 + 4\frac{A^2}{a^2} \right) \frac{12}{a} \ln\left(1 - \frac{a}{p} \right) \\
&\quad + \left(9a^2 - 3b^2 - c^2 + 4\frac{A^2}{b^2} \right) \frac{2}{b} \ln\left(1 - \frac{b}{p} \right) \\
&\quad \left. + \left(9a^2 - b^2 - 3c^2 + 4\frac{A^2}{c^2} \right) \frac{2}{c} \ln\left(1 - \frac{c}{p} \right) \right].
\end{aligned}
\tag{F.11}
$$

In these expressions T denotes a generic triangular patch, a, b, c denote the lengths of the triangle's edges, A denotes the area and $p = (a + b + c)/2$ is the half-perimeter of the

triangle.

F.4   Integration over patches sharing an edge or a vertex

When the integration triangles share an edge or a vertex as well as when they are coincident, the integral over T' of the extracted singular terms in (7.27), (7.28) has a closed form. The other integral over T is subsequently evaluated via a Gaussian quadrature rule for triangles. Following the scheme proposed by Oijala and M. Taskinen [18], we give here the formulas to calculate the integrals of extracted singular and non-continuously differentiable terms

$$K_1^{-1} = \int\limits_{T'} \frac{1}{R} dS', \qquad \mathbf{K}_2^{-1} = \int\limits_{T'} \boldsymbol{\rho}_\beta \frac{1}{R} dS', \tag{F.12}$$

$$K_1^1 = \int\limits_{T'} R \, dS', \qquad \mathbf{K}_2^1 = \int\limits_{T'} \boldsymbol{\rho}_\beta R \, dS', \tag{F.13}$$

present in equations (7.27) and (7.28). We make the assumption that the vertex β of the triangle T is denoted by the position vector $\mathbf{q}_3$ (see Fig. F.3) and we rewrite the known results found in [18]

$$I_i^{-1} = \int\limits_{\partial_i T'} \frac{1}{R} d\ell' = \ln\left(\frac{R_i^+ + s_i^+}{R_i^- + s_i^-}\right), \tag{F.14}$$

$$K_1^{-3} = \int\limits_{T'} \frac{1}{R^3} dS' = \begin{cases} 0, & \text{if } w_0 = 0, \\ \dfrac{1}{|w_0|} \sum\limits_{i=1}^{3} \beta_i, & \text{otherwise,} \end{cases} \tag{F.15}$$

where $\partial_i T'$, $i = 1,\ 2,\ 3$, are the edges of T' and where

$$\beta_i = \arctan\left(\frac{t_i^0 s_i^+}{(R_i^0)^2 + |w_0| R_i^+}\right) - \arctan\left(\frac{t_i^0 s_i^-}{(R_i^0)^2 + |w_0| R_i^-}\right). \tag{F.16}$$

The other variables are defined as

$$
\begin{aligned}
&\mathbf{u} = \frac{\mathbf{q}_2 - \mathbf{q}_1}{\ell_3}, && w_0 = (\mathbf{r} - \mathbf{q}_1) \cdot \mathbf{n}, \\
&\mathbf{v} = \mathbf{n} \times \mathbf{u}, && v_0 = (\mathbf{r} - \mathbf{q}_1) \cdot \mathbf{v}, \\
&u_3 = (\mathbf{q}_3 - \mathbf{q}_1) \cdot \mathbf{u}, && u_0 = (\mathbf{r} - \mathbf{q}_1) \cdot \mathbf{u}, \\
&v_3 = \frac{2A}{\ell_3}, && \\
&s_1^- = -\frac{(\ell_3 - u_0)(\ell_3 - u_3) + v_0 v_3}{\ell_1}, && s_1^+ = s_1^- + \ell_1, \\
&s_2^- = -\frac{u_3(u_3 - u_0) + v_3(v_3 - v_0)}{\ell_2}, && s_2^+ = s_2^- + \ell_2, \\
&s_3^- = -u_0, && s_3^+ = s_3^- + \ell_3, \\
&t_1^0 = \frac{v_0(u_3 - \ell_3) + v_3(\ell_3 - u_0)}{\ell_1}, && R_1^+ = R_2^- = |\mathbf{r} - \mathbf{q}_3|, \\
&t_2^0 = \frac{u_0 v_3 - v_0 u_3}{\ell_2}, && R_2^+ = R_3^- = |\mathbf{r} - \mathbf{q}_1|, \\
&t_3^0 = v_0, && R_3^+ = R_1^- = |\mathbf{r} - \mathbf{q}_2|, \\
&R_i^0 = \sqrt{(t_i^0)^2 + w_0^2}.
\end{aligned}
\tag{F.17}
$$

Here, ℓ_i, $i = 1,\ 2,\ 3$, are the lengths of the edges $\partial_i T'$, $\mathbf{q}_i$, $i = 1,\ 2,\ 3$, are the vertices of T', and A denotes the area of T', see Fig. F.3.
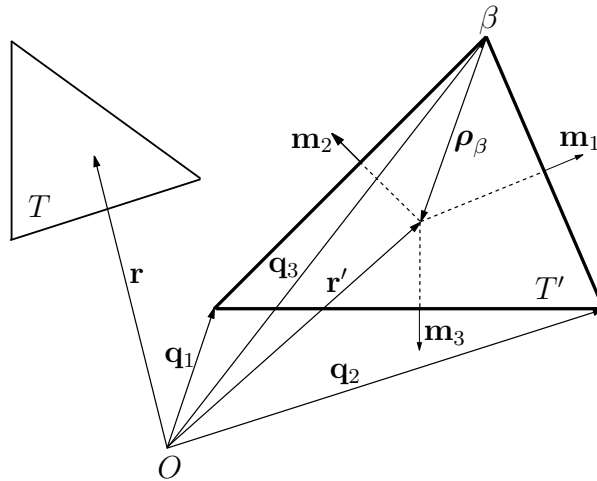
Figure F.3: *Notation for analytical formulas of integrals on triangle T' as in [18].*

Now, by using the above notation we can write (F.12) and (F.13) in closed form as

$$
K_1^{-1} = \begin{cases} \sum_{i=1}^{3} t_i^0 I_i^{-1}, & w_0 = 0, \\ -w_0^2 K_1^{-3} + \sum_{i=1}^{3} t_i^0 I_i^{-1}, & w_0 \neq 0, \end{cases}
\tag{F.18}
$$

$$
K_1^1 = \begin{cases} \dfrac{1}{3} \sum_{i=1}^{3} t_i^0 I_i^1, & w_0 = 0, \\ \dfrac{1}{3} \left(-w_0^2 K_1^{-1} + \sum_{i=1}^{3} t_i^0 I_i^1 \right), & w_0 \neq 0, \end{cases}
\tag{F.19}
$$

$$
\mathbf{K}_2^{-1} = \mathbf{I}_m^1 + (\mathbf{r} - \mathbf{q}_3) K_1^{-1},
\tag{F.20}
$$

$$
\mathbf{K}_2^1 = \frac{1}{3}\mathbf{I}_m^3 + (\mathbf{r} - \mathbf{q}_3) K_1^1,
\tag{F.21}
$$

where

$$
\mathbf{I}_m^1 = \mathbf{m}_1 I_1^1 + \mathbf{m}_2 I_2^1 + \mathbf{m}_3 I_1^1,
\tag{F.22}
$$

$$
\mathbf{I}_m^3 = \mathbf{m}_1 I_1^3 + \mathbf{m}_2 I_2^3 + \mathbf{m}_3 I_1^3,
\tag{F.23}
$$

and where $\mathbf{r}$ is the observation point on triangle T, $\mathbf{n}$ is the unit normal of T', and $\mathbf{m}_i$ is the outer unit normal of the edge $\partial_i T'$, $i = 1,\ 2,\ 3$, see Fig. F.3. In addition, we need also the following recursive formula

$$
I_i^1 = \int_{\partial_i T'} R d\ell' = \frac{1}{2} \left(s_i^+ R_i^+ - s_i^- R_i^- + \left(R_i^0 \right)^2 I_i^{-1} \right),
\tag{F.24}
$$

$$
I_i^3 = \int_{\partial_i T'} R^3 d\ell' = \frac{1}{4} \left(s_i^+ \left(R_i^+ \right)^3 - s_i^- \left(R_i^- \right)^3 + 3 \left(R_i^0 \right)^2 I_i^1 \right).
\tag{F.25}
$$

Appendix G

Evaluation of integrals for a wire attached to a planar surface

In this appendix we give an insight into the manner in which all integrals occurring in the attachment mode can be calculated. With the aid of analytical techniques, all weakly singular integrands have been accounted for.

The developed method is not optimized in details but it proves that the introduction of a special attachment basis function in combination with the Galerkin MoM (Sec. 8.2) does not lead to computational problems. Implementations of dedicated (ad-hoc) routines to evaluate the integrals described below could lead to a more efficient code.

G.1 Types of integrals for matrix elements

In this section we describe the numerical procedure developed for the computation of the elements of sub-matrices $\underline{\underline{\mathbf{Z}}}^a$, $\underline{\underline{\mathbf{C}}}^{B,a}$, $\underline{\underline{\mathbf{C}}}^{W,a}$ in (8.37) when the singularity occurs. Looking at the integral expressions (8.40), (8.50), (8.58) of these sub-matrix elements, we recognize nine different types of integrals

$$
I_1[n] = \int\limits_{z=n\Delta z}^{(n+1)\Delta z} \int\limits_{z'=0}^{\Delta z} \int\limits_{\varphi=0}^{2\pi} G(\mathbf{r}-\mathbf{r}') \left(1 - \frac{z'}{\Delta z}\right)\left(1 - \frac{z}{\Delta z} + n\right) d\varphi dz' dz, \quad n = 0, 1, \ldots, N, \quad \text{(G.1)}
$$

$$
I_2[n] = \int\limits_{z=(n-1)\Delta z}^{n\Delta z} \int\limits_{z'=0}^{\Delta z} \int\limits_{\varphi=0}^{2\pi} G(\mathbf{r}-\mathbf{r}') \left(1 - \frac{z'}{\Delta z}\right)\left(1 + \frac{z}{\Delta z} - n\right) d\varphi dz' dz, \quad n = 1, 2, \ldots, N, \quad \text{(G.2)}
$$

$$I_3[n] = \int\limits_{z=n\Delta z}^{(n+1)\Delta z} \int\limits_{z'=0}^{\Delta z} \int\limits_{\varphi=0}^{2\pi} G(\mathbf{r} - \mathbf{r}')d\varphi dz' dz, \qquad n = 0, 1, \ldots, N, \tag{G.3}$$

where $|\mathbf{r} - \mathbf{r}'| = \sqrt{(z - z')^2 + 4a^2 \sin^2(\varphi/2)}$,

$$I_4 = \int\limits_{r=a}^{b} \int\limits_{r'=a}^{b} \int\limits_{\varphi=0}^{2\pi} G(\mathbf{r} - \mathbf{r}')(r' - b)(r - b)\cos\varphi d\varphi dr' dr, \tag{G.4}$$

$$I_5 = \int\limits_{r=a}^{b} \int\limits_{r'=a}^{b} \int\limits_{\varphi=0}^{2\pi} G(\mathbf{r} - \mathbf{r}')d\varphi dr' dr, \tag{G.5}$$

where $|\mathbf{r} - \mathbf{r}'| = \sqrt{r^2 + r'^2 - 2rr'\cos\varphi}$,

$$I_6[n] = \int\limits_{z=n\Delta z}^{(n+1)\Delta z} \int\limits_{r'=a}^{b} \int\limits_{\varphi=0}^{2\pi} G(\mathbf{r} - \mathbf{r}')d\varphi dr' dz, \qquad n = 0, 1, \ldots, N, \tag{G.6}$$

where $\qquad |\mathbf{r} - \mathbf{r}'| = \sqrt{r'^2 + a^2 - 2ar'\cos\varphi + z^2}$, and

$$I_7 = \int\limits_{T} \int\limits_{z'=0}^{\Delta} \int\limits_{\phi'=0}^{2\pi} G(\mathbf{r} - \mathbf{r}')dz' d\phi' dS, \qquad \mathbf{r}' = a\cos\phi'\mathbf{i}_x + a\sin\phi'\mathbf{i}_y + z'\mathbf{i}_z, \tag{G.7}$$

$$I_8 = \int\limits_{T} \int\limits_{r'=a}^{b} \int\limits_{\phi'=0}^{2\pi} G(\mathbf{r} - \mathbf{r}')dr' d\phi' dS, \qquad \mathbf{r}' = r'\cos\phi'\mathbf{i}_x + r'\sin\phi'\mathbf{i}_y, \tag{G.8}$$

$$I_9 = \int\limits_{T} \int\limits_{r'=a}^{b} \int\limits_{\phi'=0}^{2\pi} G(\mathbf{r} - \mathbf{r}')(r' - b)\mathbf{i}_r(\phi') \cdot \boldsymbol{\rho}(\mathbf{r})dr' d\phi' dS, \quad \mathbf{r}' = r'\cos\phi'\mathbf{i}_x + r'\sin\phi'\mathbf{i}_y, \tag{G.9}$$

and $\mathbf{r} = r\cos\phi\mathbf{i}_x + r\sin\phi\mathbf{i}_y$ belongs to the triangular patch T. As already explained in Sec. 8.2.4 all these integrals contain a free space Green's function $G(\mathbf{r} - \mathbf{r}')$, which exhibits a singular behavior when the distance $|\mathbf{r} - \mathbf{r}'|$ approaches zero. In this appendix we describe how the integrations (G.1)-(G.9) are carried out. Basically integrals (G.1)-(G.3) are computed by following the same procedure developed for the single wire (see Sec. 3.3), where the singular behavior of the integrand function is extracted and integrated analytically. The other integrals (G.4)-(G.9) are carried out by introducing a series expansion of the Green's function for the Helmholtz operator in cylindrical coordinates (see [89, pag. 888]). The procedure has been implemented in FORTRAN.

We recall that the attachment self matrix $\underline{\underline{Z}}^a$ consists of a single element (8.40) and its computation requires the evaluation of

$$
\begin{aligned}
Z^a \;=\;& j\omega\mu\frac{1}{2\pi}I_1[0] + \frac{1}{j\omega\epsilon}\frac{1}{2\pi\Delta z^2}I_3[0] + j\omega\mu\frac{1}{2\pi(b-a)^2}I_4 \\
+\;& \frac{1}{j\omega\epsilon}\frac{1}{2\pi(b-a)^2}I_5 - \frac{1}{j\omega\epsilon}\frac{1}{\pi(b-a)\Delta z}I_6[0].
\end{aligned}
\tag{G.10}
$$

The matrix $\underline{\underline{C}}^{B,a}$ is a column vector of M elements, where M is the number of RWG expansion functions used in the discretization of the planar surface. This means that for the calculation of each m-th vector element, from equation (8.50), we have

$$
\begin{aligned}
C_m^{B,a} \;=\;& -j\omega\mu\frac{\ell_m}{4\pi(b-a)}\left(\frac{1}{A_m^+}I_9^+ + \frac{1}{A_m^-}I_9^-\right) - \frac{1}{j\omega\epsilon}\frac{\ell_m}{2\pi\Delta z}\left(\frac{1}{A_m^-}I_7^- - \frac{1}{A_m^+}I_7^+\right) \\
&- \frac{1}{j\omega\epsilon}\frac{\ell_m}{2\pi(b-a)}\left(\frac{1}{A_m^+}I_8^+ - \frac{1}{A_m^-}I_8^-\right), \qquad \text{with } m=1,\ldots,M,
\end{aligned}
\tag{G.11}
$$

where the superscript $+$ or $-$ shows that the integration region is T_m^+ or T_m^-. Finally, from (8.58), the sub-matrix $\underline{\underline{C}}^{W,a}$, which is a column vector of N elements (i.e., N rooftop functions are used in the wire current expansion) can be computed as

$$
\begin{aligned}
C_n^{W,a} \;=\;& -j\omega\mu\frac{1}{2\pi}(I_1[n] + I_2[n]) - \frac{1}{j\omega\epsilon}\frac{1}{2\pi\Delta z^2}(I_3[n] - I_3[n-1]) \\
&- \frac{1}{j\omega\epsilon}\frac{1}{2\pi(b-a)\Delta z}(I_6[n-1] - I_6[n]) \qquad \text{with } n=1,\ldots,N.
\end{aligned}
\tag{G.12}
$$

G.1.1   Computation of integrals I_1, I_2 and I_3

By using the exact kernel definition (2.64), integrals I_1, I_2 and I_3 in (G.1)-(G.3) can be written as

$$
I_1[n] = 2\pi \int\limits_{z=n\Delta z}^{(n+1)\Delta z} \int\limits_{z'=0}^{\Delta z} \left(1 - \frac{z'}{\Delta z}\right)\left(1 - \frac{z}{\Delta z} + n\right) K_E(z - z')dz'dz,
\tag{G.13}
$$

$$
I_2[n] = 2\pi \int\limits_{z=(n-1)\Delta z}^{n\Delta z} \int\limits_{z'=0}^{\Delta z} \left(1 - \frac{z'}{\Delta z}\right)\left(1 + \frac{z}{\Delta z} - n\right) K_E(z - z')dz'dz,
\tag{G.14}
$$

$$
I_3[n] = 2\pi \int\limits_{z=n\Delta z}^{(n+1)\Delta z} \int\limits_{z'=0}^{\Delta z} K_E(z - z')dz'dz.
\tag{G.15}
$$

Changing the variables x and x' as follows

$$
\begin{cases}
x = \dfrac{z}{\Delta z} - n, \\[2mm]
x' = \dfrac{z'}{\Delta z},
\end{cases}
\tag{G.16}
$$

leads to

$$I_1[n] = 2\pi\Delta z^2 \int\limits_{x=0}^{1} \int\limits_{x'=0}^{1} (1-x')(1-x)K_E\left(\Delta z(x-x'+n)\right) dx' dx, \tag{G.17}$$

$$I_2[n] = 2\pi\Delta z^2 \int\limits_{x=-1}^{0} \int\limits_{x'=0}^{1} (1-x')(1+x)K_E\left(\Delta z(x-x'+n)\right) dx' dx, \tag{G.18}$$

$$I_3[n] = 2\pi\Delta z^2 \int\limits_{x=0}^{1} \int\limits_{x'=0}^{1} K_E\left(\Delta z(x-x'+n)\right) dx' dx. \tag{G.19}$$

Next a second change of variables is applied

$$\begin{cases} s = x - x', \\ s' = x + x', \end{cases} \tag{G.20}$$

which, after carrying out the integration in s', yields

$$I_1[n] = \pi\Delta z^2 \int\limits_{s=0}^{1} \left(\frac{2}{3} - s + \frac{s^3}{3}\right) \left[K_E\left((n+s)\Delta z\right) + K_E\left((n-s)\Delta z\right)\right] ds, \tag{G.21}$$

$$I_2[n] = \pi\Delta z^2 \left(\int\limits_{s=1}^{2} \frac{(2-s)^3}{3} K_E\left((n-s)\Delta z\right) ds \right.$$

$$\left. + \int\limits_{s=0}^{1} \left(2s - 2s^2 + \frac{s^3}{3}\right) K_E\left((n-s)\Delta z\right) ds \right), \tag{G.22}$$

$$I_3[n] = 2\pi\Delta z^2 \int\limits_{s=0}^{1} (1-s) \left[K_E\left((n+s)\Delta z\right) + K_E\left((n-s)\Delta z\right)\right] ds. \tag{G.23}$$

In conclusion, each of the integrals in (G.21)-(G.23) can be written as a sum of integrals of the form

$$\text{Int}[n] = \int\limits_{s=s_1}^{s_2} P(s)K_E\left((s+n)\Delta z\right) ds, \tag{G.24}$$

where $P(s)$ is a polynomial. We have not been able to find a more simple closed form expression for any of the required integrals. The main problem in the numerical evaluation of (G.24) is again the singular behavior of the kernel function K_E. We proceed as already

proposed in Sec. 3.3. Thus we decompose the integral (G.24) into two terms

$$\text{Int}[n] = \int_{s=s_1}^{s_2} P(s) \left[K_E \left((s+n)\Delta z \right) - K_{\text{sing}} \left((s+n)\Delta z \right) \right] ds + \int_{s=s_1}^{s_2} P(s) K_{\text{sing}} \left((s+n)\Delta z \right) ds,$$

$$(G.25)$$

where K_{sing} is a function that follows the asymptotic behavior of K_E when its argument approaches 0 (see Sec. 3.3.2). The integrand of the first term is non-singular and its integral is finite and it is carried out numerically using a Gaussian quadrature rule. The second integral

$$\text{Int}_{\text{sing}}[n] = \int_{s=s_1}^{s_2} P(s) K_{\text{sing}} \left((s+n)\Delta z \right) ds, \qquad (G.26)$$

is evaluated analytically.

Analytical expression of singular integral Int_{sing}

The first step in evaluating the second term of (G.25) (i.e., Int_{sing} in (G.26)) is the change of variable $v = (s+n)\Delta z$. Substituting the explicit expression of K_{sing} (3.51) in equation (G.26) leads to

$$\text{Int}_{\text{sing}}[n] = \frac{1}{4\pi^2 a \Delta z} \int_{v=v_1}^{v_2} P\left(\frac{v}{\Delta z} - n \right) \left(- \ln |v| + |v| - 1 \right) dv, \qquad (G.27)$$

valid for $|v| < 1$. Otherwise $K_{\text{sing}} = 0$ and also the integral (G.27) vanishes. All the polynomials P in (G.21)-(G.23) have an order less or equal to 3 and can be written in the general form

$$P\left(\frac{v}{\Delta z} - n \right) = \alpha(n) + \beta(n)v + \gamma(n)v^2 + \delta(n)v^3, \qquad (G.28)$$

where the expressions of coefficients α, β, γ, δ are different for each polynomial and for each set of integration boundaries v_1, v_2 as summarized in Table G.1. Finally, the integral (G.27) can be expressed in the following closed form

$$\begin{aligned}
\text{Int}_{\text{sing}}[n] &= \frac{1}{4\pi^2 a \Delta z} \left[\alpha v \left(\frac{|v|}{2} - \ln |v| \right) + \frac{\beta}{2} v^2 \left(\frac{2}{3} |v| - \ln |v| - \frac{1}{2} \right) \right. \\
&\quad + \left. \frac{\gamma}{3} v^3 \left(\frac{3}{4} |v| - \ln |v| - \frac{2}{3} \right) + \frac{\delta}{4} v^4 \left(\frac{4}{5} |v| - \ln |v| - \frac{3}{4} \right) \right] \Bigg|_{v_a}^{v_b},
\end{aligned} \qquad (G.29)$$

where the values of v_1 and v_2 are found by distinguishing between the five cases listed in Table G.2 when the integration boundaries in equation (G.27) are $v_1 = n\Delta z$, $v_2 = (n+1)\Delta z$. By replacing the dummy argument n with $n+1$ in Table G.2 we can derive the values of v_1 and v_2 when the integration boundaries are $v_1 = (n+1)\Delta z$, $v_2 = (n+2)\Delta z$.

Table G.1: *Polynomial coefficients in equation (G.28).*

eq.	v_1	v_2	α	β	γ	δ
(G.21)	$n\Delta z$	$(n+1)\Delta z$	$\dfrac{2}{3} - n - \dfrac{n^3}{3}$	$\dfrac{\left(-1+n^2\right)}{\Delta z}$	$-\dfrac{n}{\Delta z^2}$	$\dfrac{1}{3\Delta z^3}$
(G.22)	$n\Delta z$	$(n+1)\Delta z$	$-2n - 2n^2 - \dfrac{n^3}{3}$	$\dfrac{\left(2+4n+n^2\right)}{\Delta z}$	$\dfrac{-2-n}{\Delta z^2}$	$\dfrac{1}{3\Delta z^3}$
(G.22)	$(n+1)\Delta z$	$(n+2)\Delta z$	$\dfrac{8}{3} + 4n + 2n^2 + \dfrac{n^3}{3}$	$\dfrac{\left(-4-4n-n^2\right)}{\Delta z}$	$\dfrac{2+n}{\Delta z^2}$	$-\dfrac{1}{3\Delta z^3}$
(G.23)	$n\Delta z$	$(n+1)\Delta z$	$1+n$	$-\dfrac{1}{\Delta z}$	0	0

Table G.2: *Values of v_a and v_b valid when the integration boundaries in equation (G.27) are $v_1 = n\Delta z$, $v_2 = (n+1)\Delta z$.*

condition	v_a	v_b
$n < -1 - \dfrac{1}{\Delta z}$	$\text{Int}_{\text{sing}} = 0$	
$-1 - \dfrac{1}{\Delta z} < n < -\dfrac{1}{\Delta z}$	-1	$(n+1)\Delta z$
$-\dfrac{1}{\Delta z} < n < -1 + \dfrac{1}{\Delta z}$	$n\Delta z$	$(n+1)\Delta z$
$-1 + \dfrac{1}{\Delta z} < n < \dfrac{1}{\Delta z}$	$n\Delta z$	1
$n > \dfrac{1}{\Delta z}$	$\text{Int}_{\text{sing}} = 0$	

G.1.2 Computation of the integrals I_4 and I_5

The two integrals I_4, I_5 in (G.4), (G.5) are carried out by a series expansion of the Green's function of the Helmholtz operator in cylindrical coordinates, (see [89, pag. 888]), which leads to

$$I_4 = -j\frac{1}{4\pi}\sum_{m=0}^{\infty}\epsilon_m\int_{r=a}^{b}(r-b)\int_{r'=a}^{b}(r'-b)\int_{\varphi=0}^{2\pi}\cos(m\varphi)\cos\varphi d\varphi\times$$

$$\left(\int_{\lambda=0}^{k}J_m(\lambda r)J_m(\lambda r')\frac{\lambda}{\sqrt{k^2-\lambda^2}}d\lambda+\int_{\lambda=k}^{\infty}J_m(\lambda r)J_m(\lambda r')\frac{\lambda}{-j\sqrt{\lambda^2-k^2}}d\lambda\right)dr'dr, \quad \text{(G.30)}$$

$$I_5 = -j\frac{1}{4\pi}\sum_{m=0}^{\infty}\epsilon_m\int_{r=a}^{b}\int_{r'=a}^{b}\int_{\varphi=0}^{2\pi}\cos(m\varphi)d\varphi\times$$

$$\left(\int_{\lambda=0}^{k}J_m(\lambda r)J_m(\lambda r')\frac{\lambda}{\sqrt{k^2-\lambda^2}}d\lambda+\int_{\lambda=k}^{\infty}J_m(\lambda r)J_m(\lambda r')\frac{\lambda}{-j\sqrt{\lambda^2-k^2}}d\lambda\right)dr'dr, \quad \text{(G.31)}$$

where J_m is the Bessel function of the first kind of order m and ϵ_m is the Neumann factor

$$\epsilon_m = \begin{cases} 1, & m=0, \\ 2, & m=1,2,3,\ldots. \end{cases} \quad \text{(G.32)}$$

Because of the orthogonality property of cosine functions

$$\int_{\varphi=0}^{2\pi}\cos(m\varphi)\cos(n\varphi)d\varphi = \begin{cases} 2\pi, & m=n=0, \\ \pi, & m=n, \\ 0, & m\neq n, \end{cases} \quad \text{(G.33)}$$

the previous two infinite sums of integrals in (G.30), (G.31) in fact consist of only one term in separable variables. Thus, we can write

$$I_4 = -j\frac{1}{2}\int_{\lambda=0}^{k}\left(\int_{r=a}^{b}J_1(\lambda r)(r-b)dr\right)\left(\int_{r'=a}^{b}J_1(\lambda r')(r'-b)dr'\right)\frac{\lambda}{\sqrt{k^2-\lambda^2}}d\lambda$$

$$+\frac{1}{2}\int_{\lambda=k}^{\infty}\left(\int_{r=a}^{b}J_1(\lambda r)(r-b)dr\right)\left(\int_{r'=a}^{b}J_1(\lambda r')(r'-b)dr'\right)\frac{\lambda}{\sqrt{\lambda^2-k^2}}d\lambda, \quad \text{(G.34)}$$

$$I_5 = -j\frac{1}{2} \int\limits_{\lambda=0}^{k} \left(\int\limits_{r=a}^{b} J_0(\lambda r)dr \right) \left(\int\limits_{r'=a}^{b} J_0(\lambda r')dr' \right) \frac{\lambda}{\sqrt{k^2 - \lambda^2}} d\lambda$$

$$+ \frac{1}{2} \int\limits_{\lambda=k}^{\infty} \left(\int\limits_{r=a}^{b} J_0(\lambda r)dr \right) \left(\int\limits_{r'=a}^{b} J_0(\lambda r')dr' \right) \frac{\lambda}{\sqrt{\lambda^2 - k^2}} d\lambda. \tag{G.35}$$

We note that the integrand functions exhibit a root-like singularity when λ approaches k. Therefore, numerical problems can be experienced in the evaluation of these integrals. By introducing the following change of variables

$$p^2 = k^2 - \lambda^2, \qquad \text{integration interval } [0, k], \tag{G.36}$$

$$p^2 = \lambda^2 - k^2, \qquad \text{integration interval } [k, \infty), \tag{G.37}$$

we remove the singular behavior of the integrand. Then, by applying a change of variable $r = r'$ integrals (G.34), and (G.35) are simplified to

$$I_4 = -j\frac{1}{2} \int\limits_{p=0}^{k} \left(\int\limits_{r=a}^{b} J_1(r\sqrt{k^2 - p^2})(r - b)dr \right)^2 dp$$

$$+ \frac{1}{2} \int\limits_{p=0}^{\infty} \left(\int\limits_{r=a}^{b} J_1(r\sqrt{k^2 + p^2})(r - b)dr \right)^2 dp, \tag{G.38}$$

$$I_5 = -j\frac{1}{2} \int\limits_{p=0}^{k} \left(\int\limits_{r=a}^{b} J_0(r\sqrt{k^2 - p^2})dr \right)^2 dp + \frac{1}{2} \int\limits_{p=0}^{\infty} \left(\int\limits_{r=a}^{b} J_0(r\sqrt{k^2 + p^2})dr \right)^2 dp. \tag{G.39}$$

The integrals I_4 and I_5 consist of two contributions: integrals over a finite and a semi-infinite interval, respectively. A first integration in r with finite boundaries, and a second integration in p with finite or semi-infinite boundaries have to be carried out. For each value of p, integrals of the Bessel functions J_1 and J_0 can be calculated numerically. In the evaluation of I_4 and I_5, we follow two different approaches depending on which subinterval is considered. For the first contribution (i.e., interval $[0, k]$), we evaluate the following integrals

$$\int\limits_{r=a}^{b} J_1(r\sqrt{k^2 - p^2})(r - b)dr, \qquad \int\limits_{r=a}^{b} J_0(r\sqrt{k^2 - p^2})dr, \tag{G.40}$$

using a 1D quadrature, adaptive rule suited for oscillating, non-singular integrands, (NAG routine D01AKF [66]). The other integration in p is carried out by applying NAG routine

D01AHF which implements the method proposed by Patterson suited for definite integrals over a finite range.

In order to reduce the CPU time required in carrying out the second semi-infinite integral contribution (i.e., interval $[0, \infty)$), maintaining a predefined accuracy, we proceed as follows. The integrals in (G.38), (G.39) are rewritten as

$$\int_{r=a}^{b} J_1(\alpha r)(r-b)dr, \qquad \int_{r=a}^{b} J_0(\alpha r)dr, \tag{G.41}$$

where $\alpha = \sqrt{k^2 + p^2}$. We know that, for large values of its argument, the Bessel functions J_1 and J_0 have asymptotic forms, (see [39, eq. 9.2.1]), therefore the expressions in (G.41) become

$$\int_{r=a}^{b} J_1(\alpha r)(r-b)dr \approx \int_{r=a}^{b} \sqrt{\frac{2}{\pi \alpha r}} \cos\left(\alpha r - \frac{3\pi}{4}\right)(r-b)\, dr, \tag{G.42}$$

$$\int_{r=a}^{b} J_0(\alpha r)dr \approx \int_{r=a}^{b} \sqrt{\frac{2}{\pi \alpha r}} \cos\left(\alpha r - \frac{\pi}{4}\right) dr, \tag{G.43}$$

and these integrals are calculated as

$$\int_{r=a}^{b} \sqrt{\frac{2}{\pi \alpha r}} \cos\left(\alpha r - \frac{3\pi}{4}\right)(r-b)\, dr = -\alpha^{-\frac{3}{2}} \sqrt{\frac{r}{\pi}} \left[\sin(\alpha r) + \cos(\alpha r)\right]\Bigg|_{r=a}^{b}$$

$$+ \frac{1}{\alpha^2 \sqrt{2}} \left[Si\left(\sqrt{\frac{2\alpha r}{\pi}}\right) + Ci\left(\sqrt{\frac{2\alpha r}{\pi}}\right)\right]\Bigg|_{r=a}^{b}$$

$$+ \frac{b\sqrt{2}}{\alpha} \left[Ci\left(\sqrt{\frac{2\alpha r}{\pi}}\right) - Si\left(\sqrt{\frac{2\alpha r}{\pi}}\right)\right]\Bigg|_{r=a}^{b}, \tag{G.44}$$

$$\int_{r=a}^{b} \sqrt{\frac{2}{\pi \alpha r}} \cos\left(\alpha r - \frac{\pi}{4}\right) dr = \frac{\sqrt{2}}{\alpha} \left[Ci\left(\sqrt{\frac{2\alpha r}{\pi}}\right) + Si\left(\sqrt{\frac{2\alpha r}{\pi}}\right)\right]\Bigg|_{r=a}^{b}, \tag{G.45}$$

where Ci and Si are Fresnel's cosine and sine integrals, (see [39, eq. 7.3.1, 7.3.2]). We use these closed forms (G.44), (G.45) when the Bessel functions' argument (i.e., αr) is larger than $\beta_{s1} = 250$, for J_1 and larger than $\beta_{s0} = 150$ for J_0. These switching values have been chosen based on practical experience. We observe indeed that the Bessel functions' approximated values (calculated with their asymptotic forms) for β_{s1} and β_{s0} are accurate up to

the fourth decimal. For arguments smaller than β_{s1}, β_{s0}, we compute the Bessel functions $J_1(x)$ and $J_0(x)$ using NAG routines S17AFF and S17AEF, and the integrals (G.41) are then carried out with a 1D quadrature, adaptive method (i.e., NAG routine D01AKF) as previously implemented for $0 \leq p \leq k$. Finally, the evaluation of the external integral on the semi-infinite interval $p \in [0, \infty)$ is carried out by using NAG routine D01AMF which applies a change of integration variable and then uses an adaptive procedure based on Gauss and Kronrod rules [66].

G.1.3   Computation of the integrals I_6

The integral I_6 in (G.6) is carried out following the same procedure already developed in Sec. G.1.2. First, a Green's function series expansion (see [89, pag. 888]) is applied in the integral (G.6), which yields

$$I_6[n] = -j\frac{1}{4\pi}\sum_{m=0}^{\infty}\epsilon_m \int_{z=z_1}^{z_2}\int_{r'=a}^{b}\int_{\varphi=0}^{2\pi}\cos(m\varphi)d\varphi\left(\int_{\lambda=0}^{k}J_m(\lambda r')J_m(\lambda a)\frac{\exp(-jz\sqrt{k^2-\lambda^2})\lambda}{\sqrt{k^2-\lambda^2}}d\lambda\right.$$

$$\left.+\int_{\lambda=k}^{\infty}J_m(\lambda r')J_m(\lambda a)\frac{\exp(-z\sqrt{\lambda^2-k^2})\lambda}{-j\sqrt{\lambda^2-k^2}}d\lambda\right)dr'dz, \tag{G.46}$$

where $z_1 = n\Delta z$ and $z_2 = (n+1)\Delta z$. Owing to the orthogonality property (G.33), the latter can be written as a product of integrals in appropriate variables in which the problem can be separated

$$I_6[n] = -j\frac{1}{2}\int_{\lambda=0}^{k}J_0(\lambda a)\left(\int_{r'=a}^{b}J_0(\lambda r')dr'\right)\left(\int_{z=z_1}^{z_2}\frac{\exp(-jz\sqrt{k^2-\lambda^2})}{\sqrt{k^2-\lambda^2}}dz\right)\lambda d\lambda$$

$$+\frac{1}{2}\int_{\lambda=k}^{\infty}J_0(\lambda a)\left(\int_{r'=a}^{b}J_0(\lambda r')dr'\right)\left(\int_{z=z_1}^{z_2}\frac{\exp(-z\sqrt{\lambda^2-k^2})}{\sqrt{\lambda^2-k^2}}dz\right)\lambda d\lambda. \tag{G.47}$$

At this stage we observe that when $\lambda \to k$ the integrand in (G.47) has a root-like singularity. By carrying out the integral in z analytically, and by applying the change of variables (G.36) and (G.37), (G.47) changes into

$$I_6[n] = \frac{1}{2}\int_{p=0}^{k}J_0(a\sqrt{k^2-p^2})\left(\int_{r'=a}^{b}J_0(r'\sqrt{k^2-p^2})dr'\right)\frac{\exp(-jz_2p)-\exp(-jz_1p)}{p}dp$$

$$-\frac{1}{2}\int_{p=0}^{\infty}J_0(a\sqrt{k^2+p^2})\left(\int_{r'=a}^{b}J_0(r'\sqrt{k^2+p^2})dr'\right)\frac{\exp(-z_2p)-\exp(-z_1p)}{p}dp. \tag{G.48}$$

We distinguish again between two different procedures used to carry out the finite and the second semi-infinite integral:

1. for the finite subinterval, the integral of the Bessel function J_0 in r' is evaluated using a 1D quadrature, adaptive rule (i.e., NAG routine D01AKF [66]) and the 1D integral in p is carried out by using NAG routine D01AHF;

2. for the semi-infinite subinterval, we make again a distinction. If the argument of the Bessel function J_0 is larger than the switching value β_{s0}, the asymptotic form of the Bessel function is used (see [39, eq. 9.2.1])

$$
\int\limits_{r'=a}^{b} J_0(r'\alpha)dr' \approx \int\limits_{r'=a}^{b} \sqrt{\frac{2}{\pi\alpha r'}} \cos\left(\alpha r' - \frac{\pi}{4}\right) dr', \tag{G.49}
$$

and the integral over r' is therefore calculated as

$$
\int\limits_{r'=a}^{b} \sqrt{\frac{2}{\pi\alpha r'}} \cos\left(\alpha r' - \frac{\pi}{4}\right) dr' = \sqrt{\frac{2}{\alpha}} \left[Ci\left(\sqrt{\frac{2r'\alpha}{\pi}}\right) + Si\left(\sqrt{\frac{2r'\alpha}{\pi}}\right) \right] \Bigg|_{r'=a}^{b}, \tag{G.50}
$$

with $\alpha = \sqrt{k^2 + p^2}$. If the argument of the Bessel function J_0 is smaller than the switching value β_{s0} then NAG routine S17AEF is used for the calculation of J_0 and routine D01AKF carries out the integrals in r'. Finally NAG routine D01AMF is used to carry out the integral over the semi-infinite interval $p \in [0, \infty)$.

G.1.4   Computation of the integrals I_7 and I_8

The expressions (G.7) and (G.8) of integrals I_7 and I_8 contain a first 2D integration over the triangular surface T and a second 2D integration along the mantle of the attached wire segment (S^{aW}) or over the disk (S^{aD}). In order to carry out these integrals, a series expansion of the Green's function (see [89, pag. 888]) and the orthogonality property (G.33) of the cosine functions are again employed. Thus, expressions (G.7), (G.8) can be

written as integrals in appropriate variables in which the problem can be separated

$$
I_7 = -jA \int\limits_{\lambda=0}^{k} J_0(\lambda a) \left(\int\limits_{z'=0}^{\Delta z} \frac{\exp(-jz'\sqrt{k^2-\lambda^2})}{\sqrt{k^2-\lambda^2}} dz' \right) \left(\int\limits_{\xi_1=0}^{1} \int\limits_{\xi_2=0}^{1-\xi_1} J_0(\lambda r(\xi_1,\xi_2)) d\xi_2 d\xi_1 \right) \times
$$
$$
\frac{\lambda}{\sqrt{k^2-\lambda^2}} d\lambda + A \int\limits_{\lambda=k}^{\infty} J_0(\lambda a) \left(\int\limits_{z'=0}^{\Delta z} \frac{\exp(-z'\sqrt{\lambda^2-k^2})}{\sqrt{\lambda^2-k^2}} dz' \right) \times
$$
$$
\left(\int\limits_{\xi_1=0}^{1} \int\limits_{\xi_2=0}^{1-\xi_1} J_0(\lambda r(\xi_1,\xi_2)) d\xi_2 d\xi_1 \right) \frac{\lambda}{\sqrt{\lambda^2-k^2}} d\lambda, \tag{G.51}
$$

$$
I_8 = -jA \int\limits_{\lambda=0}^{k} \left(\int\limits_{r'=a}^{b} J_0(\lambda r') dr' \right) \left(\int\limits_{\xi_1=0}^{1} \int\limits_{\xi_2=0}^{1-\xi_1} J_0(\lambda r(\xi_1,\xi_2)) d\xi_2 d\xi_1 \right) \frac{\lambda}{\sqrt{k^2-\lambda^2}} d\lambda
$$
$$
+A \int\limits_{\lambda=k}^{\infty} \left(\int\limits_{r'=a}^{b} J_0(\lambda r') dr' \right) \left(\int\limits_{\xi_1=0}^{1} \int\limits_{\xi_2=0}^{1-\xi_1} J_0(\lambda r(\xi_1,\xi_2)) d\xi_2 d\xi_1 \right) \frac{\lambda}{\sqrt{\lambda^2-k^2}} d\lambda, \tag{G.52}
$$

where A is the area of triangle T. Note that the integration over the triangular surface T is written in local normalized area coordinates ξ_1, ξ_2 (see Appendix F.1) and therefore r is now a function of them (i.e., $r(\xi_1,\xi_2)$).

Looking at the integral I_7, we note that the 1D integration over the interval $[0,\Delta z]$ can be carried out analytically. Subsequently the changes of variables (G.36) and (G.37) are introduced for both the integrals I_7, I_8, which results in

$$
I_7 = A \int\limits_{p=0}^{k} J_0\left(a\sqrt{k^2-p^2}\right) \left(\int\limits_{\xi_1=0}^{1} \int\limits_{\xi_2=0}^{1-\xi_1} J_0\left(r(\xi_1,\xi_2)\sqrt{k^2-p^2}\right) d\xi_2 d\xi_1 \right) \frac{\exp(-jp\Delta z)-1}{p} dp
$$
$$
-A \int\limits_{p=0}^{\infty} J_0\left(a\sqrt{k^2+p^2}\right) \left(\int\limits_{\xi_1=0}^{1} \int\limits_{\xi_2=0}^{1-\xi_1} J_0\left(r(\xi_1,\xi_2)\sqrt{k^2+p^2}\right) d\xi_2 d\xi_1 \right) \frac{\exp(-p\Delta z)-1}{p} dp,
$$
$$
\tag{G.53}
$$

$$
I_8 = -jA \int\limits_{p=0}^{k} \left(\int\limits_{r'=a}^{b} J_0\left(r'\sqrt{k^2-p^2}\right) dr' \right) \left(\int\limits_{\xi_1=0}^{1} \int\limits_{\xi_2=0}^{1-\xi_1} J_0\left(r(\xi_1,\xi_2)\sqrt{k^2-p^2}\right) d\xi_2 d\xi_1 \right) dp
$$
$$
+A \int\limits_{p=0}^{\infty} \left(\int\limits_{r'=a}^{b} J_0\left(r'\sqrt{k^2+p^2}\right) dr' \right) \left(\int\limits_{\xi_1=0}^{1} \int\limits_{\xi_2=0}^{1-\xi_1} J_0\left(r(\xi_1,\xi_2)\sqrt{k^2+p^2}\right) d\xi_2 d\xi_1 \right) dp.
$$
$$
\tag{G.54}
$$

In both integrals, we recognize a first 2D integration over the triangular surface (i.e., ξ_1, ξ_2) and a second integration in p over a finite interval $[0, k]$ and a semi-infinite interval $[0, \infty)$. The integral I_8 contains an extra integration in r' over the interval $[a, b]$. Both expressions (G.53), (G.54) can be carried out numerically in the following way. Focusing on integral I_7 we consider

1. firstly the integral over the finite interval $[0, k]$. The 2D integral of the Bessel function J_0 is evaluated efficiently using a Gaussian quadrature rule applied in local normalized area coordinates (see Appendix F.2). The Bessel function J_0 is calculated with NAG routine S17AEF and the 1D integral in p is carried out by using NAG routine D01AHF [66];

2. secondly the semi-infinite interval is considered. When the argument of the Bessel function J_0 is larger than the switching value β_{s0}, then the asymptotic form of the Bessel function is used (see [39, eq. 9.2.1]). Otherwise NAG routines S17AEF is employed for the calculation. Then, for both cases, the 2D integral is carried out using a Gaussian quadrature rule applied in local normalized area coordinates (see Appendix F.2). The final integral on the semi-infinite interval $[0, \infty)$ is carried out by employing NAG routine D01AMF [66].

The same procedure is applied for the calculation of integral I_8. In this case the extra 1D integral of the Bessel function J_0 is carried out by NAG routine D01AKF when the first term in (G.54) is considered (i.e., $p \in [0, k]$) or when the second term (i.e., $p \in [0, \infty)$) is calculated and the argument of J_0 is smaller than the switching value β_{s0}. In the other case (i.e., argument larger than β_{s0} and integral over the semi-infinite interval) the integration is analytically evaluated as in (G.50).

G.1.5   Computation of the integrals I_9

The integral I_9 in (G.9) contains a first 2D integration over the triangular surface T and a second 2D integration over the attachment disk (S^{aD}). The first step in carrying out these integrations is to write the Green's function of the Helmholtz operator as

$$
I_9 = -j\frac{A}{2\pi} \sum_{m=0}^{\infty} \epsilon_m \int_{\xi_1=0}^{1} \int_{\xi_2=0}^{1-\xi_1} \int_{r'=a}^{b} \int_{\phi'=0}^{2\pi} \cos(m(\phi - \phi'))\mathbf{i}_r(\phi') \cdot \boldsymbol{\rho}(\xi_1, \xi_2)(r' - b)dr' \times
$$

$$
\left(\int_{\lambda=0}^{k} J_m(\lambda r)J_m(\lambda r')\frac{\lambda}{\sqrt{k^2 - \lambda^2}}d\lambda + \int_{\lambda=k}^{\infty} J_m(\lambda r)J_m(\lambda r')\frac{\lambda}{-j\sqrt{\lambda^2 - k^2}}d\lambda \right) d\phi' dr' d\xi_2 d\xi_1, \quad \text{(G.55)}
$$

having applied the series expansion in cylindrical coordinates (see [89, pag. 888]). We would like to write the inner product $\mathbf{i}_r(\phi') \cdot \boldsymbol{\rho}(\mathbf{r})$ such that it is a function of $\cos(\phi - \phi')$. In this way, owing to the orthogonality property (G.33), the infinite sum in (G.55) is reduced to only one term.

Recalling that the triangular surface and the disk S^{aD} are coplanar, we have introduced a local cylindrical coordinate system with its origin in the attachment point as illustrated in Fig. G.1.
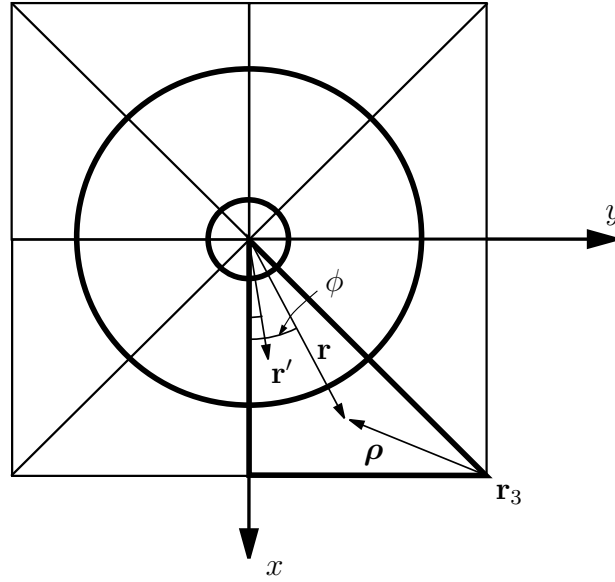
Figure G.1: *Geometry of the attachment problem on the (x, y)-plane.*

Next, an observation point $\mathbf{r}$ is chosen in a triangular patch involved in the attachment

$$\mathbf{r} = r \cos \phi \mathbf{i}_x + r \sin \phi \mathbf{i}_y. \tag{G.56}$$

By knowing the triangle vertex $\mathbf{r}_3 = x_3 \mathbf{i}_x + y_3 \mathbf{i}_y$ in Cartesian coordinates, we can write the vector $\boldsymbol{\rho}$ as

$$\boldsymbol{\rho} = \mathbf{r} - \mathbf{r}_3 = (r \cos \phi - x_3) \mathbf{i}_x + (r \sin \phi - y_3) \mathbf{i}_y. \tag{G.57}$$

Therefore the inner product can be written as

$$\mathbf{i}_r(\phi') \cdot \boldsymbol{\rho} = r \cos(\phi - \phi') - x_3 \cos \phi' - y_3 \sin \phi', \tag{G.58}$$

where the cylindrical coordinates r, ϕ are functions of the local normalized coordinates (ξ_1, ξ_2), see Appendix F.1. Once the point $\mathbf{r}$ is chosen, by applying the orthogonality

property of the cosine functions

$$
\int\limits_{\varphi=0}^{2\pi} \cos(m(\phi - \phi')) \cos(\phi - \phi') \, d\phi' = \begin{cases} \pi, & m = 1, \\ 0, & m \neq 1, \end{cases} \tag{G.59}
$$

the integral is carried out as:

$$
\int\limits_{\phi'=0}^{2\pi} \cos(m(\phi - \phi')) \mathbf{i}_r(\phi') \cdot \boldsymbol{\rho} d\phi' =
$$

$$
r \int\limits_{\phi'=0}^{2\pi} \cos(m(\phi - \phi')) \cos(\phi - \phi') \, d\phi' - x_3 \int\limits_{\phi'=0}^{2\pi} \cos(m(\phi - \phi')) \cos \phi' d\phi'
$$

$$
-y_3 \int\limits_{\phi'=0}^{2\pi} \cos(m(\phi - \phi')) \sin \phi' d\phi'. \tag{G.60}
$$

Therefore, we can finally write

$$
\int\limits_{\phi'=0}^{2\pi} \cos(m(\phi - \phi')) \mathbf{i}_r(\phi') \cdot \boldsymbol{\rho} d\phi' = \begin{cases} \pi \left(r - x_3 \cos(\phi) - y_3 \sin \phi \right), & m = 1, \\ 0, & m \neq 1. \end{cases} \tag{G.61}
$$

Substituting the latter in (G.55) yields

$$
I_9 = -jA \int\limits_{\lambda=0}^{k} \left(\int\limits_{\xi_1=0}^{1} \int\limits_{\xi_2=0}^{1-\xi_1} J_1(r\lambda) \left(r - x_3 \cos \phi - y_3 \sin \phi \right) d\xi_2 d\xi_1 \right) \times
$$

$$
\left(\int\limits_{r'=a}^{b} J_1(r'\lambda)(r' - b) dr' \right) \frac{\lambda}{\sqrt{k^2 - \lambda^2}} d\lambda
$$

$$
+A \int\limits_{\lambda=k}^{\infty} \left(\int\limits_{\xi_1=0}^{1} \int\limits_{\xi_2=0}^{1-\xi_1} J_1(r\lambda) \left(r - x_3 \cos \phi - y_3 \sin \phi \right) d\xi_2 d\xi_1 \right) \times
$$

$$
\left(\int\limits_{r'=a}^{b} J_1(r'\lambda)(r' - b) dr' \right) \frac{\lambda}{\sqrt{\lambda^2 - k^2}} d\lambda, \tag{G.62}
$$

where the dependence on (ξ_1, ξ_2) is omitted. We note that integral I_9 consists of two terms, basically a 1D finite and a 1D semi-infinite integral in p. For each value of p the product between a 2D integral over the triangular surface T and a 1D integral over $r' \in [a, b]$ has

to be evaluated. To overcome the numerical problem due to the root-like singularity in the integrand function for $\lambda \to k$, we apply the change of variables (G.36), (G.37). Thus, the integral (G.62) becomes

$$
\begin{aligned}
I_9 = -jA \int\limits_{p=0}^{k} & \left(\int\limits_{\xi_1=0}^{1} \int\limits_{\xi_2=0}^{1-\xi_1} J_1(r\sqrt{k^2-\lambda^2})\,(r - x_3\cos\phi - y_3\sin\phi)\,d\xi_2 d\xi_1 \right) \times \\
& \left(\int\limits_{r'=a}^{b} J_1(r'\sqrt{k^2-\lambda^2})(r'-b)dr' \right) dp \\
+ A \int\limits_{p=k}^{\infty} & \left(\int\limits_{\xi_1=0}^{1} \int\limits_{\xi_2=0}^{1-\xi_1} J_1(r\sqrt{\lambda^2-k^2})\,(r - x_3\cos\phi - y_3\sin\phi)\,d\xi_2 d\xi_1 \right) \times \\
& \left(\int\limits_{r'=a}^{b} J_1(r'\sqrt{\lambda^2-k^2})(r'-b)dr' \right) dp.
\end{aligned}
\tag{G.63}
$$

We focus our attention first on the finite integral. By employing a Gaussian quadrature rule (see Appendix F.2), the 2D integral of the Bessel function J_1 is evaluated. The other 1D integration is carried out by NAG routine D01AKF and the external 1D integral in p is computed via NAG routine D01AHF [66].

Second, the integral over a semi-infinite interval $[0, \infty)$ is calculated as follows. If the argument of the Bessel function J_1 is larger than the switching value β_{s1}, the asymptotic form of the Bessel function is used (see [39, eq. 9.2.1]), and therefore the 1D integral over $r' \in [a, b]$ has the expression (G.44). The 2D integral is carried out again using a Gaussian quadrature rule. When the argument of the Bessel function J_1 is smaller than the switching value β_{s1}, we employ NAG routine D01AKF for the 1D integral in r and a Gaussian quadrature rule for the 2D integration. Finally, for both cases (i.e., independently from β_{s1}), the integral on the semi-infinite interval $p \in [0, \infty)$ is carried out by employing NAG routine D01AMF.

G.2   Known excitation element

Starting from the expression (8.63) of the known excitation element

$$
F_e^a = \frac{1}{2\pi} \left[\int_{z=0}^{\Delta z} \int_{\phi=0}^{2\pi} \left(1 - \frac{z}{\Delta z}\right) \left(V(\omega)\delta(z - z_g)\mathbf{i}_z + \mathbf{E}^i(\mathbf{r})\right) \cdot \mathbf{i}_z d\phi dz \right]_{\{r=a\}}
$$

$$
+ \frac{1}{2\pi(b-a)} \left[\int_{r=a}^{b} \int_{\phi=0}^{2\pi} (r-b)\left(V(\omega)\delta(z - z_g)\mathbf{i}_z + \mathbf{E}^i(\mathbf{r})\right) \cdot \mathbf{i}_r(\mathbf{r}) d\phi dr \right]_{\{z=0\}}, \qquad (G.64)
$$

we describe the way we calculate this term. Knowing that $\mathbf{i}_z \cdot \mathbf{i}_r = 0$ and substituting in (G.64) the explicit form of an incident plane wave

$$
\mathbf{E}^i(\mathbf{r}) = \mathbf{E}_0 \exp(-j\mathbf{k}^i \cdot \mathbf{r}), \qquad (G.65)
$$

we obtain

$$
F_e^a = \left(1 - \frac{z_g}{\Delta z}\right)V(\omega) + \frac{1}{2\pi} \left[\int_{z=0}^{\Delta z} \int_{\phi=0}^{2\pi} \left(1 - \frac{z}{\Delta z}\right) \mathbf{E}_0 \cdot \mathbf{i}_z \exp(-j\mathbf{k}^i \cdot \mathbf{r}) d\phi dz \right]_{\{r=a\}}
$$

$$
+ \frac{1}{2\pi(b-a)} \left[\int_{r=a}^{b} \int_{\phi=0}^{2\pi} (r-b)\,\mathbf{E}_0 \cdot \mathbf{i}_r(\mathbf{r}) \exp(-j\mathbf{k}^i \cdot \mathbf{r}) d\phi dr \right]_{\{z=0\}}. \qquad (G.66)
$$

First, we consider the 2D integral on the surface S^{aW} of the attached wire, that is

$$
\frac{1}{2\pi} \left[\int_{z=0}^{\Delta z} \int_{\phi=0}^{2\pi} \left(1 - \frac{z}{\Delta z}\right) \mathbf{E}_0 \cdot \mathbf{i}_z \exp(-j\mathbf{k}^i \cdot \mathbf{r}) d\phi dz \right]_{\{r=a\}}, \qquad (G.67)
$$

where $\mathbf{r} \in S^{aW}$

$$
\mathbf{r} = a\cos\phi\,\mathbf{i}_x + a\sin\phi\,\mathbf{i}_y + z\,\mathbf{i}_z, \qquad \text{with } 0 \le z \le \Delta z. \qquad (G.68)
$$

In the Cartesian coordinate system of Fig. G.2, recalling the derivation in Sec. 2.2.6, we can write

$$
\mathbf{k}^i \cdot \mathbf{r} = -k^i a \sin\theta_i \cos(\phi_i - \phi) - k^i z \cos\theta_i, \qquad (G.69)
$$

$$
\mathbf{E}_0 \cdot \mathbf{i}_z = -E_{0\theta} \sin\theta_i \exp(jzk^i \cos\theta_i) \exp(jak^i \sin\theta_i \cos(\phi_i - \phi)). \qquad (G.70)
$$

Therefore substituting (G.69), (G.70) in the integral (G.67) leads to

$$-\frac{1}{2\pi}E_{0\theta}\sin\theta_i\int\limits_{z=0}^{\Delta z}\left(1-\frac{z}{\Delta z}\right)\exp(jzk^i\cos\theta_i)dz\int\limits_{\phi=0}^{2\pi}\exp\left((jak^i\sin\theta_i\cos(\phi_i-\phi)\right)d\phi.$$

(G.71)

Carrying out this integration analytically yields

$$J_0(ak^i\sin\theta_i)E_{0z}\left(\frac{1-j\Delta zk_z^i-\exp(-j\Delta zk_z^i)}{\Delta z(-k_z^i)^2}\right),$$

(G.72)

where $E_{0z}=-E_{0\theta}\sin\theta_i$, $k_z^i=-k^i\cos\theta_i$ and where J_0 is the Bessel function of the first kind and order zero (see [39, eq. 9.1.21]). For thin wires (i.e., $ak^i\ll 1$) we approximate $J_0(ak^i\sin\theta_i)\approx 1$ estimating a second-order error of $(ak^i\sin\theta_i)^2/4$. Thus, we can finally write

$$E_{0z}\left(\frac{1-j\Delta zk_z^i-\exp(-j\Delta zk_z^i)}{\Delta zk_z^{i^2}}\right).$$

(G.73)

PSfrag replacements
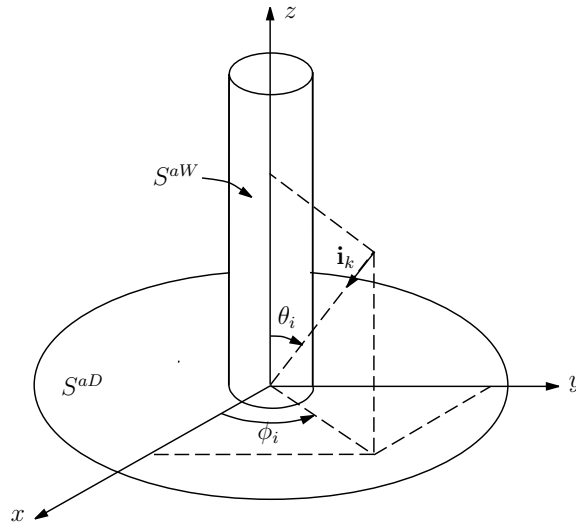
Δz

$\mathbf{i}_z$

$\mathbf{i}_r$

Figure G.2: *Geometrical parameters associated with a wire-to-surface junction.*

Second, we consider the 2D integral over S^{aD} in equation (G.66)

$$\frac{1}{2\pi(b-a)}\left[\int\limits_{r=a}^{b}\int\limits_{\phi=0}^{2\pi}(r-b)\,\mathbf{E}_0\cdot\mathbf{i}_r(\mathbf{r})\exp(-j\mathbf{k}^i\cdot\mathbf{r})d\phi dr\right]_{\{z=0\}},$$

(G.74)

where

$$\mathbf{r} = r \cos \phi \mathbf{i}_x + r \sin \phi \mathbf{i}_y, \qquad \text{with } a \le r \le b. \tag{G.75}$$

In this case $\mathbf{r}$ is on the attachment disk S^{aD}, and therefore we have

$$\mathbf{k}^i \cdot \mathbf{r} = -k^i \sin \theta_i r \cos(\phi_i - \phi), \tag{G.76}$$
$$\mathbf{E}_0 \cdot \mathbf{i}_r = (E_{0x} \cos \phi + E_{0y} \sin \phi) \exp(jk^i \cos \theta_i r \cos(\phi_i - \phi)), \tag{G.77}$$

where

$$E_{0x} = E_{0\theta} \cos \theta_i \cos \phi_i - E_{0\phi} \sin \phi_i, \tag{G.78}$$
$$E_{0y} = E_{0\theta} \cos \theta_i \sin \phi_i + E_{0\phi} \cos \phi_i. \tag{G.79}$$

Substituting equations (G.76), (G.77) in expression (G.74) leads to

$$\frac{1}{2\pi(b-a)} \int\limits_{r=a}^{b} \int\limits_{\phi=0}^{2\pi} (r-b) \left(E_{0x} \cos \phi + E_{0y} \sin \phi\right) \exp(-jk_z^i r \cos(\phi_i - \phi)) d\phi dr. \tag{G.80}$$

This integration is carried out numerically by using an adaptive multidimensional routine DCUHRE [65]. In conclusion, from equation (G.66), with the aid of (G.73), (G.80) we write

$$F_e^a = \left(1 - \frac{z_g}{\Delta z}\right) V(\omega) + E_{0z} \left(\frac{1 - j\Delta z k_z^i - \exp(-j\Delta z k_z^i)}{\Delta z k_z^{i\,2}}\right)$$
$$+ \frac{1}{2\pi(b-a)} \int\limits_{r=a}^{b} \int\limits_{\phi=0}^{2\pi} (r-b) \left(E_{0x} \cos \phi + E_{0y} \sin \phi\right) \exp(-jk_z^i r \cos(\phi_i - \phi)) d\phi dr, \tag{G.81}$$

which, for $k_z^i = 0$ becomes

$$F_e^a = \left(1 - \frac{z_g}{\Delta z}\right) V(\omega) + \frac{\Delta z E_{0z} \exp(-j\Delta z k_z^i)}{2}$$
$$+ \frac{1}{2\pi(b-a)} \int\limits_{r=a}^{b} \int\limits_{\phi=0}^{2\pi} (r-b) \left(E_{0x} \cos \phi + E_{0y} \sin \phi\right) d\phi dr. \tag{G.82}$$

Bibliography

[1] E. S. A. M. Lepelaars, *Electric Current Calculations for Thin Wire Configurations with Exact Kernel*, TNO Report, TNO-DV 2008 A069, February 2008.

[2] G.J. Burke and A.J. Poggio, *Numerical Electromagnetics Code (NEC4), Method of Moments, Part I: User's Manual*, Lawrence Livermore Laboratories, January, 1992.

[3] G.J. Burke and A.J. Poggio, *Numerical Electromagnetics Code (NEC4), Method of Moments, Part II: Program Description: Theory*, Lawrence Livermore Laboratories, January, 1992.

[4] A. Poggio and E. K. Miller, "Integral equation solutions of three-dimensional scattering problems", in *Computer Techniques for Electromagnetics*, R. Mittra (ed.), New York: Ed. Pergamon, pp. 159–264, 1973.

[5] R. F. Harrington, *Field Computation by Moment Methods*, New York: IEEE Press, 1993.

[6] O. C. Zienkiewicz and R. L. Taylor, *The Finite Element Method - Fourth Edition - Vol. 1 - Basic Formulation and Linear Problem*, London: McGraw-Hill, 1989.

[7] B. P. Rynne, "Convergence of Galerkin method solutions of the integral equation for thin wire antennas", *Adv. Comp. Math.*, Vol. 12, pp. 251–259, 2000.

[8] A. F. Peterson, S. L. Ray and R. Mittra, *Computational Methods for Electromagnetics*, New York: IEEE Press Series on Electromagnetic Wave Theory, 1998.

[9] H. C. Pocklington, "Electrical oscillations in wires", *Proc. Cambr. Phil. Soc.*, pp. 324–332, 1897.

[10] E. Hallén, "Theoretical investigations into the transmitting and receiving qualities of antennae", *Nova Acta Regiae Societatis Scientiarum Upsaliensis*, Vol. 11, series IV, 1938.

[11] F. Edelvik et. al., "An unconditionally stable subcell model for arbitrarily oriented thin wires in the FETD method", *IEEE Trans. Antennas and Propagat.*, Vol. 51, No. 8, pp. 1797–1805, Aug. 2003.

[12] J. Nadobny et. al., "A thin-rod approximation for the improved modeling of bare and insulated cylindrical antennas using the FDTD method", *IEEE Trans. Antennas and Propagat.*, Vol. 51, No. 8, pp. 1780–1796, Aug. 2003.

[13] A. G. Tijhuis, Z. Q. Peng and A. Rubio Bretones, "Transient excitation of a straight thin-wire segment: a new look at an old problem", *IEEE Trans. Antennas and Propagat.*, Vol. 40, No. 1, pp. 1132–1146, Oct. 1992.

[14] M. C. van Beurden and A. G. Tijhuis, "Analysis and regularization of thin-wire integral equation with reduced kernel", *IEEE Trans. Antennas and Propagat.*, Vol. 55, No. 1, pp. 120–129, Jan. 2007.

[15] P.J. Davies, D. B. Duncan and S. A. Funken, "Accurate and efficient algorithms for frequency domain scattering from a thin wire", *Journal of Computational Physics*, Vol. 168, pp. 155–183 , March 2001.

[16] D. R. Wilton, S. S. M. Rao and A. W. Glisson, *Electromagnetic Scattering by Surface of Arbitrary Shape*, Technical Report, RADC-TR-79-325, Rome Air Development Center, Griffiths AFB, NY, 1980.

[17] D. R. Wilton, S. S. M. Rao and A. W. Glisson, "Electromagnetic scattering by surface of arbitrary shape", *IEEE Trans. Antennas and Propagat.*, Vol. 30, No. 3, pp. 409–418, May 1982.

[18] P. Ylä-Oijala and M. Taskinen, "Calculation of CFIE impedance matrix elements with RWG and $n\times$ RWG functions", *IEEE Trans. Antennas and Propagat.*, Vol. 51, No. 8, pp. 1837–1846, Aug. 2003.

[19] P. Arcioni, M. Bressan and L. Perregrini, "On the evaluation of double surface integrals arising in the application of the boundary integral method to 3-D problems", *IEEE Trans. Microwave Theory and Tech.*, Vol. 45, No. 3, pp. 436–439, March 1997.

[20] E. H. Newman and D. M. Pozar, "Electromagnetic modeling of composite wire and surface geometries", *IEEE Trans. Antennas and Propagat.*, Vol. 26, No. 6, pp. 784–788, Nov. 1978.

[21] D. M. Pozar and E. H. Newman, "Analysis of a monopole mounted near or at the edge of a half-plane", *IEEE Trans. Antennas and Propagat.*, Vol. 29, No. 3, pp. 488–495, May 1981.

[22] B. M. Kolundžija and B. D. Popović, "General localised junction model in the analysis of wire-to-plate-junctions", *IEE Proc. Microw. Antennas and Propagat.*, Vol. 141, No. 1, Feb. 1994.

[23] G. A. Thiele and T. H. Newhouse, "A hybrid technique for combinig moment methods with the geometrical theory of diffraction", *IEEE Trans. Antennas and Propagat.*, Vol. 23, No. 1, pp. 62–69, Jan. 1975.

[24] A. B. Smolders, *Microstrip Phased-Array Antennas: A Finite-Array Approach*, Ph.D. Dissertation, Eindhoven University of Technology, Eindhoven, Oct. 1994.

[25] M. C. van Beurden, *Integro-differential Equations for Electromagnetic Scattering: Analysis and Computation for Objects with Electric Contrast*, Ph.D. Dissertation, Eindhoven University of Technology, Eindhoven, Sept. 2003. [Online]. Available: http://www.darenet.nl

[26] Y. Rahmat-Samii, "Genetic algorithm (GA) and particle swarm optimization (PSO) in engineering electromagnetics", *Proc. of* 17*th ICECom*, 1–3 Oct. 2003, Dubrovnik, Croatia.

[27] Y. Rahmat-Samii and C. C. Christodoulou, "Guest editorial for special issue on synthesis and opimization techniques in electromagnetics and antenna design", *IEEE Trans. Antennas and Propagat.*, Vol. 55, No. 3, pp. 518–522, March 2007.

[28] A. Rogovich, C. Marasini et. al., "Design of wire antennas by using an evolved particle swarm optimization algorithm", *Proc. of ICEAA '07 - International Conference on Electromagnetics in Advanced Application*, 17–21 Sept. 2007, Torino, Italy.

[29] E. K. Miller, A. J. Poggio, and G. J. Burke, "An integro-differential equation technique for the time-domain analysis of thin wire structures", *Journal of Computational Physics*, Vol. 12, pp. 24–48, May 1973.

[30] C. M. Butler and D. R. Wilton, "Analysis of various numerical techniques applied to thin-wire scatterers", *IEEE Trans. Antennas and Propagat.*, Vol. 23, No. 4, pp. 534–540, July 1975.

[31] A. G. Tijhuis, "Iterative techniques for the solution of integral equations in transient electromagnetic scattering", J. A. Kong and T. K. Sarkar, editors, *PIER 5: Application of Conjugate Gradient Method to Electromagnetics and Signal Analysis*, pp. 455–538, New York: Elsievier Science Publishing Co., 1991.

[32] R. C. J. Smets, *Electromagnetic Excitation of a Thin Wire. An Analytic Approach*, M.Sc. Thesis, Eindhoven University of Technology, Eindhoven, 1994.

[33] D. S. Jones, *The Theory of Electromagnetics*, Oxford: Pergamon Press Ltd., 1964.

[34] D. S. Jones, "Traveling waves on a wire", *The Arabian Journal for Science and Engineering*, Vol. 17, No. 4B, pp. 541–563, 1992.

[35] B. P. Rynne, "The well-posedness of the integral equations for thin wire antennas", *IMA J. Appl. Math.*, Vol. 49, Part H, pp. 35–44, 1992.

[36] B. P. Rynne, "On the well-posedness of Pocklington's equation for a straight wire antenna and convergence of numerical solutions", *Journal of Electromagnetic Waves and Applications*, Vol. 14, No. 11, pp. 1489–1503, 2000.

[37] B. P. Rynne, "The well-posedness of the integral equations for thin wire antennas with distributional incident field", *Quart. J. Mech. Appl. Math.*, Vol. 52, pp. 489–497, 1999.

[38] D. J. Jones, "Note on the integral equation for a straight wire antenna", *IEE Proceedings*, Vol. 128, Part H, pp. 114–116, 1981.

[39] M. Abramowitz and I. A. Stegun, *Handbook of Mathematical Functions with Formulas, Graphs and Mathematical Tables*, New York: Dover Publications Inc., 1970.

[40] H. A. van der Vorst, "Bi-CGSTAB: a fast and smoothly converging variant of Bi-CG for the solution of nonsymmetric linear systems", *SIAM Journal Sci. Stat. Comput.*, Vol. 13, No. 2, pp. 631–644, March 1992.

[41] C. Marasini, *Analisi di un Antenna a Microstriscia su Substrato Dielettrico Utilizzando il Metodo Ibrido CG-FFT*, M.Sc. Thesis, Faculty of Telecommunication Engineering, University of Pisa, Pisa, 2001.

[42] R. Barrett et al., *Templates for the Solution of Linear System: Building Blocks for Iterative Methods*, Aug. 2006. [Online]. Available: http://www.siam.org/books

[43] G. H. G. Golub and C. F. Van Loan, *Matrix Computations*, Baltimore and London, The Johns Hopkins University Press, 1996.

[44] D. R. Wilton and C. M. Butler, "Efficient numerical techniques for solving Pocklington's equation and their relationships to other methods", *IEEE Trans. Antennas and Propagat.*, Vol. 24, No. 1, pp. 83–86, Jan. 1976.

[45] A. Kaw, *Textbook Notes of Romberg Rule of Integration*, Dec. 2007. [Online]. Available: http://numericalmethods.eng.usf.edu

[46] R. C. Jonson and H. Jasik, *Antenna Engineering Handbook*, New York: McGraw-Hill, 1961.

[47] L-C. Shen, "An experimental study of the antenna with nonreflecting resistive loading", *IEEE Trans. Antennas and Propagat.*, Vol. 15, No. 5, pp. 606–611, Sept. 1967.

[48] B. D. Popović and M. B. Dragović, "Simple broadband cylindrical antenna with quasidistributed capacitive loading", *Electronics Letters*, Vol. 8, No. 6, pp. 148–149, March 1972.

[49] B. D. Popović, M. B. Dragović and A. R. Djordjević, *Analysis and Synthesis of Wire Antennas*, Letchworth: Research Studies Press, 1983.

[50] C. E. Baum, "The singularity expansion method", *Topics in Applied Physics: Transient Electromagnetic Fields*, Editor: L. B. Felsen, Vol. 10, pp. 129–179, 1976.

[51] C. E. Baum, "On the singularity expansion method for the solution of electromagnetic interaction problems", *Interaction Notes 88*, Kirtland: Air Force Weapons Laboratory, Dec. 1971.

[52] C. E. Baum, "The singularity expansion method: background and developments", *IEEE Antennas and Propagat. Society Newsletter*, Vol. 28, No. 4, pp. 14–23, Aug. 1986.

[53] F. M. Tesche, "On the analysis of scattering and antenna problems using the singularity expansion technique", *IEEE Trans. Antennas and Propagat.*, Vol. 21, No. 1, pp. 53–62, Jan. 1973.

[54] F. M. Tesche, "Application of the singularity expansion method to the analysis of impedance loaded linear antennas", *Sensor and Simulation Note 177*, New Mexico: The Dikewood Corporation Albuquerque, May 1973.

[55] W. H. Press et. al., *Numerical Recipes in FORTRAN 77: The Art of Scientific Computing. Vol. 1 of Fortran Numerical Recipes*, Cambridge University Press, 1992.

[56] C. Marasini, E. S. A. M. Lepelaars and A. P. M. Zwamborn, "Analysis of the resonant behavior of a complex loaded wire by using the Exact Kernel MoM", *Proc. of ICEAA '05 - International Conference on Electromagnetics in Advanced Application*, 12–16 Sept. 2005, Torino, Italy.

[57] A. G. Tijhuis, M. C. van Beurden and A. P. M. Zwamborn "Using extrapolation in the iterative solution of scattering problems with a varying parameter", *Proc. of the XXVIIth General Assembly of the International Union of Radio Science URSI*, 2002, Maastricht, The Netherlands.

[58] G. B. Arfken and H. J. Weber, *Mathemathical Methods for Physicists-Fourth Edition*, San Diego: Academic Press, 1995.

[59] R. Mittra and L. W. Pearson, "A variational method for efficient determination of SEM poles", *IEEE Trans. Antennas and Propagat.*, Vol. 26, No. 2, pp. 354–358, March 1978.

[60] A. G. Tijhuis, *Electromagnetic Inverse Profiling: Theory and Numerical Implementation*, Utrecht: VNU Science Press, 1987.

[61] C. Marasini, E. S. A. M. Lepelaars and A. P. M. Zwamborn, "Interpolation algorithm for fast evaluation of EM coupling between wires", *EMTS 2007 International URSI Commission B - Electromagnetic Theory Symposium*, 26–28 July 2007, Ottawa, Canada.

[62] C. Marasini, E. S. A. M. Lepelaars and A. P. M. Zwamborn, "Efficient evaluation of EM coupling between wires by interpolation on a non-uniform grid", *Radio Science Journal*, 2008, submitted for publication.

[63] L. Xu, et al., "Spatial interpolation method for solution of electromagnetic scattering from objects located in half-space", *Proc. of 4th Int. Conf. on Microwave and Millimiter Wave Technology - ICMMT 2004* , 18–21 Aug. 2004, Beijing, China.

[64] A. Boag, E. Michielssen and A. Brandt, "Nonuniform polar grid algorithm for fast field evaluation", *IEEE Antennas and Wireless Propagat. Lett.*, Vol. 1, No. 1, pp. 142–145, 2002.

[65] J. Berntsen, T. O. Espelid and A. Genz "An adaptive multidimensional integration routine for a vector of integrals", revised version published *ACM Trans. Math. Software*, Vol. 17, pp. 452–456, 1991.

[66] *NAG Fortran Library Manual Set*, Oxford: Numerical Algorithms Group Ltd., 1997.

[67] A. C. Ludwig, "Wire grid modeling of surfaces", *IEEE Trans. Antennas and Propagat.*, Vol. 35, No. 9, pp. 1045–1048, Sept. 1987.

[68] J. H. Richmond, "A wire-grid model for scattering by conducting bodies", *IEEE Trans. Antennas and Propagat.*, Vol. 14, No. 6, pp. 782–786, Nov. 1966.

[69] W. C. Thacker, "A brief review of techniques for generating irregular computational grids", *Int. J. Num. Meths. in Eng.*, Vol. 15, No. 9, pp. 1335–1341, 1980.

[70] M. H. C. van Eeuwijk, *Evaluation of the Rao, Wilton and Glisson Basis Function for Application in Antenna Modelling*, TNO Report, Rep. FEL-98-S156, June 1998.

[71] A. M. F. Van de Water, *Integral Equations for Scattering by 3D-Objects of Arbitrary Shape*, M.Sc. Thesis, Eindhoven University of Technology, Eindhoven, Feb. 2002.

[72] D. A. Dunavant, "High degree efficient symmetrical Gaussian quadrature rules for the triangle", *Int. J. Num. Meths. in Eng.*, Vol. 21, pp. 1129–1148, 1985.

[73] S. N. Makarov, *Antenna and EM Modeling with MATLAB*, Wiley-Interscience, New York: J. Wiley and Sons, 2002.

[74] F. Çalişkan and A. F. Peterson, "The need for mixed-order representations with the locally corrected Nyström method", *IEEE Antennas and Wireless Propagat. Lett.*, Vol. 2, pp. 1537–1537, 2003.

[75] D. M. Pozar and E. H. Newman, "Analysis of a monopole mounted near an edge or a vertex", *IEEE Trans. Antennas and Propagat.*, Vol. 30, No. 3, pp. 401–408, May 1982.

[76] S. U. Hwu, D. R. Wilton and S. M. Rao, "Electromagnetic scattering and radiation by arbitrary conducting wire/surface configurations", *1988 International Symposium Digest-Antennas and Propagat.*, Syracuse, NY, June 1988.

[77] S. U. Hwu and D. R. Wilton, *Electromagnetic Scattering and Radiation by Arbitrary Configurations of Conducting Bodies and Wires*, Technical Document 1325, Applied Electromagnetic Laboratory, Department of Electrical Engineering, University of Houston, Aug. 1988.

[78] J. F. Shaeffer and L. N. Medgyesi-Mitschang, "Radiation from wire antennas attached to bodies of revolution: the junction problem", *IEEE Trans. Antennas and Propagat.*, Vol. 29, No. 3, pp. 479–408, May 1987.

[79] C. A. Balanis, *Antenna Theory - Analysis and Design*, New York: J. Wiley and Sons, 1982.

[80] S. R. Best, "A discussion on the properties of electrically small self-resonant wire antennas", *IEEE Antennas and Propagation Magazine*, Vol. 46, No. 6, pp. 9–22, Dec. 2004.

[81] L. Mattioni and G. Marrocco, "Design of a broadband HF antenna for multimode naval communications", *IEEE Antennas and Wireless Propagat. Lett.*, Vol. 4, pp. 179–182, 2005.

[82] A. Boag et. al., "Design of electrically loaded wire antennas using genetic algorithms", *IEEE Trans. Antennas and Propagat.*, Vol. 44, No. 5, pp. 687–695, May 1996.

[83] J. Kennedy and R. C. Eberhart, "Particle swarm optimization", *Proc. IEEE Conf. Neural Networks IV*, pp. 1942–1948, 1995, Piscataway, NJ.

[84] J. Robinson and Y. Rahmat-Samii, "Particle swarm optimization in electromagnetics", *IEEE Trans. Antennas and Propagat.*, Vol. 52, No. 2, pp. 397–407, Feb. 2004.

[85] Z. Altman, R. Mittra and A. Boag, "New design of ultra wide-band communication antennas using a genetic algorithm", *IEEE Trans. Antennas and Propagat.*, Vol. 45, No. 10, pp. 1494–1501, Oct. 1997.

[86] H. Hancock, *Theory of Elliptic Functions*, Dover, 1958.

[87] G. Almkvist and B. Berndt, "Gauss, Landes, Ramanujan, the arithmetic-geometric mean, ellipses, π and the ladies diary", *American Mathematical Monthly*, Vol. 95, No. 7, pp. 585–608, Aug.–Sep. 1988.

[88] M. C. Bonnet, *Boundary Integral Equation Methods for Solids and Fluids*, New York: J. Wiley and Sons, 1995.

[89] P.M. Morse and H. Feshbach, *Methods of Theoretical Physics-Part I*, New York: McGraw-Hill Book Company Inc, 1953.

Summary

Efficient computation techniques for Galerkin MoM antenna design

In this thesis, an appropriate computational method for the modeling and the synthesis of wire antennas is formulated. To this end, we study the electromagnetic behavior of structures consisting of wires, surfaces and wire-surface junctions which represent the three key elements of our modeling tool. The basis of this method is the Electric Field Integral Equation (EFIE), which is numerically solved with the Galerkin Method of Moments (MoM). A system of linear equations is formulated and numerically solved by a Conjugate Gradient (CG) iterative scheme. In general, MoM matrix elements express the interaction between a "source" element (support of a basis function) and an "observation" element (support of a testing function). In particular, interactions between source and observation points belonging to the same geometrical support are referred to as self terms and correspond to diagonal matrix elements.

The first problem is the calculation of the total current along a single wire illuminated by an incident plane wave and/or fed by a delta-gap voltage source. The motivation for considering only the total current is that this quantity governs the behavior of the scattered field. We have presented two thin-wire integro-differential equations, namely Pocklington's equation with reduced kernel and Pocklington's equation with exact kernel. As known from the literature, the exact kernel exhibits a singular behavior when the distance between the source and the observation points goes to zero. By combining a singularity extraction and a Landen transform, we have developed a numerical method to compute accurately the total current distribution along a wire. We have found in many examples that by refining the discretization, results obtained by a reduced-kernel formulation show oscillatory behavior near the end faces of the wire and where the delta-gap voltage is applied. In contrast with this anomalous behavior, our results show a stable behavior. We conclude therefore, that

the numerical effort in handling the exact-kernel singularity is well rewarded. Besides, by means of a convergence study of a wire current distribution, an estimation of the discretization error introduced by the Method of Moments can be given and analyzed.

Aiming at the design of wire antennas, broadband performance can be achieved by loading antennas with RLC circuits represented by complex valued impedance loads. Consequently, our numerical code has been extended to the analysis of wires loaded with lumped as well as distributed loadings. In this case the generalized MoM matrix can be regarded as a sum of a matrix corresponding to the unloaded wire configuration and a (sparse) matrix that includes the effects of the loading.

Moreover, the numerical method for the analysis of (unloaded and loaded) thin wires has been extended to calculate natural frequencies of this kind of structures. This analysis is performed in the complex plane of Laplace's variable s. Examining how these poles change their locations in the complex s-plane when some characteristic parameters (e.g., length-radius wire ratio, discretization number, impedance profile, etc.) are varied gives an insight into the electromagnetic behavior of wires. Natural frequencies are obtained by performing the Singular Value Decomposition (SVD) of the MoM matrix together with a suitable searching algorithm. In particular, for loaded wires, by gradually increasing the impedance value, a marching-on-in-loading approach is adopted. Since the SVD method gives also useful information to characterize the time-domain current, it represents a valid alternative to more conventional methods such as searching zeros of the MoM-matrix determinant. By comparing natural frequencies of an unloaded thin wire as calculated by our numerical scheme with those in the literature, an agreement of about one percent is found. Additionally, this study offers a further validation of the proposed method.

Next, we have discussed the electromagnetic interaction between two or more arbitrarily oriented wires. In general, the current along a "source" wire radiates a field which illuminates all the other "observation" wires. In particular this field can be regarded as generated by a current on the source wire axis (thin-wire axis approximation) or by a current along the source wire mantle (thin-wire mantle approximation). The first approach leads to a one-dimensional integration while the second approach requires a two-dimensional integration. An additional double integral is needed for the evaluation of the current induced along the observation wire mantle. The two approaches have been investigated and compared in terms of accuracy and CPU time. From the results, it is concluded that the axis approximation is considerably less expensive than the mantle approximation. Besides, the RMS error introduced by the thin-wire approximation is usually negligible compared to the discretization error introduced by the Galerkin Method of Moments. On the other hand, for the mantle approximation we have also presented an interpolation algorithm that

significantly reduces the computation time involved in the coupling matrix evaluation.

The second problem is the calculation of the current distribution on an open surface illuminated by an incident plane wave. In this case, the well-known Rao-Wilton-Glisson (RWG) functions (defined over triangular domains) are used as basis and testing functions in the Method of Moments, this leads to two times two-dimensional integrals in the computation of system matrix elements. Taking advantage of the existing literature, we have implemented efficient algorithms to deal with all the occurring singularities. Moreover, by means of numerical examples we have investigated how the grid of points selected to represent the surface current can influence the final result.

The third problem concerns the study of the electromagnetic interaction between wires and open surfaces including the wire-surface connection. To describe the physical behavior of the current distribution in the neighborhood of a wire-surface junction, a proper basis function (attachment mode) has been introduced. As a consequence, the interaction between three types of basis functions needs to be computed: rooftop basis functions along wire segments, RWG basis functions on triangular patches and the attachment mode. The resulting evaluation of MoM matrix elements leads to four-dimensional integrals whose integrands exhibit a singular behavior when source and observation points coincide. The increased numerical complexity of the problem is reduced by using analytical techniques in the treatment of all integrable singularities. The test cases analyzed show numerical results in agreement with the literature. However, code efficiency can be improved by implementing dedicated (ad-hoc) routines beneficial for a further reduction of computation time.

Finally, the developed numerical code has been embedded in a stochastic optimization algorithm (Particle Swarm Optimization) for the synthesis and design of loaded wire antennas. As practical design problem, a loaded monopole over a ground plane operating in a wide frequency range with a high gain level and a specified VSWR is studied. Positions and (R,L,C) values of the loadings are optimization parameters in the PSO algorithm which is used to synthesize a suitable configuration fulfilling the specifications. To enhance efficiency in terms of computation time, we have proposed a tailored scheme for the computation of MoM matrix elements. Besides, we have described an improved procedure for the velocity update of the swarm's particles in the PSO algorithm. The improved convergence appears evident in the presented results where stagnation in local minima is avoided.

Samenvatting

Efficient computation techniques for Galerkin MoM antenna design

In dit proefschrift wordt een geschikte rekenmethode voor het modelleren en de synthese van draadantennes geformuleerd. Deze rekenmethode is in staat om objecten bestaande uit draden, oppervlakten en draden aangesloten op oppervlakten te modelleren. Met deze drie belangrijke basiselementen kunnen we het gedrag van complexe elektromagnetische structuren nauwkeurig bestuderen en uiteindelijk voorspellen. De basis van de methode wordt gevormd door de bekende Electric Field Integral Equation (EFIE), die numeriek wordt opgelost met behulp van de Galerkin Momenten Methode (MoM). Deze methode levert een systeem van lineaire vergelijkingen dat vervolgens numeriek wordt opgelost door een iteratieve Conjugeerde Gradiënten (CG) methode. De elementen van de MoM matrix representeren de interactie tussen een "bron"-element dat wordt gedefinieerd door een basisfunctie en een "waarnemings"-element dat wordt beschreven door een testfunctie. De diagonaal-elementen zijn de zogenaamde zelf-termen en treden op als de bron- en observatiepunten corresponderen met hetzelfde geometrische element.

Het eerste probleem dat in dit proefschrift wordt beschouwd betreft de berekening van de geïnduceerde stroom langs een enkele draad welke wordt belicht door een vlakke, invallende golf en/of door een excitatie met de zogenaamde delta-gap spanningsbron. De motivatie voor het berekenen van de geïnduceerde stroom is dat, als deze bekend is, het verstrooide veld in de volledige driedimensionale ruimte kan worden berekend. We hebben de keuze uit twee dunne-draad integro-differentiaalvergelijkingen, namelijk de vergelijking van Pocklington met gereduceerde kern en de vergelijking van Pocklington met de exacte kern. Zoals bekend uit de literatuur heeft de exacte kern een singulariteit wanneer de afstand tussen de bron- en de observatiepunt naar nul gaat. Door het singuliere gedrag af te trekken van de integrand en door gebruik te maken van de Landen transformatie ver-

krijgen we een nauwkeurige numerieke methode om de totale geïnduceerde stroom langs een draad te berekenen. In het onderzoek is geconstateerd dat bij het verfijnen van de discretisatie, de numerieke resultaten met de gereduceerde kern zowel aan de uiteinden van de draad als bij de delta-gap spanningsbron oscillerend gedrag vertonen. Onze numerieke resultaten vertonen dit instabiele gedrag niet. Daarom mag worden geconcludeerd dat de extra numerieke bewerkingen bij de berekening van de complexere exacte-kern singulariteit de moeite waard zijn. Een schatting van de discretisatiefout die wordt veroorzaakt door de Momenten Methode is door middel van een convergentiestudie van de geïnduceerde stroom op een draad uitgevoerd en nader toegelicht.

Bij het ontwerpen van breedband draadantennes worden in de regel parallel- of serieschake-lingen van discrete weerstanden (R), spoelen (L) en condensatoren (C) gebruikt. De nu-merieke code is uitgebreid om de elektromagnetische analyse van dradenstructuren met deze discrete RLC-elementen te kunnen uitvoeren. Dit is verkregen door de introductie van een gegeneraliseerde MoM systeemmatrix die de som is van de originele MoM systeem-matrix en een sparse matrix die specifiek hoort bij de numerieke discrete RLC-elementen. De numerieke implementatie is gebruikt om de natuurlijke frequenties van dunne draad-structuren te analyseren. Deze analyse is uitgevoerd in het complexe Laplace domein met complexe variabele s waar de polen in het complexe vlak overeenkomen met de natuur-lijke frequenties van het systeem. Onderzocht is welke contour deze polen in het complexe vlak doorlopen waarbij een aantal karakteristieke parameters (bijvoorbeeld lengte/straal verhouding van de draad, aantal discretisatie elementen, impedantie-profiel, enz.) zijn gevarieerd. Dit onderzoek heeft inzicht in het elektromagnetische gedrag van dergelijke draadstructuren gegeven. De natuurlijke frequenties zijn berekend door gebruik te maken van de Singular Value Decomposition (SVD) van de MoM matrix gecombineerd met een geschikt zoekalgoritme. Voor draden met complexe impedanties is, door geleidelijke ver-hoging van de waarde van de weerstand, de marching-on-in-loading methode met succes toegepast. De SVD methode is een gebruikte methode en een geschikt alternatief voor de meer traditionele methoden zoals het zoeken van polen in de determinant van de MoM-matrix. We hebben de natuurlijke frequenties van een dunne draad zonder impedanties met onze methode berekend en die vergeleken met de literatuur. De resultaten stemmen binnen ongeveer een procent met elkaar overeen. Dit kan worden beschouwd als een extra validatie van de door ons ontwikkelde methode.

Vervolgens wordt de elektromagnetische interactie tussen twee of meer willekeurig georiën-teerde draden beschouwd. In het algemeen straalt een stroom op een "bron"-draadelement uit en belicht alle andere naburige "waarnemings"-draadelementen. Het invallend veld op het "waarnemings"-draadelement wordt veroorzaakt door een stroom op de as van de

"bron"-draad (dunne draad as-benadering) of door een stroom op de mantel van de "bron"-draad (dunne draad mantel-benadering). De eerste benadering leidt tot één ééndimensionale integratie, terwijl de tweede benadering één tweedimensionale integratie vereist. Een extra integratie is ook nodig voor de evaluatie van de geïnduceerde stroom op de mantel van de "waarnemings"-draad. Beide benaderingen zijn onderzocht en vergeleken in termen van nauwkeurigheid en CPU tijd. De benadering op de as van de draad is aanzienlijk efficiënter dan de benadering die uitgaat van de mantel van de draad. Daarbij komt dat de RMS-fout geïntroduceerd door de dunne-draad benadering doorgaans te verwaarlozen is ten opzichte van de discretisatiefout die wordt geïntroduceerd door het gebruik van de Galerkin Momenten Methode. Om de benaderingsmethode op de mantel efficiënter te maken hebben we een interpolatiealgoritme ontwikkeld, dat een aanzienlijke vermindering van de rekentijd van de berekening van de MoM systeemmatrix oplevert.

Het tweede probleem betreft de berekening van de oppervlaktestroomdichtheid op een open oppervlak dat wordt belicht door een vlakke invallende golf. In dit geval gebruiken we de bekende Rao-Wilton-Glisson (RWG) functies (gedefinieerd over driehoekige domeinen) als basis- en testfuncties in de Momenten Methode. Deze procedure leidt tot herhaalde tweedimensionale integralen bij de berekening van de MoM systeem matrixelementen. Uit de bestaande literatuur halen en gebruiken we efficiënte algoritmen om de integralen van de aanwezige singulariteiten te kunnen berekenen. Aan de hand van numerieke voorbeelden is door ons bovendien onderzocht welke invloed het gekozen grid van de RWG functies heeft op de berekening van de oppervlaktestroomdichtheid.

Het derde probleem heeft betrekking op de studie van de elektromagnetische interactie tussen draden en open oppervlakken, inclusief de draad/oppervlakte verbindingen. Het fysische gedrag van de oppervlaktestroomdichtheid in de buurt van een draad/oppervlakte knooppunt wordt verdisconteerd door een geschikte basisfunctie (met een knooppuntmodus voor de stroomverdeling) te ontwikkelen. Bij een dergelijk knooppunt dient de interactie tussen drie soorten basisfuncties te worden berekend: rooftop basisfuncties langs de draadsegmenten, RWG basisfuncties op driehoekige oppervlakken en de basisfunctie op de knooppuntmodus. De berekening van de MoM matrixelementen leidt tot vierdimensionale integralen waarvan de integranden een singulier gedrag vertonen als bron- en observatiepunt samenvallen. De toegenomen numerieke complexiteit van dit probleem is verkleind door gebruik te maken van analytische technieken om alle integreerbare singulariteiten op de juiste wijze te evalueren. De numerieke resultaten van de berekeningen zijn in overeenstemming met die in de literatuur. De computercode kan echter efficiënter worden gemaakt

door gebruik te maken van specifieke (ad-hoc) routines.

Tenslotte zijn de ontwikkelde numerieke routines in een stochastisch optimalisatie algoritme (Particle Swarm Optimalisatie) gebruikt om de synthese en het ontwerp van draadantennes met impedanties te onderzoeken. Als praktische testcasus is gebruik gemaakt van een monopool met meerdere complexe impedanties die is aangesloten op een vlak. Met specificaties zoals een hoge versterking en een breed frequentiebereik met een bepaalde staandegolfverhouding (VSWR) is de toepasbaarheid van dit ontwerptool onderzocht. De te optimaliseren parameters zijn de locaties van de impedanties evenals de (R, L, C) waarden. Deze parameters zijn in het PSO algoritme geoptimaliseerd om zodoende een configuratie te verkrijgen die aan de gestelde specificaties voldoet. Ter verbetering van de efficiëntie in termen van rekentijd, hebben wij een op maat gesneden schema voor de berekening van MoM matrixelementen gepresenteerd. Om de snelheid verder te verhogen is een verbeterde procedure voor de update-snelheid van de deeltjeszwerm in het PSO-algoritme geïntroduceerd. De verbeterde convergentie blijkt duidelijk uit de verkregen resultaten waarbij stagnatie in lokale minima wordt vermeden.

Curriculum Vitae

Cecilia Marasini was born in Lucca, Italy, on November 19, 1973. After she finished secondary school in 1992 at the Istituto Lorenzini in Pescia, she started as a student in Telecommunication Engineering at the University of Pisa. From March until September 1999, with an award from the European "Socrates Free Movers" Scholarship she had the opportunity to be a guest student at the Electromagnetic Department of Chalmers University of Technology in Göteborg, Sweden. There, under the supervision of prof. P.-S. Kildal she performed part of her final project developing a software implementation of the CG-FFT numerical method for calculating the electromagnetic properties of conducting elements placed on, or embedded in, a multilayer planar structure. After an internship with Hewlett Packard, in May 2001 she received the M.Sc. degree in Telecommunication Engineering from the University of Pisa. From October 2001 until November 2003 she worked as a System/Software Engineer in the Motorola Technology Centre in Torino, where she was involved in the integration of dual-mode UMTS/GSM terminals in mobile service networks working on interoperability testing process. Her interest in applied electromagnetic research took her back to the academic world, and from January 2004 to December 2007 she carried out her Ph.D. project at TNO under the supervision of prof. A.G. Tijhuis, prof. A.P.M. Zwamborn and dr. E.S.A.M. Lepelaars. Since March 2008, she is employed at TNO as a research scientist in the Radar and Electronic Warfare group.

Acknowledgements

If I would look at these four years all at once, I would spontaneously exclaim: "what a learning experience!". Without the generous help of many persons this accomplishment could never be achieved: to them I would like to express my gratitude.

First and foremost, I would like to thank my supervisors at TNO: prof. Peter Zwamborn and dr. Eugene Lepelaars. Your encouragement and trust have supported me during these four years. You both were able to maintain the aim of the project alive. Thank you for all the suggestions and help from electromagnetics to life matters. Peter, thank you for coaching me in my personal development, increasing my assertiveness and self confidence. Eugene, I thank you for being such a good roommate, colleague, and a trustworthy friend. Besides I am very grateful for the many stimulating discussions, in which you showed your contagious enthusiasm and shared your mathematical and electromagnetic skills. Thank you for the long evening hours invested in revising my work.

I would like to express my gratitude to prof. Anton Tijhuis, the chief of the Electromagnetic Section at the Technical University of Eindhoven, my examiner and promotor, for his guidance and support throughout the writing and the revision of this dissertation. Thank you for your critical and original points of view which helped me in reformulating and clarifying some concepts on this thesis.

Thank you to ir. Jeroen Dezaire, the group leader of the Radar and Electronic Warfare Group at TNO for giving me the opportunity to finish writing this thesis, while having started as employee at TNO.

Special thanks go to dr. Stefan Vossen, whose supportive attitude provided me with a more clear vision of the role of a researcher at TNO. To dr. Rik Naus, for the interesting discussion and for theoretical comments on my research. To ir. Jan Punt and ir. Jan Rhebergen for helping me with LaTeX and Gnuplot.

I am thankful to my present and previous colleagues of the Radar and Electronic Warfare Group at TNO who contribute to create a pleasant atmosphere to work in. My gratitude goes also to those people who have given a friendly air during lunchtime, let me mention

Arnold, Yolanda, Aad, Arne, Laura, Onno, Rob, Wim, but there are many more.

I would also like to thank dr. Andrea Neto for being the first contact point with my supervisors, prof. Giampiero Gerini for being a "bridge" to Eindhoven during the last few months and dr. Stefania Monni who has given me suggestions in organizing the promotion. Thank you very much to all the Electromagnetic Section at the Technical University of Eindhoven. Even if we have not seen nearly often, basically at gatherings and conferences, I always enjoy the good time spent with you. In particular, I owe a great deal of gratitude towards dr. Martijn van Beurden for the very helpful suggestions and fruitful discussions on the topics covered by this thesis. I regard you as more than a good colleague. Thank you dr. Frank van de Water for allowing me to experiment with your software for the planar surface.

I would like to thank ir. Bart van Leersum, former colleague at TNO (currently with the Defense Material Organization) for his practical and engineering view providing me useful inputs for wire-antennas' design. Many thanks to ir. Bryan Tjon Kam at the Defense Material Organization for his supportive attitude concerning this research work.

I am indebted to dr. Alessandro Rogovich, of the Microwave and Radiation Laboratory Department of the University of Pisa, for the many conversations even in front of a pizza and for initiating me into the stochastic optimization world, which formed the basis for Chapter 9 of this thesis.

My sincere thanks go to prof. Giuliano Manara, prof. Agostino Monorchio and prof. Angelo Freni who were my Italian principal former teachers in the electromagnetic wave field theory and stirred up my interest towards research. Their courses formed a sound educational background to pursue a career in electromagnetic.

I would like to thank all my friends in the Netherlands, especially Elly and Marco, who make me enjoy my free time, whose friendship I can always count on.

Very special thanks go to my parents Giuseppina and Pieralberto for their moral support, always believing in me and constantly encouraging me to go forward.

My thanks go to my cousin Claudia, who during these four years has shared with me the "feelings" of being a PhD student, spurring on, the one with the other, we have made the same steps towards the accomplishment of our research works.

Last but not least, thank you Luca, for being simply Luca, for weathering my major crisis of confidence, for never doubting. Your smile and unconditional love owed my gratitude. This work would not be without you.